System Configuration and Control Using Hydraulic Transformers

A DISSERTATION
SUBMITTED TO THE FACULTY OF THE GRADUATE SCHOOL
OF THE UNIVERSITY OF MINNESOTA
BY

Sangyoon Lee

IN PARTIAL FULFILLMENT OF THE REQUIREMENTS
FOR THE DEGREE OF
Doctor of Philosophy

Advisor: Dr. Perry Y. Li

May, 2018

Acknowledgements

This work is performed within the Center for Compact and Efficient Fluid Power (CCEFP) supported by the NSF under grant EEC-05040834. Component donations from Takako Industries, Parker Hannifin, and Sun Hydraulics are gratefully acknowledged. Sangyoon Lee was supported by a 2016-2017 Doctoral Dissertation Fellowship at the University of Minnesota.

I would like to extend my gratitude to everyone who has helped me along my Ph.D. Firstly, I thank my advisor Dr. Perry Y Li for all the learning opportunities I had in the lab. I gained so much invaluable experience and insights working with you. I also thank my committee members: Dr. Kim Stelson for being a chair in my committee and for valuable discussions in the CCEFP; Dr. James Van de Ven for taking his time for valuable discussions in my modeling and experimental works, and inviting me to his group meetings for even more discussions; and Dr. Demoz Gebre-Egziabher for teaching me valuable courses on the optimal estimation.

I would like to thank my fellow researchers, especially Pieter Gagnon. Without his insight and knowledge on the hardware aspect of the project, putting together a prototype and testbed would have taken much longer time. I also thank Mohsen Saadat, Kai Loon Cheong, Zhekang Du, Andrew Stewart for their collaboration and companionship throughout my Ph.D. career.

Thank you, Chris Hogan, John Gardner, Jennifer Dahal, and Richard Maharaj for your support within the department. I appreciate Mike Gust and Alyssa Burger for providing me with many valuable opportunities and guidance within the CCEFP. You have allowed me to gain so much valuable experience that will serve me well as I move to the next steps in my career.

Jay Ankeny at Eaton provided me with much practical insights on understanding axial piston pumps. Rachel Wang and Neng Piyabongkarn at Eaton provided me with an opportunity to apply my knowledge and learning in real-world applications.

I thank my family for being able to accomplish this milestone in my life. Thank you, my

sisters, Dr. Hyunju Lee (이현주) and Miju Lee (이미주) for raising me so well. I would not be standing here today without you. I also thank Dr. Yongwan Chun (전용완), Hyunju's husband and my brother-in-law, for his advice and support throughout my youth. Also thank you, my wife, Jeongeun Shin (신정은) for being there, helping me grow, giving me motivations to finish. We now take another step in our beautiful lives together.

Finally, I thank my late parents, Dr. Inchul Lee (이인철) and Younsik Shin (신연식) who would have been so proud of me for reaching this milestone. I dearly miss you.

Dedication

To my parents in heaven. To my wife.

Abstract

Hydraulic power transmission offers multiple benefits over competing technologies including an order of magnitude higher power density than electric systems, relatively low cost, fast response, and flexible packaging. Hydraulics are often used in high-performance mobile robots that demand power, precision, and compactness. However, typical hydraulic systems suffer from low system efficiency from the wide usage of throttle valves. The research described in this dissertation focuses on developing hydraulic transformers that transforms hydraulic power from one set of pressure and flow to the other set of pressure and flow to replace throttle valves such that a compact and efficient fluid power system can be realized.

A dynamic model capable of capturing operating characteristics and losses is developed to establish a quantitative comparison between two major designs of the hydraulic transformer. A traditional design where a pump and motor are coupled together in a single package is chosen for the research. This design has three possible configurations with unique operating characteristics, and if these configuration modes can be switched, the resulting transformer is shown to be more compact and efficient.

A trajectory tracking controller for a cylinder and force controller for a hydraulic human power amplifier is developed to demonstrate potential applications for the hydraulic transformer. The controller developed proves that utilizing hydraulic transformer need not sacrifice the control performance.

Control methodologies ensuring efficiency of the transformer driven system are developed. Transformer operating speed is optimized to minimize the power loss through the transformer. Transformer configuration is switched actively to operate the transformer in its most optimal mode. These methods further improve the efficiency benefit of using the transformer.

A hydraulic transformer system utilizing developed controllers compared against a throttle valve system tracking a trajectory with various loading conditions reveals that transformer system can achieve an efficiency of 81.2% which is more than threefold increase over the throttling system with an efficiency of 26.2%. This efficiency improvement is possible with the ability of a transformer to capture regenerative energy to reduce the net energy consumption. This dissertation successfully presents the controller development for a hydraulic transformer that captures both precision and efficiency.

Contents

List of Tables

List of Figures

Chapter 1

Introduction

1.1 Background

Hydraulics systems are fast, accurate and robust power transmission methods that use pressurized hydraulic fluid to power machineries. Their main advantage over other transmission methods is high power density: a hydraulic actuator is an order of magnitude lighter and smaller than an electric actuator of the same torque, force, or power. For this reason, they are widely used in high load, high force applications such as construction equipments and avionics.

Hydraulic systems are also finding their way into the next generation of application of human scale robots that assist and interact with humans [34] [57]. These robots must be powerful enough to do significant physical work, energetically independent (e.g. not limited by the length of power cord) and compact to be truly effective. For these applications, electric motors cannot provide the required power without becoming too bulky, making hydraulics the natural choice for this type of applications. However, the average efficiency for hydraulic systems, estimated to be only at 22% [63], poses a major barrier to employing hydraulics. With this low efficiency, the weight savings in the actuators are outweighed by the requirement for large and heavy battery packs.

For people unfamiliar with hydraulics, hydraulic systems are best explained by making analogies to electric circuits: pressure is like voltage and fluid flow rate is like current. In electrical circuits, multiple loads are plugged into a common supply power with a constant voltage. Often times, attached loads require voltage lower than the supplied voltage. For example, a typical mobile phone charger only needs 5V to charge the battery while the wall outlets provide 120V AC electricity in the United States. In such a case, an electrical transformer is used to adjust the voltage after rectifying the AC power into a DC power.

Using a large resistor for this purpose will be uneconomical, as it will dissipate most of the useful power simply into a heat. Equivalently in hydraulics, multiple actuators can connect to a common pressure rail (CPR) providing a constant pressure. Currently, when the required pressure is lower than the pressure of the CPR, throttling control valves are used to simply reduce the pressure, which is similar to attaching a resistor to reduce the voltage in an electric circuit. This is illustrated in Fig. 1.1 with a vertical line. This approach draws more power from the common pressure rail than what is needed from the actuator, and excess power is dissipated as heat in the throttling valve. This power loss is the largest contributor of inefficiency in hydraulic systems [63].

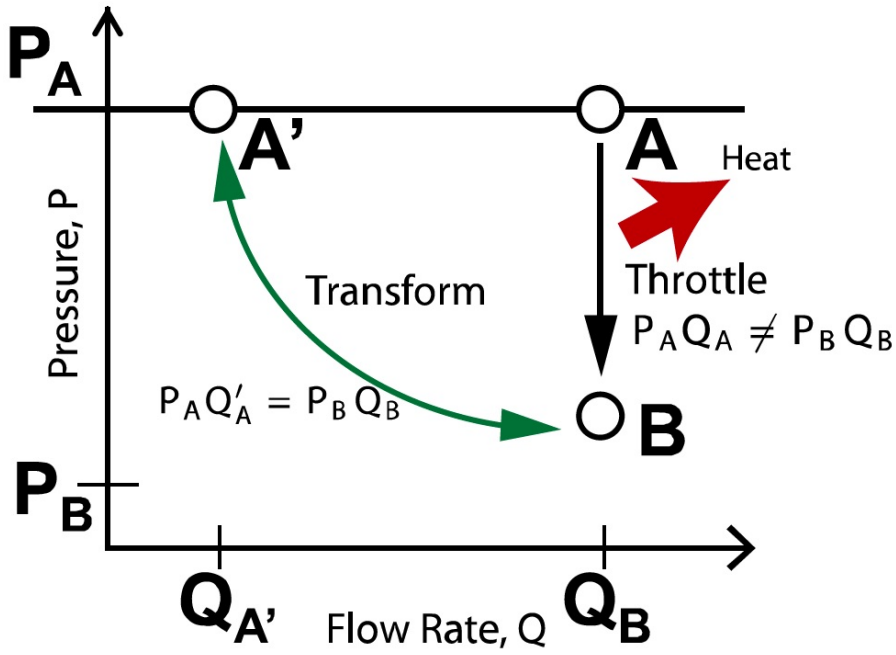

Figure 1.1: Pressure vs. Flow curve. Transformer allows pressure adjustment without power loss, whereas throttling makes the power loss inevitable

Hydraulic transformer is the hydraulic equivalence of an electric transformer that transforms hydraulic power at one pressure and flow combination to another pressure and flow combination while conserving power. This is similar to what an electrical transformer does for a set of voltage and current combinations and illustrated by the curved line on Fig. 1.1. One very important aspect of transformer is that it can increase (boost) as well as decrease (buck) pressure. This ability to boost pressure allows a lower common rail pressure to be used, which means smaller and lighter components could be utilized to improve efficiency. Since many losses increases with respect to the size of the machine, this can end up in reduced energy loss.

This ability to transform pressure also enables recuperation of braking energy. For instance, when a forklift lowers a load, the gravitational energy potential can be brought back to the common pressure rail to be reused by other actuators or stored for later usage.

Despite these advantages, hydraulic transformers have yet to replace throttling control valves. It is because throttling valves, despite being inefficient, offer compact packaging as well as fast and precise motion control performance. Previous attempts in developing hydraulic transformers have limited operating ranges that results in the transformers being bulky and inefficient. Also, whether transformers can achieve sufficiently high control performance has not been demonstrated. In order to fully replace the throttling control valves, it is essential that the hydraulic transformers be compact, efficient, and achieve fast and precise performance for their applications.

This dissertation is interested in utilizing aforementioned advantages and developing a hydraulic transformer that is capable of replacing throttling control valves. In the next section, a survey on previous literature discussing a hydraulic transformer is presented to reveal the current state-of-the-art in hydraulic transformer research, and to motivate the research objectives for this dissertation.

1.2 Literature Review

The most basic design of hydraulic transformer is by combining two axial piston pump and motor through a common shaft, as shown in Fig. 1.2. In this design, which is found in literature as early as in 1971 [48], the input flow drives the rotating group (D_1 unit) acting as a motor. This then drives the other unit (D_2 unit) on the same shaft acting as a pump.

$$J\dot{\omega} = \underbrace{(P_A - P_T)\frac{D_1}{2\pi}}_{\text{Motor}} + \underbrace{(P_T - P_B)\frac{D_2}{2\pi}}_{\text{Pump}} \tag{1.1}$$

$$\frac{P_B - P_T}{P_A - P_T} = \frac{D_1}{D_2} \tag{1.2}$$

Equation (1.1) describes the dynamic torque equation for the transformer shown in Fig. 1.2. If the transformer is at the steady state such that $\dot{\omega} = 0$, rearranging an equation reveals that difference in relative displacement between D_1 and D_2 units governs a pressure transformation as seen in Eq. (1.2). In this design, there are four ports serving three functions. By alternating the assigned function of the shared port, two additional configurations can be achieved using the same transformer as seen in Fig. 1.3.

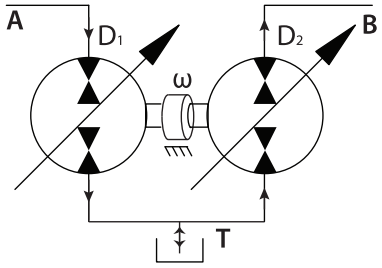

Figure 1.2: Hydraulic schematic for PM transformer with shared port connected to a return pressure line

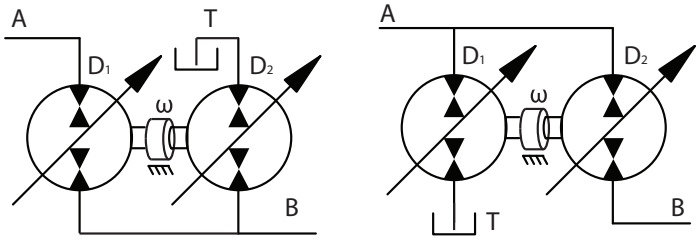

Figure 1.3: Two additional configurations are possible by altering port connections

Achten at al [2] (1997) claims this design is bulky and expensive as they propose their Innas Hydraulic Transformer (IHT), that combines the role of a pump and motor in a traditional transformer into a single displacement unit through the introduction of rotatable valve plate (Fig. 1.4). As the valve plate rotates, the relative flows ported to A, B, and T are varied within a single rotating group, eliminating the need to have a separate rotating group to have different input and output displacement. For example, if the rotation angle θ in Fig. 1.4 is 0 such that port A sits right on the top dead center (TDC), the net flow from port A will be zero. As the angle θ increases, the displacement of port A increases. At the same time, displacement of port B will decrease. Port T serves as a make-up port, giving extra flow when output flow is larger than input flow and taking extra flow when output port flow is smaller than input flow. This design promised compactness and efficiency coming from operating just a single rotating unit.

In addition to the hydraulic transformer based off from an axial piston rotating groups such as traditional pump and motor transformer or an IHT, there have also been various proposed ideas to develop hydraulic transformers from other design principles. Clarke (2001) proposed a hydraulic transformer utilizing variable displacement gear pumps [21]. By varying the distance between the drive gear and idler gear, displacement of gear pumps

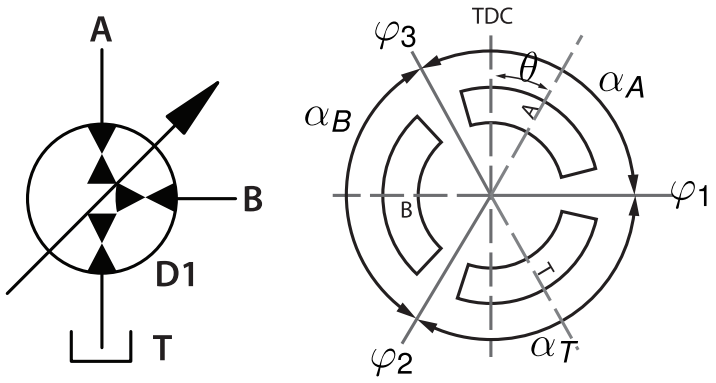

Figure 1.4: Hydraulic schematic for a IHT with its rotatable 3 ported valve plate

can be varied. Y. Kita (2002) from Hirose Valve Industry patented a radial pump transformer [46], where eccentricity of pumping pistons are altered to obtain variable displacement. D.C Hale (2002) from Caterpillar Inc developed a transformer using a pair of vane pump and motor. In this design, a displacement of one vane pump is varied by changing the eccentricity between its rotor and the pump housing. These designs all work in the same principle as PM transformer except that they are non-axial piston designs. On the other hand, E.D. Bishop (2012) utilized area differences of a stepped shaft to form a digital transformer [15]. In the digital transformer, a series of solenoids valves are placed strategically around the stepped shaft to utilize the appropriate pressure for the actuator being driven, as illustrated in Fig. 1.5. The area ratio in the stepped shaft and control of the valves placed around the stepped shaft govern the pressure transformation.

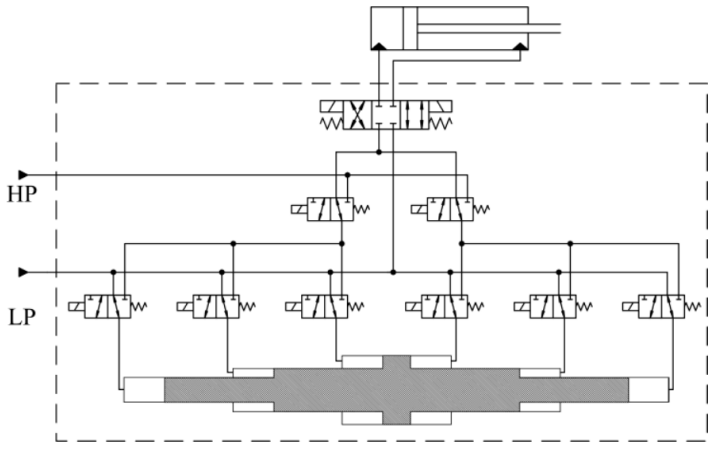

Figure 1.5: A digital transformer utilizing the area differences of a stepped shaft

However, these additional designs are only available as patents thus the description of

them are limited to what is available in patents, and no academic literature could be found on them except for digital hydraulic transformer [16]–[14]. Therefore the performance of these devices is not known and the major research focus will be on IHT and PM transformers that are both built on axial piston rotating groups in this dissertation.

Regardless of which particular design is being studied, the literature on hydraulic transformers can be roughly categorized into two major areas: (i) Design and analysis of a hydraulic transformer as a component and (ii) Configuration and/or Control of such component itself and/or within a system.

1.2.1 Design and Analysis of Hydraulic Transformer Component Itself

Since the introduction of the IHT in 1997, the majority of research works found on hydraulic transformers focus on the IHT concept to realize this new design in hydraulic systems. While a maximum unit efficiency of 88% is observed for the initial prototype, Vael et al (2000) [3] identified major challenges in making IHT a regular fluid power component to be noise, flow ripple, and the operating stability at the low shaft speed condition. Noise and flow ripple come from the fact that commutation from one port to the other mostly occurs outside the top and bottom dead centers of the piston movement for the IHT [3]. CFD simulations of IHT performed by Ma et al (2005) [40] confirms these findings. As a piston transitions from one port to the other, there is a moment where piston chamber volume is expanding at a rate faster than the incoming flow into the chamber. This moment leads to a local cavitation during piston transition from one port to the other, creating excessive noise and wear during operation. In order to address this problem, a shuttle technology is proposed by Achten et al (2001) [7]. In this approach, the 'shuttles', or small pistons that are free to move for a limited stroke between two end positions are introduced as illustrated in Fig. 1.6. Each end of the piston is one of the piston chambers in the cylinder barrel. At each end positions, the shuttle acts as a check valve, preventing two piston chambers from communicating each other. In between the two end positions, the shuttle acts as a piston, pushed by oil from a piston chamber with higher pressure. These shuttles act to alter the dead volume within the piston chamber during the commutation from one port to the other by about 10% of the volume of a single piston chamber and damp out the pressure spike and reduce cavitation. These shuttles are shown to improve the stability of IHT operation, and reduce noise at high shaft speeds. However, shuttles do not completely address the flow ripple problem in the IHT. Even with the reduced pressure spike, the fact that pistons transition from one port to another while the their flow is not at zero still contributes heavily to the flow ripple.

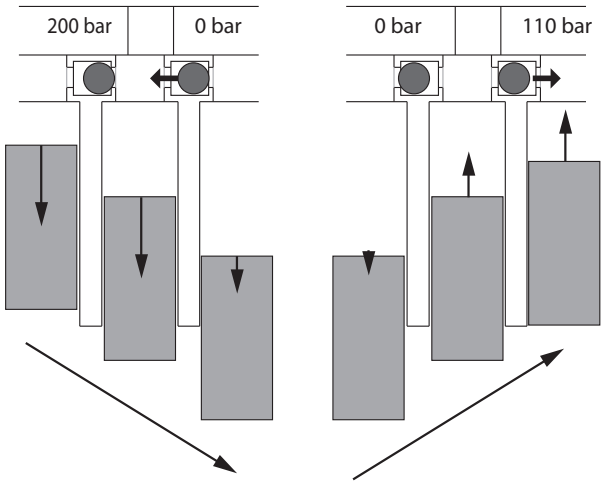

Figure 1.6: Shuttle behavior as it transitions from one port to the other, adapted from [7]

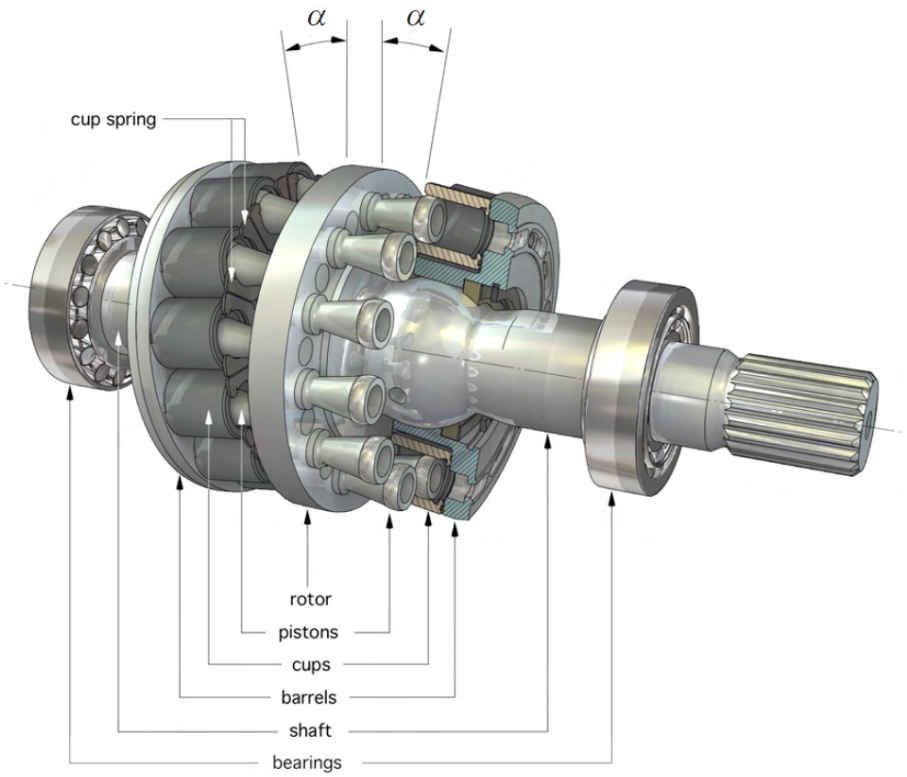

Figure 1.7: Exploded view of floating cup principle, taken from [8]

In order to address these fundamental drawbacks of IHT, Achten et al. (2002) [9] proposed a dedicated design for IHT, called a 'floating cup' principle. In this design principle shown in Fig. 1.7, there exist 24 displacement volumes equivalent to piston chambers in an axial piston pump, and the swashplate angle is only 9 degrees. Pistons are rigidly connected to a rotor, arranged in double ring configuration having one ring of pistons on each side of this rotor back-to-back. In place of piston chambers, there are free moving cuplike cylinders, which gives the floating cup principle its name. As the pistons interact with these cups without bushings, the friction in this area can be minimized. Combined with a reduced swashplate angle, it results in a low start-up torque. The higher number of pistons strongly reduces the flow ripple of the transformer, and is expected to reduce the noise produced by the transformer. In order to experimentally validate this new design principle, the floating cup design on a fixed displacement pump (2003, 2004) [11, 5] and variable displacement pump (2005) [8, 82] were developed for 28 cc/rev total displacement and showed up to 97% peak efficiency in experiments. However, only a simulation analysis is found for the floating cup IHT [6], with no evidence of working prototype floating cup IHT to this date. In [10], Achten et al. proposed an 'oiler transformer', which is an IHT built on their floating cup design. In an oiler transformer, the swash block is supported by a spherical bearing, which results in three rotational degrees of freedom. These extra degrees of freedom are expected to allow an unlimited control range of the IHT. The design principles are laid out with CAD drawings but no actual prototype was presented. How to precisely regulate the rotation of swash block in 3D manner is yet to be determined [10].

Although INNAS has produced extensive *qualitative* analysis of the operating mechanisms and losses in their transformer, documentation of rigorous simulation model and presentation of closed-form equation describing their transformer provided by them is quite limited in the open literature. Various other groups, especially ones in China, have undertaken efforts to understand and realize IHT on their own. Ma et al. from Zhejiang University (2005) [40] utilized a software package FLUENT to perform a Computational Fluid Dynamics (CFD) analysis for the flow and pressure distribution inside a prototype IHT that was built by modifying an existing bent axis pump. The simulation results were shown to correlate satisfactorily with their experiments on noise and the volumetric losses. They concluded that operating IHT at a low control angle below 60 degrees, which corresponds to a pressure transformation ratio below 0.5, will lead to local cavitation as piston commutates from one port to the other, creating excessive noise and wear during operation. Li et al. from Beijing Institute of Technology (2009) established a mathematical model to describe the efficiency of the prototype IHT built on a bent axis pump. They

create a model using a constant laminar coefficient of leakage, a coefficient of friction, and coefficient of viscous drag. The coefficients are determined experimentally. Jiang et al. from Harbin Institute of Technology (2010) [39] modeled the relationship between the angle of the valve plate rotation and the transformation ratio of the IHT using kinematic flow equations. They presented sets of closed-form equations that can be used to understand the behavior of IHT with respect to the transformation ratio. Liu et al from Wuhan Second Ship Design Institute (2012) [91] utilized a software package AMEsim to model and simulate an IHT constructed based on a bent axis pump. From their simulation, they found that the IHT transformation ratio is not in accordance with theoretical value and there exists an upper limit on transformation due to viscous friction and leakage. Aforementioned groups all used a prototype IHT modified from existing bent axis pumps, even after the introduction of the floating cup design from INNAS.

Some new design improvement and principles were proposed as well. Ouyang et al. from Zhejiang University (2005, 2008) [74, 75] presented a new design for the 3-ported valve plate. In the original implementation of the rotatable valve plate, the rotation creates an orifice throttling condition between the valve plate and the port block, limiting the useful operating range of the IHT. Their proposed design for the valve plate reduces such throttling and widens the operating region of the IHT. Yang and Jiang from Harbin Institute of Technology (2015) [90] proposed a 'variable hydraulic transformer' (VHT), which has not only a rotatable valve plate but also a variable swashplate angle. The extra degree of freedom provided by variable swashplate angle is used to achieve a flow control of the transformer. In their work, they provided a set of dynamic equations that model instantaneous flow at each port of the transformer assuming incompressible flow. However, the impact on enclosure size due to the needed swashplate actuation is not discussed with this new design.

Not many works are found on the component design aspect of the traditional hydraulic transformer where pump and motor are mechanically coupled together (shortened as PM transformer for convenience). Dantlgraber (1997) [23] filed a patent on PM transformer design that combines pump and motor into a single housing as seen in Fig. 1.8. In this design, the shaft coupling between the pump and motor units are enclosed in a case to eliminate an external shaft coupling. Moreover, the pistons of the two units rest on a common swashplate to reduce the total size of this transformer.

Modeling of PM transformer with closed-form equations are mostly found within a controller development framework, which will be discussed in the next section.

In terms of comparing between IHT and PM transformer as components, Werndin

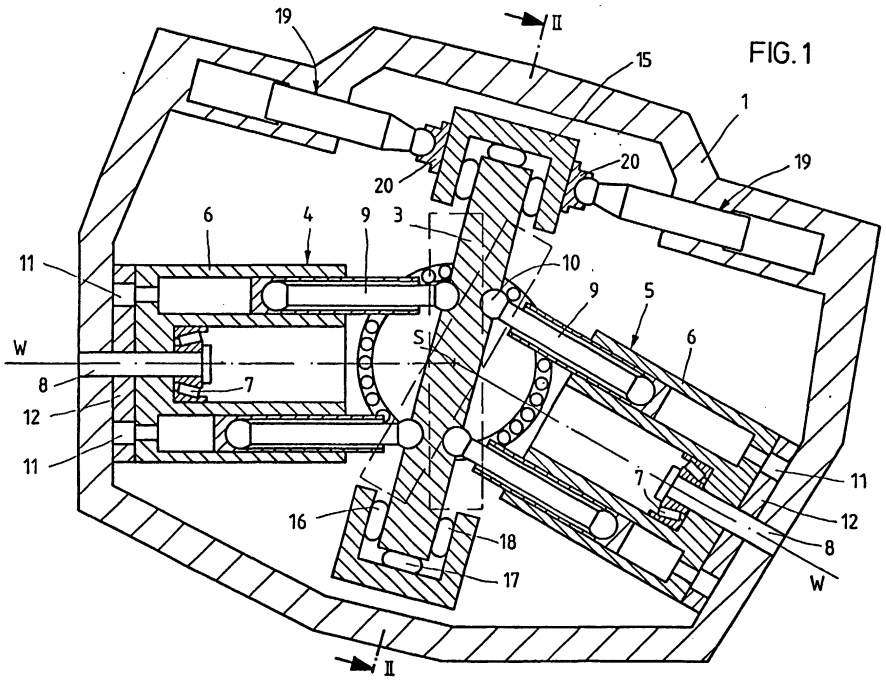

Figure 1.8: Dantlgraber's PM transformer in a single case with common swashplate

and Palmberg (2003) [89] is the only one to provide such comparison besides the developers of IHT themselves. Werndin and Palmberg conducted a quantitative comparison study between IHT and PM transformer in terms of efficiency, weight, and size. While the comparison is quantitative in nature, their work is limited in that the efficiency for transformers were only 'roughly estimated,' scaling published efficiency contours for a pump and a motor. This method fails to capture the difference in efficiency trend for two different configurations of PM transformers presented in their work. The work in this dissertation clearly indicates each configuration has a distinct region where it performs better than the other configurations. Also, the exact details and assumptions of how they arrived at the size and weight comparison were not specified. The comparison was made for just one specific operating scenario rather than wide range of operating conditions. It is very well possible that different operating scenario will yield a different conclusion.

1.2.2 System Control Using Hydraulic Transformer

While the majority of transformer literature focuses only on the transformer itself as a component, several authors explored many potential applications and operating scenarios for a hydraulic transformer, also paying attention to how to control hydraulic transformer

in each application. Vael et al. (1998) [81] outlined various methods IHT could be used to control a forklift, in conjunction with a free piston engine developed by the same company, INNAS. The lift and tilt system for the 30 kW class forklift is outfitted with an IHT. Citing a lack of development in electro-hydraulic secondary control and associated expensive cost, they decide to control the lift and tilt system by controlling the valve plate angle of IHT in open loop manner. They acknowledge that open loop control leads to poor disturbance rejection, but this is considered acceptable for the forklift application as the human operator can compensate for potential slow down or stop due to the disturbance by simply increasing the valve plate angle manually. While extensive *qualitative* analysis is given to describe the working principles of the hydraulic system for the lift and tilt system and vehicle drive strategy, no experimental or simulation results are presented on the performance of the proposed forklift outfitted with an IHT and a free piston engine. Shen et al. (2013) [77] presented a robust controller for the IHT valve plate with parameter uncertainties and load disturbance that would have allowed closed loop control of the forklift lift and tilt system. Shen et al. designed the guaranteed cost control (GCC) for the IHT along with PI control. Simulation results show that both GCC and PI control achieve a good step response, but GCC produces better robustness than PI control for a sinusoidal response for the valve plate angle tracking. However, the disturbance being simulated is not realistic as only a constant disturbance is considered. No motion control arising from this port plate control is presented.

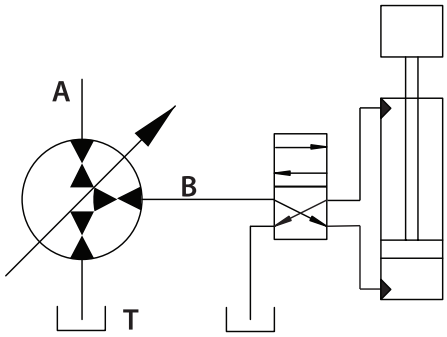

Figure 1.9: Cylinder is connected to a transformer through a directional valve

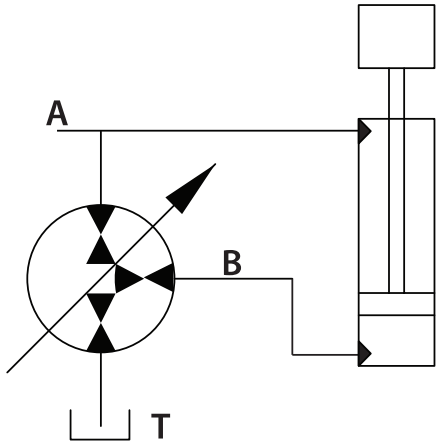

Figure 1.10: Cylinder cap side is connected to a transformer, and rod side is connected to the CPR

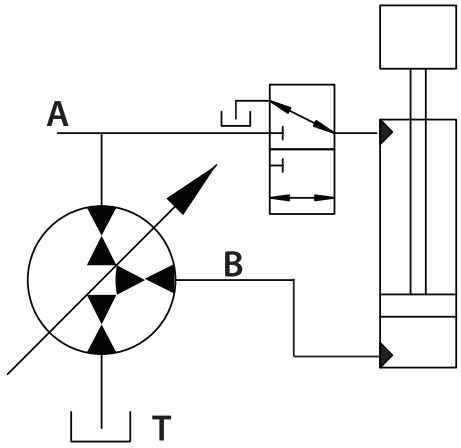

Figure 1.11: Cylinder cap side is connected to a transformer, and road side can be connected to either the CPR or return pressure line

After the development of floating cup principle, Achten et al. (2003) [84] evaluated different layouts that could be employed to utilize an IHT to drive a hydraulic cylinder. The first option shown in Fig. 1.9 is connecting a cylinder to an IHT with a directional valve. The second option in Fig. 1.10 is to connect the cap side of the cylinder to IHT, while the rod side is pressurized to the common pressure rail (CPR) pressure. The last option considered in Fig. 1.11 is to connect the cap side of the cylinder to IHT, while the rod side is switched between CPR pressure or return line pressure. After qualitatively considering the operational characteristics of each layout option, they found the last option to be suitable for an experiment with the excavator, which they claim will be used for the first

functional testing of the floating cup IHT. In their following work on the said excavator [83], an extensive qualitative description of the control strategy is provided. However, the details of the controller, simulations and experimental results were not presented. In their later work, Achten et al. (2007, 2009) [4, 1] has started promoting the hydraulic hybrid vehicle as a good application for the IHT. Again, qualitative evaluation of various circuit layouts is performed to realize a four-quadrant operation suitable for the vehicle driving conditions, but no simulation or experimental results are presented.

Volvo Construction Equipment, in collaboration with Achten and Innas, (2011) [6] presented a simulation study in which a 33-ton wheel loader is outfitted with floating cup IHTs for its wheel drive and main lift cylinders. For the duty cycle simulated, they showed a reduction in fuel consumption by 51.4% compared to the original system with mechanical transmission and load sensing hydraulic circuit. This reduction is contributed largely to the energy recuperation of the cylinders. Shen et al. (2013) [78] presented an analysis of a hydraulic hybrid excavator, outfitted with bent-axis pump based IHTs. Through simulation, they demonstrated 21% reduction in fuel consumption possible with the hydraulic transformer, and 32% reduction possible if a downsized engine were to be employed. This reduction is contributed by the energy recuperation from the actuators as well.

Werndin and Palmberg (2001) [87] analyzed the potential control strategies for IHT concept, addressing concerns with a low-speed operation that shows strong torque variations due to low inertia of the transformer. No control law or experimental results were presented in this work. In their following work, Werndin and Palmberg (2002) [88] simulated a model-based estimator and feed-forward loop placed in parallel with a PI controller to control the linear actuator position by automatically adjusting the valve plate angle of an IHT in a closed loop manner. Satisfactory tracking results are shown for a cylinder position tracking, yet no experimental results are presented. They concluded that IHT design needs more design improvement to reduce torque variations and to be more controllable.

Lu [64] designed gears specially designed for an IHT such that the valve plate can be automatically controlled using a servo motor. He applied a fuzzy adaptive tuning PID control to experimentally validate the feasibility of a closed-loop control for an IHT system. Due to the small driving torque of the servo motor, it is prone to be overloaded with hydraulic power. The actuator response will be slower in that case.

Shen et al. (2014) [79] developed a controller for an IHT driving a hydraulic cylinder. In analyzing the system dynamics, they noted that the valve plate angle alters the output flow in a trigonometric relationship. This nonlinear change in output flow makes the control of an IHT difficult challenge. From their simulation, they identified that there should be an

upper limit on the valve plate angle placed at 1.75 radian, which translates to a pressure transformation ratio of 2. Beyond this angle, the efficiency is greatly reduced such that the benefit of being able to boost pressure higher is not helpful. They utilized a fuzzy control theory to address the challenge with nonlinear behavior and experimentally proved the effectiveness of their algorithm. However, the results revealed that the response of the system was slow and suggested advanced control algorithm to be employed to optimize the control.

On controlling a pump and motor transformer, Shigeru et al. (2005) [35] and Ahn and Ho (2008) [31] both take a similar frequency domain approach, treating component losses as model uncertainties, to develop a robust position controller for a cylinder driven by a transformer. Ueno et al. (2005) [80] extends Shigeru et al.'s work to develop a robust controller to achieve velocity tracking. The derivation process is discussed in detail and results are verified with simulation and experiment for a potential application with an injection molding machine. However, only step responses are shown for both position and velocity controllers. Only one PM transformer configuration was simulated, and only one displacement ratio is used for control, meaning operating conditions for transformer was not necessarily optimized in designing the control. Ahn and Ho (2009) [32] expanded their controller algorithm by considering three directional control valves placed in the hydraulic circuit to aid the operation of the hydraulic transformer connected to a cylinder. Depending on the position of those valves, eight different operating modes are identified and an algorithm to determine the operating mode is presented. A simulation of this circuit under five different duty cycles showed a reduction in energy consumption by more than 50% for one of the cases while showing 0% to 20% for the remaining cycles. Their work has the same limitation as Ueno et al.'s work [80] in that only one unit in the transformer is variable displacement, limiting its operating region.

Inoguchi et al. (2012) [36] thoroughly investigated transformer's ability to regenerate fluid power back to the common pressure rail from an overrunning load. They examined the recovery of energy from a mass load on a cylinder being raised and lowered vertically in the presence of gravitational forces. Up to 83.1% of the energy that would have been lost in throttling valve can be recovered by utilizing a hydraulic transformer.

As seen, the control and application aspect of the hydraulic transformer leaves room for improvement. Many works are only qualitative in nature and do not provide any simulation or experimental results. Even the works that do provide simulation results often do not provide a complete set of equations that could be utilized to build the controller discussed. There exists a clear opportunity to investigate the control aspect of hydraulic

transformer delivering both good control tracking performance and efficiency improvement over throttling circuit.

1.3 Research Objectives

Above literature review reveals that academic research heavily focuses on the design aspect of the hydraulic transformer, especially in understanding and improving the IHT principle. Quantitative comparisons between IHT and PM transformers has not been studied in an exhaustive manner. Rather, it is often taken for granted that IHT design will be better. Moreover, the lack of work on system control using hydraulic transformer leaves any reader wondering whether hydraulic transformer can fully replace the throttling valves and deliver the similar dynamic response.

This dissertation seeks to fill in the gap by

- Comparing the existing hydraulic transformer configurations in a quantitative manner for full range of operating conditions
- Discovering new transformer configurations that are more efficient and compact than previously designed transformers
- Developing control algorithms so as to demonstrate in real life applications that transformers can achieve high control performance
- Minimizing energy consumption compared to a similar system driven by throttling valves

These will answer the key research question of this dissertation: "Can we design a compact hydraulic transformer that can significantly improve efficiency over throttling valves yet still achieves similar dynamic control response performance?"

1.4 Dissertation Overview

The rest of this dissertation is organized as follows:

Chapter 2 presents the development of mathematical models utilized in order to analytically understand the behavior and characteristics of hydraulic transformers. A simple kinematic model is first established, and then fluid compressibility and dynamics losses are added to present various versions of the transformer model used throughout this dissertation.

Chapters 3 and 4 present the efforts to quantitatively compare the traditional pump and motor transformer (PM transformer) in three different configurations and Innas Hydraulic Transformer (IHT). The comparison is performed with respect to three key aspects of the transformer operating characteristics: displacement sizing, flow ripple, and efficiency. By utilizing the model built in Ch. 2 rather than scaling a manufacturer provided data, the comparison is established in an objective manner. From the analysis, it was discovered that the PM transformer could benefit from being able to switch among different configurations.

Chapter 5 introduces the prototype mode switching transformer built as a result of the comparison study performed. Individual components of the prototype, especially the mechanisms to utilize the configuration switch, are presented.

Chapter 6 presents the trajectory tracking control developed for hydraulic transformer, and Chapter 7 presents the force tracking control performed on a hydraulic human power amplifier.

Chapter 8 presents a hardware-in-the-loop (HIL) platform that allows testing of the prototype transformer at any desired operating condition. Control methodologies to maximize the operating efficiency of the hydraulic transformer driven system are presented.

Chapter 9 compares the efficiencies between a system driven by hydraulic transformers against one driven by throttling valves. Efficiencies are compared for different loading conditions and the energy saving potential of a transformer is demonstrated.

Finally, summary of findings and recommendations for future work presented in Chapter 10, along with concluding remarks, and a summary of the research and contributions presented in this dissertation.

Chapter 2

Modeling of Transformer

This chapter details the transformer models used as a tool for quantitative comparison of transformer configurations and control development. Both IHT and PM transformer are typically configured on axial piston rotating groups. The mathematical models of axial piston pump and motors are well established and published on various books [72], [38] [37] [70], some of which are utilized as course materials for undergraduate level classes.

One of the oldest work on modeling axial piston pump and motor is "Hydraulic Control Systems" by Merritt (1966) [72], which provides governing equations for various components in a hydraulic system, and representation of their dynamic behavior. This work is still widely cited by virtually all researchers seeking to develop their own version of pump and motor model.

More recently, Ivantysyn and Ivantysynova's book titled "Hydrostatic pumps and motors: principles, design, performance, modelling, analysis, control and testing" [38] [37] updates the work by Merritt with equations for leakage flow through the slipper and swash plate, and leakage flow through the clearance between the cylinder block. In the meantime, Merritt's work [72] only provided a leakage flow through the clearance between the piston and the cylinder block.

Manring [67] developed closed-form equations to represent the kinematic and dynamics of variable displacement pumps. In [68], he presented a detailed loss model that predicts the mechanical loss within the axial piston pump arising from the friction inside the piston chamber. In another work [69], Manring presented the closed-form expressions describing the characteristics of the flow ripple for an ideal pump with the incompressible flow. After analyzing both ripple height and the pulse frequency of the flow ripple, he added pump leakage and fluid compressibility to analyze flow ripple height and the pulse frequency of the flow ripple for an actual pump. His works on pump modeling including various losses

are summarized in [70].

Bergada is another researcher who is widely cited by researchers in fluid power. In his prior work, Bergada [13] paid particular attention to the pressure distribution, leakage, force, and torque between the barrel and the valve plate of an axial piston pump. He presented a set of equations for modeling these and demonstrated accuracy by comparing CFD model and the equation model. Bergada [12] also presented a piston pump model based on the leakage equations he developed that is capable of simulating the pump output pressure ripple with great detail.

Aforementioned works are widely adapted by various researchers. For example, Li (2005) [62] documented in detail the derivation process to obtain a kinematic model and a dynamic model incorporating the fluid compressibility to predict pump failure. Guan et al. (2013) [30] gathered various literature to establish a pump flow model in order to study the flow ripple arising from the valve plate design. In summary, subcomponent level model for an axial piston rotating group taking into consideration of various losses is readily available.

The literature on modeling hydraulic transformers that take subcomponent level losses are not readily available. Li et al. [61] developed a mathematical model for an IHT, but rather than modeling each loss item, they utilize a loss model that depends on various coefficients of losses in which the coefficients are empirically determined through trial and error. Werndin and Palmberg [89] developed a model for both PM transformer and IHT, but this is done by simply scaling a manufacturer published data. This makes the efficiency comparison between IHT and PM transformer incomplete. To compare them in most fair manner, the same subcomponent level loss models should be used for both designs.

In this chapter, the existing literature on modeling axial piston rotating groups are adapted and expanded to develop models specific for transformers. These models will be used throughout the dissertation for analysis. The same derivation process will be taken for PM transformer and IHT to highlight the similarities in working principles and differences arising from the configuration.

Section 2.1 starts with a derivation of flow and torque model for axial piston pump and motors and then expand those model for transformers to establish an average model of a transformer. Section 2.2 incorporates the fluid compressibility in order to establish an instantaneous flow model to study flow characteristics of the transformer arising from different valve plate design. Finally in Section 2.3 and Section 2.4, dynamic loss models are incorporated to study the efficiency of transformer configuration.

2.1 Average Model for PM Transformer and IHT

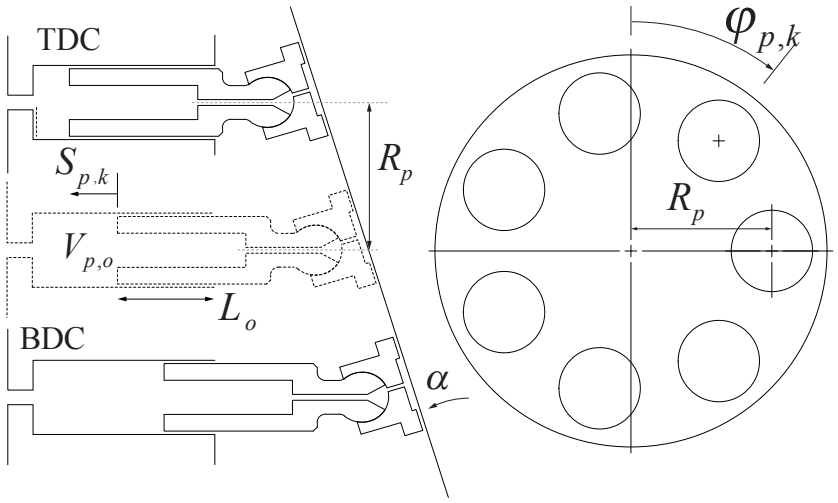

Figure 2.1: Piston Movement Geometry

In an axial piston pump or motor, such as one shown in Fig. 2.1, the pistons are placed in a circular array within a cylinder barrel rotating around the shaft. The reciprocating motion is generated by a swash plate, which allows pistons to travel in and out. Variable displacement pump or motor allows the angle of swash plate with respect to the perpendicular to be adjusted.

A cylinder barrel is held tightly against a valve plate like ones shown in left side of Fig. 2.2. When the drive shaft rotates, either through a torque input to the shaft or through hydraulic power driving the shaft, it rotates the pistons and the cylinder barrel together. The piston displacement is directly related to the swashplate angle. Swashplate titled at an angle causes the pistons to move back and forth within the piston chamber as the shaft rotates. As pistons reciprocate within the cylinder barrel, they pass over the suction and discharge ports respectively. In case of IHT, pistons pass over 3 ports to perform the task of suction or discharge which can be set by the valve plate rotation. The additional port serves as a make-up port, balancing the flow difference between suction and discharge ports.

In this section, we derive an average torque and flow model for pump or motor and expand them for transformers. For the comparison, it is assumed that both PM Transformer and IHT are built on axial piston displacement machines. The same modeling approach will be taken to highlight the similarities in working principles and differences arising from valve plate design.

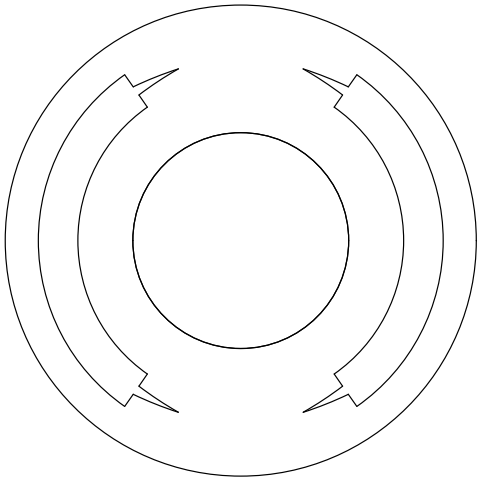

Figure 2.2: Valve Plate in Axial Piston Pump

2.1.1 Average Model of Axial Piston Pump and Motor

Derivation of Average Flow

To obtain a flow equation of a single piston within an axial piston pump/motor, consider an axial piston machine shown in Fig. 2.1 with radial distance of piston center from the shaft center R_p with a swashplate angle α. The angular location $\varphi_{p,k}(t)$ of the k-th piston is given by

$$\varphi_{p,k}(t) = \varphi(t) + (k-1)\frac{2\pi}{n} \tag{2.1}$$

where n is the total number of pistons in a single pump/motor unit and $\varphi(t)$ is the angular displacement of the entire rotating group measured at the $k = 1$ piston with respect to the top dead center (TDC). The piston group and cylinder block assembly is commonly referred as a rotating group.

The linear displacement $S_{p,k}$ of the k-th piston is:

$$S_{p,k} = R_p \tan(\alpha)(\cos\varphi_{p,k}(t)) \tag{2.2}$$

With $\alpha > 0$, $\varphi_{p,k}(t) = 0$ corresponds to a position where the piston is fully extended ($\cos 0 = 1$) with the chamber volume at its minimum (TDC) whereas $\varphi_{p,k}(t) = \pi$ corresponds to a position where the piston is fully retracted ($\cos\pi = -1$) with the chamber volume at its maximum (BDC).

Taking the time rate of change of the piston displacement, the linear velocity of the

piston could be found:

$$v_{p,k}(t) = \frac{dS_{p,k(t)}}{dt} = \frac{dS_{p,k(t)}}{d\varphi_{p,k}(t)} \underbrace{\frac{d\varphi_{p,k}(t)}{dt}}_{\omega(t)} = -\omega(t) R_p \tan(\alpha) \sin(\varphi_{p,k}(t)) \tag{2.3}$$

where $\omega(t)$ is the rotational velocity of the rotating group. Summing the swept volume from the linear displacement of the piston with the initial volume, the instantaneous volume of the piston chamber $V_{p,k}(t)$ is given as:

$$V_{p,k}(t) = V_{p,0} - A_p S_{p,k}(t) \tag{2.4}$$

where $V_{p,0}$ is the dead volume of the piston chamber when the swashplate angle is 0 or when the piston is at the center of its rotation (ie. $\varphi = \pi/2$ or $\varphi = 3\pi/2$), and A_p is the cross-sectional area of the piston. Multiplying the linear velocity of the piston with is cross-sectional area, the rate of change of the piston chamber volume is defined:

$$\dot{V}_{p,k} = v_{p,k}(t) A_p = -\omega(t) R_p A_p \tan(\alpha) \sin(\varphi_{p,k}(t)) \tag{2.5}$$

In the absence of the compressibility, the volume change in piston chamber directly translates to the flow into or out of the piston chamber to the port. A hydraulic pump/motor has two ports 'I' and 'II'. With a swashplate angle $\alpha > 0$ and shaft speed $\omega > 0$, the port 'I' serves as a suction port while port 'II' serves as a discharge port. Sign convention is defined such that positive flow means flow is coming out of the unit while negative flow means flow is going into the unit. The average flow rate from a single k-th piston over one revolution is defined to be:

$$\begin{aligned} Q_{I,k} &= \frac{1}{2\pi} \int_0^{2\pi} C_I^k(\varphi_{p,k}) \dot{V}_{p,k}(t) d\varphi_{p,k} \\ Q_{II,k} &= \frac{1}{2\pi} \int_0^{2\pi} C_{II}^k(\varphi_{p,k}) \dot{V}_{p,k}(t) d\varphi_{p,k} \end{aligned} \tag{2.6}$$

where $C_P^k(\varphi_{p,k})$ is an indicator function that is 1 if k-th piston is oriented such that is is communicating with P-th port that is under consideration

$$C_P^k(\varphi_{p,k}) = \begin{cases} 1 & \varphi_{p,k} \in R_P^u \\ 0 & \text{else} \end{cases} \tag{2.7}$$

where R_P^u indicates the ranges of the line connections for u-th unit in consideration. For

a single unit of pump/motor in consideration, $u = 1$ and

$$\begin{aligned} R_I^1 &= [0, \pi) \\ R_{II}^1 &= [\pi, 2\pi) \end{aligned} \tag{2.8}$$

Utilizing the above definition, the per piston flow rate in Eq. (2.6) is summed up across n number of pistons in the unit to yield the volumetric flow rate:

$$Q_I = \sum_{k=1}^{n} Q_{I,k} = \underbrace{-2nA_pR_p \tan(\alpha)}_{D_I} \frac{1}{2\pi}\omega \tag{2.9}$$

$$Q_{II} = \sum_{k=1}^{n} Q_{II,k} = \underbrace{2nA_pR_p \tan(\alpha)}_{D_{II}} \frac{1}{2\pi}\omega \tag{2.10}$$

where D_I and D_{II} are the port displacements that determine the volumetric flow rate per revolution (m^3/rev):

$$D_I = -2nA_pR_p \tan(\alpha) = -D \tag{2.11}$$

$$D_{II} = 2nA_pR_p \tan(\alpha) = D \tag{2.12}$$

and D is the 'total displacement' of an axial piston pump/motor per revolution. Thus, the average volumetric flow rate of port I and II in an axial piston pump and motor is given by: (m^3/rad)

$$\begin{aligned} Q_I &= -\frac{D}{2\pi}\omega \\ Q_{II} &= \frac{D}{2\pi}\omega \end{aligned} \tag{2.13}$$

sign convention is defined such that for a positive displacement unit with $\alpha > 0$, a positive shaft speed $\omega > 0$ makes the flow at port I is going into the unit with $Q_I < 0$, and the flow at port II is coming from the unit with $Q_{II} > 0$.

Derivation of Average Torque

To obtain torque from a single piston, consider the same Fig. 2.1. As a piston travels from TDC to BDC, its cross-sectional area A_p will be exposed a port pressure P_P and translate this linear force to the shaft through the swashplate geometry, causing positive acceleration to the shaft velocity. With a throttling not modeled in an average model, the

port pressure is assumed to be the same as piston chamber pressure. This relationship can be generalized as a product between the applied force moment arm causing a torque to the shaft. Then, torque delivered by a piston interacting with port pressure P_P to the shaft is given by

$$T_{p,k} = -\frac{dS_{p,k(t)}}{d\varphi} \cdot P_P A_p = P_P A_p R_p \tan(\alpha) \sin(\varphi_{p,k}(t)) \tag{2.14}$$

where positive torque means accelerating shaft velocity ω to the positive direction. The port pressures defined with respect to the reservoir pressure P_T are:

$$P_P = \begin{cases} P_I & \text{if } 0 < \varphi_{p,k}(t) \leq \pi \\ P_{II} & \text{if } \pi < \varphi_{p,k}(t) \leq 2\pi \end{cases} \tag{2.15}$$

where P_I and P_{II} are the pressure at port I and port II of the pump or motor. For a positive shaft speed $\omega > 0$, $P_I > P_{II}$ for a motor, and $P_I < P_{II}$ for a pump.

Evaluating the integral of torque equation in (2.14) for the full revolution yields the average torque given by a single piston per revolution:

$$\int_0^{2\pi} T_{p,k}(t)dt = P_I \underbrace{A_p R_p \tan(\alpha)}_{\frac{D}{2n}} \underbrace{(\cos 0 - \cos \pi)}_{2} + P_{II} A_p R_p \tan(\alpha)(\cos \pi - \cos 2\pi) \tag{2.16}$$

Multiplying above integral by total number of pistons n and dividing by 2π rad/rev gives the total average torque:

$$\begin{aligned} \sum T = P_I \underbrace{2nA_p R_p \tan(\alpha)}_{D} \frac{1}{2\pi} + P_{II} \cdot \underbrace{-2nA_p R_p \tan(\alpha)}_{-D} \frac{1}{2\pi} \\ = -P_I \frac{D_I}{2\pi} - P_{II} \frac{D_{II}}{2\pi} = (P_I - P_{II}) \frac{D}{2\pi} \end{aligned} \tag{2.17}$$

Eqs. (2.13) and (2.17) are the average flow and torque equation for an single axial piston pump or motor with two ports. Now, these results are expanded to be fit with transformers.

2.1.2 Average Model of Pump/Motor Transformer

As described, a transformer is constructed by joining two pump/motors (with volumetric displacement D_1 and D_2) on a common shaft and inertia. It has an input port (A),

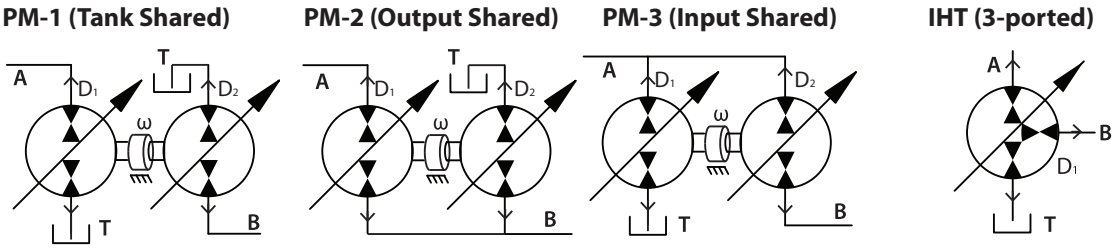

Figure 2.3: Three configurations for PM Transformer and IHT

and output port (B) and a tank port(T) connected to a D_1 unit or D_2 unit.

In one configuration (PM-1 configuration), as shown on the left side of Fig. 2.3, 'A' is connected to port I of D_1 unit ranging from 0 to π on the port plate, and and 'B' is connected to port II of D_2 ranging from π to 2π. The remaining ports from two units are connected to 'T' to form a common port. Adapting Eqn. (2.13) (2.17) to obtain flow and torque over an appropriate port region, we obtain following governing equations:

PM-1:

$$\begin{aligned} J\dot{\omega} &= \underbrace{(P_A - P_T)\frac{D_1}{2\pi}}_{\text{Motor}} + \underbrace{(P_T - P_B)\frac{D_2}{2\pi}}_{\text{Pump}} \\ Q_A &= -\frac{D_1}{2\pi}\omega \\ Q_B &= \frac{D_2}{2\pi}\omega \\ Q_T &= \frac{D_1 - D_2}{2\pi}\omega \end{aligned} \tag{2.18}$$

where J is the inertia of the transformer shaft, ω is the rotational speed of transformer, P_x describes the acting pressure on port A, B, or T. With $\omega > 0$, D_1 unit acts as a motor and D_2 unit acts as a pump. Its flows are given by the product of the port displacement and shaft speed. At steady-state ($\dot{\omega} = 0$), the relationship between D_1 and D_2, or the flow ratio, is related to the pressure transformation λ

$$\lambda = -\frac{Q_A}{Q_B} = \frac{D_1}{D_2} = \frac{P_B - P_T}{P_A - P_T} \tag{2.19}$$

If $P_T = 0$ or negligible, the displacement ratio directly relates P_B and P_A at steady-state. In short, hydraulic transformer can be described as a device that performs a role of pump and motor simultaneously which provides a pressure transformation through varying the volumetric displacement of each port.

With the same pump and motor, two additional configurations PM-2 and PM-3, as shown in in Fig. 2.3 can be created by connecting the common port to "A" or "B" instead.

Each configuration has unique performance characteristics, and their equations are given by:

PM-2:

$$\begin{aligned} J\dot{\omega} &= (P_A - P_B)\frac{D_1}{2\pi} + (P_T - P_B)\frac{D_2}{2\pi} \\ &= (P_A - P_T)\frac{D_1}{2\pi} - (P_B - P_T)\left(\frac{D_1 + D_2}{2\pi}\right) \\ Q_A &= -\frac{D_1}{2\pi}\omega \\ Q_B &= \frac{D_1 + D_2}{2\pi}\omega \\ Q_T &= -\frac{D_2}{2\pi}\omega \\ \lambda &= \frac{P_B - P_T}{P_A - P_T} = \frac{D_1}{D_1 + D_2} \end{aligned} \tag{2.20}$$

PM-3:

$$\begin{aligned} J\dot{\omega} &= (P_A - P_T)\frac{D_1}{2\pi} + (P_A - P_B)\frac{D_2}{2\pi} \\ &= (P_A - P_T)\left(\frac{D_1 + D_2}{2\pi}\right) - (P_B - P_T)\frac{D_2}{2\pi} \\ Q_A &= -\frac{D_1 + D_2}{2\pi}\omega \\ Q_B &= \frac{D_2}{2\pi}\omega \\ Q_T &= \frac{D_1}{2\pi}\omega \\ \lambda &= \frac{P_B - P_T}{P_A - P_T} = \frac{D_1 + D_2}{D_2} \end{aligned} \tag{2.21}$$

Table 2.1: Configuration Port Connections

Range	PM1	PM2	PM3	IHT
R_A^1	$[0, \pi)$	$[0, \pi)$	$[0, \pi)$	$[-\frac{\pi}{3}, \frac{\pi}{3}) + \theta(t)$
R_A^2			$[0, \pi)$	-
R_B^1		$[\pi, 2\pi)$		$[\pi, \frac{5\pi}{3}) + \theta(t)$
R_B^2	$[\pi, 2\pi)$	$[\pi, 2\pi)$	$[\pi, 2\pi)$	-
R_T^1	$[\pi, 2\pi)$			$[\frac{\pi}{3}, \pi) + \theta(t)$
R_T^2	$[0, \pi)$	$[0, \pi)$	$[\pi, 2\pi)$	-

Table 2.1 gives the R_P^u values that indicate the ranges of the line connections for each of the three transformer unit configurations. The ranges reflect which two pressure lines bridge each of the rotating groups. For example, unit 1 is connected to the rail line A and the tank line T in both the PM-1 and PM-3 configurations, and the rail line A and the

load line B in the PM-2 configuration. In case of IHT, there only exists one unit whose angle ranges are translated by the valve plate rotation $\theta(t)$ relative to the swashplate.

2.1.3 Average Model of Innas Hydraulic Transformer

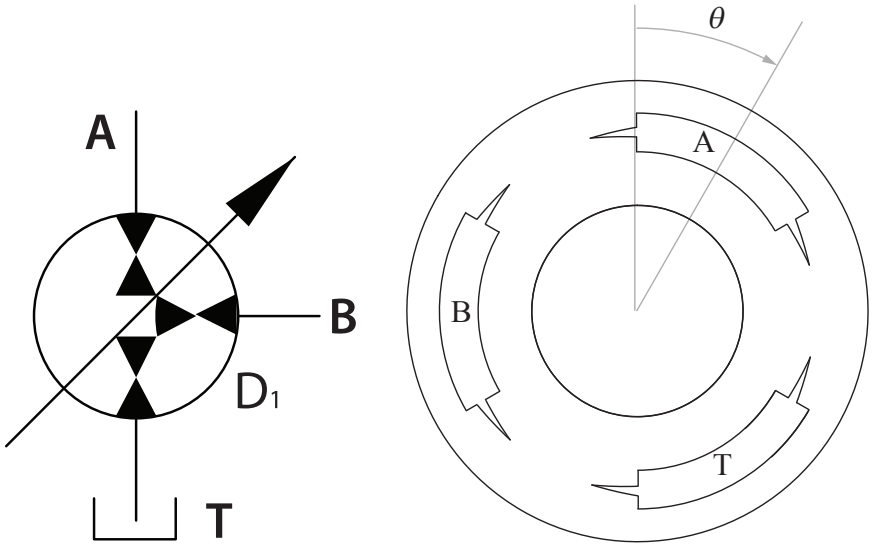

Figure 2.4: IHT and its 3 ported valve plate

The Innas Hydraulic Transformer (IHT) configuration (Fig. 2.4), which will be compared against 3 configurations of PM Transformer mentioned above, combines the roles of pump and motor into a single unit through introducing a rotatable 3-port valve plate. As each piston interfaces with the input (A), output (B), and tank (T) port alternately, it performs the motoring, pumping, and filling/return functions respectively. By varying the angle of valve plate θ relative to the initial position, the relative flows ported to A, B, and T, and thus the pressure transformation ratio, are varied. The angular region for each port is given as follow:

$$\begin{aligned} R_A &= \left[-\frac{\pi}{3}, \frac{\pi}{3}\right] + \theta \\ R_T &= \left[\frac{\pi}{3}, \pi\right] + \theta \\ R_B &= \left[\pi, \frac{5\pi}{3}\right] + \theta \end{aligned} \tag{2.22}$$

Using this region, the same approach as in PM transformer is used to establish the volumetric displacement at input (A), tank (T), and output (B) ports (m^3/rev):

$$\begin{aligned} D_A(\theta) &= nA_pR_p\tan(\alpha)\left[\cos(\pi/3+\theta)-\cos(-\pi/3+\theta)\right] \\ &= -\frac{D}{2}\sqrt{3}\sin(\theta) \\ D_T(\theta) &= nA_pR_p\tan(\alpha)\left[\cos(\pi+\theta)-\cos(\pi/3+\theta)\right] \\ &= -\frac{D}{2}\sqrt{3}\sin\left(\frac{2\pi}{3}+\theta\right) \\ D_B(\theta) &= nA_pR_p\tan(\alpha)\left[\cos(5\pi/3+\theta)-\cos(\pi+\theta)\right] \\ &= -\frac{D}{2}\sqrt{3}\sin\left(\frac{4\pi}{3}+\theta\right) \end{aligned} \tag{2.23}$$

For the torque equation in Eq (2.14), IHT has following pressure relationship for each of 3 ports:

$$P_P = \begin{cases} P_A & \text{if } -\frac{\pi}{3}+\theta < \varphi_{p,k}(t) \le \frac{\pi}{3}+\theta \\ P_T & \text{if } \frac{\pi}{3}+\theta < \varphi_{p,k}(t) \le \pi+\theta \\ P_B & \text{if } \pi+\theta < \varphi_{p,k}(t) \le \frac{5\pi}{3}+\theta \end{cases} \tag{2.24}$$

Integrating for those region in same manner as in Eq (2.16), we arrive at the torque contribution of each port to the transformer.

$$\begin{aligned} T = P_A\frac{1}{2\pi}\frac{D}{2}\sqrt{3}\sin(\theta) + P_T\frac{1}{2\pi}\frac{D}{2}\sqrt{3}\sin\left(\frac{2\pi}{3}+\theta\right) + P_B\frac{1}{2\pi}\frac{D}{2}\sqrt{3}\sin\left(\frac{4\pi}{3}+\theta\right) \\ = -(P_A-P_T)\frac{D_A(\theta)}{2\pi} - (P_B-P_T)\frac{D_B(\theta)}{2\pi} \end{aligned} \tag{2.25}$$

Utilizing (2.23) and (2.25), we get the following governing equations for IHT:

IHT:

$$\begin{aligned} J\dot{\omega} &= -(P_A-P_T)\frac{D_A(\theta)}{2\pi} - (P_B-P_T)\frac{D_B(\theta)}{2\pi} \\ Q_A &= \frac{D_A(\theta)}{2\pi}\omega \\ Q_B &= \frac{D_B(\theta)}{2\pi}\omega \\ Q_T &= \frac{D_T(\theta)}{2\pi}\omega \\ \lambda &= \frac{P_B-P_T}{P_A-P_T} = -\frac{\sin(\theta(t))}{\sin(4\pi/3+\theta(t))} \end{aligned} \tag{2.26}$$

The relationship between the valve plate angle θ and pressure transformation ratio λ for the IHT can be visualized with Fig. 2.5. These average model will be used to compare

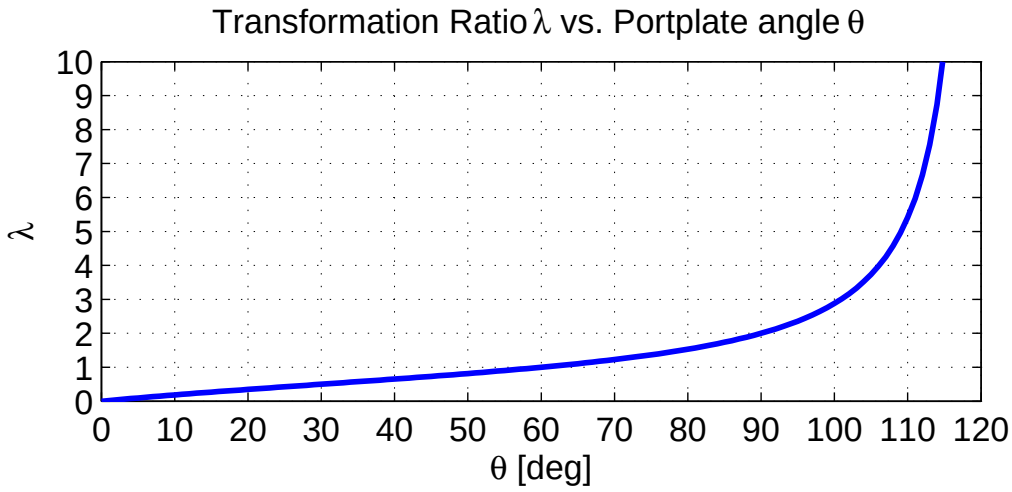

Figure 2.5: IHT's transformation ratio versus port plate angle θ

the total displacement necessary to build comparable transformers in Section 3.1.

2.2 Instantaneous Flow Model of Transformer

In order to study the flow characteristics of transformer designs, a model that shows the output flow at each instant of time contributed by each piston of the transformer is needed rather than an overall average model. This section will derive a piston-by-piston dynamic flow model to compare the flow characteristics of transformers, especially focusing on the flow ripple arising from utilizing axial piston rotating groups.

2.2.1 Instantaneous pressure and flow

Fig. 2.6 shows the single piston chamber which is the fluid volume of the study. There are two elements resulting from the piston motion: the rate of change of piston chamber volume: $\dot{V}_{p,k}$, piston chamber flow to the port $Q_{p,k}(t)$. The pressure dynamics to describe the instantaneous rate of change of the pressure within the piston chamber is obtained from the definition of bulk modulus:

$$\frac{d\rho}{\rho} = -\frac{dV}{V} = \frac{dP}{\beta(P)} \tag{2.27}$$

where ρ is the fluid density, V is the instantaneous volume of the piston chamber, and P is the piston chamber pressure. With m being the mass of the fluid in the chamber,

$$m = \rho V \tag{2.28}$$

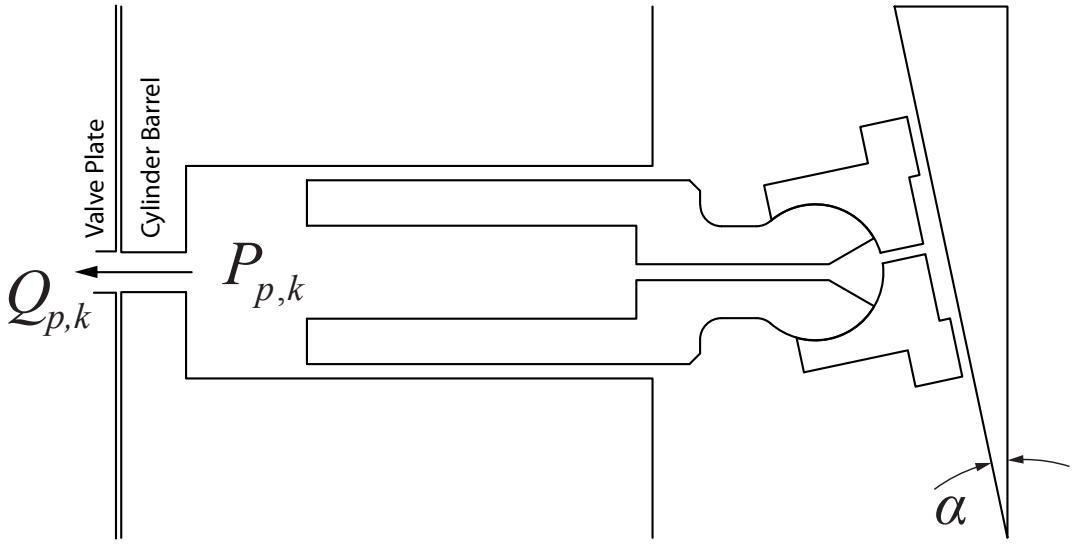

Figure 2.6: Single-piston chamber schematic

differentiating both sides yields

$$dm = \rho dV + V d\rho \tag{2.29}$$

substituting Eq. (2.27),

$$dm = \rho dV + V\rho \frac{dP}{\beta(P)} \tag{2.30}$$

Taking the introduction of mass into the system as the summation of the flow of the k-th piston chamber to the port P over time, the equation could be re-written as

$$-\rho\left(Q_{P,k}(t)\right)dt = \rho\left(dV + \frac{V(t)}{\beta(P)}dP\right) \tag{2.31}$$

Canceling ρ and re-arranging to solve for pressure change term dP yields

$$dP = -\frac{\beta(P)}{V(t)}\left(dV(t) + Q_{P,k}\right) \tag{2.32}$$

Now the generic P term will be replaced with the specific term $P_{p,k}(t)$ which describes the instantaneous pressure within the k-th piston chamber. Likewise the generic $dV(t)$ term will be replaced with the specific term $\dot{V}_{p,k}(t)$ that describes the instantaneous piston volume change rate in k-th piston chamber. With this, the k-th piston chamber pressure

dynamics is given as:

$$\dot{P}_{p,k}(t) = -\frac{\beta(P_{p,k})}{V_{p,k}(t)}\left(\dot{V}_{p,k}(t) + Q_{p,k}(t)\right) \tag{2.33}$$

Here, $\beta(P_{p,k})$ is the pressure dependent bulk modulus [20]. $V_{p,k}(t)$ is the instantaneous piston chamber volume as defined in:

$$V_{p,k}(t) = V_{p,0} - A_p S_{p,k}(t) \tag{2.34}$$

where $V_{p,0}$ is the dead volume of the piston chamber when the swashplate angle is 0 or when the piston is at the center of its rotation (ie. $\varphi = \pi/2$ or $\varphi = 3\pi/2$), and A_p is the cross-sectional area of the piston, $S_{p,k}(t)$ is the piston displacement (Eq. (2.2)).

With the pressure dynamics above, the k-th piston chamber flow to the port P is defined as $Q_{P,k}(t)$ and modeled using the fluid orifice equation:

$$Q_{P,k}(t) = C_d A_{o,P,k}(t)\sqrt{\frac{2|P_{p,k}(t) - P_P(t)|}{\rho}} sgn(P_{P,k}(t) - P_P(t)) \tag{2.35}$$

where $P_P(t)$ is the pressure of the external port to which the piston chamber is connected to, C_d is a coefficient of discharge for the orifice, ρ is the density of the hydraulic fluid, and $A_{o,P,k}(t)$ is the instantaneous discharge area of the orifice to the port P described in the next section.

2.2.2 Instantaneous discharge areas

Flow rate $Q_{P,k}(t)$ given in (2.35) depends on the discharge area $A_{o,k}$. Optimization of the design for discharge areas to reduce the flow ripple (pulsation) during the port transition is discussed by Martin et al. [71] and Wang [86]. In this dissertation, we assume a symmetric geometry shown in Fig. 2.2, where triangular notches (i.e., relieving grooves) are added to reduce pressure spikes during port transitions and enhance the rate of pre-pressurization of the piston chambers.

A plot showing the orifice discharge area for one piston during a full revolution is shown in Fig. 2.7 for both PM and IHT. As observed, IHT has three distinct ports whose starting and ending region can vary according to the valve plate rotation angle θ, whereas PM transformer will have two ports whose transition regions are fixed at TDC and BDC. These regions are given in Table. 2.1. The vertical lines A, B, and C correspond to the angular locations shown in Fig. 2.8. The opening area $A_o(\varphi_{p,k})$ can be described by the

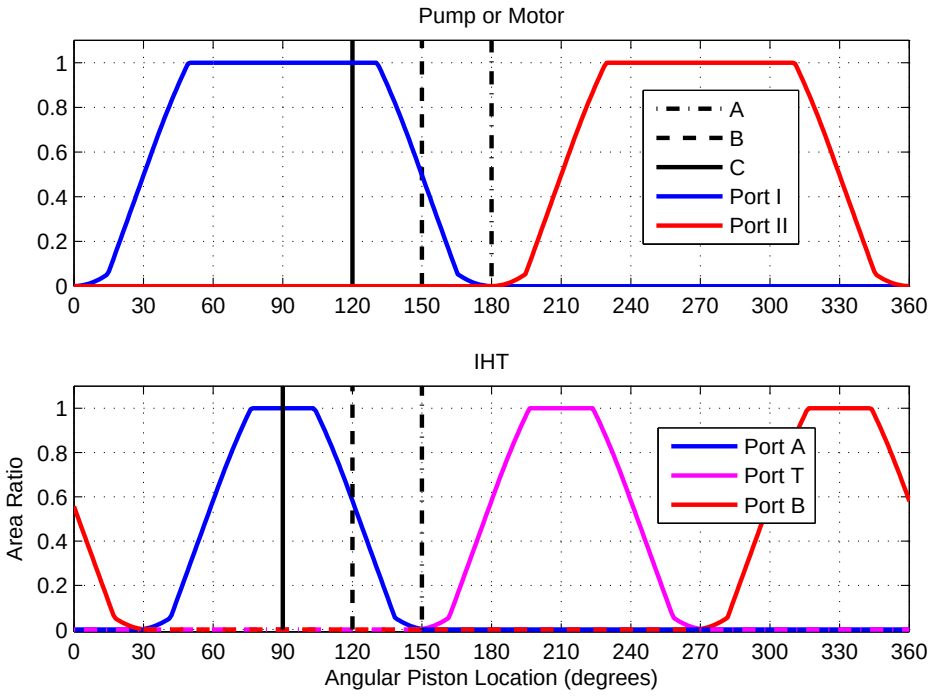

Figure 2.7: Port opening area to the piston chamber as piston travels one full revolution

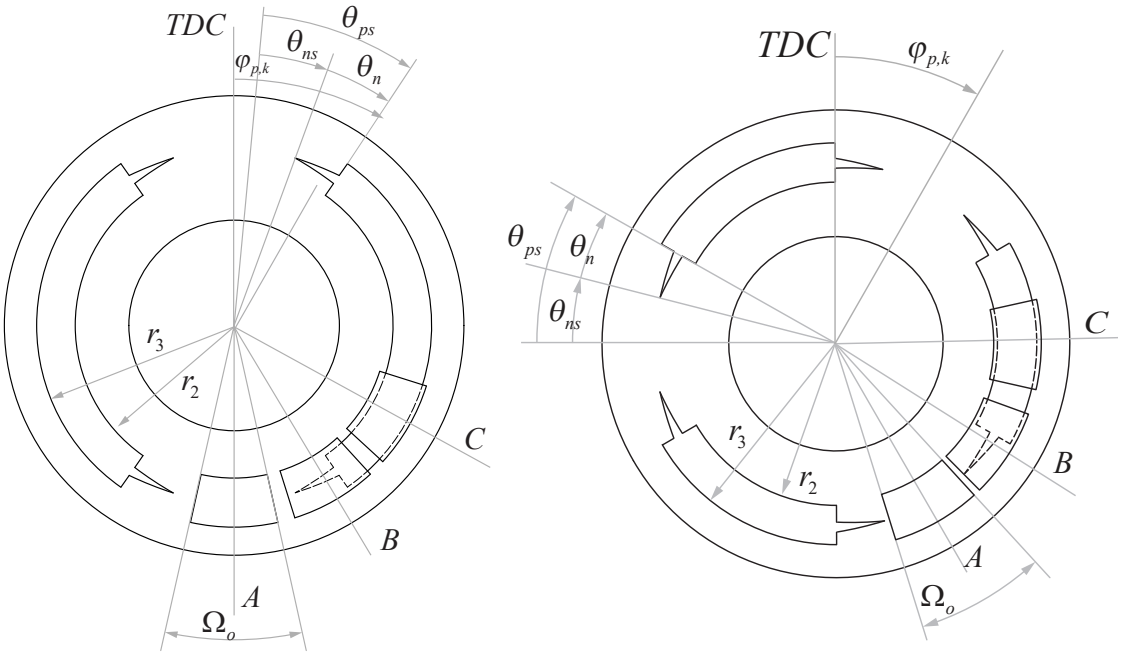

Figure 2.8: Valve plate port geometry for PM and IHT

piecewise function:

$$A_o(\varphi_{p,k}) = \begin{cases} 0 & \varphi_{p,k} + \frac{\Omega_o}{2} < \theta_{ns}, \\ \left(\frac{\varphi_{p,k}+\omega_o-\theta_{ns}}{\theta_n}\right)^2 A_n & \theta_{ns} \leq \varphi_{p,k} + \frac{\Omega_o}{2} < \theta_{ps}, \\ A_n + (\varphi_{p,k} + \omega_o - \theta_{ps})\beta_0 & \theta_{ps} \leq \varphi_{p,k} + \frac{\Omega_o}{2} < \theta_{ns} + \Omega_o, \\ \left(A_n - \left(\frac{\varphi_{p,k}+\omega_o-\theta_{ns}}{\theta_n}\right)^2 A_n\right) & \\ \qquad +(\varphi_{p,k} + \frac{\Omega_o}{2} - \theta_{ps})\beta_o & \theta_{ps} \leq \varphi_{p,k} + \frac{\Omega_o}{2} < \theta_{ps} + \Omega_o, \\ \Omega_0\beta_o & \text{else} \end{cases} \tag{2.36}$$

where θ_{ns} is the angular location of the start of the feathering notch, θ_{ps} is the angular location of the start of the main section of the port opening, and θ_n is the angular size of one of the notches. A_n is the total area of one of the notches and Ω_o is the angular size of the opening in the cylinder block, as seen in Fig. 2.2. The term β_o is a parameter characterizing the area per unit angle of the main section of the port opening and is given by:

$$\beta_o = \frac{\left(r_3^2 - r_2^2\right)\pi}{2\pi} = \frac{\left(r_3^2 - r_2^2\right)}{2} \tag{2.37}$$

where r_2 and r_3 are the inner and outer radii of the port opening in the port plate, as shown in Fig. 2.2. For the IHT with equal port angles, the angle ranges are translated by the valve plate rotation $\theta(t)$ relative to the TDC.

2.2.3 Total Unit Flow Rate

Now a summarizing model is needed to aggregate the individual flow rates associated with each piston. The quantities of interest are the hydraulic oil flow rates along each of the connecting lines. These are the pressure line, load line, and tank line, referred to as Q_A, Q_B, and Q_T respectively. The total flow rate to and from the transformer for each line is the summation of the contributing flow from each of the two rotating groups:

$$\begin{aligned} Q_A &= \bar{Q}_A^1 + \bar{Q}_A^2 \\ Q_B &= \bar{Q}_B^1 + \bar{Q}_B^2 \\ Q_T &= \bar{Q}_T^1 + \bar{Q}_T^2 \end{aligned} \tag{2.38}$$

where $\bar{Q}_P^u$ is the flow rate from the u-th unit to the P-th port. In other words, $\bar{Q}_P^u$ is the summation of the individual piston flow rates $Q_{P,k}$ that are currently communicating with

the P-th port and the leakage flow rate associated with the valve plate Q_{lv} (modeled in Section 2.3.4):

$$\bar{Q}_P^u = \left[\sum_{k_1=1}^{n} Q_{P,k}\right] - Q_{lv} \tag{2.39}$$

This model will be used to establish flow ripple comparison in Section 3.3

2.3 Dynamic Flow Model for Transformer with Volumetric Losses

In this section, the modeling results from Section. 2.1 and 2.2 are expanded to incorporate both volumetric and mechanical losses determining the efficiency of the transformer.

2.3.1 Instantaneous pressure with losses

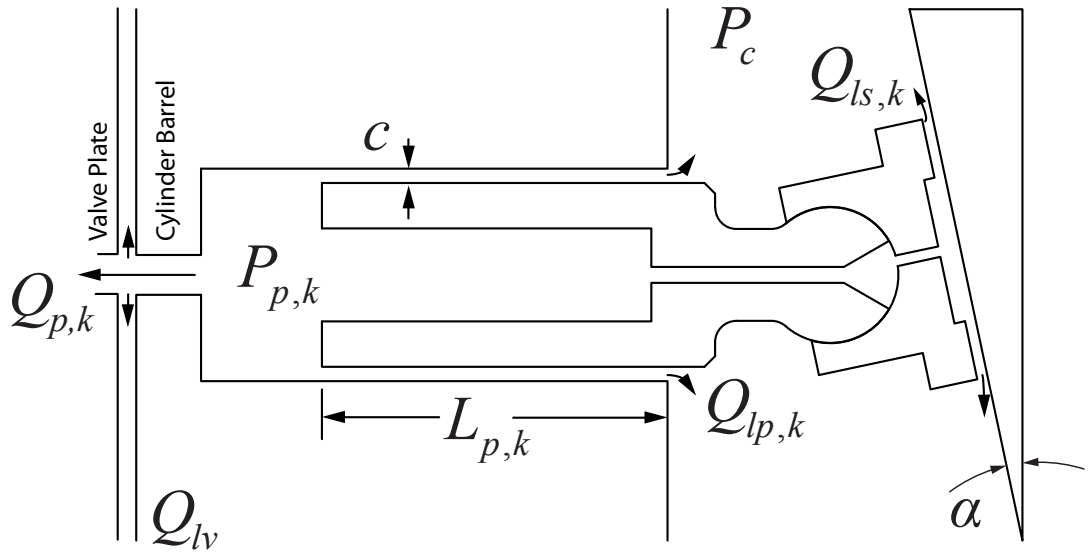

Figure 2.9: Single-piston chamber schematic showing flow leakage pathways

Fig. 2.9 shows the expanded version of Fig. 2.6 displaying the single piston chamber which is the control fluid volume of the study. There are four elements resulting from the piston motion: the rate of change of piston chamber volume: $\dot{V}_{p,k}$, piston chamber flow to the port $Q_{p,k}(t)$, the leakage flow from the piston chamber $Q_{lp,k}(t)$, and the leakage flow from the piston shoe $Q_{ls,k(t)}$.

With additional leakage terms, the piston chamber pressure dynamics in Eq. (2.33) is now:

$$\dot{P}_{P,k}(t) = -\frac{\beta(P_{p,k})}{V_{p,k}(t)}\left(\dot{V}_{p,k}(t) + Q_{p,k}(t) + Q_{lp,k}(t) + Q_{ls,k(t)}\right) \tag{2.40}$$

where $P_{p,k}(t)$ is the instantaneous pressure within the piston chamber, $\beta(P_{p,k})$ is the pressure dependent bulk modulus [20]. The orifice equation in Eq. (2.35) is unchanged:

$$Q_{P,k}(t) = C_d A_{o,k}(t)\sqrt{\frac{2|P_{p,k}(t) - P_P(t)|}{\rho}} sgn(P_{p,k}(t) - P_P(t)) \tag{2.41}$$

2.3.2 Piston Chamber Leakage

The leakage rate in the bore for an eccentrically located piston has been modeled by [72]:

$$Q_{lp,k} = \frac{\pi d_p c^3(1 + 1.5e^2)}{12\mu L_{p,k}}(P_{p,k} - P_c) \tag{2.42}$$

where d_p is the diameter of the piston, c is the nominal gap size between the piston and the bore wall, P_c is the pressure of the case of the hydraulic transformer, μ is the absolute viscosity of the hydraulic fluid, and e is the eccentricity of the piston. The piston eccentricity is taken as 90% of the physical maximum ($e = 0.9c$) throughout this analysis to capture the experimentally observed trend that pistons loaded under pressure tend to be supported by a relatively thin hydrodynamic film approaching a mixed lubrication regime [28]. $L_{p,k}$ is the instantaneous sealing length given by

$$L_{p,k}(t) = L_0 - S_{p,k}(t) \tag{2.43}$$

where L_0 is the initial overlap length of the piston and cylinder block if the swashplate angle is 0.

2.3.3 Shoe Slipper Leakage

The leakage flow through the shoe slipper and the swash plate as visualized in Fig. 2.10 is given by [70]:

$$Q_{ls,k} = \frac{\pi h_s^3}{6\mu \ln(r_o/r_i)}(P_{r,k} - P_c) \tag{2.44}$$

where h_s is the height of the gap between the shoe slipper and the swashplate, r_i and r_o are the inner and outer radius of the shoe sealing land, respectively. $P_{r,k}$ is the pressure

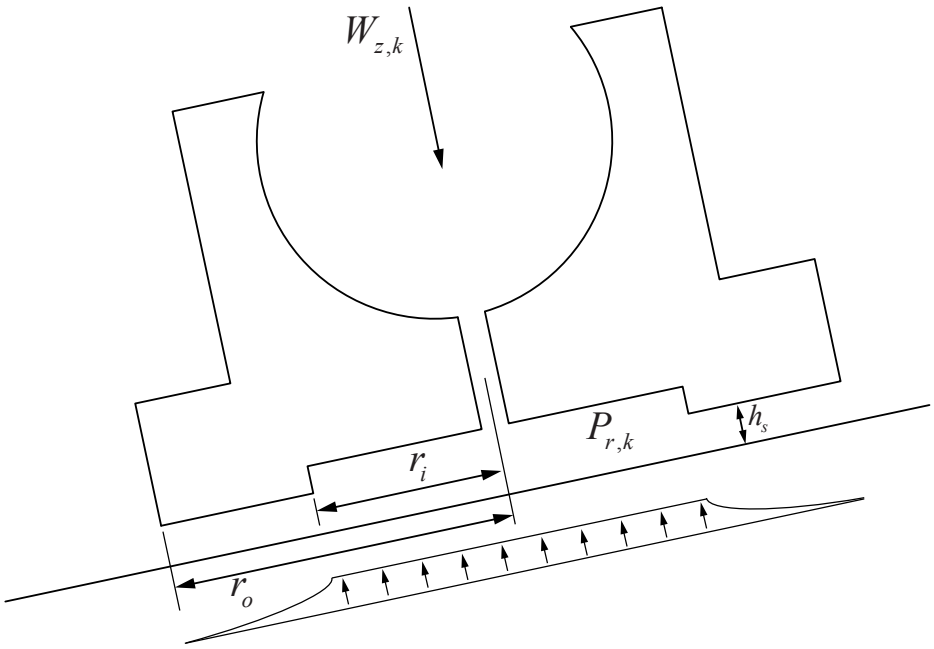

Figure 2.10: Piston shoe slipper geometry

of the fluid under the shoe slipper recess given by:

$$P_{r,k} = W_{z,k} \frac{2\ln(r_o/r_i)}{\pi(r_o^2 - r_i^2)} \tag{2.45}$$

where $W_{z,k}$ is the normal reaction force being applied on the shoe slipper,

$$W_{z,k} = P_{p,k} A_p + P_c A_{net} \tag{2.46}$$

A_{net} is the net surface area on which the case pressure acts upon, defined as

$$A_{net} = r_o^2 \pi - A_p \tag{2.47}$$

2.3.4 Valve Plate Leakage

In addition to the leakage flow rates associated with individual pistons, there is also leakage associated with the valve plate of each of the rotating groups. For a uniform gap h_v between the cylinder block and the valve plate, the leakage flow from a port at pressure P_P can be obtained by the following equation, as described in [30]:

$$Q_{lv} = \frac{h_v^3}{12\mu} \left[\frac{1}{\ln(r_2/r_1) + \ln(r_4/r_3)} \right] (P_P - P_c) \tag{2.48}$$

where r_1, r_2, r_3,and r_4 are internal and external annuli around the valve plate as shown in figure 2.11 and P_c is the pressure of the transformer case. A more detailed approach that considers a tilted cylinder block is described in [13].

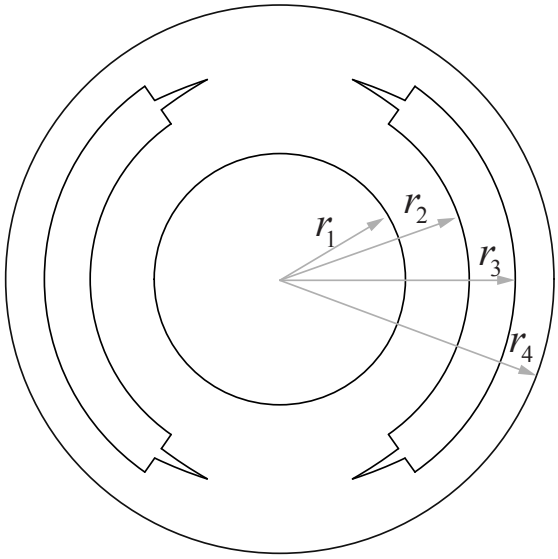

Figure 2.11: Valve plate port geometry

2.4 Dynamic Torque Model for Transformer with Mechanical Losses

In this section, the inertial dynamics of the hydraulic transformer shaft $\dot{\omega}$ is derived. In Sections 2.4.1–2.4.4, losses that occur within each individual piston are modeled. These are the contact friction between the piston and the cylinder bore, Poiseuille and Couette shearing friction, viscous friction from relative motion between the piston shoes and the swashplate. In Section 2.4.5, the torque loss from the relative motion between the cylinder block and the valve plate is modeled. In Section 2.4.6, the net torque is obtained gathering all modeled losses.

2.4.1 Friction Losses between Piston and Cylinder Bore

The frictional forces within the cylinder bores of the transformer are obtained using a mathematical model developed by Manring in [68]. The model takes account the tilt of the piston as prompted by the slipper reaction force, and models the interaction of the piston and the cylinder bore as two point contacts, as shown in Fig. 2.12. In this figure, the

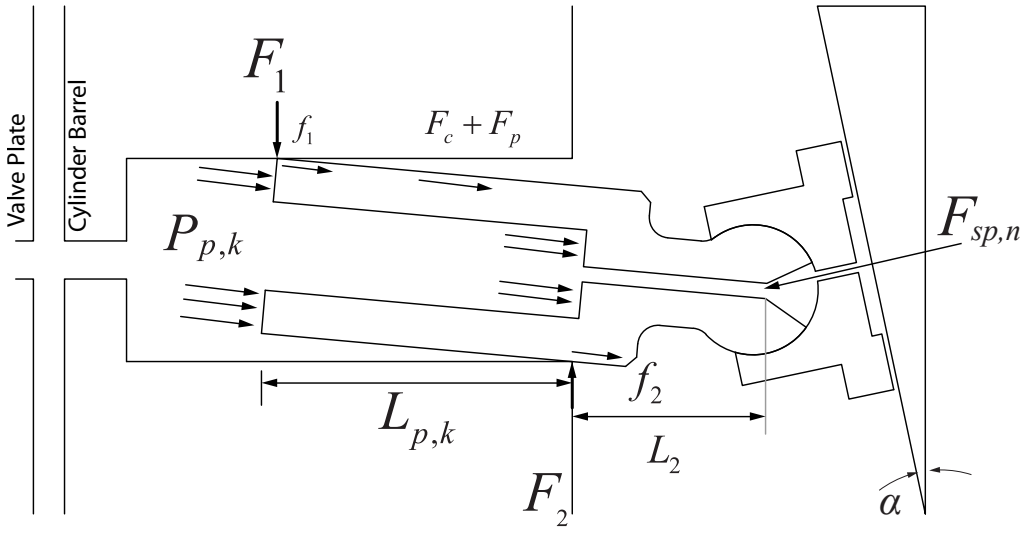

Figure 2.12: Piston chamber schematic showing relevant forces loss forces will be determined in the following section

tilted configuration is exaggerated for the illustrative purpose. The equations presented in this dissertation are the simplified implementation of Manring's approach and takes the pistons as having negligible mass and acceleration.

From Fig. 2.12, by summing the forces acting on the piston in along the piston's major axis and the vertical direction, the following governing equation results:

$$\begin{aligned} 0 &= F_{sp,n}\cos(\alpha) - (A_p P_{p,k} + F_c + F_p + f_1 + f_2) \\ 0 &= -F_{sp,n}\sin(\alpha) - F_1 + F_2 \end{aligned} \tag{2.49}$$

where $F_{sp,n}$ is the reaction force between the slipper shoes and the swashplate, $A_p P_{p,k}$ is the force on the piston face due to the piston chamber pressure, (F_1, f_1) and (F_2, f_2) are the normal reactive forces and the tangential friction forces at the contact points of the piston bore modeled as:

$$\begin{aligned} f_1(t) &= F_1(t)u_1(t)sgn(v_{p,k}(t)) \\ f_2(t) &= F_2(t)u_2(t)sgn(v_{p,k}(t)) \end{aligned} \tag{2.50}$$

where $u_1(t)$ and $u_2(t)$ are the coefficients of the friction to be described in Section 2.4.1, and the sign convention takes is dependent on the piston velocity. Utilizing Eq. 2.49 and Eq. 2.50, the reaction forces F_1 and F_2 are determined as the functions of the net force

F_{net} on the piston and the geometry of the piston and cylinder bore:

$$F_1(t) = \left(\frac{L_2(t)}{L_{p,k}(t)} F_{net} \sin(\alpha) - \frac{d_p}{2L_{p,k}(t)} F_{net}(t) \sin(\alpha) u_2(t) sgn(v_{p,k}) \right) \frac{1}{D(t)} \tag{2.51}$$

$$F_2(t) = \left(\frac{L_2(t) + L_{p,k}(t)}{L_{p,k}(t)} F_{net}(t) \sin(\alpha) - \frac{d_p}{2L_{p,k}(t)} F_{net}(t) \sin(\alpha) u_1(t) sgn(v_{p,k}) \right) \frac{1}{D(t)} \tag{2.52}$$

where,

$$D(t) = \cos(\alpha) + \frac{d_p}{L_{p,k}(t)} u_1(t) u_2(t) \sin(\alpha) - \left(\frac{d_p}{2L_{p,k}} (u_1(t) - u_2(t)) \cos(\alpha) + u_2(t) \sin(\alpha) + \frac{L_2(t)}{L_{p,k}(t)} (u_1(t) - u_2(t)) \sin(\alpha) \right) sgn(v_{p,k}(t)) \tag{2.53}$$

and u_1 and u_2 are the coefficients of friction at the contact points. Refer to Section 2.4.1 for the determination of these values. As stated, acceleration and mass of the piston are assumed to be negligible for this analysis. F_{net} is the net force aligned with the piston major axis, and is given by Eq. (2.54), where viscous forces from Couette and Poiseuille flows are given in Eq. (2.65) and Eq. (2.69). The pressure force from the fluid in the piston chamber is assumed to be applied normal to the piston face it is in communication with, and the viscous forces from the Couette and Poiseuille flows are applied as distributed forces normal to the piston face. The piston was taken as having zero mass:

$$F_{net} = A_p P_{p,k} + F_c + F_p \tag{2.54}$$

L_2 is the distance from the plane of the face of the cylinder block to the center of the piston shoe ball joint, given by:

$$L_2 = L_{p,0} - L_{p,k} \tag{2.55}$$

where $L_{p,0}$ is the distance from the plane of the end of the piston to the center of the piston shoe ball joint.

Obtaining the Coefficient of Friction

The coefficients of friction at contact points are given through modeling the Stribeck curve, which describes the variation of the coefficient of friction between two sliding surfaces.

Three zones exist on the curve: boundary lubrication, mixed lubrication, and hydrodynamic lubrication. Refer to [68] for a complete discussion of the following equations.

The coefficients of friction u_1 and u_2 are given by the following equations, which capture the tendency of the wedge-shaped gap created by a tilted piston in motion to generate a hydrodynamic lifting force.

$$u_1(t) = \begin{cases} \hat{u} \exp\left(-\left(\frac{2L_{p,k}\sqrt{6K^*}}{h^*} \right)^2 \frac{\mu v_{p,k}}{(F_1/d)} \right) + \frac{1}{\sqrt{6K}} \sqrt{\frac{\mu v_{p,k}}{(F_1/d)}} & v_{p,k} > 0 \\ \hat{u} & v_{p,k} \leq 0 \end{cases} \tag{2.56}$$

$$u_2(t) = \begin{cases} \hat{u} & v_{p,k} \geq 0 \\ \hat{u} \exp\left(\left(\frac{2L_{p,k}\sqrt{6K^*}}{h^*} \right)^2 \frac{\mu v_{p,k}}{(F_2/d)} \right) + \frac{1}{\sqrt{6K}} \sqrt{\frac{-\mu v_{p,k}}{(F_2/d)}} & v_{p,k} < 0 \end{cases} \tag{2.57}$$

where h^* is the critical fluid-film thickness at which the transition between mixed and hydrodynamic lubrication occurs. h^* is given by

$$h^* = 3\sqrt{R_a^2 + R_b^2} \tag{2.58}$$

where R_a and R_b are RMS surface roughness of the piston and bore. K and ζ describe fluid-film thickness, and K^* is the special case for K when $h_{min} = h^*$.

$$K = \frac{2(2-\zeta) + \zeta \ln(\zeta - 1)}{\zeta(\zeta - 2)^2} \tag{2.59}$$

$$\zeta = \frac{h_{max}}{h_{min}} + 1 \tag{2.60}$$

h_{min} and h_{max} are the minimum and maximum gap heights along the length of the tilted piston. h_{max} is taken to be twice the nominal clearance within the bore to capture the absence of hydrodynamic lifting on the opposite side of the piston, and the minimum fluid film thickness can be determined for a particular piston velocity $v_{p,k}$ and loading condition W by:

$$h_{min} = l\sqrt{6K\frac{\mu U}{W}} \tag{2.61}$$

Having determined coefficients of friction u_1 and u_2 in equations (2.56) and (2.57), normal contact forces F_1 and F_2 in equations (2.51) and (2.52), and piston velocity $v_{p,k}$

in Eq. (2.3), the frictional forces are determined as in Eq. (2.50):

$$f_1(t) = F_1(t)u_1(t)sgn(v_{p,k}(t))$$
$$f_2(t) = F_2(t)u_2(t)sgn(v_{p,k}(t))$$

where $v_{p,k}$ is the linear velocity of the piston given by Eq. (2.3).

2.4.2 Couette Viscous Friction

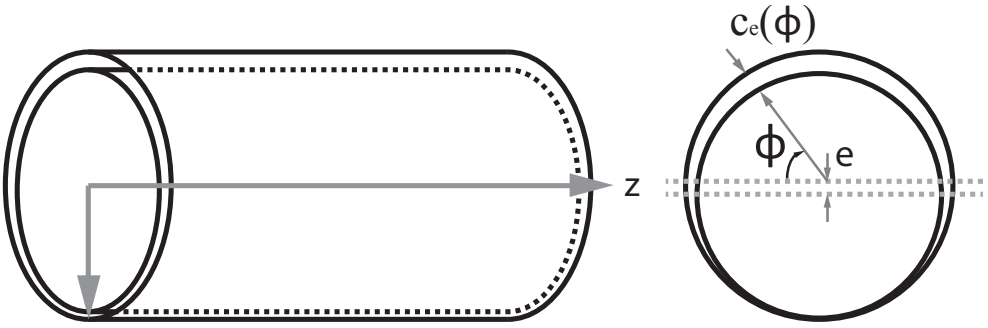

Figure 2.13: Piston Eccentric Clearance

The motion of the piston relative to the cylinder bore generates a shearing viscous force, which is approximated by Couette flow equations [26]. Couette flow was modeled for an eccentric piston shown in Fig. 2.13 where the clearance is given by:

$$c_e(\phi) = c + e\cos(\phi) \tag{2.62}$$

where c is the nominal clearance of the piston bore, e is the eccentricity, and ϕ is the angular position on the piston geometry.

Couette flow can be described by the following equation in the clearance:

$$v_c(\phi, y) = v_{p,k}\left(1 - \frac{y}{c_e(\phi)}\right) \tag{2.63}$$

where $v_{p,k}$ is the piston velocity and $y \in (0, c_e)$. From Newton's law of viscous flow for fluids with a dynamic viscosity of μ, the local shear stress τ can be obtained by:

$$\tau_c(\phi, y) = -\mu\frac{dv_c}{dy} = \mu\frac{v_{p,k}}{c + e\cos(\phi)} \tag{2.64}$$

where μ is the dynamic viscosity of the fluid. The fluid friction force, acting on the piston along the direction of piston linear displacement z and resulting from τ_c is represented as

follows:

$$F_c = \int_0^{2\pi} \int_0^{L_{p,k}} \frac{\mu v_{p,k}}{c + e\cos\phi} dz d\phi = \frac{v_{p,k} L_{p,k} \mu d_p \pi}{\sqrt{c^2 - e^2}} \tag{2.65}$$

where d_p is the diameter of the piston.

2.4.3 Poiseuille Viscous Friction

The pressure difference across the piston causes the fluid to flow through the clearance gap between a piston and the cylinder bore. This generates a viscous shearing force in the direction of fluid motion that can be determined from Poiseuille flow equations [26] For Poiseuille flow in the clearance we have:

$$v_f = -\frac{1}{2\mu}(c_e - y) y \frac{dP}{dz} \tag{2.66}$$

where the rate of pressure drop $\frac{dP}{dz}$ is taken as constant along the axial length of the piston clearance:

$$\frac{dP}{dz} = -\frac{P_{p,k} - P_c}{L_{p,k}} \tag{2.67}$$

Combining Eq. (2.66) and Eq. (2.67) with Newton's law of viscous flow, the local shear stress from Poiseuille flow can be obtained:

$$\tau_f(\phi, y) = \mu \frac{dv_f}{dy} = \mu \left[\frac{P_{p,k} - P_c}{2\mu L_{p,k}} (c + e\cos(\phi) - 2y) \right] \tag{2.68}$$

where $y \in (0, c_e)$ and $\phi \in (0, 2\pi)$. Evaluating the shear stress τ_f at the piston surface, where $y = 0$ along the piston length $L_{p,k}$ arrives at the shearing viscous force from poiseuille flow:

$$\begin{aligned} F_p &= 2 \int_0^{\pi} \int_0^{L_{p,k}} \frac{P_{p,k} - P_c}{2\mu L_{p,k}} (c + e\cos(\varphi) - 2y) r_p dz d\varphi \\ &= \int_0^{\pi} (P_{p,k} - P_c)(c + e\cos(\varphi)) r_p d\varphi \\ &= (P_{p,k} - P_c) r_p \int_0^{\pi} (c + e\cos(\varphi)) d\varphi \\ &= (P_{p,k} - P_c) r_p \pi c \end{aligned} \tag{2.69}$$

2.4.4 Piston Shoe Viscous Friction

The relative motion between the piston shoes and the swashplate generates a viscous shearing force. The exact nature of the hydrodynamic lubrication between the two is not

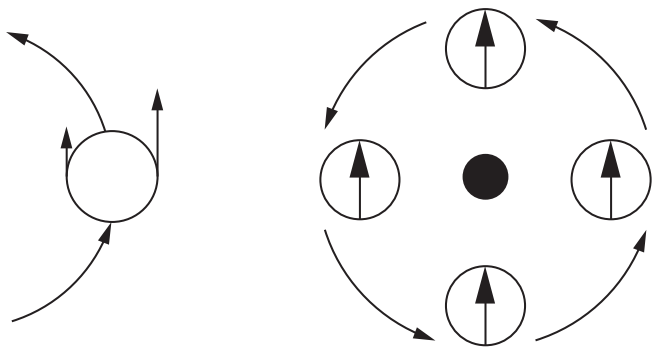

Figure 2.14: Left: Piston shoe is Exposed to Different Linear Velocity as It travels with respect to the shaft; Right: The resulting shoe orientation as a result

well understood and is an active area of research. However, serval numerical studies indicate that a properly designed piston shoe will be fully supported on a fluid film without transition to mixed lubrication [43, 76]. Thus, this dissertation assumes full boundary lubrication where losses are completely viscous and dependent on the velocity of the surface, the viscosity of the fluid, and gap height between two surfaces.

In order to determine the loss due to a viscous friction, it is necessary to obtain the velocity between the two surfaces. In this case, the two surfaces are each piston shoe and the swashplate. If the piston were to rotate rigidly with the cylinder block, then the outer edge of the piston shoe would move faster than the inner edge. This would expose the piston shoe to different levels of friction, and as a result, the piston would spin with respect to its own center in the direction opposite to the shaft movement. The resulting motion of the piston shoe is taken as a combination of rotation around the shaft and rotation around the piston center, as shown in and Fig. 2.15.

The actual rotational speed of this resulting piston spinning movement depends on the force balance arising from friction forces between the piston and the piston bore in the piston chamber in the ball joint connecting piston shoes and pistons in addition to the force balance between the shoe and swashplate. In this dissertation, it is assumed that the global angular orientation of the piston and shoe assembly does not change as a function of its current angular position $\varphi_{p,k}$ as seen in Fig. 2.14.

Note that the velocity magnitude contributed by considering the pistons spinning with respect to their own center is quite small, and will not change dramatically even if other assumptions are utilized.

Figure 2.16 shows a sample set of both velocity components as well as the total velocity vector as they would be dispersed on a shoe for one of seven pistons in a 3.15 cc rotating

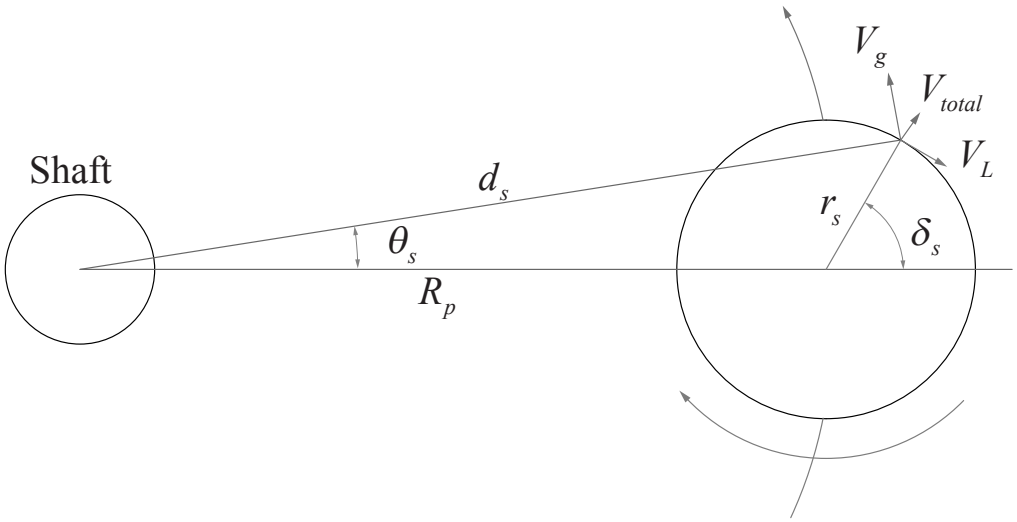

Figure 2.15: Piston Shoe Velocity components displayed with a shaft

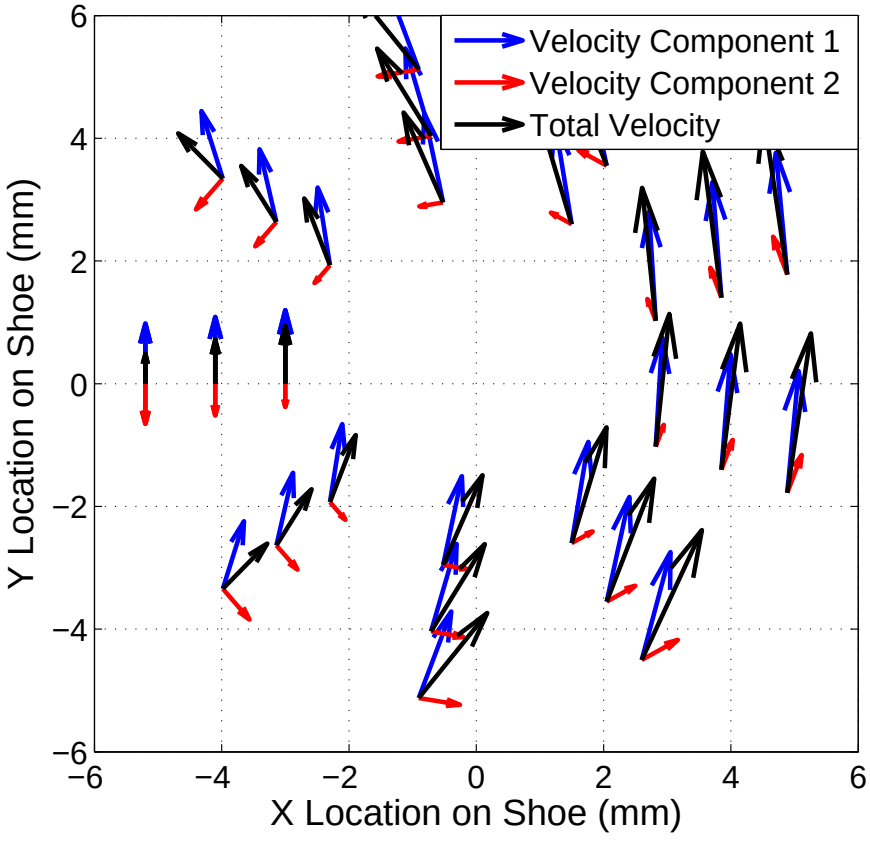

Figure 2.16: Piston Shoe Velocity Vectors for a single piston

group. The instantaneous tangential and radial velocity component arising from the shaft rotation for an infinitesimal point on the shoe can be obtained as:

$$\begin{aligned} v_{1t}(t) &= d_s\omega(t) \\ v_{1\theta}(t) &= \theta_s(t) - \frac{\pi}{2} \end{aligned} \tag{2.70}$$

where d_s and θ_s describes the location of a given infinitesimal point on the shoe as shown in Fig. 2.15 given by:

$$\begin{aligned} d_s(t) &= \sqrt{R_p^2 + r_s^2 - 2R_p r_s \cos(\pi - \delta_s(t))} \\ \theta_s(t) &= \sin^{-1}\left(r_s \sin\left(\frac{\pi - \delta_s(t)}{d_s}\right)\right) \end{aligned} \tag{2.71}$$

Through the similar geometrical consideration, the velocity component arising from the shoe spinning around the piston center could be obtained for the same infinitesimal point:

$$\begin{aligned} v_{2t}(t) &= r_s\omega(t) \\ v_{2\theta}(t) &= \theta_s(t) + \pi \end{aligned} \tag{2.72}$$

These coordinates can be translated to give the x and y components of the velocity vectors shown in Fig. 2.16:

$$\begin{aligned} v_x(t) &= v_{1t}(t)\cos(v_{1\theta}(t)) + v_{2t}(t)\cos(v_{2\theta}(t)) \\ v_y(t) &= v_{1t}(t)\sin(v_{1\theta}(t)) + v_{2t}(t)\sin(v_{2\theta}(t)) \end{aligned} \tag{2.73}$$

From this, we have the following velocity magnitude for a given point on the shoe, which comes from the resultant velocity vector from $v_x(t)$ and $v_y(t)$:

$$v_s = \sqrt{v_x^2(t) + v_y^2(t)} \tag{2.74}$$

Having obtained the velocity magnitude the shearing stress can be obtained as:

$$\tau_s = \mu\frac{1}{h_s}v_s \tag{2.75}$$

Using the relationship between power in the linear mechanical domain and the rotational mechanical domain:

$$\tau_s v_s = \frac{dT_s}{dA}\omega \tag{2.76}$$

where dA is the area of the infinitesimal point under consideration. The values can be

rearranged to solve for torque T_s, and then integrated over the entire area of the shoe sealing land to obtain the total torque exerted by the k-th piston on the transformer:

$$T_{s,k} = \int_{r_i}^{r_o} \int_0^{2\pi} \tau_s v_s(t) \frac{1}{\omega(t)} r_s d\delta_s dr_s \tag{2.77}$$

2.4.5 Valve Plate Viscous Friction

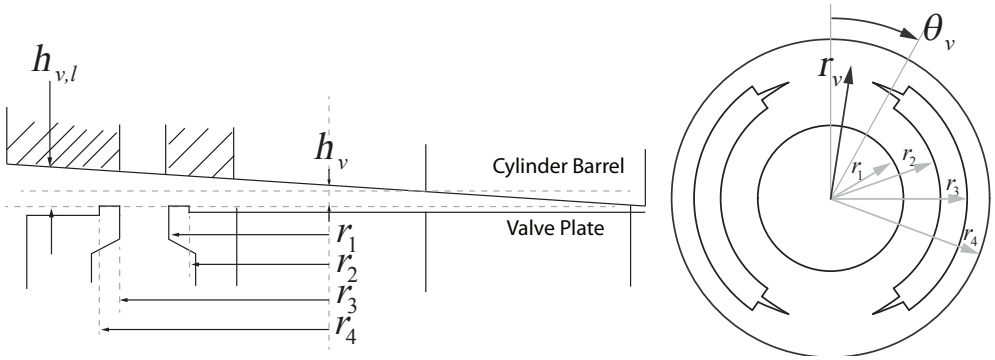

Figure 2.17: Geometry between piston barrel and valve plate

Another viscous friction being modeled is one between the valve plate and the cylinder barrel. Taking into account the tilt, the local valve plate gap height $h_{v,l}$ can be obtained by (Fig. 2.17):

$$h_{v,l} = h_v + r_v \tan\left(tan^{-1}\left(\frac{h_v}{r_4}\right)\right)\cos(\theta_v) \tag{2.78}$$

The local shear stress can be found through viscous shearing:

$$\tau_v = \mu \frac{1}{h_{v,l}} v_v = \mu \frac{1}{h_{v,l}} \omega(t) r \tag{2.79}$$

Translating linear domain to rotational domain similar to Eq. 2.76, the total torque from the valve plate can be obtained by integrating the torque contribution from the viscous shearing:

$$T_v = \int_{r_1}^{r_2} \int_0^{2\pi} \mu \frac{1}{h_{v,l}} \omega(t) r^3 d\theta_v dr_v \tag{2.80}$$

2.4.6 Net Torque and Rotational Speed Dynamics

Using the normal component of the net forces $(F_2 - F_1)$ exerted by a piston on the cylinder block and subtracting the viscous torque losses from the shoes $T_{s,k}$, the torque contribution

from each individual piston is obtained:

$$T_{p,k}(t) = (F_2(t) - F_1(t))\, R_p \sin(\varphi_{p,k}(t)) - T_{s,k}(t) \tag{2.81}$$

where F_1 and F_2 are given by Eq. 2.51 and Eq. 2.52 and $T_{s,k}$ is given by Eq. (2.77). R_p is the radial distance of the piston center from the shaft center in Fig. 2.1.

Note in ideal situation where there are no friction (ie $u_1 = u_2 = F_c = F_p = T_{s,k} = 0$), the torque equation in Eq. (2.81) reduces to

$$T_{p,k}(t) = A_p P_{p,k} \tan(\alpha) R_p \sin(\varphi_{p,k}(t))$$

which is the same equation observed in Eq. (2.14)

Summing the contributions across all of the pistons within a rotating group and applying the viscous torque losses from the valve plate, the total torque of the u-th rotating group T^u is obtained:

$$T^u = \left[\sum_{k_1=1}^{n} T_{p,k} \right] + T_v \tag{2.82}$$

The rotational acceleration can then be determined, where J is the total rotational inertia of the rotating components with respect to the axis of the transformer shaft:

$$J\dot{\omega} = T^1 + T^2 \tag{2.83}$$

In case of IHT, there only exits one unit such that only T^1 components remain for the dynamics equation.

2.5 Chapter Summary

This chapter presented the mathematical modeling for hydraulic transformers. As hydraulic transformers are built on axial piston pumps and motors, the modeling process started with understanding the operating principle of the axial piston pump/motors and expanded the result to the appropriate configuration of the transformers. The main difference between regular pump/motor and transformer comes from how the valve plate is routed to each port. The models established here are used as tools to analyze the performance of the hydraulic transformers throughout this thesis.

Chapter 3

Sizing and Flow Ripple Comparison of Transformer Designs

In this and the next chapter, we compare the existing designs of hydraulic transformers to understand the characteristics of each design and set the design principle to be used for developing the prototype. As mentioned in Chapter 1, previous literature on transformer research heavily focuses on the design aspect of IHT. A quantitative analysis that compares IHT against PM transformer is still lacking. Filling in this apparent gap in transformer research is one of the contributions of this dissertation.

PM transformer and IHT are compared against each other in three areas: displacement sizing, flow ripple, and efficiency. These areas are among the most critical considerations in developing a hydraulic component [89]. The sizing and flow ripple will be studied in this chapter, and the efficiency will be analyzed in the next chapter. This is not the very first attempt in establishing a quantitative comparison. Werndin and Palmberg [89] previously established a quantitative comparison between IHT and PM transformer in terms of efficiency, weight, and size. They compared a PM-1 (tank-shared), PM-3 (input-shared) configurations and an INNAS transformer. Scaling a published efficiency data for pump and motors, they found the IHT to be more efficient than the PM transformer. The weight and size ratio of PM transformers against the IHT design is also established, indicating the PM transformer design is at minimum 90% larger than IHT in terms of total size. Their comparison work leaves some room for further investigation. First, only two of the three possible PM transformer configurations were considered. Second, the efficiency comparison was established by scaling a published efficiency data rather than

building a model specific to the transformer. Lastly, the methods utilized in establishing their size comparison is unclear at best. In terms of flow ripple, it was acknowledged by the developers of the IHT [3] [11] that flow ripple is one of the major setbacks for the IHT. This chapter will study the flow ripple for PM transformer and the IHT by adapting Manring's extensive work on flow ripple of the axial piston rotating group [69] which considered both incompressible flow and compressible flow.

The rest of the chapter is organized as following. Section 3.1 examines the difference in total volumetric displacements between PM transformer and IHT in order to deliver the similar output flow for the range of transformation ratio λ if the same maximum speed is imposed for all configurations. Section 3.2 takes a slightly different approach in sizing comparison where the maximum speed is the consequence of viscous friction rather than a pre-defined limit. Section 3.3 compares the flow ripple characteristics of the PM transformers and IHT.

3.1 Displacement Sizing

3.1.1 Comparison Methods

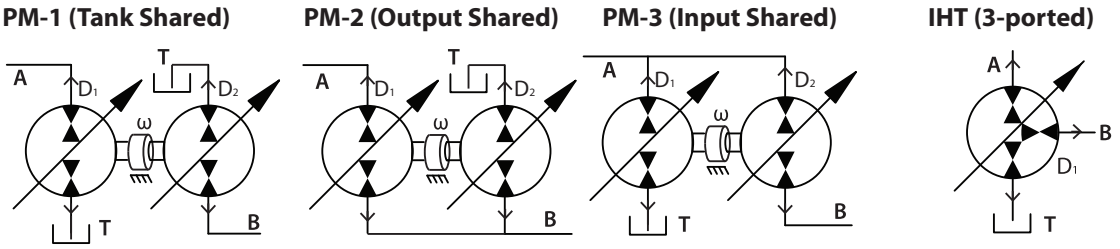

Figure 3.1: Three configurations for PM Transformer and IHT

Since the transformer needs to be a compact hydraulic component, it is important to understand the inherent difference arising from the different design principles and configurations. Since the IHT configuration consists of a single axial piston unit while PM consists of two pump/motors, IHT design can be more compact than PM [2, 89]. In this section, we quantify the relative sizes that the PM configurations in Fig. 3.1 are required in order to have rated power similar to the IHT.

For hydraulic transformers, their rated power depends on the volumetric displacement per port, maximum speed, and maximum allowable pressure. Therefore, if the maximum speed and maximum allowable pressure are assumed to be the same, and valve plate is assumed to have a symmetric shape as seen on Fig. 2.2, what determines the output power

of the transformer is the volumetric displacement. Even with a novel design to reduce the enclosure size of the transformers, the volumetric displacement required to deliver the flow to achieve power specification remains the same. Therefore, we make the 'size' comparison solely for the maximum total volumetric displacement of all the pistons in the transformers to achieve the maximum flow output using idealized models for a given shaft speed over the interested range of pressure transformation ratio. For the PM configuration this is $D_{1,max} + D_{2,max}$; for the IHT, this is D. For each PM configuration or IHT, the 'flow capability' at each pressure transformation ratio λ is defined to be the maximum input or output flows (with choice of $D_1(t)$ and $D_2(t)$ for the PM, and $\theta(t)$ for IHT) for a given shaft speed ω.

Using IHT with an unit displacement D as the basis for comparison, three methods are defined to compare the necessary PM size to match the output flow of IHT over the interested range of pressure transformation. The comparison could be established using PM transformer as a basis instead, yielding the same result. In method I, the minimum combined displacements $D_{1,max} + D_{2,max}$ is found such that its flow capability at *each* transformation ratio λ matches or exceeds those of the IHT for $\lambda \in [0, \infty)$. In method II, the maximum total displacement $D_{1,max} + D_{2,max}$ is found such that its flow capability at *each* transformation ratio λ is less than or equal to that of the IHT for $\lambda \in [0, \infty)$. Finally in method III, the smallest combined PM displacement that also minimizes the 2-norm of the difference between the flow capabilities of two transformers over the entire range of $\lambda \in [0, \infty)$ is found. These methods are mathematically summarized below:
Method I: For given IHT with total displacement D:

$$\begin{aligned} \min_{D_{1,max}, D_{2,max}} \quad & D_{1,max} + D_{2,max} \\ \text{subject to} \quad & \text{PM flow} \geq \text{IHT flow} \quad \text{for } \lambda \in [0, \infty) \text{ and same } \omega_{max} \end{aligned} \tag{3.1}$$

Method II: For given IHT with total displacement D:

$$\begin{aligned} \max_{D_{1,max}, D_{2,max}} \quad & D_{1,max} + D_{2,max} \\ \text{subject to} \quad & \text{IHT flow} \geq \text{PM flow} \quad \text{for } \lambda \in [0, \infty) \text{ and same } \omega_{max} \end{aligned} \tag{3.2}$$

Method III: For given IHT with total displacement D:

$$\min_{D_{1,max}, D_{2,max}} \quad ||\text{PM flow} - \text{IHT flow}|| \quad \text{for } \lambda \in [0, \infty) \text{ and same } \omega_{max} \tag{3.3}$$

where $||\text{PM flow} - \text{IHT flow}||$ is the 2-norm of the difference between the flow capabilities

Table 3.1: Displacements $D_{1,max}$, $D_{2,max}$ and $D_{1,max}+D_{2,max}$ normalized by the displacement of the IHT

	Sizing Method	PM-1	PM-2	PM-3
I.	PM flow $\geq$ IHT	0.867 / 0.867 — 1.734	0.864 / 0.864 — 1.727	0.864 / 0.864 — 1.727
II.	IHT flow $\geq$ PM	0.750 / 0.750 — 1.50	0.433 / 0.433 — 0.866	0.433 / 0.433 — 0.866
III.	$\min \|\text{PM} - \text{IHT}\|$	0.826 / 0.826 — 1.652	0.631 / 0.571 — 1.202	0.635 / 0.635 — 1.27

of two transformers for the range of λ. The output flow equations for the transformers are given by Eqs. (2.18)–(2.21) and Eq. (2.26).

The total volumetric displacements of PM-1, 2, 3 that meet the three sizing criteria are obtained using Matlab's optimization function. The optimization function finds the $D_{1,max} + D_{2,max}$ necessary to meet each of the sizing criteria.

3.1.2 Sizing Results

Figures 3.2-3.4 show the input and output flow for IHT along with those from PM transformer with the volumetric displacement found from the three sizing methods along with the displacement ratio necessary to achieve the pressure transformation. It can be seen that as intended, the output flow curve for sizing method I is always higher than or equal to that of the IHT, and the output flow curve for sizing method II is always lower than or equal to that of the IHT. On the other hand, the output flow curve for sizing method III can be higher or lower than that of IHT as seen in the figures.

Table 3.1 summarizes the relative displacement with respect to the IHT necessary to meet each of the sizing methods. Since PM transformer consist of two units, $D_{1,max}$ and $D_{2,max}$ are presented along with $D_{1,max} + D_{2,max}$. In each of the PM configuration, sizing method I results in the largest PM size relative to IHT, method II results in the smallest, and method III results in the intermediate size. With methods 2 and 3, PM-2 and 3 could be smaller than IHT.

The optimal displacements for the two units are the same with the exception of PM-2 with Method III. In this case, $D_{1,max} = 0.631$ and $D_{2,max} = 0.571$. With methods II and III, PM-2 and PM-3 are smaller than the IHT. Overall, it can be seen that PM-1 is 50-73% larger than IHT, whereas PM-2 and PM-3 range from 18% smaller to 73% larger than IHT. The large range is due to PM-2/3 and IHT have different output port flow advantages at different transformation ratios. Instead of establishing the comparison for the whole range of pressure transformation ratio $\lambda \in [0, \infty)$, we could limit the range of comparisons

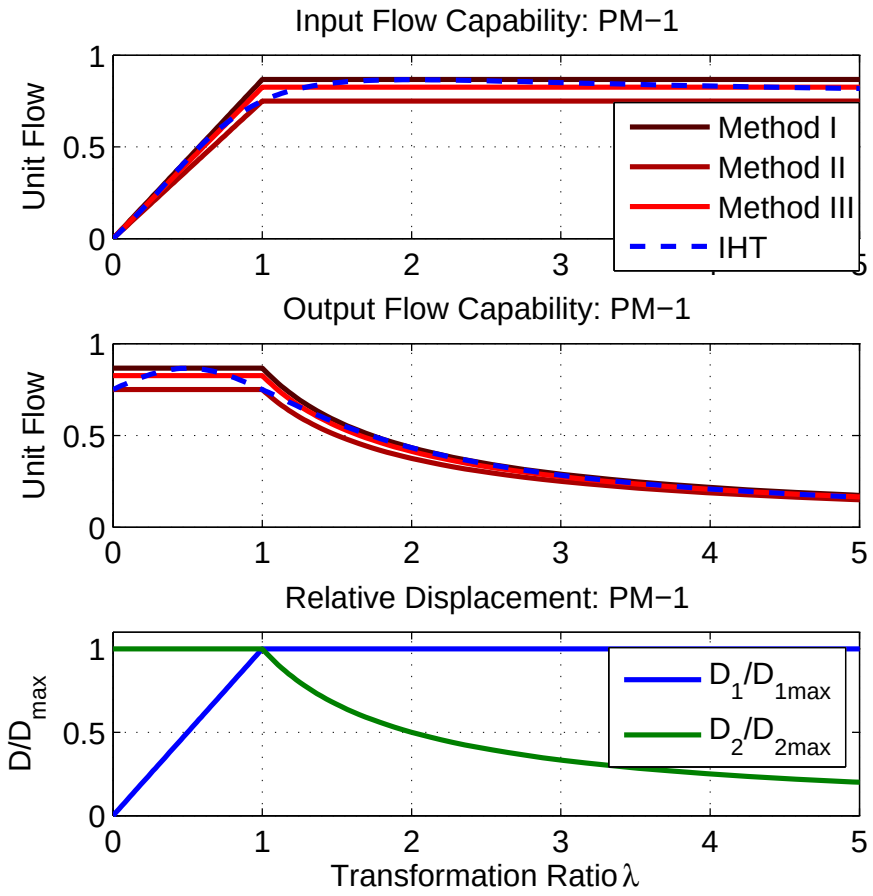

Figure 3.2: TOP: Input and output flow for PM-1 with the total displacement according to three different sizing methods, plotted against input and output flow of IHT normalized by $D\omega$. BOTTOM: displacement ratio necessary to achieve the pressure transformation ratio

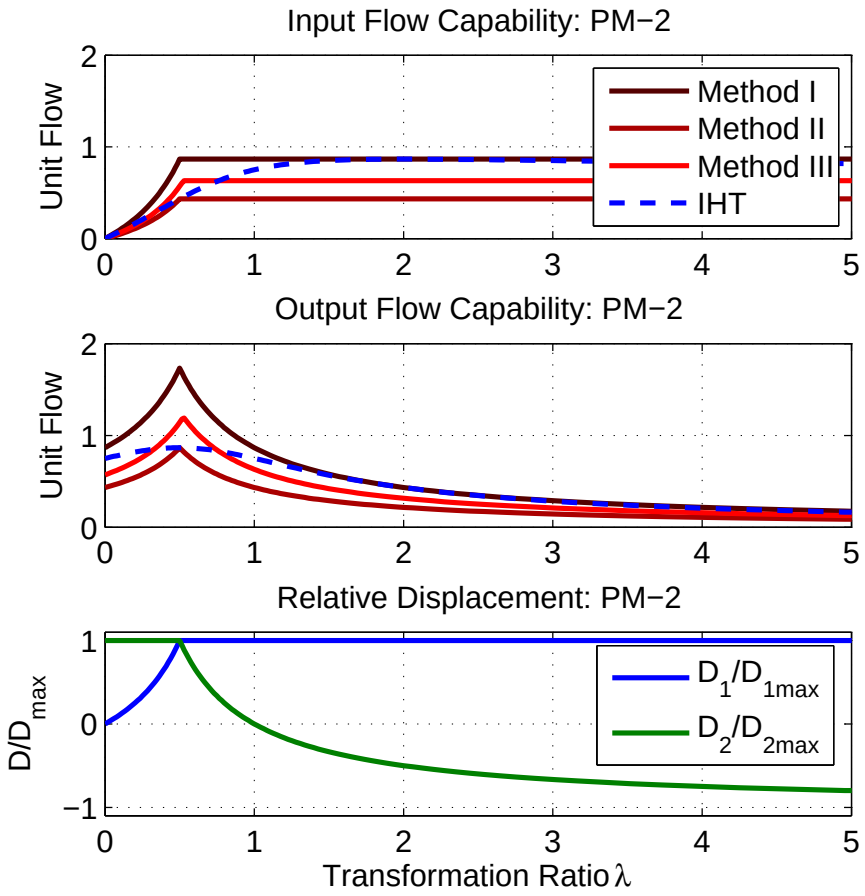

Figure 3.3: TOP: Input and output flow for PM-2 with the total displacement according to three different sizing methods, plotted against input and output flow of IHT normalized by $D\omega$. BOTTOM: displacement ratio necessary to achieve the pressure transformation ratio

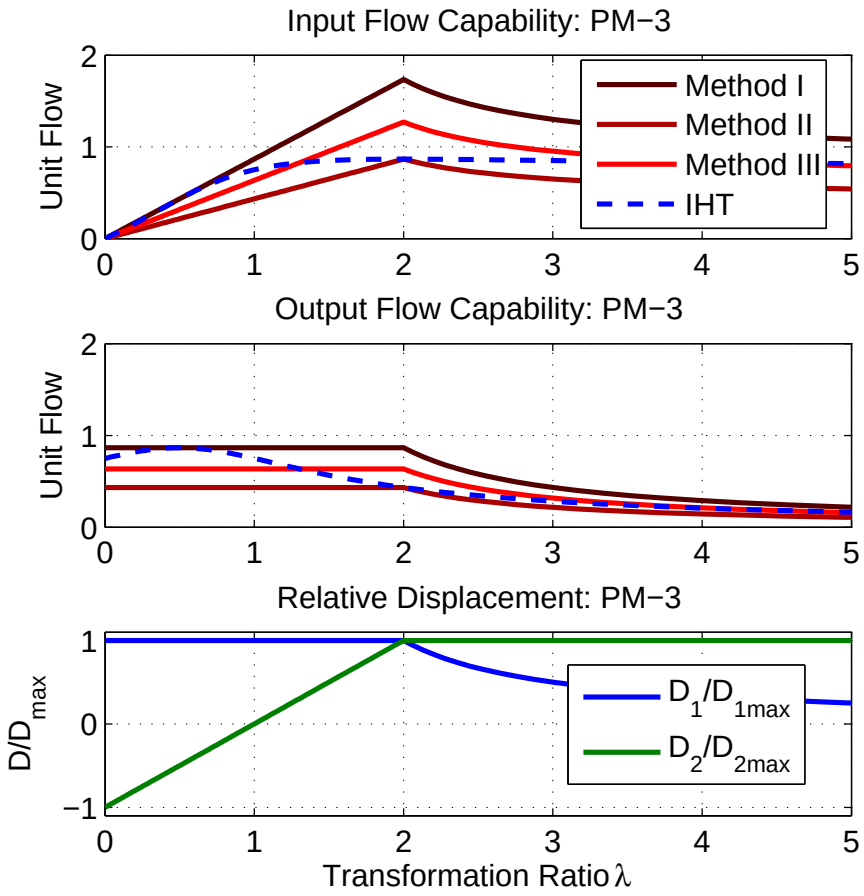

Figure 3.4: TOP: Input and output flow for PM-3 with the total displacement according to three different sizing methods, plotted against input and output flow of IHT normalized by $D\omega$. BOTTOM: displacement ratio necessary to achieve the pressure transformation ratio

Table 3.2: Displacements $D_{1,max}$, $D_{2,max}$ and $D_{1,max} + D_{2,max}$ normalized by the displacement of the IHT if PM transformer is allowed to switch its configuration mode

	Sizing Method	port switching PM
I.	PM flow $\geq$ IHT	0.75 / 0.75 — 1.50
II.	IHT flow $\geq$ PM	0.433 / 0.433 — 0.866
III.	$\min \|\|\text{PM} - \text{IHT}\|\|$	0.585 / 0.56 — 1.145

to be $\lambda \in [0, 2)$, instead. However, sizing results comes out to be the exactly same as performing comparison over $\lambda \in [0, \infty)$. This is because the distinct flow characteristics all happen within $\lambda \in [0, 2)$. Beyond $\lambda = 2$, the flow capability is only monotonically decreasing with respect to λ, and adding this region do not affect the sizing results. Even with the difference rate of decrease in output flow, what affects the sizing is output flow in $\lambda \in [0, \infty)$.

3.1.3 Configuration Mode Switching

Figures 3.2-3.4 show that each of the three PM configurations has a different region of transformation ratio with higher output flow than the other configurations. For example, it is seen PM-2 yields the highest output flow for $\lambda = 0.5$ while PM-1 yields the highest output flow for $\lambda = 1$.

This gives rise to an opportunity. If the port configuration can be altered such that the same PM transformer can operate in multiple configurations rather than a fixed one, a PM transformer could achieve higher flow capabilities across its entire range of pressure transformation ratio by selecting the best configuration according to the transformation ratios. The results of the three sizing methods allowing port switching are summarized on Table 3.2, showing the $D_{1,max}$, $D_{2,max}$ and combined $D_{1,max} + D_{2,max}$ necessary to satisfy the three sizing methods.

In this case, the size of PM configuration needs only be 0.866 to 1.5 times that of IHT configuration. Focusing only on Method II, it can be seen the PM transformer can be sized 14% smaller than the IHT in terms of the total volumetric displacement. This is contrary to the previous understanding that the PM transformer is inevitably larger than the IHT. Focusing on Method III, the switching reduces the required volumetric sizing to be 14.5% larger as opposed to 20% to 65% larger observed in Table 3.1.

The input and output flow for the PM transformer sized with three sizing methods are shown in Fig. 3.5. The optimized switching utilizes PM-2 and PM-3 only (transition at $\lambda = 1$ from PM-2 to PM-3), but not PM-1. This switching could be implemented with

a control valve and will be discussed in Chapter 5. Because of symmetry, port switching does not make any difference to the flow capability of an IHT with equal port angles. Limiting the transformation ratio range to $\lambda \in [0, 2)$ yields the same sizing result.

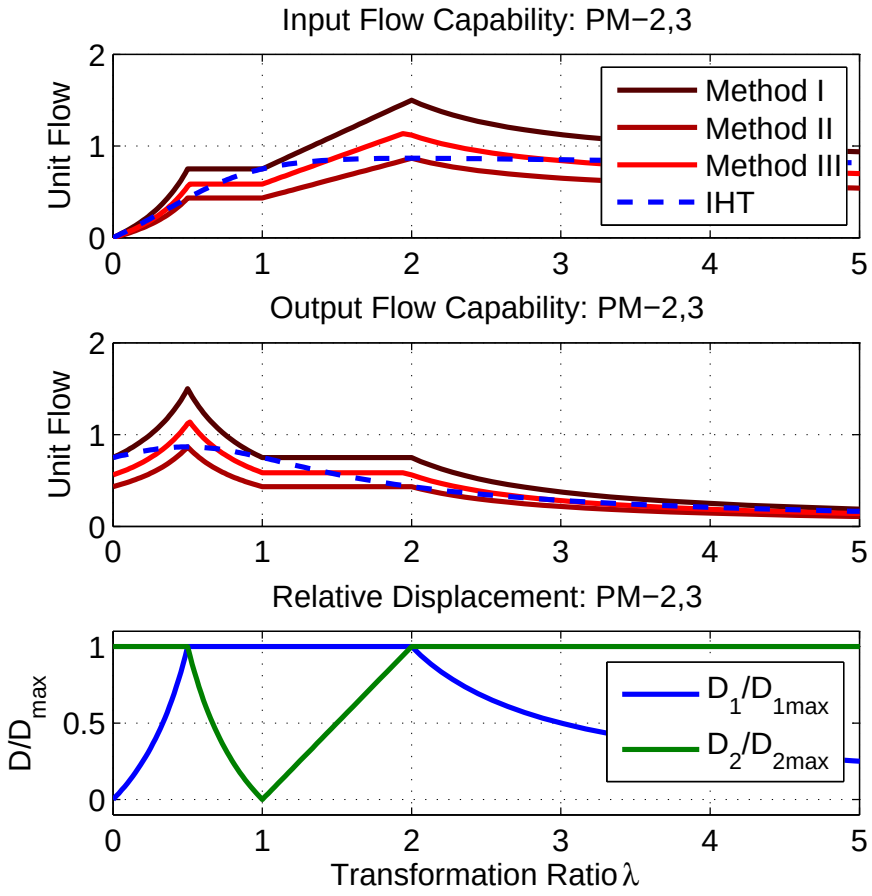

Figure 3.5: TOP: Input and output flow for PM transformer that can switch its configuration mode with the total displacement according to three different sizing methods, plotted against input and output flow of IHT. BOTTOM: displacement ratio necessary to achieve the pressure transformation ratio

Note that the volume of the mechanism for varying displacements is not included in the sizing comparison. For the PM transformers, this involves actuators for rotating the swash-plates (typically solenoids or hydraulic piston) whereas, for the IHT, this involves rotating the port plate or the cylinder barrel (typically an electric motor). It is likely that the IHT displacement adjustment will be more compact than that of PM transformer. However, the resulting size difference will not be as large as twice as hinted by earlier literature on IHT [2].

3.2 Sizing with the Friction Loss

In this section, we take another approach for the sizing comparison: in the previous section, an ideal model was used in making the sizing comparison assuming the same shaft speed for all configurations. In this section, a model with viscous friction will be used to find the maximum flow for each pressure transformation ratio λ. The maximum shaft speed limit will not be imposed. Rather, a shaft speed that corresponds to the maximum flow for each lambda will be declared as the maximum shaft speed.

3.2.1 Determining the Maximum Flow and Shaft Speed for Transformer

Considering a viscous friction to the transformers introduces the additional term '$-b\omega$' into the torque equation where b is the coefficient of viscous friction working against the transformer shaft. With this, the dynamic equations for the transformer will be:

$$J\dot{\omega} = \begin{cases} (P_A - P_T)\frac{D_1}{2\pi} + (P_T - P_B)\frac{D_2}{2\pi} - b\omega & \text{PM-1} \\ (P_A - P_B)\frac{D_1}{2\pi} + (P_T - P_B)\frac{D_2}{2\pi} - b\omega & \text{PM-2} \\ (P_A - P_T)\frac{D_1}{2\pi} + (P_A - P_B)\frac{D_2}{2\pi} - b\omega & \text{PM-3} \\ -(P_A - P_T)\frac{D_A(\theta)}{2\pi} - (P_B - P_T)\frac{D_B(\theta)}{2\pi} - b\omega & \text{IHT} \end{cases} \tag{3.4}$$

where D_1 and D_2 are the displacements of the two units in PM transformers that can vary within the maximum displacement such that $|D_1| \leq D_{1,max}$ and $|D_2| \leq D_{2,max}$. For an IHT, $D_P(\theta)$ is the port displacement at port 'A', 'B', and 'T' of the unit that results from the valve plate rotation angle θ with total volumetric displacement with D as observed in Eq. (2.23).

The output flow of the transformer Q_B is defined as

$$Q_B = \begin{cases} \frac{D_2}{2\pi}\omega & \text{PM-1} \\ \frac{D_1 + D_2}{2\pi}\omega & \text{PM-2} \\ \frac{D_2}{2\pi}\omega & \text{PM-3} \\ \frac{D_B(\theta)}{2\pi}\omega & \text{IHT} \end{cases} \tag{3.5}$$

these are the equations from Eq. (2.26) and (2.18)–(2.21). For the PM transformer with maximum displacement $D_{1,max}$ and $D_{2,max}$, we perform the following maximization in order to find the maximum flow obtainable for a given pressure transformation ratio λ.
For given a given PM transformer configuration with $D_{1,max}$ and $D_{2,max}$, and pressure

transformation ratio λ:

$$\begin{aligned} \max_{\omega, D_1, D_2} \quad & Q_B \\ \text{subject to} \quad & |D_1| \leq D_{1,max} \\ & |D_2| \leq D_{2,max} \\ & J\dot{\omega} = 0 \end{aligned} \tag{3.6}$$

where Q_B is the output flow of PM transformers given in Eq. (3.5) and $J\dot{\omega}$ is a function of P_A, P_B, P_T, D_1 and D_2 as seen in Eq. (3.4). Performing the above maximization for the range of pressure transformation ratio $\lambda \in [0, \infty)$ will yield the maximum shaft speed and flow as a function of pressure transformation ratio λ for each transformer configuration.

With IHT, the above formulation is modified slightly to be the following:

$$\begin{aligned} \max_{\omega, \theta} \quad & Q_B \\ \text{subject to} \quad & J\dot{\omega} = 0 \end{aligned} \tag{3.7}$$

where Q_B is the function of port plate rotation θ as seen in Eq. (3.5), and $J\dot{\omega}$ is a function of P_A, P_B, P_T, D and θ as seen in Eq. (3.4). The difference in transformer configurations and their dynamics will result in different maximum speed obtainable for each configuration and values of λ.

PM-1

To illustrate the above process of finding the maximum obtainable flow, assume $P_T = 0$ such that the transformation ratio is defined as $\lambda = P_B/P_A$ [1]. At steady-state ($\dot{\omega} = 0$), the torque equation for PM-1 reduces to

$$0 = \frac{D_1}{2\pi} P_A - \frac{D_2}{2\pi} P_B - b\omega \tag{3.8}$$

If D_1 is given and P_A, λ are known, the above equation can be rearranged to be solved for D_2 to be determined

[1] The results are the same for the arbitrary P_T with $\lambda = \frac{P_B - P_T}{P_A - P_T}$ if P_A is substituted by $P_A - P_T$ and P_B is substituted by $P_B - P_T$

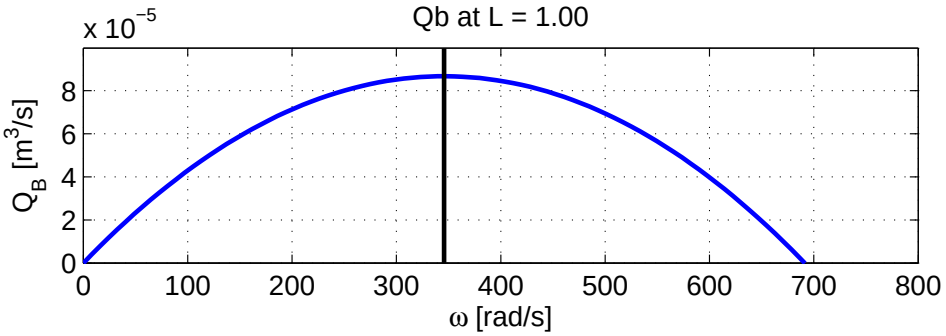

Figure 3.6: Flow vs Shaft Speed for $\lambda = 1$ and $b = 0.005$ for PM-1

$$\begin{aligned} \frac{D_2}{2\pi} \underbrace{P_B}_{P_B=\lambda P_A} &= \frac{D_1}{2\pi} P_A - b\omega \\ \frac{D_2}{2\pi} \lambda P_A &= \frac{D_1}{2\pi} P_A - b\omega \\ D_2 &= \left(D_1 - \frac{b\omega \cdot 2\pi}{P_A} \right) \frac{1}{\lambda} \end{aligned} \tag{3.9}$$

Plug in the result from Eq. (3.9) to the output flow equation for PM-1 in Eq. (3.5), then the output flow is:

$$Q_B = \left(\frac{D_1}{2\pi} - \frac{b\omega \cdot}{P_A} \right) \frac{1}{\lambda} \cdot \omega \tag{3.10}$$

which is a concave down function of ω as illustrated in Fig. 3.6. We see that this function has a maximum point at certain ω beyond which the flow starts decreasing with respect to the increasing shaft speed.

Now evaluate the derivative of this flow equation with respect to the shaft speed $\frac{\partial Q_B}{\partial \omega} = 0$ to obtain the maximum flow obtainable for given λ

$$\begin{aligned} \frac{\partial Q_B}{\partial \omega} &= 0 \\ \frac{D_1}{2\pi} - \frac{2b\omega}{P_A} &= 0 \end{aligned} \tag{3.11}$$

Solving above equation for ω, we get the shaft speed that will bring the maximum flow.

$$\omega^* = \frac{D_1}{4\pi b} P_A \tag{3.12}$$

Utilizing the ω^* that gives the maximum flow with respect to the value of ω, the maximum flow is

$$Q_{B,max} = \frac{D_1^2 P_A}{16\pi^2 \lambda b} \tag{3.13}$$

With the physical constraint $|D_1| \leq D_{1,max}$, we see that $D_1 = \pm D_{1,max}$ will give the maximum flow.

$$Q_{B,max} = \frac{D_{1,max}^2 P_A}{16\pi^2 \lambda b} \tag{3.14}$$

However, this condition cannot be used for all λ. The value obtained for D_2 for given λ should not violate the physical constraint. Setting $|D_2| \leq D_{2,max}$, following expression can be obtained:

$$-D_{2,max} \leq \frac{D_{1,max}}{2\lambda} \leq D_{2,max} \tag{3.15}$$

Solving above inequality in terms of λ, the range of λ for which Eq. (3.14) provided the maximum flow is:

$$\lambda \geq \frac{D_{1,max}}{2D_{2,max}} \tag{3.16}$$

An expression to obtain the maximum flow when $\lambda < \frac{D_{1,max}}{2D_{2,max}}$ needs to be established. Consider now the case that $\lambda < \frac{D_{1,max}}{2D_{2,max}}$. In order to figure out what needs to be done, re-visit Eq. (3.8) in terms of ω at the steady-state condition with D_2 given:

$$\begin{aligned} 0 &= \frac{D_1}{2\pi} P_A - \frac{D_2}{2\pi} P_B - b\omega \\ \omega &= (D_1 - D_2\lambda)\frac{P_A}{2\pi b} \end{aligned} \tag{3.17}$$

with this shaft speed, the output flow is

$$Q_B = D_2(D_1 - D_2\lambda)\frac{P_A}{4\pi^2 b} \tag{3.18}$$

It can be easily seen that setting $D_1 = \mathrm{sgn}(D_2)D_{1,max}$ will give the maximum flow for any D_2. Plugging in this choice of D_1 to the above equation Eq. (3.18), we have:

$$Q_B = D_2(\mathrm{sgn}(D_2)D_{1,max} - D_2\lambda)\frac{P_A}{4\pi^2 b} \tag{3.19}$$

For the range of $0 < \lambda < \frac{D_{1,max}}{2D_{2,max}}$ being considered, Q_B is positive. It can be seen that $D_2 = \pm D_{2,max}$ maximizes the Q_B. Then the maximum flow is given by:

$$Q_{B,max} = D_{2,max}(D_{1,max} - D_{2,max}\lambda)\frac{P_A}{4\pi^2 b} \tag{3.20}$$

In summary, the following is established for the maximum flow obtainable given λ.

$$Q_{B,max} = \begin{cases} \frac{D_{1,max}^2 P_A}{16\pi^2 \lambda b} & \text{if } \lambda \geq \frac{D_{1,max}}{2D_{2,max}} \\ D_{2,max}(D_{1,max} - D_{2,max}\lambda)\frac{P_A}{4\pi^2 b} & \text{otherwise} \end{cases} \tag{3.21}$$

with corresponding maximum shaft speed:

$$\omega^* = \pm \begin{cases} \frac{D_{1,max}}{4\pi b} P_A & \text{if } \lambda \geq \frac{D_{1,max}}{2D_{2,max}} \\ (D_{1,max} - D_{2,max}\lambda)\frac{P_A}{2\pi b} & \text{otherwise} \end{cases} \tag{3.22}$$

with the displacements

$$D_1 = \pm D_{1,max} \forall \lambda \tag{3.23}$$

and

$$D_2 = \pm \begin{cases} \frac{D_{1,max}}{2\lambda} & \lambda \geq \frac{D_{1,max}}{2D_{2,max}} \\ D_{2,max} & \text{otherwise} \end{cases} \tag{3.24}$$

PM-2

For PM-2, with $P_T = 0$, the torque equation is following:

$$J\dot{\omega} = \frac{D_1}{2\pi}(P_A - P_B) - \frac{D_2}{2\pi}P_B - b\omega \tag{3.25}$$

At steady state, with P_A, λ, and D_1 given we can solve for D_2:

$$\begin{aligned} \frac{D_2}{2\pi} \underbrace{P_B}_{P_B = \lambda P_A} &= \frac{D_1}{2\pi}(P_A - P_B) - b\omega \\ \frac{D_2}{2\pi}\lambda P_A &= \frac{D_1}{2\pi}(P_A - \lambda P_A) - b\omega \\ D_2 &= \left((1-\lambda)D_1 - \frac{b\omega \cdot 2\pi}{P_A}\right)\frac{1}{\lambda} \end{aligned} \tag{3.26}$$

In the meantime, the output flow equation for PM-2 is:

$$Q_B = \left[\frac{D_1}{2\pi} + \frac{D_2}{2\pi}\right]\omega \tag{3.27}$$

Plug in the result from (3.26), then

$$\begin{aligned} Q_B &= \left[\frac{D_1}{2\pi} + \frac{D_2}{2\pi}\right]\omega \\ &= \left[\frac{D_1}{2\pi} + \left(\frac{(1-\lambda)}{\lambda}\frac{D_1}{2\pi} - \frac{b\omega}{\lambda P_A}\right)\right]\omega \\ &= \left[\frac{1}{\lambda}\frac{D_1}{2\pi} - \frac{b\omega}{\lambda P_A}\right]\omega \\ &= \left[\frac{D_1}{2\pi} - \frac{b\omega}{P_A}\right]\frac{1}{\lambda}\omega \end{aligned} \tag{3.28}$$

Evaluate the derivative with respect to shaft speed ω to obtain the maximum flow:

$$\begin{aligned} \frac{\partial Q_B}{\partial \omega} &= 0 \\ \frac{D_1}{2\pi} - \frac{2b\omega}{P_A} &= 0 \end{aligned} \tag{3.29}$$

Solving above for ω, above result can be used to establish the maximum shaft speed that will bring maximum flow:

$$\omega^* = \frac{D_1}{4\pi b} P_A \tag{3.30}$$

with ω^* we found, the maximum flow is

$$Q_{B,max} = \frac{D_1}{4\pi} \frac{1}{\lambda} \frac{D_1}{4\pi b} P_A = \frac{D_1^2 P_A}{16\pi^2 \lambda b} \tag{3.31}$$

Again, it is obvious that $D_1 = \pm D_{1,max}$ will be needed to get the maximum flow.

Also, let's consider the physical constraint $|D_2| \leq D_{2,max}$, from Eq. (3.26), the maximum flow and shaft speed is only satisfied if

$$\frac{D_{1,max}}{2(D_{1,max} + D_{2,max})} \leq \lambda \leq \frac{D_{1,max}}{2(D_{1,max} - D_{2,max})} \tag{3.32}$$

Two cases that are outside the boundary of this condition needs to be considered

A Case where $\lambda < \frac{D_{1,max}}{2(D_{1,max}+D_{2,max})}$:

Solve the torque equation with D_2 given in terms of ω:

$$\omega = \left[(1-\lambda)D_1 - D_2\lambda\right] \frac{P_A}{2\pi b} \tag{3.33}$$

With this shaft speed, the output flow is

$$Q_B = \left(D_1^2(1-\lambda) + D_1 D_2(1-2\lambda) - D_2^2\lambda\right) \frac{P_A}{4\pi^2 b} \tag{3.34}$$

It can be seen that $D_1 = \text{sgn}(D_2) D_{1,max}$ will give the maximum flow for any D_2. Plug in this choice of D_1 we obtain:

$$Q_B = \left(D_{1,max}^2(1-\lambda) + \text{sgn}(D_2) D_{1,max} D_2(1-2\lambda) - D_2^2\lambda\right) \frac{P_A}{4\pi^2 b} \tag{3.35}$$

For the range $\lambda < \frac{D_{1,max}}{2(D_{1,max}+D_{2,max})}$ being considered, Q_B is positive. It can be seen

that $D_2 = \pm D_{2,max}$ maximizes the Q_B, then the maximum flow is given by:

$$Q_B = \left(D_{1,max}^2(1-\lambda) + \text{sgn}(D_2)D_{1,max}D_{2,max}(1-2\lambda) - D_{2,max}^2\lambda\right)\frac{P_A}{4\pi^2 b} \tag{3.36}$$

A Case where $\lambda > \frac{D_{1,max}}{2(D_{1,max}-D_{2,max})}$:

For this case, start with the output flow equation solved with given D_1 to obtain:

$$Q_B = \left(D_1^2(1-\lambda) + D_1D_2(1-2\lambda) - D_2^2\lambda\right)\frac{P_A}{4\pi^2 b} \tag{3.37}$$

For the range of $\lambda > \frac{D_{1,max}}{2(D_{1,max}-D_{2,max})}$ being considered, it can be shown that setting $D_2 = -\text{sgn}(D_1)D_{2,max}$ gives the maximum flow which is given by:

$$Q_B = \left(D_1^2(1-\lambda) - D_1\text{sgn}(D_1)D_{2,max}(1-2\lambda) - D_{2,max}^2\lambda\right)\frac{P_A}{4\pi^2 b} \tag{3.38}$$

This flow is a concave up function in D_1, and thus evaluating the derivative with respect to D_1 yields the D_1 that will maximize the flow:

$$\begin{aligned} \frac{\partial Q_B}{\partial D_1} &= 0 \\ D_1 &= \pm D_{2,max}\frac{1-2\lambda}{2(1-\lambda)} \end{aligned} \tag{3.39}$$

However, this D_1 should not violate the physical constraint $|D_1| < D_{1,max}$

$$-D_{1,max} \leq D_{2,max}\frac{1-2\lambda}{2(1-\lambda)} \leq D_{1,max} \tag{3.40}$$

solving this in terms of λ yields

$$\lambda \geq \frac{2D_{1,max} - D_{2,max}}{2(D_{1,max} - D_{2,max})} \tag{3.41}$$

which means in this region, the maximum flow is given by:

$$Q_{B,max} = D_1^{c2}(1-\lambda) - D_1^c\text{sgn}(D_1)D_{2,max}(1-2\lambda) - D_{2,max}^2\lambda)\frac{P_A}{4\pi^2 b} \tag{3.42}$$

where $D_1^c = \pm D_{2,max}\frac{1-2\lambda}{2(1-\lambda)}$.

For $\frac{D_{1,max}}{2(D_{1,max}-D_{2,max})} < \lambda < \frac{2D_{1,max}-D_{2,max}}{2(D_{1,max}-D_{2,max})}$, $D_1 = \pm D_{1,max}$ results in the maximum flow

$$Q_{B,max} = D_{1,max}^2(1-\lambda) - D_{1,max}D_{2,max}(1-2\lambda) - D_{2,max}^2\lambda)\frac{P_A}{4\pi^2 b} \tag{3.43}$$

This result is positive as long as

$$\lambda < \frac{D_{1,max}^2 - D_{1,max}D_{2,max}}{(D_{1,max} - D_{2,max})^2} = \frac{D_{1,max}}{D_{1,max} - D_{2,max}} \tag{3.44}$$

note that the inequality condition satisfies

$$\frac{2D_{1,max} - D_{2,max}}{2(D_{1,max} - D_{2,max})} < \frac{D_{1,max}}{D_{1,max} - D_{2,max}} \tag{3.45}$$

Therefore the $Q_{B,max}$ is always positive in the range of λ being considered.

In summary the following cases hold true to obtain the maximum flow for PM-2 configuration

$$Q_{B,max} = \begin{cases} \frac{D_{1,max}^2 P_A}{16\pi^2 \lambda b} & \text{if } \frac{D_{1,max}}{2(D_{1,max} + D_{2,max})} \leq \lambda \\ & \lambda \leq \frac{D_{1,max}}{2(D_{1,max} - D_{2,max})} \\ (D_{1,max}^2(1-\lambda) + D_{1,max}\text{sgn}(D_1)D_{2,max}(1-2\lambda) & \text{if } \lambda < \frac{D_{1,max}}{2(D_{1,max}+D_{2,max})} \\ \qquad -D_{2,max}^2\lambda)\frac{P_A}{4\pi^2 b} & \\ (D_{1,max}^2(1-\lambda) - D_{1,max}\text{sgn}(D_1)D_{2,max}(1-2\lambda) & \text{if } \lambda > \frac{D_{1,max}}{2(D_{1,max}-D_{2,max})} \\ \qquad -D_{2,max}^2\lambda)\frac{P_A}{4\pi^2 b} & \\ ({D_1^c}^2(1-\lambda) - D_1^c\text{sgn}(D_1)D_{2,max}(1-2\lambda) & \text{if } \lambda > \frac{D_{1,max}}{2(D_{1,max} - D_{2,max})} \\ \qquad -D_{2,max}^2\lambda)\frac{P_A}{4\pi^2 b} & \text{and } D_{1,max} > D_{2,max} \end{cases} \tag{3.46}$$

where, $D_1^c = D_{2,max}\frac{1-2\lambda}{2(1-\lambda)}$.

and,

$$\omega^* = \pm \begin{cases} \frac{D_{1,max}}{4\pi b} P_A & \text{if } \frac{D_{1,max}}{2(D_{1,max}+D_{2,max})} \leq \lambda \leq \frac{D_{1,max}}{2(D_{1,max}-D_{2,max})} \\ [(1-\lambda)D_{1,max} - D_{2,max}\lambda]\frac{P_A}{2\pi b} & \text{if } \lambda < \frac{D_{1,max}}{2(D_{1,max}+D_{2,max})} \\ [(1-\lambda)D_{1,max} + D_{2,max}\lambda]\frac{P_A}{2\pi b} & \text{if } \lambda > \frac{D_{1,max}}{2(D_{1,max}-D_{2,max})} \\ [(1-\lambda)D_1^c + D_{2,max}\lambda]\frac{P_A}{2\pi b} & \text{if } \lambda > \frac{D_{1,max}}{2(D_{1,max} - D_{2,max})} \\ & \text{and } D_{1,max} > D_{2,max} \end{cases} \tag{3.47}$$

with

$$D_1 = \begin{cases} \pm D_{1,max} & \text{if } \frac{D_{1,max}}{2(D_{1,max}+D_{2,max})} \leq \lambda \leq \frac{D_{1,max}}{2(D_{1,max}-D_{2,max})} \\ \text{sgn}(D_2) D_{1,max} & \text{if } \lambda < \frac{D_{1,max}}{2(D_{1,max}+D_{2,max})} \\ \pm D_{1,max} & \text{if } \lambda > \frac{D_{1,max}}{2(D_{1,max}-D_{2,max})} \\ \pm D_{2,max}\frac{1-2\lambda}{2(1-\lambda)} & \text{if } \lambda > \dfrac{D_{1,max}}{2(D_{1,max}-D_{2,max})} \\ & \quad \text{and } D_{1,max} > D_{2,max} \end{cases} \tag{3.48}$$

$$D_2 = \begin{cases} \pm \dfrac{D_1(1-2\lambda)}{2\lambda} & \text{if } \frac{D_{1,max}}{2(D_{1,max}+D_{2,max})} \leq \lambda \leq \frac{D_{1,max}}{2(D_{1,max}-D_{2,max})} \\ \pm D_{2,max} & \text{if } \lambda < \frac{D_{1,max}}{2(D_{1,max}+D_{2,max})} \\ -\text{sgn}(D_1) D_{2,max} & \text{if } \lambda > \frac{D_{1,max}}{2(D_{1,max}-D_{2,max})} \\ -\text{sgn}(D_1) \dfrac{D_{2,max} - 2D_1^c + 2D_{1,max}\lambda}{2\lambda} & \text{if } \lambda > \dfrac{D_{1,max}}{2(D_{1,max}-D_{2,max})} \\ & \quad \text{and } D_{1,max} > D_{2,max} \end{cases} \tag{3.49}$$

PM-3

Finally, for PM-3, the approach is rather similar to what was done to handle PM-1. Start with a torque equation, given $P_T = 0$:

$$J\dot{\omega} = \frac{D_1}{2\pi} P_A - \frac{D_2}{2\pi}(P_B - P_A) - b\omega \tag{3.50}$$

With P_A, λ, and D_1 given, the above equation can be rearranged to in terms of D_2

$$\begin{aligned} \frac{D_1 + D_2}{2\pi} P_A &= \frac{D_2}{2\pi} P_B + b\omega \\ \frac{D_1 + D_2}{2\pi} P_A &= \frac{D_2}{2\pi} \lambda P_A + b\omega \\ \frac{D_2}{2\pi}\lambda P_A - \frac{D_2}{2\pi} P_A &= \frac{D_1}{2\pi} P_A - b\omega \\ \frac{D_2}{2\pi}(\lambda - 1) P_A &= \frac{D_1}{2\pi} P_A - b\omega \\ D_2 &= \left(D_1 - \frac{b\omega \cdot 2\pi}{P_A} \right) \frac{1}{\lambda - 1} \end{aligned} \tag{3.51}$$

The output flow equation for PM-3, utilizing the result above for D_2 is:

$$Q_B = \frac{D_2}{2\pi}\omega = \left(\frac{D_1}{2\pi} - \frac{b\omega}{P_A}\right)\frac{\omega}{\lambda - 1} \tag{3.52}$$

In the same way as in PM-1 and PM-2, the maximum flow with respect to the shaft speed ω can be found utilizing $\frac{\partial Q_B}{\partial \omega}$.

$$\begin{aligned} \frac{\partial Q_B}{\partial \omega} &= 0 \\ \frac{D_1}{2\pi} - \frac{2b\omega}{P_A} &= 0 \end{aligned} \tag{3.53}$$

From the evaluation above, we can obtain the shaft speed that will deliver the maximum flow for given D_1.

$$\omega^* = \frac{D_1}{4\pi b}P_A \tag{3.54}$$

Plug ω^* into Eq (3.52), to obtain the maximum flow for given D_1:

$$Q_{B,max} = \frac{D_1^2 P_A}{16\pi^2(\lambda - 1)b} \tag{3.55}$$

In order to have this flow maximized, we desire $D_1 = \pm D_{1,max}$. However, as with other configurations, setting $D_1 = \pm D_{1,max}$ may result in violating the physical constraint $|D_2| \leq D_{2,max}$. From Eq. (3.51), we could establish

$$\lambda \geq 1 + \frac{D_{1,max}}{2D_{2,max}} \tag{3.56}$$

is necessary to utilize Eq. (3.54) to obtain maximum flow in Eq. (3.55).

When $\lambda < 1 + \frac{D_{1,max}}{2D_{2,max}}$, solve the torque equation in terms of ω with a given D_2 to obtain:

$$\omega = (D_1 - D_2(\lambda - 1))\frac{P_A}{2\pi^2 b} \tag{3.57}$$

With this shaft speed, the output flow is

$$Q_B = (D_1 D_2 - D_2^2(\lambda - 1))\frac{P_A}{4\pi^2 b} \tag{3.58}$$

Setting $D_1 = \text{sgn}(D_2)D_{1,max}$ gives the maximum flow for any D_2. In the similar way to PM-1 derivation, plug in this choice of D_1 into Q_B. For the range of λ considered here,

Q_B is positive. Then, it can be seen that $D_2 = \pm D_{2,max}$ maximizes Q_B.

$$Q_{B,max} = (D_{1,max}D_{2,max} - D_{2,max}^2(\lambda - 1))\frac{P_A}{4\pi^2 b} \tag{3.59}$$

and above flow works when

$$\lambda < 1 + \frac{D_{1,max}}{2D_{2,max}} \tag{3.60}$$

In summary, the maximum flow for the PM-3 for λ is determined by following equations

$$Q_{B,max} = \begin{cases} \frac{D_{1,max}^2 P_A}{16\pi^2(\lambda-1)b} & \text{if } \lambda \geq 1 + \frac{D_{1,max}}{2D_{2,max}} \\ D_{2,max}(D_{1,max} - D_{2,max}(\lambda - 1))\frac{P_A}{4\pi^2 b} & \text{otherwise} \end{cases} \tag{3.61}$$

with the maximum shaft speed defined by

$$\omega_{max} = \pm \begin{cases} \frac{D_{1,max}}{4\pi b} P_A & \text{if } \lambda \geq 1 + \frac{D_{1,max}}{2D_{2,max}} \\ (D_{1,max} - D_{2,max}(\lambda - 1))\frac{P_A}{2\pi^2 b} & \text{otherwise} \end{cases} \tag{3.62}$$

with displacements

$$D_1 = \pm D_{1,max} \forall \lambda \tag{3.63}$$

and

$$D_2 = \pm \begin{cases} \dfrac{D_{1,max}}{2(\lambda - 1)} & \lambda \geq \frac{D_{1,max}}{2D_{2,max}} \\ D_{2,max} & \text{otherwise} \end{cases} \tag{3.64}$$

IHT

For the IHT, the approach is different due to the trigonometric relationship between the displacement to each port P $D_P(\theta)$ and the valve plate rotation angle θ. The dynamic equation of the IHT is given by (From Eq. (2.26)):

$$\begin{aligned} J\dot{\omega} &= -(P_A - P_T)\frac{D_A(\theta)}{2\pi} - (P_B - P_T)\frac{D_B(\theta)}{2\pi} - b\omega \\ Q_B &= \frac{D_B(\theta)}{2\pi}\omega \end{aligned} \tag{3.65}$$

Given the λ with $P_T = 0$ at the steady-state, the above equation becomes:

$$0 = -P_A\frac{D_A(\theta)}{2\pi} - \lambda P_A\frac{D_B(\theta)}{2\pi} - b\omega \tag{3.66}$$

Solving it in terms of ω yields,

$$\omega = -\frac{P_A}{b \cdot 2\pi} \left(D_A(\theta) + \lambda D_B(\theta) \right) \tag{3.67}$$

To obtain the maximum obtainable flow for each λ, plug Eq. (3.67) into the flow equation in Eq. (3.65)

$$Q_B = -\frac{D_B(\theta) P_A}{4\pi^2 b} \left(D_A(\theta) + \lambda D_B(\theta) \right) \tag{3.68}$$

and optimize the output flow equation with respect to θ. The closed-form solution for obtaining this θ^* is difficult to obtain, so a numerical solution is used.

With the θ^* found, the shaft speed that delivers the maximum flow is:

$$\omega^* = -\frac{P_A}{b \cdot 2\pi} \left(D_A(\theta^*) + \lambda D_B(\theta^*) \right) \tag{3.69}$$

and the maximum output flow is:

$$Q_{B,max} = \frac{D_B(\theta^*)}{2\pi} \omega^* \tag{3.70}$$

3.2.2 Summary of Maximum Flow and its Shaft Speed

In order to see how all the terms interact with each other, Define the total displacement $D_{Total} = D_{1,max} + D_{2,max}$, and $D_{1,max} = x D_{Total}$, and $D_{2,max} = y D_{Total}$, where $x + y = 1$ and $0 < x, y \leq 1$.

PM-1

$$Q_{B,max}(D_{Total}, \lambda) = \begin{cases} \dfrac{x^2 D_{Total}^2}{4\lambda} \dfrac{P_A}{4\pi^2 b} & \text{if } \lambda \geq \frac{D_{1,max}}{2D_{2,max}} \\ D_{Total}^2 \left[xy - y^2 \lambda \right] \dfrac{P_A}{4\pi^2 b} & \text{otherwise} \end{cases} \tag{3.71}$$

$$\omega^* = \begin{cases} x D_{Total} \dfrac{P_A}{4\pi b} & \text{if } \lambda \geq \frac{D_{1,max}}{2D_{2,max}} \\ D_{Total}(x - y\lambda) \dfrac{P_A}{2\pi b} & \text{otherwise} \end{cases} \tag{3.72}$$

$$D_1 = \pm D_{1,max} \forall \lambda \tag{3.73}$$

and

$$D_2 = \pm \begin{cases} \dfrac{D_{1,max}}{2\lambda} & \lambda \geq \frac{D_{1,max}}{2D_{2,max}} \\ D_{2,max} & \text{otherwise} \end{cases} \tag{3.74}$$

PM-2

$$Q_{B,max}(D_{Total},\lambda) =$$
$$\begin{cases} \dfrac{x^2 D_{Total}^2}{4\lambda}\dfrac{P_A}{4\pi^2 b} & \text{if } \dfrac{D_{1,max}}{2(D_{1,max}+D_{2,max})} \le \lambda \\ & \quad \lambda \le \dfrac{D_{1,max}}{2(D_{1,max}-D_{2,max})} \\ D_{Total}^2\left[x^2(1-\lambda)+xy(1-2\lambda)-y^2\lambda\right]\dfrac{P_A}{4\pi^2 b} & \text{if } \lambda < \dfrac{D_{1,max}}{2(D_{1,max}+D_{2,max})} \\ D_{Total}^2\left[x^2(1-\lambda)+xy(1-2\lambda)-y^2\lambda\right]\dfrac{P_A}{4\pi^2 b} & \text{if } \lambda > \dfrac{D_{1,max}}{2(D_{1,max}-D_{2,max})} \\ D_{Total}^2 y^2\left[\dfrac{-(1-2\lambda)^2-4(1-\lambda)\lambda}{4(1-\lambda)}\right]\dfrac{P_A}{4\pi^2 b} & \text{if } D_{1,max} > D_{2,max} \text{ and} \\ & \quad L > \dfrac{2D_{1,max}-D_{2,max}}{2(D_{1,max}-D_{2,max})} \end{cases} \tag{3.75}$$

$$\omega^* = \pm\begin{cases} xD_{Total}\dfrac{P_A}{4\pi b} & \text{if } \frac{D_{1,max}}{2(D_{1,max}+D_{2,max})} \le \lambda \le \frac{D_{1,max}}{2(D_{1,max}-D_{2,max})} \\ D_{Total}\left[x+\lambda(x+y)\right]\dfrac{P_A}{2\pi b} & \text{if } \lambda < \frac{D_{1,max}}{2(D_{1,max}+D_{2,max})} \\ D_{Total}\left[x-\lambda(x-y)\right]\dfrac{P_A}{2\pi b} & \text{if } \lambda > \frac{D_{1,max}}{2(D_{1,max}-D_{2,max})} \\ D_{Total}\dfrac{y}{2}\dfrac{P_A}{2\pi b} & \text{if case 4} \end{cases} \tag{3.76}$$

with

$$D_1 = \begin{cases} \pm D_{1,max} & \text{if } \frac{D_{1,max}}{2(D_{1,max}+D_{2,max})} \le \lambda \le \frac{D_{1,max}}{2(D_{1,max}-D_{2,max})} \\ \mathrm{sgn}(D_2)D_{1,max} & \text{if } \lambda < \frac{D_{1,max}}{2(D_{1,max}+D_{2,max})} \\ \pm D_{1,max} & \text{if } \lambda > \frac{D_{1,max}}{2(D_{1,max}-D_{2,max})} \\ \pm D_{2,max}\frac{1-2\lambda}{2(1-\lambda)} & \text{if } \lambda > \dfrac{D_{1,max}}{2(D_{1,max}-D_{2,max})} \\ & \quad \text{and } D_{1,max} > D_{2,max} \end{cases} \tag{3.77}$$

$$D_2 = \begin{cases} \pm\dfrac{D_1(1-2\lambda)}{2\lambda} & \text{if } \frac{D_{1,max}}{2(D_{1,max}+D_{2,max})} \leq \lambda \leq \frac{D_{1,max}}{2(D_{1,max}-D_{2,max})} \\ \pm D_{2,max} & \text{if } \lambda < \frac{D_{1,max}}{2(D_{1,max}+D_{2,max})} \\ -\text{sgn}(D_1)D_{2,max} & \text{if } \lambda > \frac{D_{1,max}}{2(D_{1,max}-D_{2,max})} \\ -\text{sgn}(D_1)\dfrac{D_{2,max}-2D_1^c+2D_{1,max}\lambda}{2\lambda} & \text{if } \lambda > \dfrac{D_{1,max}}{2(D_{1,max}-D_{2,max})} \\ & \text{and } D_{1,max} > D_{2,max} \end{cases} \tag{3.78}$$

PM-3

$$Q_{B,max}(D_{Total},\lambda) = \begin{cases} \dfrac{x^2 D_{Total}^2}{4(\lambda-1)}\dfrac{P_A}{4\pi^2 b} & \text{if } \lambda \geq 1+\frac{D_{1,max}}{2D_{2,max}} \\ D_{Total}^2\left[xy-y^2(\lambda-1)\right]\dfrac{P_A}{4\pi^2 b} & \text{otherwise} \end{cases} \tag{3.79}$$

$$\omega^* = \begin{cases} xD_{Total}\dfrac{P_A}{4\pi b} & \text{if } \lambda \geq 1+\frac{D_{1,max}}{2D_{2,max}} \\ D_{Total}\left[x-y(\lambda-1)\right]\dfrac{P_A}{2\pi b} & \text{otherwise} \end{cases} \tag{3.80}$$

$$D_1 = \pm D_{1,max} \forall \lambda \tag{3.81}$$

and

$$D_2 = \pm \begin{cases} \dfrac{D_{1,max}}{2(\lambda-1)} & \lambda \geq \frac{D_{1,max}}{2D_{2,max}} \\ D_{2,max} & \text{otherwise} \end{cases} \tag{3.82}$$

IHT

$$Q_{B,max}(D,\lambda) = \frac{D_B(\theta^*)}{2\pi}\omega^* \tag{3.83}$$

with

$$\omega^* = -\frac{P_A}{b\cdot 2\pi}\left(D_A(\theta^*)+\lambda D_B(\theta^*)\right) \tag{3.84}$$

where θ^* is the optimal solution numerically obtained for

$$\max_{\theta} \quad Q_B = -\frac{D_B(\theta)P_A}{4\pi^2 b}\left(D_A(\theta)+\lambda D_B(\theta)\right) \tag{3.85}$$

3.2.3 Sizing Comparison Methods

The maximum obtainable flow at each transformation ratio λ for the given size and configuration are given in Eqs. (3.71)–(3.80). The same methods used in Section 3.1 are applied

to these equations to obtain the necessary displacements to match the output flows of PM transformers and IHT. Those methods were:
Method I: For given IHT with a displacement $D = 1$:

$$\begin{aligned} \min_{xD_{Total}, yD_{Total}} \quad & D_{Total} \\ \text{subject to} \quad & \text{PM flow} \geq \text{IHT flow} \quad \text{for } \lambda \in [0, \infty) \end{aligned} \tag{3.86}$$

Method II: For given IHT with a displacement $D = 1$:

$$\begin{aligned} \min_{xD_{Total}, yD_{Total}} \quad & D_{Total} \\ \text{subject to} \quad & \text{IHT flow} \geq \text{PM flow} \quad \text{for } \lambda \in [0, \infty) \end{aligned} \tag{3.87}$$

Method III: For given IHT with a displacement $D = 1$:

$$\min_{xD_{Total}, yD_{Total}} \quad ||\text{PM flow} - \text{IHT flow}|| \quad \text{for } \lambda \in [0, \infty) \tag{3.88}$$

where $||\text{PM flow} - \text{IHT flow}||$ is the 2-norm of the difference between the flow capabilities of two transformers for the range of λ. $D_{Total} = D_{1,max} + D_{2,max}$, $D_{1,max} = xD_{Total}$, and $D_{2,max} = yD_{Total}$, where $x + y = 1$ and $0 < x, y \leq 1$.

3.2.4 Sizing Results

Running the comparison according to Eqs. (3.86)– (3.88) for $\lambda \in [0, \infty)$, $D_{1,max}$ and $D_{2,max}$ that satisfy the sizing criteria are found, and the output flow vs. transformation ratio λ is plotted. The results are normalized by $P_A \frac{D_{Total}}{b}$ and multiplied by 1000 psi.

Figures 3.7–3.9 show the output flow capability at each λ normalized by the ratio of total displacement of the IHT to the viscous friction coefficient $\frac{D}{b}$, at the input pressure of 1000 psi. Changing the input pressure will scale the normalized flow accordingly (i.e., if 500 psi input pressure is used, all the flows will scale by 1/2). As expected from the sizing criteria, a flow curve with Sizing Method I always lies above the IHT flow curve, whereas Sizing Method II curve lies below the IHT curve all the time. On the same plots, the displacement ratios necessary to achieve the transformation ratios are shown for each of the sizing methods.

The results of the sizing analysis (i.e. the minimum sizes subject to the criteria according to the sizing methods in Eqs. (3.86)– (3.88)) is summarized in Table 3.3. Unlike in previous sizing results where the $D_{1,max} = D_{2,max}$ for most cases, these results show $D_{1,max} \neq D_{2,max}$ for most cases now. Thus the displacement ratio necessary to achieve

the given transformation ratio is different even within the same configuration. It is also interesting to note that for each of the PM configurations, there exists a region where both D_1 and D_2 are at their maximum ratio. When a maximum transformer shaft speed is imposed in Section. 3.1 rather than as a consequence of viscous friction, there exists unique one-to-one mapping between the ratio of D_1/D_2 to the transformation ratio λ as seen in Figs 3.2–3.4. In case of PM-1 with $D_{1,max} = D_{2,max}$, $D_1/D_2 = 1$ uniquely corresponds to $\lambda = 1$. Because of the viscous friction added now there exists a range of λ that corresponds D_1/D_2 combination.

As for the comparison of the total displacements when the maximum speed is a consequence of viscous friction, PM-1 with the method I is now only 50% larger than IHT, as opposed to 73% observed previously in section 3.1. The reduction in sizing is most notable for PM-3, where even with the method I, the units are expected to be only 19% larger than IHT. This is possible because of the ability of PM-3 to achieve very high shaft speed.

Table 3.3: Optimal displacements of the two units in PM transformers $D_{1,max}$, $D_{2,max}$ and $D_{1,max} + D_{2,max}$ normalized by the displacement of the IHT with consideration of viscous friction for $\lambda \in [0, \infty)$

	Sizing Method	PM-1	PM-2	PM-3
I.	PM flow $\geq$ IHT	0.868 / 0.641	0.870 / 0.809	0.730 / 0.464
		— 1.509	— 1.679	— 1.194
II.	IHT flow $\geq$ PM	0.768 / 0.730	0.557 / 0.501	0.431 / 0.431
		— 1.498	— 1.058	— 0.862
III.	$\min \|\text{PM} - \text{IHT}\|$	0.839 / 0.641	0.663 / 0.602	0.512 / 0.464
		— 1.480	— 1.265	— 0.976

Figure 3.10 shows the contours plotted with the imposed shaft speed up to the maximum shaft speed found in Eqs. (3.72), (3.76), and (3.80) with respect to the transformation ratio and output flow. In this figure, all configurations considered have the same total volumetric displacement, with equal distribution of displacements in PM units such that $D_{1,max} = D_{2,max}$. Holding the maximum displacement the same is helpful to highlight differences coming from the configurations. The envelopes for these contours correspond to the allowable operating region, and it can be easily seen that PM-3 is able to extend out to much larger output flow if the volumetric displacement is held the same. Each line in contour corresponds to 50 rad/s, showing that PM-3 being able to obtain larger operating envelope is due to the fact PM-3 can spin at much higher speed than another unit for the same displacement size. This is possible because PM-3 is connected such that shared ports from the two displacement units are connected to the input pressure. PM-3 can draw much larger torque from the supply, allowing it to spin at much higher shaft speed.

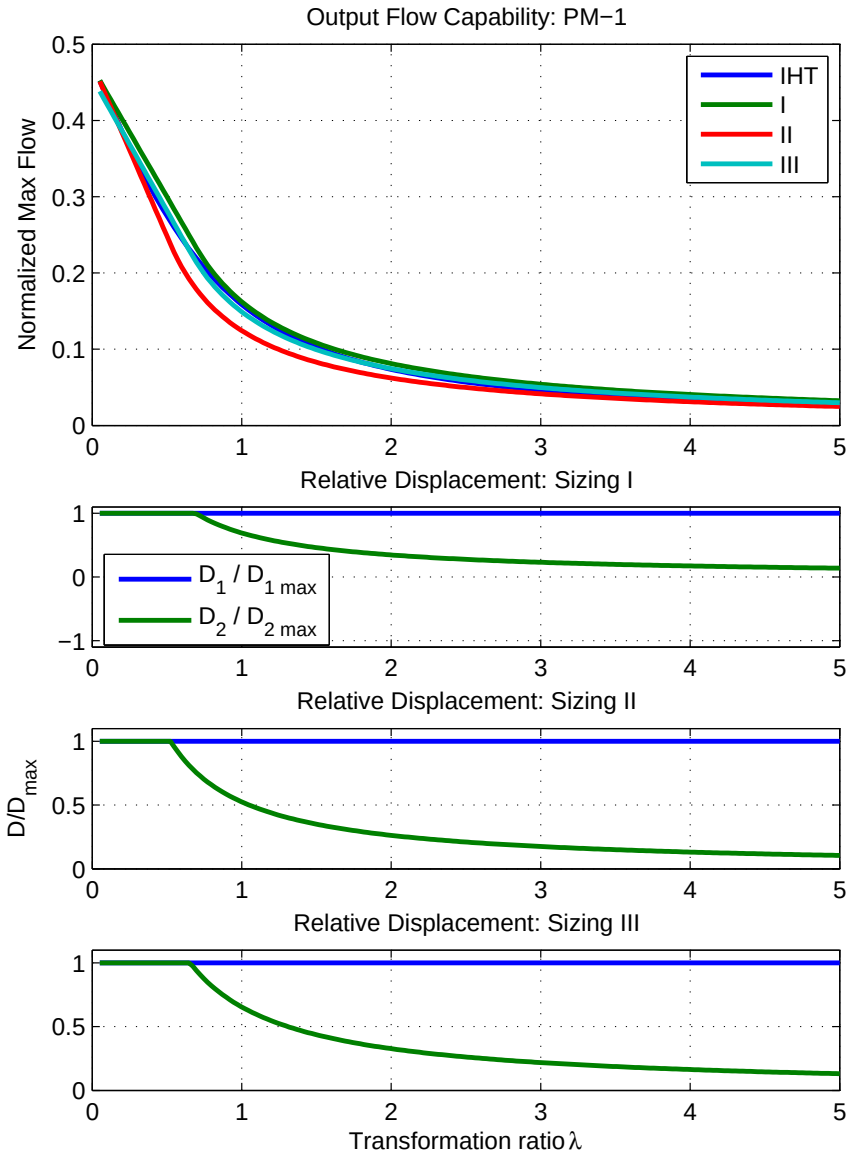

Figure 3.7: Top: Output flow capability of PM-1 configuration sized with 3 different methods plotted with output flow capability of the IHT; Bottom: The displacement ratios necessary to achieve them for each of the sizing method

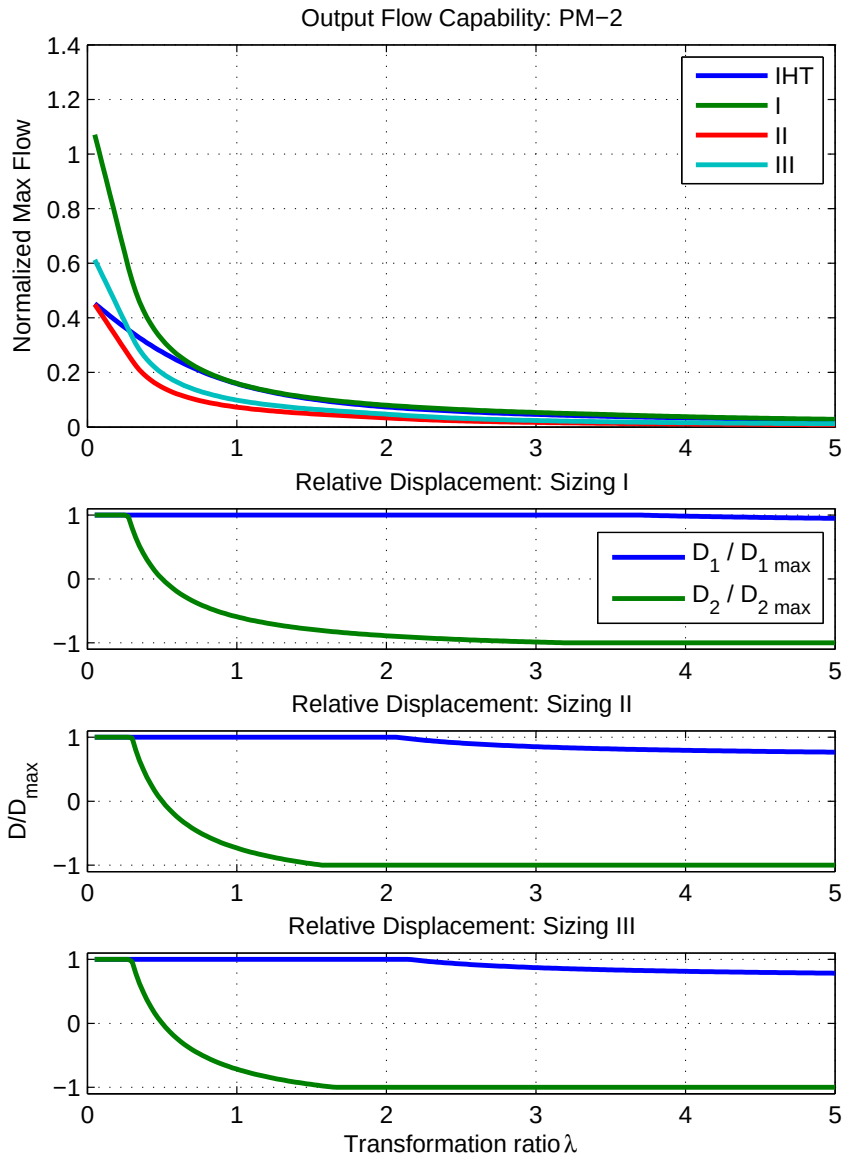

Figure 3.8: Top: Output flow capability of PM-2 configuration sized with 3 different methods plotted with output flow capability of the IHT; Bottom: The displacement ratios necessary to achieve them for each of the sizing method

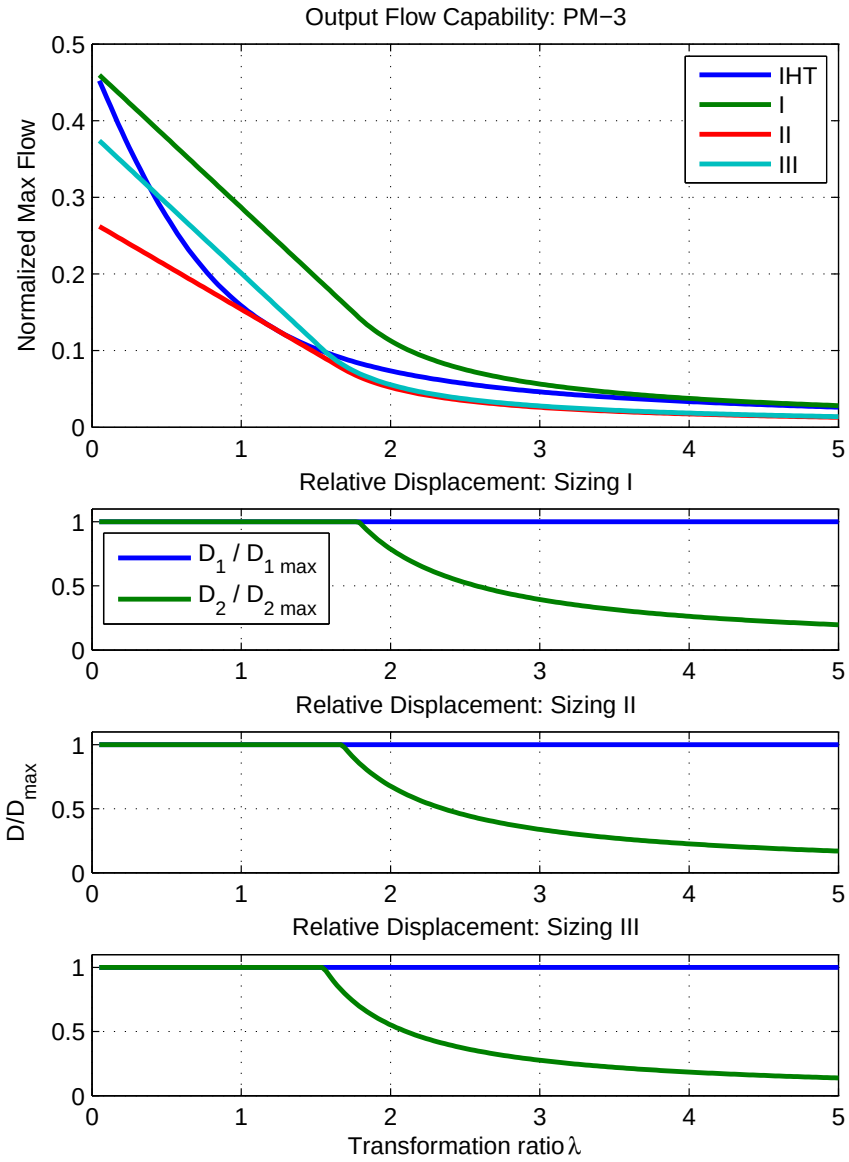

Figure 3.9: Top: Output flow capability of PM-3 configuration sized with 3 different methods plotted with output flow capability of the IHT; Bottom: The displacement ratios necessary to achieve them for each of the sizing method

Figure 3.11 shows the similar contour, but now the units are sized according to sizing method III summarized in Table 3.3. With displacement sized to match the output flow capability, the size of operating envelopes is now similar. Within the similarly sized envelop, however, one can easily spot the difference in shaft speed for each configuration. PM-3 being able to spin faster plays an advantage in sizing consideration, as smaller units can be used to deliver the same flow with faster shaft speed.

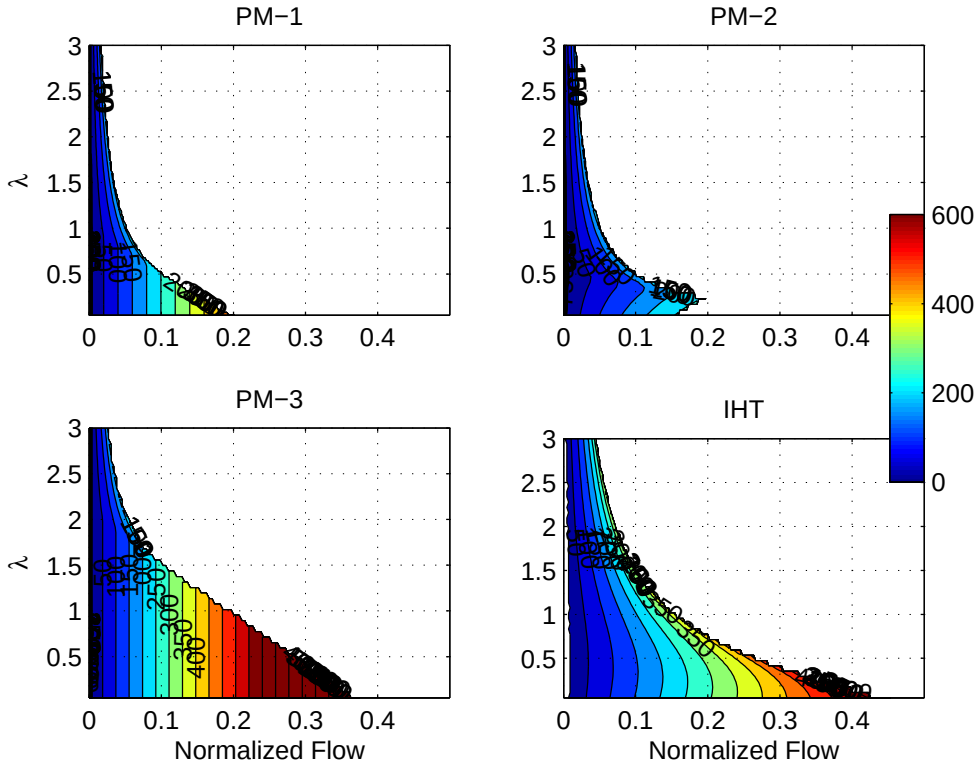

Figure 3.10: Contour of shaft speeds for transformation ratio λ and output flow Q_B normalized by $\frac{D}{b}$ illustrating the operating region for all transformers with same volumetric displacement with viscous friction loss

Table 3.4 shows the sizing results if the comparison is established only for $\lambda \in [0, 2)$. Further reduction in size is noticed. In case of Sizing III for PM-3, we are now achieving transformer that is smaller in volumetric displacement than IHT.

3.2.5 Configuration Mode Switching

The same idea for mode switching is applied with sizing comparison with friction losses. Figure 3.12 shows the flow curves resulting from three different sizing methods compared against the flow curve for IHT. In the same plot, the configuration selection that yielded

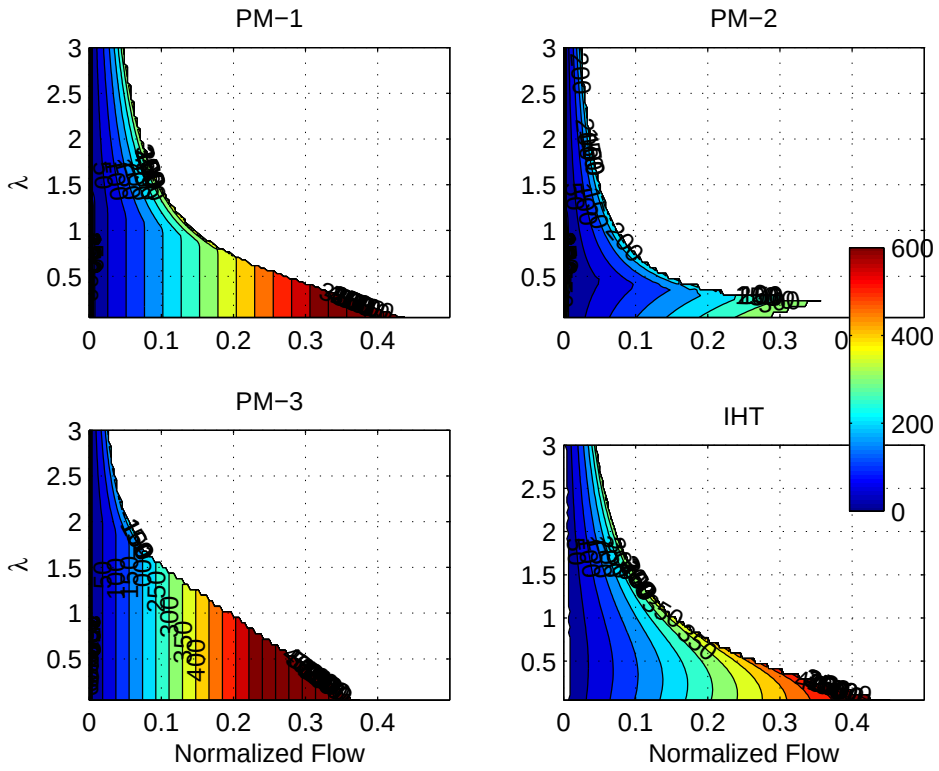

Figure 3.11: Contour of shaft speeds for transformation ratio λ and output flow Q_B normalized by $\frac{D}{b}$ illustrating the operating region for all transformers sized according to sizing method III with viscous friction loss

Table 3.4: Optimal displacements of the two units in PM transformers $D_{1,max}$, $D_{2,max}$ and $D_{1,max} + D_{2,max}$ normalized by the displacement of the IHT with consideration of viscous friction for $\lambda \in [0, 3)$

	Sizing Method	PM-1	PM-2	PM-3
I.	PM flow $\geq$ IHT	0.868 / 0.641	0.870 / 0.663	0.666 / 0.480
		— 1.509	— 1.533	— 1.146
II.	IHT flow $\geq$ PM	0.807 / 0.674	0.587 / 0.405	0.439 / 0.423
		— 1.481	— 0.992	— 0.862
III.	$\min \|\text{PM} - \text{IHT}\|$	0.843 / 0.637	0.688 / 0.420	0.480 / 0.480
		— 1.480	— 1.108	— 0.960

PM flow curves is shown. With the method I, PM-2 and PM-3 are utilized whereas with method II and III, only PM-3 are utilized for the whole range of transformation ratio being considered. Table 3.5 summarizes these results, and Fig. 3.13 shows the relative displacement necessary to achieve given λ for PM units designed through each method. Results for limiting the comparison range to $\lambda \in [0, 3)$ is summarized in Table. 3.6. Further reduction in sizing is observed for Method I, showing it is possible to achieve even smaller PM transformer for a comparable output flow of IHT.

With the consideration of maximum shaft speed obtainable from each configuration, it can be seen that PM transformer can be as compact as IHT in achieving the comparable output power. The result presented will be different depending on the selection of the viscous coefficient friction b, and if other additional losses are considered. Nevertheless, these results demonstrate that PM transformer could be designed to be as compact as IHT in terms of volumetric displacement contrary to the common belief.

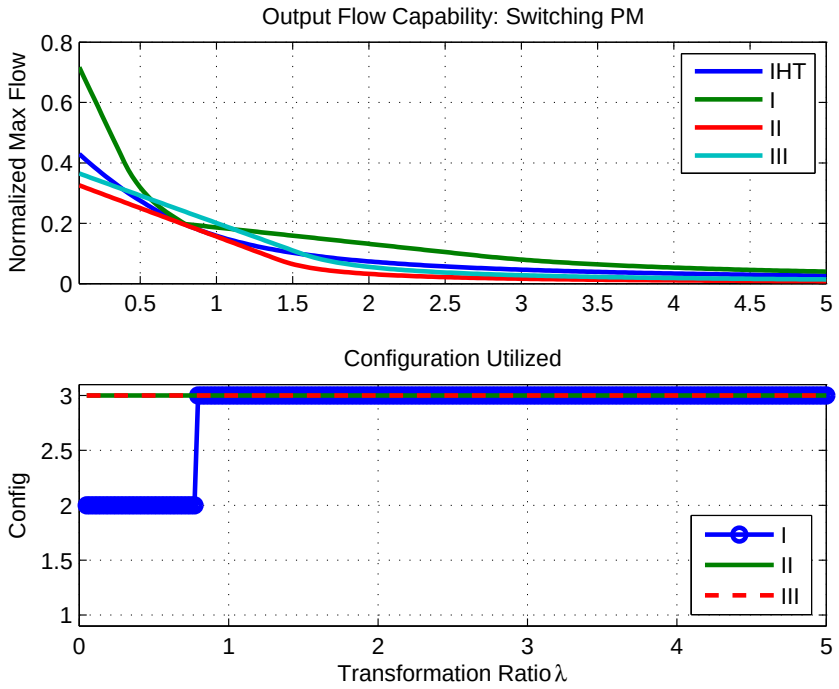

Figure 3.12: Top: the output flow capability of PM transformer sized with three sizing methods plotted with the output flow capability of the IHT if the mode switching is allowed; Bottom: The mode configuration number utilized for each λ

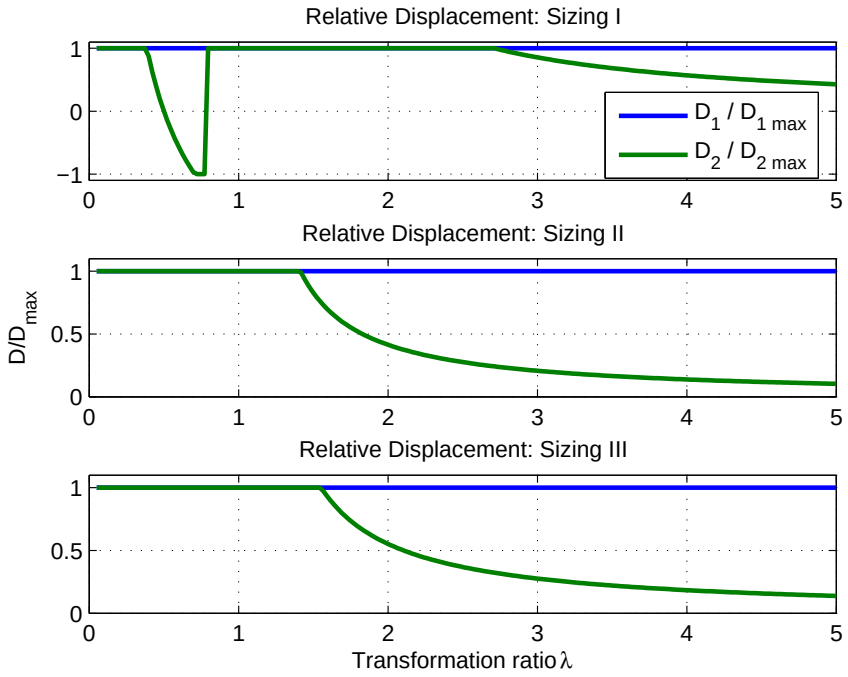

Figure 3.13: Displacement ratios $D_1/D_{1,max}$ and $D_2/D_{2,max}$ that corresponds to the output flow of PM transformer shown in Fig. 3.12

Table 3.5: Sizing Comparison with Port Switching PM Transformer with Losses for $\lambda \in [0, \infty)$

	Sizing Method	$D_{1,max}/\ D_{2,max}$ — $D_{1,max}\ +\ D_{2,max}$ Normalized by IHT Displacement D
I.	PM flow $\geq$ IHT	0.738 / 0.383 — 1.121
II.	IHT flow $\geq$ PM	0.431 / 0.431 — 0.862
III.	min $\|$PM $-$ IHT$\|$	0.512 / 0.464 — 0.976

Table 3.6: Sizing Comparison with Port Switching PM Transformer with Losses for $\lambda \in [0, 3)$

	Sizing Method	$D_{1,max}/\ D_{2,max}$ — $D_{1,max}\ +\ D_{2,max}$ Normalized by IHT Displacement D
I.	PM flow $\geq$ IHT	0.666 / 0.431 — 1.097
II.	IHT flow $\geq$ PM	0.431 / 0.431 — 0.862
III.	min $\|$PM $-$ IHT$\|$	0.480 / 0.480 — 0.960

3.3 Flow Ripple

With port flow generated by discrete pistons in axial-piston swash-plate type hydrostatic machines, flow ripples (pulsations) are inevitable and causes undesirable vibration and noise. In the following sections, we study flow ripple of transformers, considering not only the ideal flow but also the actual flow with compressibility effects. The analysis is performed assuming that swash plate does not move (no wobble) and that shaft speed is constant throughout one revolution of cylinder barrel in steady state. In Section 3.3.1, the flow ripple will be compared for the kinematic flow, which assumes incompressible flow. In this case the volume change in the piston chamber directly translates to the output flow of the transformer. In Section 3.3.2, the flow ripple will be compared for the dynamic flow with compressibility effect considered.

3.3.1 Kinematic Flow Ripple

The idealized flow of transformer is determined by considering a lossless unit displacing incompressible fluid (Eq. (2.5)). Before making the comparison of the flow ripple, the nature of the flow ripple will be described first. In an axial piston pump, a piston moves in a reciprocating motion as it slides on the swashplate. This geometry was described in Section 2.1, and the Fig. 3.14 shows the general configuration of an axial piston pump. While the valve plate is held in a fixed position, the cylinder block is driven about the

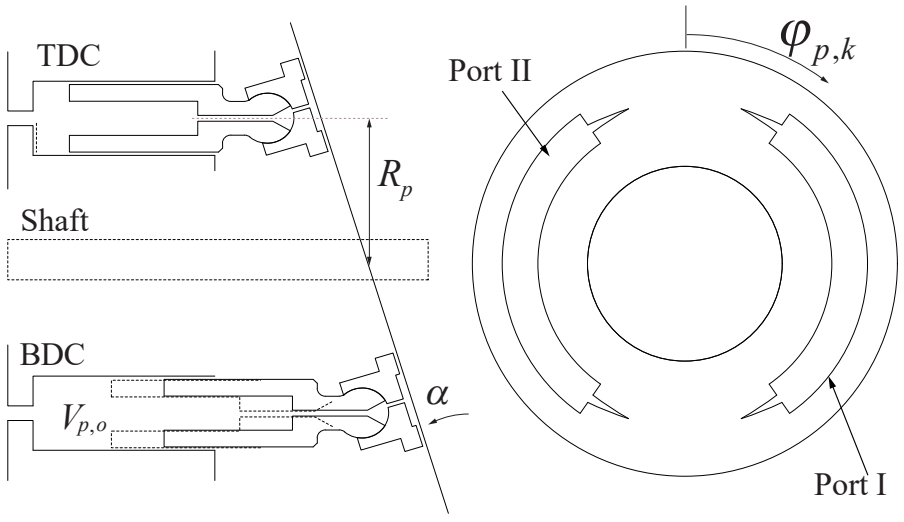

Figure 3.14: Piston Movement Geometry

shaft in a constant angular speed ω. During this motion, each piston periodically passed over the Port I and Port II that serves as suction and discharge ports on the valve plate

for ω and swashplate angle $\alpha > 0$. Because the piston shoes are held against the inclined plane of the swash plate, the pistons go through oscillatory movement in and out of the cylinder barrel. As the pistons pass over the suction port, the piston takes in the fluid, and as the pistons pass over the discharge port, the piston pushes the fluid out to the port. For the kinematic flow being considered, we assume that the transition between suction port and discharge port happens precisely at the top dead center and bottom dead center, when the flow from the piston is at zero. Figure 3.15 illustrates this behavior for a single piston traveling from the TDC. With this sinusoidal flow coming from a single piston, the flow observed at the output port will not be constant, rather it will have a characteristics apparent from the oscillatory movement.

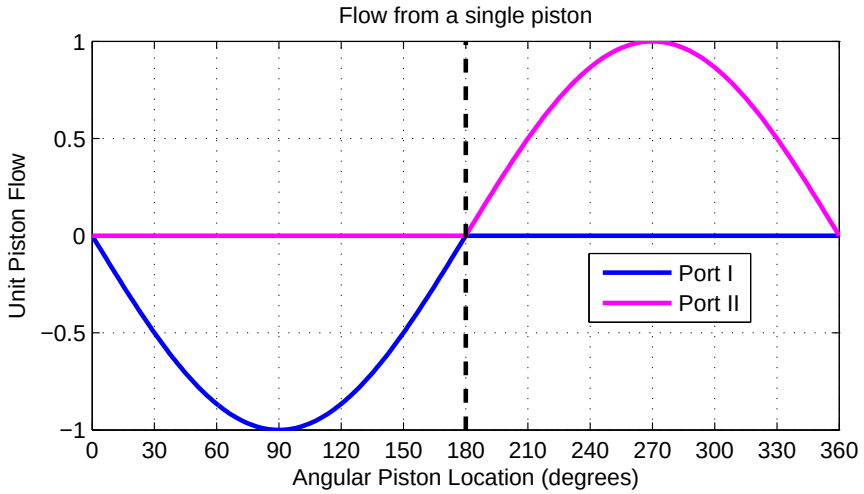

Figure 3.15: Flow Delivered by to each port by single piston in an axial piston pump

Figure 3.16 shows the output flow coming from different total number of pistons. The port flows are normalized by the total displacement of the unit to make the comparison at the same output flow capability. In case where the total number of pistons $n = 2$, there are two distinct humps, created by two pistons that are off-phase by 180 degrees. It can be seen that as the number of pistons n increases, the distinctiveness of these humps tend to flat out, yet still with some oscillations. These oscillations are called the flow ripple or pulsation, and is an inevitable nature of an axial piston pumps and motors. Since the transformer is built on an axial piston rotating groups, the transformers will also have a flow ripple.

In case of the IHT, the valve plate is no longer fixed in one position, rather it can vary with respect to the valve plate rotation angle θ. Figure 3.17 shows the geometry specific to the IHT. Now the pistons travel over 3 ports – port 'A', 'T', and 'B' each serves as an

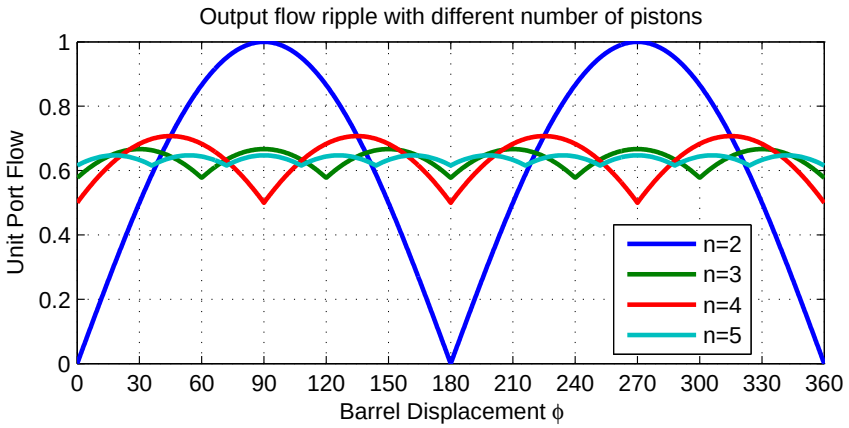

Figure 3.16: Output flow ripple in an axial piston pump as the number of pistons increases

input, make-up and an output port. This behavior was described in detail in Section 2.1. One distinct feature about the rotatable valve plate is that the transition from one port to the other occurs at locations with non-zero flows, as illustrated by Fig. 3.18. The resulting flow ripple is large in magnitude, and often has a sharp edges in flow curve, that would contribute to the noise in the system.

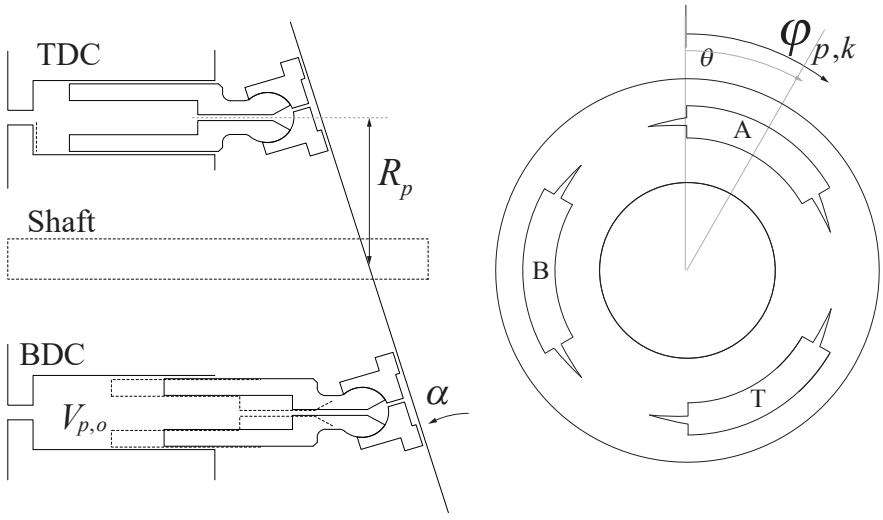

Figure 3.17: Piston movement geometry for IHT

Figure 3.19 shows the flow ripple of an IHT with a valve plate rotation angle $\theta = 30$ degrees, which corresponds to the pressure transformation ratio $\lambda = 0.5$. Notice how the the flow at each port has a saw-tooth shape rather than a rounded shape observed in Fig. 3.16.

Manring [69] presented a closed form equation presenting the normalized height of the

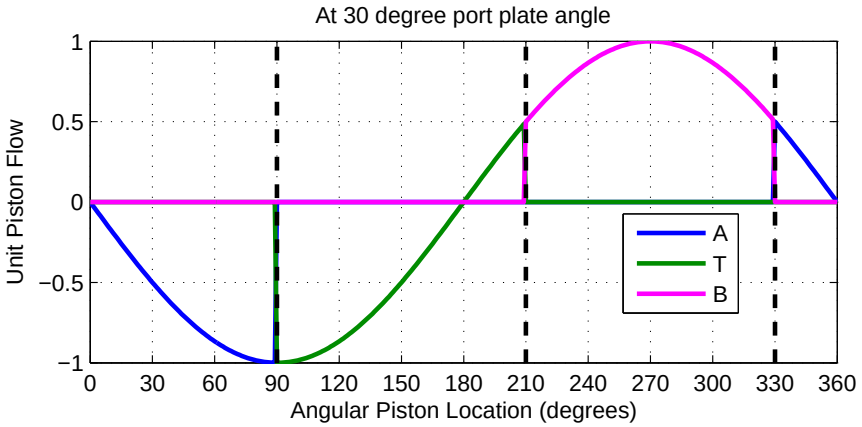

Figure 3.18: Flow Delivered by to each port by single piston in IHT with $\theta = 30$ degrees, which corresponds to the transformation ratio $\lambda = 0.5$

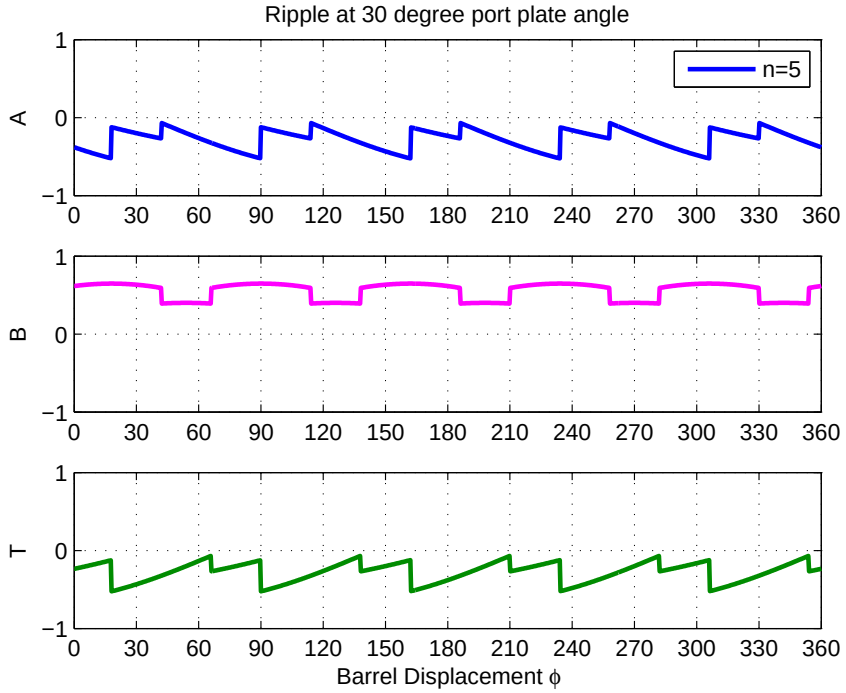

Figure 3.19: Shape of Flow Ripple in IHT with 5 pistons, when $\theta = 30$ degrees, which corresponds to the transformation ratio $\lambda = 0.5$; Top: Flow at input port, A; Middle: Flow at output port, B; Bottom: Flow at make-up port, T

flow ripple for a pump with an odd number of pistons. Using the incompressible fluid model in Eq. (2.5), we obtain our own flow ripple for PM transformer and IHT for different total number of pistons. The flow ripple size is determined by taking the difference between the peak value and the minimum value and dividing it by the mean value of the flow. In other words, for the port flow Q_P, the flow ripple is given as:

$$\text{Flow Ripple} = \frac{\max(Q_P) - \min(Q_P)}{\text{mean}(Q_P)} \tag{3.89}$$

Figure 3.20 shows the normalized flow ripple height for PM-1 transformer for any λ (since incompressible flow is considered, the displacement ratio does not affect the ripple size), and IHT at port plate rotation angle $\theta = \frac{\pi}{6}$ and $\frac{\pi}{2}$ which gives the transformation ratio $\lambda = 0.5$ and $\lambda = 2$ respectively. Two cases for IHT are considered as the flow ripple depends on the port plate rotation angle θ for IHT. For the PM with an assumption that each unit has the same number of pistons, the flow ripple size decreases monotonically in increment of 4 total pistons (2 for each unit) with 2(2n+1) pistons (odd number in each unit) being more favorable than 2(2n) total pistons (even number in each unit). Meanwhile, for the IHT, flow ripple sizes decrease in increment of 3 pistons. However, the ripple sizes are larger than in the PM case and the marginal benefit adding more piston to the decreasing amplitude of the ripple is smaller.

For the IHT, as the transformation ratio increases, the ripple amplitude at the IHT output gets larger. As described earlier, this large ripple amplitude is due to the design of the 3-ported valve plate that allows pistons to transition from one port to the next at locations other than TDC and BDC depending on the port plate rotation angle θ. Table 3.7 summarizes above findings on idealized flow ripple.

Table 3.7: Ripple Sizes for PM and IHT at select cases. Total number of pistons are used here with equal number of pistons distributed between two units in PM transformer

	PM	IHT ($\lambda = 0.5$)	IHT ($\lambda = 2$)
10 pistons	10%	19%	115%
30 pistons	0.5%	7.8%	58%

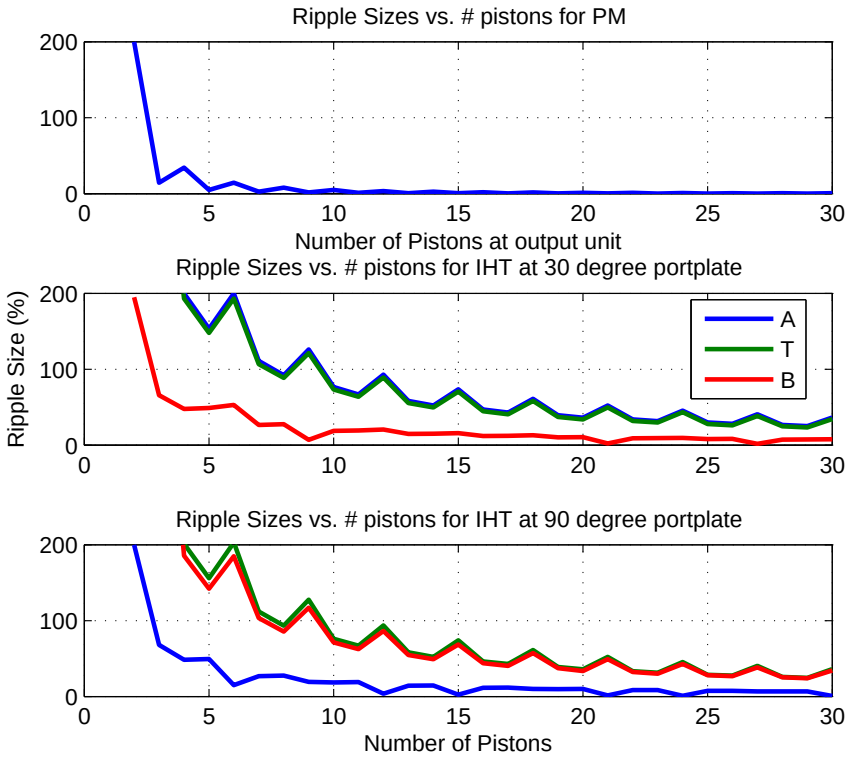

Figure 3.20: Ripple Size vs Total Number of Pistons. Top: PM-1; Middle: IHT at $\theta = 30$ degrees; Bottom: IHT at $\theta = 90$ degrees.

Figure 3.21 shows the Discrete Fourier Transform (DFT) results of the kinematic flow ripple, with amplitude normalized by the mean flow at the port and frequency normalized by the piston pass frequency, which is defined by:

$$f = \frac{n\omega}{2\pi} \tag{3.90}$$

where n is the number of pistons in a single unit.

For the PM transformer, it can be seen that having an even number of pistons results in the harmonic frequencies occurring for all piston frequencies. For the odd number of pistons, the harmonics only occur at even multiples of the piston pass frequencies. Within a given even number of piston pass frequency, it is seen that increasing the number of pistons in the output unit does result in decreasing amplitude of the DFT result.

In case of the IHT, the DFT results do match with the observations in Fig. 3.20. The amplitude is smaller for transformation ratio $\lambda = 0.5$ than $\lambda = 2$. For $\lambda = 0.5$, the output flow ripple decreased as the total number of piston increases from 7 to 9, the same result is shown with the DFT results of the flow ripple. For $\lambda = 2$, it was seen in Fig. 3.20 that increasing number of pistons from 7 to 9 resulted in increased size in flow ripple. This is visualized in the DFT result as well, where at the first piston pass frequency, the amplitude increases as piston number increases. Between IHT and PM, notice the difference in the scale of the amplitude. Amplitude for the IHT is an order of magnitude higher than that of PM transformer.

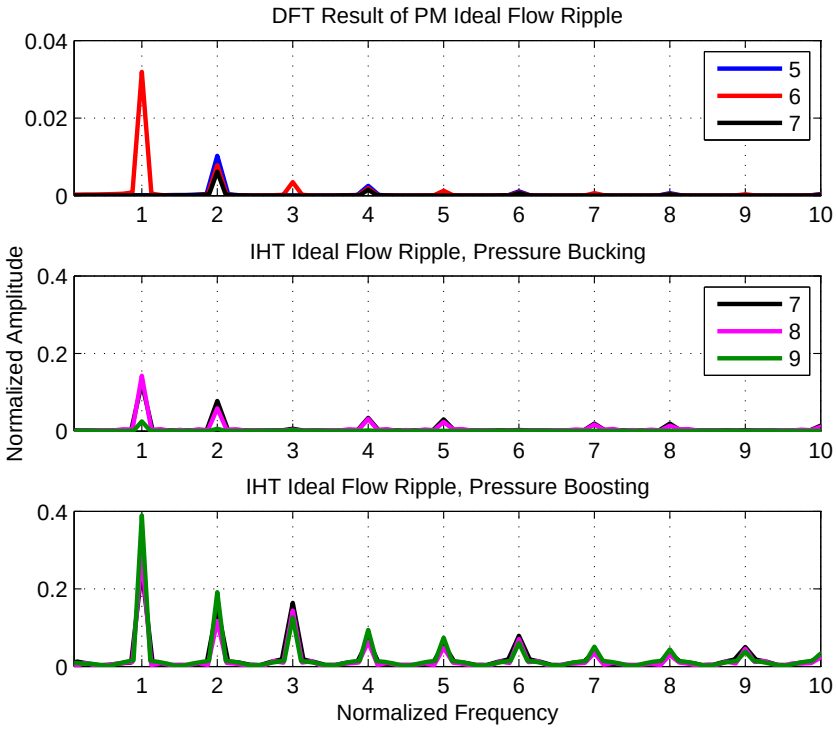

Figure 3.21: Fourier Transform results for the kinematic flow ripple. For a PM, number of pistons are for the unit providing an output flow (with D_2). Top: PM-1; Middle: IHT with $\lambda = 0.5$; Bottom: IHT with $\lambda = 2$

3.3.2 Dynamic Flow Ripple

In section 3.3.1, the fluid is assumed to be incompressible. In this section, we study the fluid with compressibility. In [69], Manring shows that flow ripple caused by compressibility effects are larger than the flow ripple caused by kinematic relationships. To better understand the flow ripple, we incorporate the compressibility effects for the analysis. An IHT with a total volumetric displacement of 15 cc/rev is compared to PM Transformer with each unit at 12 cc/rev (per Sizing Method III discussed in Section 3.1). Compressibility effects are heavily dependent on the valve plate design and choice of the nominal piston chamber initial volume V_0, and there exist countless design options to realize the same volumetric displacement.

In this study, an IHT with 7, 8, 9 pistons and PM-1 transformer with 5, 6, 7 pistons (in each unit) are considered. The total number of pistons in PM transformers will end up being more than that of IHT, but in PM-1 configuration, only one unit provides the output flow. In this case, we are giving an advantage to the IHT configuration in terms of number of pistons contributing to the output port flow. The initial volume V_0, piston diameter d_p and piston pitch radius r used for this analysis are presented in Tables 3.8-3.9. These parameters are designed such that the angular span occupied by all the pistons in a cylinder barrel is the same even with a different number of pistons. If there exists a unit with 9 pistons whose cross-sectional area span 330 degrees on a barrel with each piston spanning 36.67 degrees, the comparable unit with 8 pistons were designed to have each piston spanning 41.25 degrees such that the total span is still 330 degrees. This scaling is illustrated in Fig. 3.22.

For both PM transformer and IHT, the valve plate is designed as presented in Section 2.2.2. Since transformer in operation will serve as both pump and motor depending on the loading condition, the valve plate cannot be optimized just for one case. The symmetric valve plate is assumed to not penalize pump operation over the other or vice versa. Within each configuration, the triangular notches (relieving grooves) are optimized to deliver best flow ripple possible with the symmetric valve plate. The compressibility of the fluid to be considered is assumed to follow bulk modulus model used in 2.2, and that the entrained air ratio is constant at 1%.

It is not quite possible to normalize the ripple amplitude in the completely same manner as in the idealized case, and the result may differ depending on the scaling method being used. Still, the following comparison serves to highlight the difference arising from the inherent differences of valve plate design (fixed 2-port v. rotatable 3-port).

Operating conditions are taken to be constant at $\omega = 200$ rad/sec for one revolution of

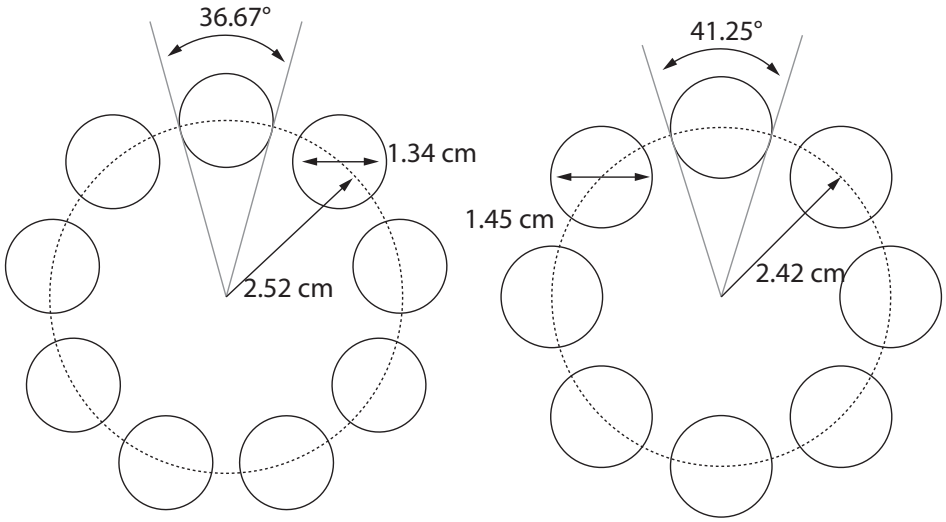

Figure 3.22: The parameter design methods illustrated for 9 piston unit on left with 8 piston unit on right. The total angular span of the pistons are the same even with different number of pistons. For a 9 piston unit, 36.67 x 9 = 330 degrees; and for a 8 piston unit, 41.25 x 8 = 330 degrees

Table 3.8: Physical Parameter Selection for IHT

	9 Pistons	8 Pistons	7 Pistons	Units
R_p	2.52	2.42	2.33	cm
d_p	1.34	1.45	1.58	cm
V_0	1.251	1.408	1.609	cm^3

Table 3.9: Physical Parameter Selection for PM

	7 Pistons	6 Pistons	5 Pistons	Units
R_p	2.18	2.08	1.84	cm
d_p	1.48	1.64	1.98	cm
V_0	1.329	1.551	1.861	cm^3

analysis, with a constant input pressure of 20 MPa, and output pressure of either 10 MPa or 35 MPa to simulate cases where $\lambda = 0.5$ and $\lambda = 1.5$, respectively. For the simulation, a transformer is provided with the specified operating conditions and is run for one full revolution at the steady state.

The resulting output flow for the PM-1 transformer is shown in Fig. 3.24, normalized by the nominal flow from the output port of the unit. In both cases, the flow ripple is larger than what was observed with Fig. 3.16. As the piston travels from one port to the other port, there will be a situation where the piston chamber volume is decreasing with an orifice area opening to the port that is not large enough for the fluid to pass through the port. In this case, the movement of piston causes the volumetric compression of the fluid that causes the pressure within the piston chamber to overshoot the pressure at the next port. On the other hand, there will be another situation where the piston chamber volume increases with an orifice area opening not large enough for the fluid to enter to the piston chamber. In the similar manner as the previous case, the piston movement causes the volumetric expansion of the fluid that will cause the pressure within the piston chamber to undershoot the pressure at the next port. In either case, the overshoot and undershoot of the pressure causes the piston chamber to have a pressure different from the port it is commutating with, which results in the backfilling of the piston chambers. The final result is the added 'tails' on the flow curve as illustrated with a single piston in Fig. 3.23. These overshooting and undershooting contribute significantly to the flow ripples.

PM with $\lambda = 1.5$ shows quite large flow ripple when compared to $\lambda = 0.5$. This is attributed to two factors. First one is due to the pressure difference in two ports connected to the displacement unit. In PM-1 configuration being considered, the output flow is coming from D_2 unit only. D_2 unit is connected to $P_T \approx 0$ on one side, and P_B on the other side. The magnitude of 'tails' present in the flow ripple is directly proportional to the pressure overshoot and undershoot while pistons transition from one port to the other. The overshoot and undershoot is directly proportional to the pressure differential across two ports in the pump or motor. For $\lambda = 1.5$ case, that pressure difference is much higher than $\lambda = 0.5$ case. The second factor in having a large flow ripple is the swashplate angle condition in achieving the pressure transformation ratio. With $\lambda = 1.5$, it means D_1 is held at maximum while D_2 varies to get to the steady state condition. This increases the dead volume within the piston chamber, which in turn, increases the fluid volume on which pressure overshoot and undershoot is acting with and results in large flow ripple. This phenomenon, however, are easily mitigated by adding more pistons. In Table 3.10, which

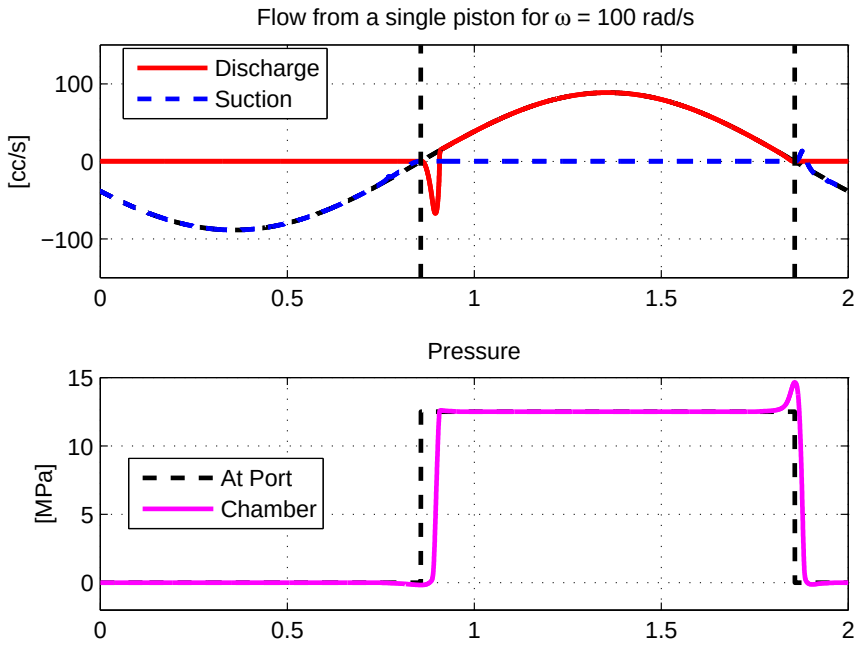

Figure 3.23: Top: A flow with compressibility delivered by a single piston in a PM transformer to each port, overlayed with a kinematic flow; Bottom: Piston chamber pressure and port pressure

summarizes the flow ripple results shown in Fig. 3.24, adding two more pistons decreases the flow ripple size by 32%.

In case of the typical axial piston pump, the valve plate geometry can be designed such that the piston will go through a pre-compression to preemptively increase the piston chamber pressure to reduce the pressure spike. However, this optimization only works in one direction. If the flow direction changes, then the valve plate design results in the worse flow ripple. It should be noted that for the PM transformer, the flow ripple size attributed more to the symmetric valve plate design than a pressure dynamics in the piston chamber and compressibility of the fluid.

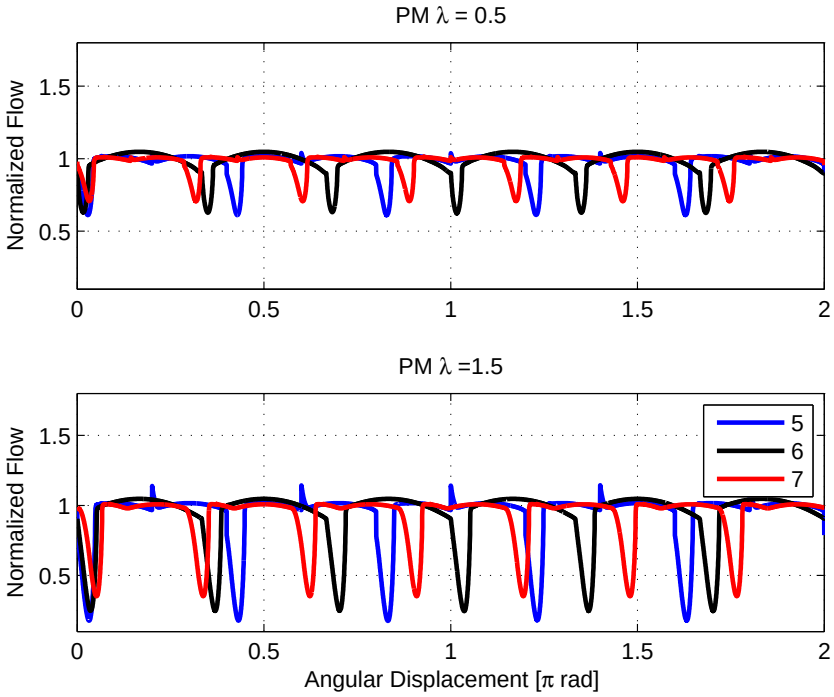

Figure 3.24: Output flow ripple of PM-1 transformer with compressibility for different number of pistons at $\lambda = 0.5$ and $\lambda = 1.5$

Table 3.10: Ripple sizes for PM at select output pressure with compressibility

λ	0.5	1.5
5 Pistons	42.9%	96.7%
6 Pistons	42.4%	80.2%
7 Pistons	30.7%	65%

On the other hand, Figure 3.26 shows the output flow for the IHT, also normalized by

the nominal flow from the output port of the unit. The IHT flow ripple was quite large in Section 3.3.1. Overshooting and undershooting of the pressure in the piston chamber as a piston transitions from one port to the other, described with a PM transformer, also happens with IHT. However, unlike with a PM transformer where adding a compressibility effect increased the flow ripple size, IHT results in a smaller flow ripple size when compressibility is considered. In Fig. 3.25, a behavior of a single piston in IHT is illustrated for $\lambda = 0.5$ case. Observe that piston transition from one port to the other occurs when the flow is not zero, and this results in the piston chamber pressure being pre-compressed. This in turn results in the sharp flow drops observed in kinematic flow ripple to be dampened out.

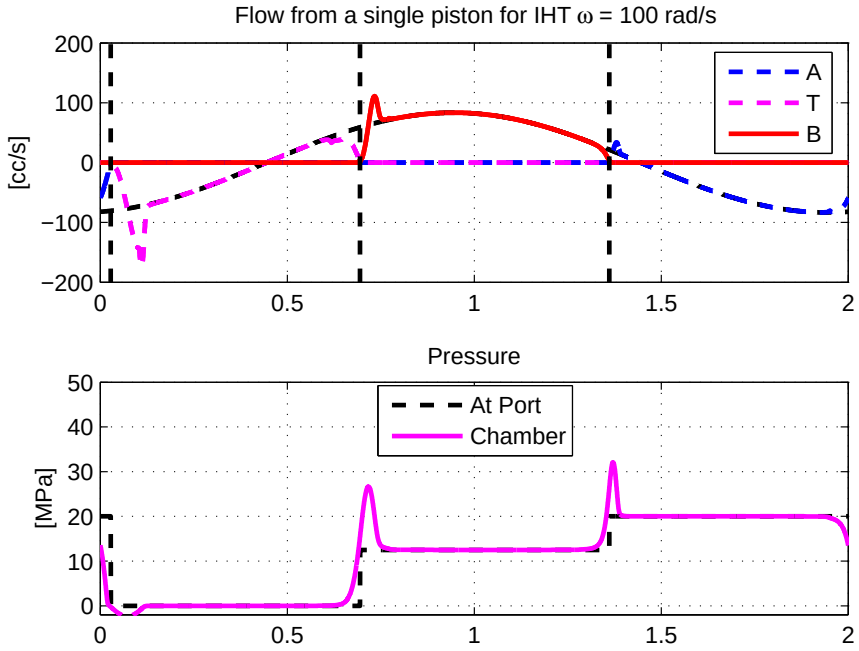

Figure 3.25: Top: A flow with compressibility delivered by a single piston in a IHT to each port, overlayed with a kinematic flow; Bottom: Piston chamber pressure and port pressure

For the pressure transformation ratio $\lambda = 1.5$, the difference in flow ripple compared with flow ripple resulting from incompressible flow is negligibly small. For this $\lambda = 1.5$ the starting kinematic flow ripple is quite large, and the valve plate condition makes the piston to transition from one port to the other where the flow delivered by the piston is at its maximum. Pre-compression effects shown in Fig. 3.25 alone are not enough to reduce the flow ripple as it was seen with $\lambda = 0.5$ case.

As with the incompressible fluid case, the flow ripple is worse when pressure is being

boosted. Table 3.11 summarizes the observations from Fig. 3.26. The flow ripple for IHT only decreases by 8% with adding two more pistons, as opposed to 32% decrease observed with PM-1 transformer.

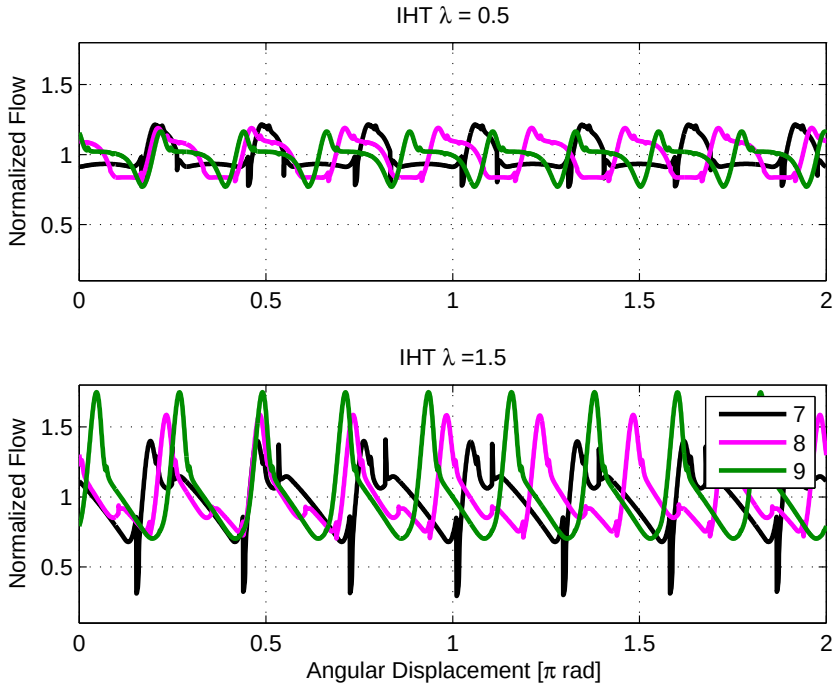

Figure 3.26: Output flow ripple of an IHT with compressibility for different number of pistons at $\lambda = 0.5$ and $\lambda = 1.5$

Table 3.11: Ripple Sizes for IHT at Select Output Pressure with compressibility

λ	0.5	1.5
7 Pistons	44.5%	114%
8 Pistons	38.1%	124%
9 Pistons	39.4%	105%

Figure 3.27 and 3.28 show the DFT results for PM and IHT with compressible flow, with amplitude normalized by the mean flow at the port and frequency normalized by the piston pass frequency defined with Eq. (3.90). Compared with the results from incompressible flow in Fig. 3.21, the amplitudes for the PM are much higher with compressible flow. This is again explained by the backfilling effects that occur as piston transitions from one port to the other. The amplitudes die out monotonically as the normalized frequency increases. Within the same frequency, increasing number of pistons do result in decrease

of the amplitude. IHT also shows larger amplitudes compared to the incompressible flow in Fig. 3.21, this also due to the pre-compression effects that results in overshooting and undershooting of the piston pressure chambers.

For IHT, it is observed that IHT still has higher amplitude, especially at the piston pass frequency. As observed in Fig. 3.20, increasing number of pistons can result in increase in amplitude. Within the same number of pistons, the amplitude does not monotonically decrease with the frequency. A 9-piston IHT at $\lambda = 1.5$ has a normalized amplitude of 0.35 at the piston pass frequency, whereas a 7-piston PM-1 transformer at the same condition has the amplitude of 0.2.

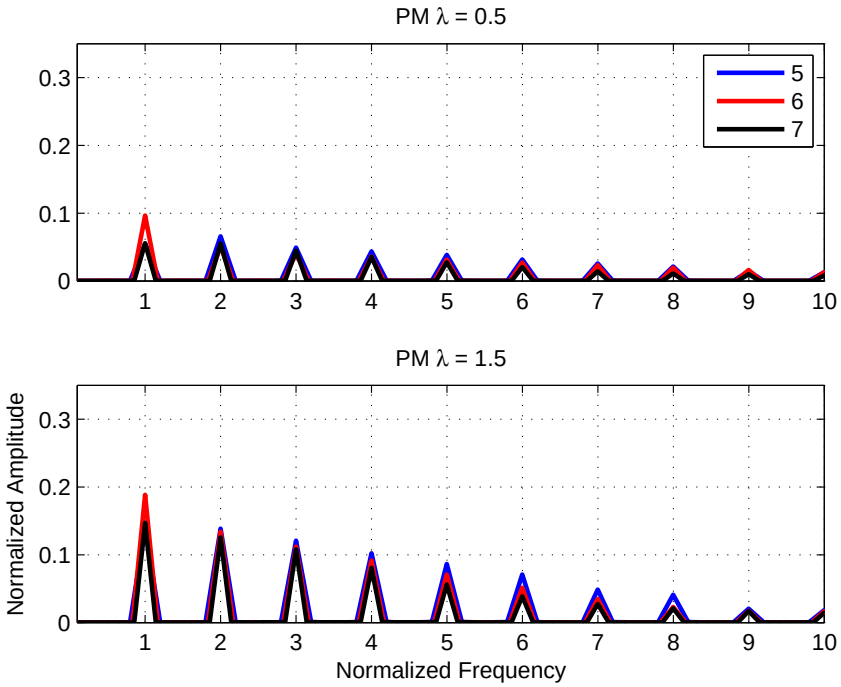

Figure 3.27: Fourier Transform results for PM-1 actual flow ripple with compressibility

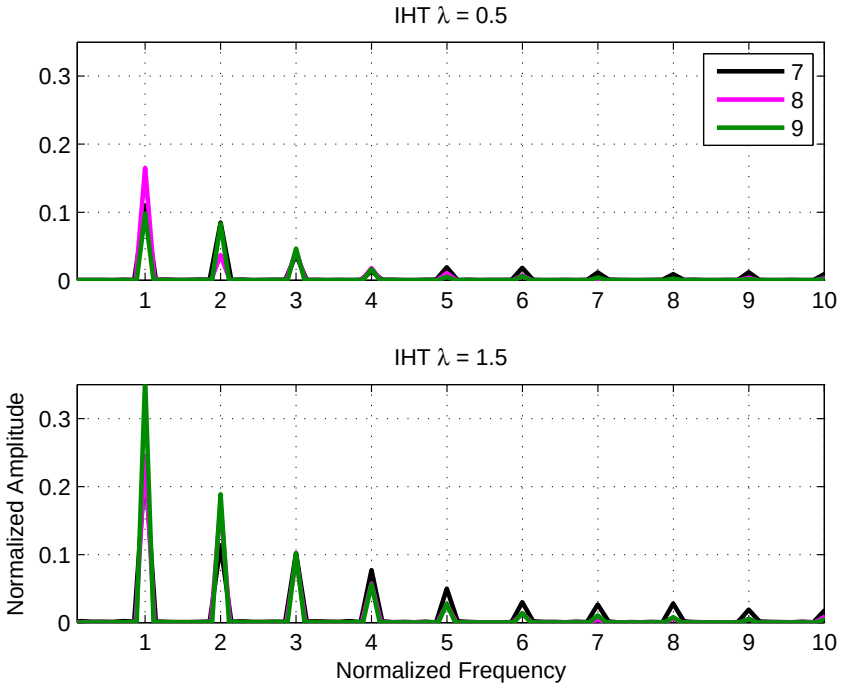

Figure 3.28: Fourier Transform results for IHT actual flow ripple with compressibility

3.4 Chapter Summary

In this chapter PM transformer in three different configurations were compared with IHT in terms of volumetric displacement sizing and flow ripple. First, the relative size of PM configurations with respect to the IHT necessary to achieve the similar output flow at the same shaft speed was determined. According to the method that seeks to minimize the difference of output flow between PM transformer and a given IHT for overall range of transformation ratio λ, PM transformer needs to be 27% to 65% larger than IHT. Using the same criteria, if the transformer is allowed to switch its configuration mode, then the PM transformer needs to be 14% larger than IHT.

In a different approach, the displacement sizing was compared for a case where transformers are not imposed with a predefined maximum shaft speed, but were allowed to spin as fast as possible to deliver the maximum possible output flow. In this case, PM transformers range from being 4% smaller to 48% larger than IHT in terms of displacement sizing to deliver the similar output flow for overall range of pressure transformation ratio λ. These are following the same sizing method in the previous approach. This study revealed that PM transformer can be competitively sized to be as compact as an IHT.

Flow ripple was compared for both incompressible flow and compressible flow. Adding

compressibility effects makes flow ripple worse for PM transformer due to the pressure overshoot and undershoot in the piston chambers. Whereas for an IHT, compressibility effects reduces the flow ripple with the pre-compression of the piston chambers dampening out the abrupt change in flow as piston transitions from one port to the other. In both cases, the IHT has a large amplitude in flow ripple, and smaller marginal benefit in reducing flow ripple as a result of adding more pistons. This is a result of IHT's rotatable valve plate that allows the pistons to transition from one port to the other when the instantaneous flow from the pistons are not at zero. PM-1 configuration was used for the flow ripple comparison. For PM-2, the output flow ripple will be smaller as two units contribute to the output flow, which means there will be twice number of the pistons providing the output flow if two units in PM transformer have equal number of pistons. PM-3 configuration has just one unit providing the output flow, so the results will be generally the same. However, since the displacement ratio required for $\lambda = 1.5$ for PM-3 is $D_2 = 1$, the output flow ripple will be smaller for PM-3 at $\lambda = 1.5$.

It should be noted that even with a novel design improvement to reduce the flow ripple for IHT, PM transformer will still have smaller flow ripple as the same improvement can be applied to PM transformer to make it even better. In the next chapter, the efficiency comparison will be established.

Chapter 4

Efficiency Comparison of Transformer Designs

Chapter 3 compared the IHT and PM transformers in terms of a total displacement sizing and flow ripple behaviors. In this chapter, we compare the efficiency of the transformer designs, one of the most important aspects of the component analysis. In order to replace throttling valves prevalent in hydraulic systems, hydraulic transformers not only need to have good sizing and flow characteristics but also need to be efficient.

Some efficiency comparisons between IHT and PM have been alluded to in [2, 89], suggesting that an IHT will achieve better efficiency. However, the efficiency comparisons are based on scaling and extrapolating published performance data for existing components, rather than developing a model specific for the transformer. Also, the total displacement for PM transformer in comparison was not competitively determined. In [89] for example, the PM transformer being considered has a total displacement of 70 cc/rev while an IHT has 40 cc/rev. We observed in Chapter 3 that PM transformer does not need to be this much larger in terms of the total displacement in delivering the similar output power. Oversized components will be inefficient compared to a properly sized component in delivering the same output power. Efficiency compared for a properly sized PM unit will likely yield a different result from the previous works.

Efficiency analysis on the pump and motors through sub-component level models are available [62], but no such work is found on PM transformers. The IHT efficiency analysis through mathematical loss model was established by Li et al. [61]. However, rather than modeling sub-component level losses, they used an empirical model. They did not consider the effect of compressibility and associated throttling loss that happens as fluid exits the piston chamber. This dissertation utilizes the models built in Chapter 2, specifically in

Section 2.3 to quantitatively compare the efficiency between PM transformer and IHT.

This chapter is organized as follows. Section 4.1 describes the geometrical parameters, as well as the operating conditions considered in establishing the efficiency comparison, along with the definition of efficiency being considered. Section 4.2 presents the efficiency contour for each of the transformer configuration. Section 4.3 explores the component level loss trend for the given output flow Q as the transformation ratio λ varies, and the loss trend for the given transformation ratio λ as the output flow Q varies. Concluding remarks of this chapter is presented in Section 4.5.

4.1 Comparison Conditions

In order for establishing a fair comparison, the simulated IHT and PM are sized to have similar flow capabilities with Method III in Section 3.1 (maximum shaft speed is imposed) for PM-1. This means each unit in PM-1 is sized so that the total displacement is 0.826 times of IHT. In terms of the number of pistons, simulated IHT and PM have 9 and 5+5 pistons respectively to yield a similar number of total pistons. The piston area was increased, and the radial pitch was decreased to maintain the same wall thickness between pistons. PM-2 and PM-3 are taken to have the same displacement size as PM-1, which results in a slightly larger unit than required to match the output flow capability, but it results in being more conservative in determining the efficiency.

A 9-piston axial piston pump was used as a basis for building an IHT. This unit was scaled realize the volumetric displacement that is 0.826 times of the original displacement. There are two methods in scaling, visualized in Fig. 4.1:

1. A–R method increases the piston area and decreases the radial pitch to maintain the wall thickness between pistons

2. R– scales only the radial pitch while keeping the piston area the same.

With the R– method, the resulting unit will be unreasonably large even though the total volumetric flow is smaller.

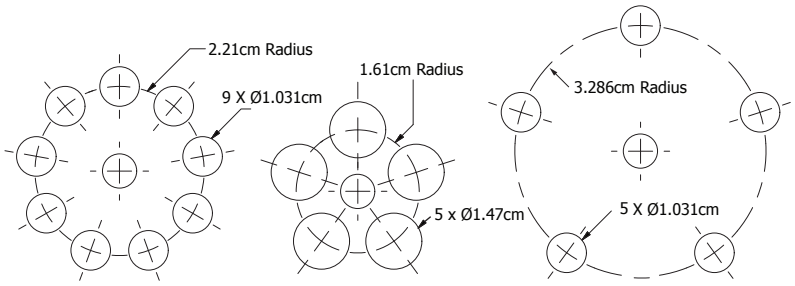

Figure 4.1: Relative size of the piston areas and their radial placements visualized. Left: a 9-piston unit; Middle: 5-piston unit with 0.826 times the displacement scaled with method A-R; Right: 5-piston unit scaled with method R-

In Section 3.3, we utilized the same scaling methods to realize the same total displacement size with different number of pistons. In the end, the IHT is designed to have a displacement of 19 cc/rev with 9 pistons, and the PM transformers are designed to have 31.4 cc/rev with 5 pistons in each of the two units for all three configurations. Maximum shaft speed is assumed to be 200 rad/s ($\approx$ 1910 rpm) for both units.

For the simulating condition, an adjustable orifice load attached at the output port of the transformer and 20 MPa pressure is imposed at the input port. The transformer model developed in Chapter 2 with mechanical and volumetric losses along with the throttling loss at the valve plate are simulated. For each of the data point which is a set of λ and Q_B generated from the simulation, an a transformer is allowed to run for a one full shaft rotation at the steady state with imposed operating condition of output pressure P_B that goes up to pressure transformation ratio $\lambda = 2$, and with the shaft speed reaching up to the maximum shaft speed.

For the PM transformers, one displacement is held at maximum while the other displacement is varied to find the steady-state condition that results in the torque balance $J\dot{\omega} = 0$. For an IHT, a valve plate rotation angle θ that brings the steady-state condition $J\dot{\omega} = 0$ is found. The input flow Q_A and the output flow Q_B are obtained by taking the mean flow over one full shaft revolution of the transformer.

Results from the simulation are taken to determine the power input and output of the system, which are defined to be the hydraulic power input and output given by:

$$\begin{aligned} W_{in} &= -(P_{in} + W_V(P_{in}, P_T))Q_A \\ W_{out} &= (P_{out} + W_V(P_{out}, P_T))Q_B \end{aligned} \tag{4.1}$$

where $P_{in} = P_A - P_T$ is the input pressure to the transformer and Q_A is the flow at the 'A' port of the transformer. Similarly, $P_{out} = P_B - P_T$ is the output pressure from the

transformer, and Q_B is the flow at the 'B' port of the transformer connected to the orifice load described above.

$W_V(P, P_T)$ is a volumetric energy density in the compressible fluid at pressure P relative to pressure P_T with pressure dependent bulk modulus $\beta(P)$ as derived in [56]. It is assumed that the compressibility of fluid will follow bulk modulus model used in 2.2. Efficiency is defined to be the ratio between power input and output of transformer for one cycle at steady-state operating condition as given by:

$$\eta = \frac{W_{out}}{W_{in}} \tag{4.2}$$

As noted in Chapter 2, $Q > 0$ is defined to be the flow coming out of the transformer while $Q < 0$ is defined to be the flow going into the transformer. In our simulation condition, $Q_A < 0$ while $Q_B > 0$ to deliver the flow to the attached orifice. Negative sign in W_{in} is necessary to have positive efficiency.

4.2 Overall Efficiency Contours

The resulting efficiency contours for all 3 configurations of PM transformer and IHT are given in Figs. 4.2-4.5.

The peak efficiencies of PM-1, PM-2, and PM-3 are 83%, 86% and 83%, respectively. The peak efficiency of IHT is 85%. It is worthwhile to note that PM-1 is the most efficient when transformation ratio is close to 1, while PM-2 and -3 are the most efficient when pressure is bucked or boosted, respectively. These conditions are also when the unit displacements D_1 and D_2 are at their maximum (i.e. swashplate angles are at maximum). Also, the peak efficiency of the IHT does not significantly outperform that of PM transformers. It is also interesting to see that IHT only has a small region with a high efficiency. Depending on the operating conditions, there exists a region where the PM transformer is more efficient than the IHT.

In terms of the operating range, PM-1 shows the maximum flow of around 400 cc/s up to transformation ratio $\lambda = 0.8$, and its maximum flow decreases as λ gets higher. PM-2 has the maximum flow around $\lambda = 0.45$, with decreasing output flow as λ deviates away from it. PM-3 shows quite uniform maximum flow up to $\lambda = 1.8$ before starting to show a decreasing trend. The maximum flow for IHT decreases as θ increases. To explain these observation, examine the ideal pressure transformation ratio equations and the output flow

equation for each of the transformer configuration from From Eq. (2.26) and (2.18)–(2.21):

$$\lambda = \frac{P_B - P_T}{P_A - P_T} = \begin{cases} \dfrac{D_1}{D_2} & \text{PM-1} \\ \dfrac{D_1}{D_1 + D_2} & \text{PM-2} \\ \dfrac{D_1 + D_2}{D_2} & \text{PM-3} \\ -\dfrac{\sin(\theta(t))}{\sin(4\pi/3 + \theta(t))} & \text{IHT} \end{cases} \tag{4.3}$$

with

$$Q_B = \begin{cases} \dfrac{D_2}{2\pi}\omega & \text{PM-1} \\ \dfrac{D_1 + D_2}{2\pi}\omega & \text{PM-2} \\ \dfrac{D_2}{2\pi}\omega & \text{PM-3} \\ \dfrac{D_B(\theta)}{2\pi}\omega & \text{IHT} \end{cases} \tag{4.4}$$

where for the IHT, $D_B(\theta) = -\frac{D}{2}\sqrt{3}\sin\left(\frac{4\pi}{3} + \theta\right)$ as in Eq. (2.23).

For a PM-1 configuration, the output flow is directly related to D_2. As the λ increases, there will be a cross-over point where D_2 starts decreasing while D_1 is held at the maximum. With the friction losses considered, this cross-over happens $\lambda < 1$. The similar explanation applies for the PM-2. The maximum output flow happens when both D_1 and D_2, and as D_1 or D_2 decreases to realize different pressure transformation ratio, the output flow decreases as well. For PM-3, D_2 stays at the maximum for the most of the λ plotted as only D_1 varies to realize different pressure transformation ratio λ.

For an IHT, it was shown in Fig. 2.5 that increasing θ corresponds to the increase in λ. The port flow D_B decreases with respect to the increasing θ in sinusoidal manner, as noted by Eq. 2.23, resulting in decreasing maximum output flow as shown in Fig. 4.5.

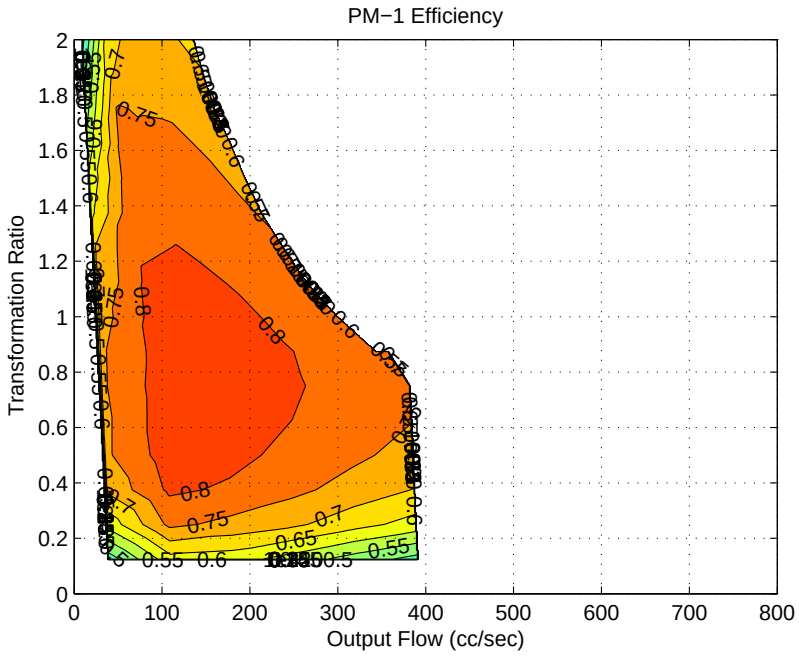

Figure 4.2: Efficiency Contour for PM1

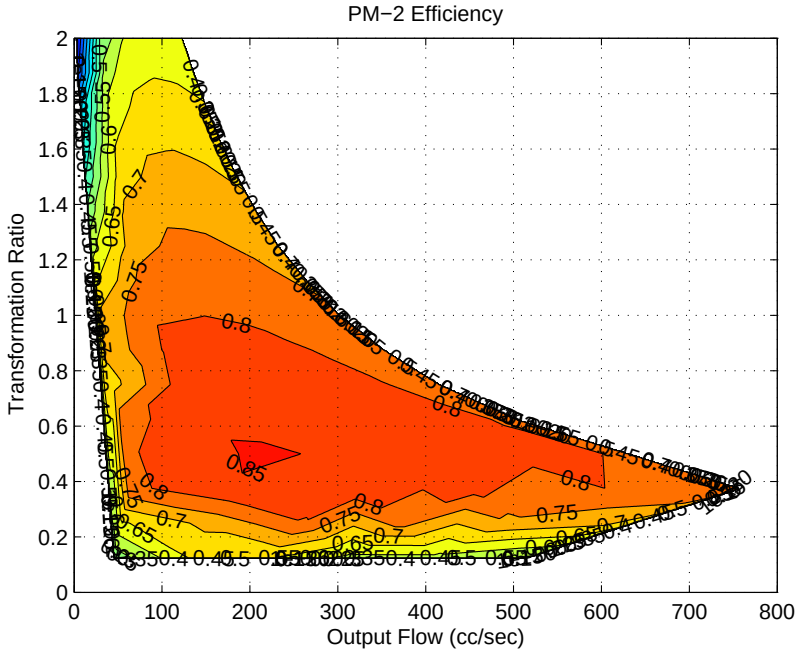

Figure 4.3: Efficiency Contour for PM2

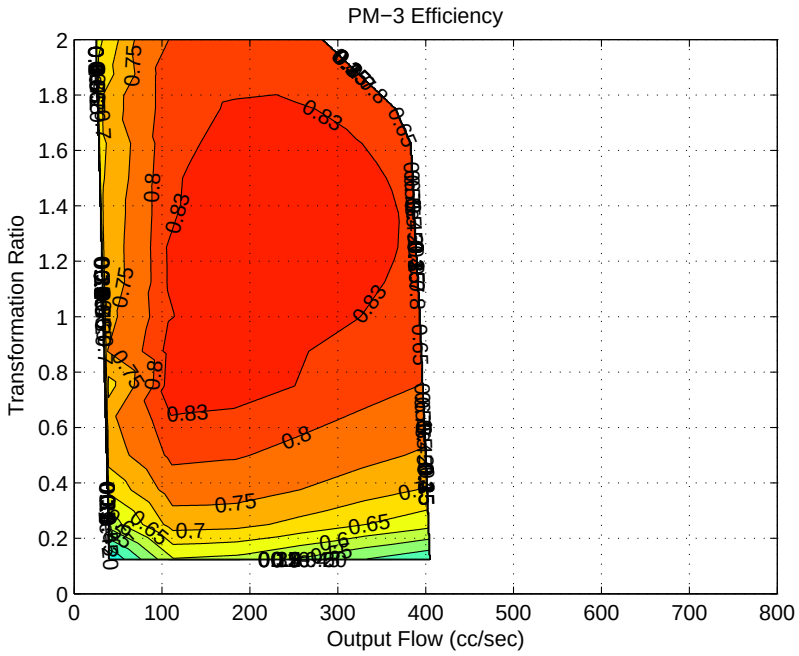

Figure 4.4: Efficiency Contour for PM3

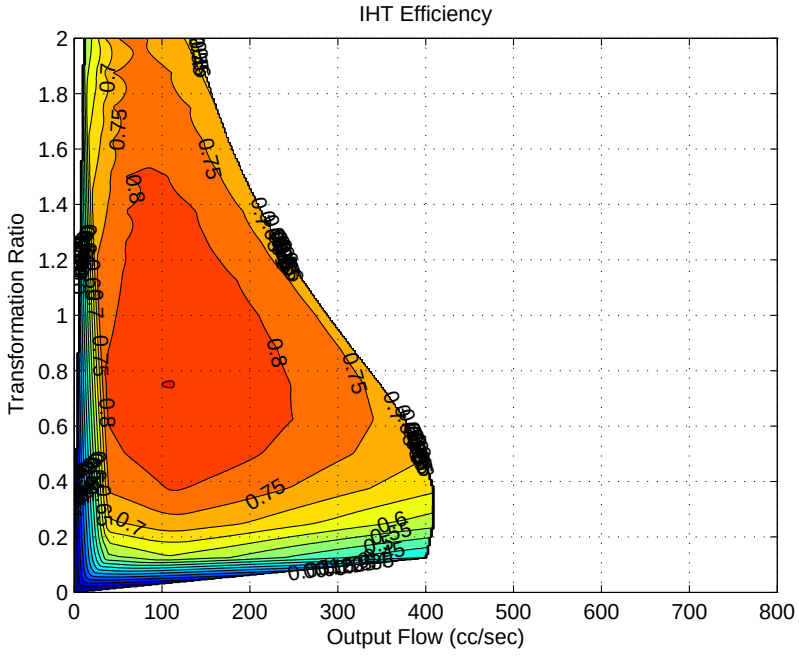

Figure 4.5: Efficiency Contour for IHT

4.3 Distribution of Losses

In this section, we examine the loss contribution from each of the component losses being considered in Chapter 2. Analysis is performed at operating points on four lines in the operation region as shown in Fig. 4.6. First two sets of operating lines involve holding transformation ratio λ constant at 0.625 and 1.375 while varying the flow. These lines will reveal the characteristics of losses that depend on output flow and operating shaft speed. The other two sets of operating lines involve holding the output flow rate Q_B constant at 100 cc/s and 330 cc/s while varying the pressure transformation ratio. These lines will reveal how the losses behave due to the pressure change. For all the plots to be presented below, the power loss is reported in unit of Watts. The power loss due to leakage losses are obtained by multiplying the flow losses modeled in Section 2.3 by the appropriate pressures at which the leakage flows occur. The power loss due to friction losses are obtained by multiplying the torque losses modeled in Section 2.4 by the shaft speed of the transformer.

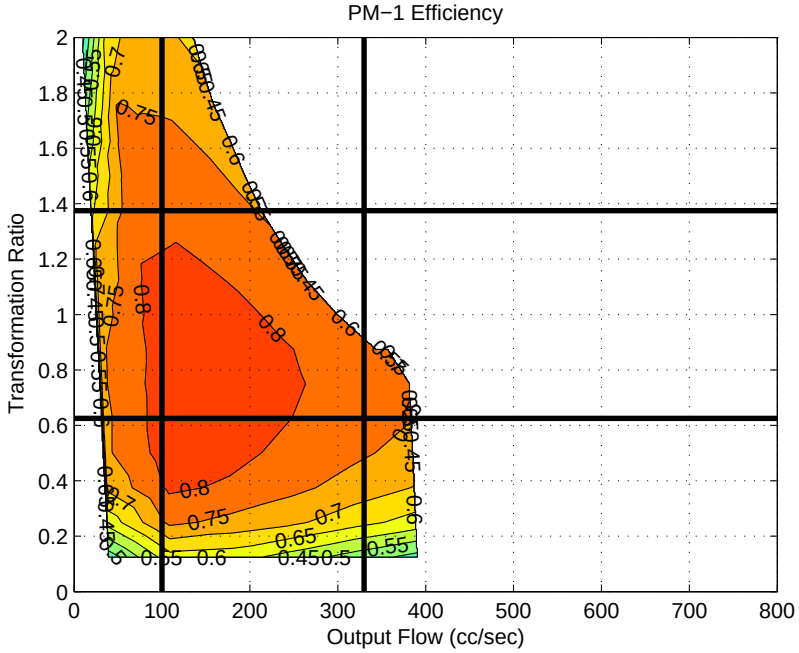

Figure 4.6: Distribution of losses will be studied along these lines

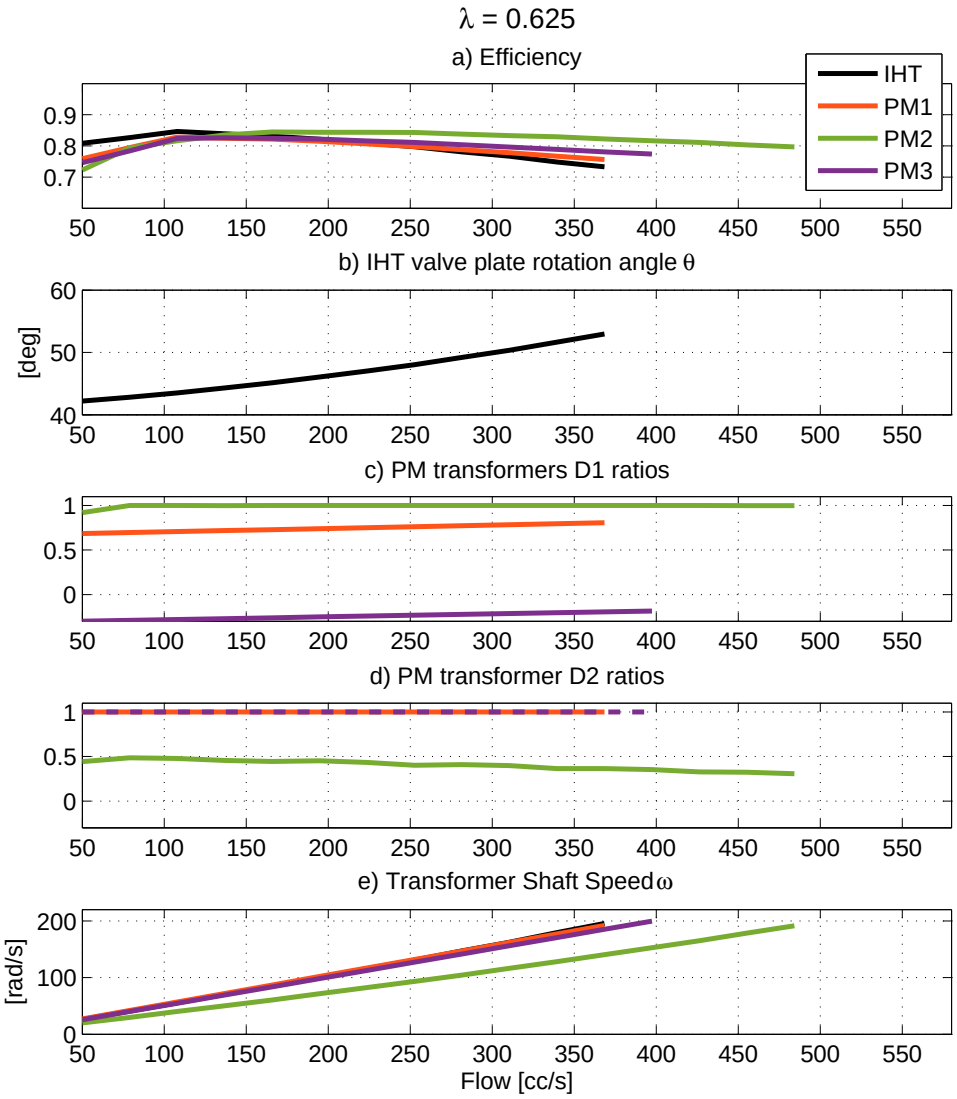

Figure 4.7: Loss trend for $\lambda = 0.625$, showing overall efficiency, displacement ratio, and shaft speed as the output flow varies

4.3.1 Constant pressure transformation ratio $\lambda = 0.625$ with varying flow

Efficiency and Operating Parameters

Figure 4.7-a shows the overall efficiency for the transformers being compared for transformation ratio λ at 0.625 as the output flow changes. IHT is the most efficient for $Q < 150$ cc/s and PM-2 is the most efficient for $Q > 150$ cc/s. Figure 4.7-e shows the shaft speed for each of the transformer configurations. PM-2 can provide the largest flow of 370 cc/s for the maximum shaft speed of 200 rad/s whereas the other configurations only provide the flow up to 210 cc/s at the same maximum shaft speed. The large output flow from PM-2 is possible because there are two units providing the output flow, unlike the other units. The effect of different shaft speed will be discussed in the analysis of mechanical losses.

Figure 4.7-b shows the valve plate rotation angle θ for the IHT. Valve plate angle θ increases as the flow Q increases even though the transformation ratio λ is held constant. This is because of the losses being considered in the simulation. With the losses, the valve plate rotation angle θ does not uniquely map to the transformation ratio λ as it was in Fig. 2.5. To provide more flow in the presence of losses, the valve plate angle θ has to increase to draw more driving torque to speed up the unit.

Figure 4.7-c and 4.7-d show the displacement ratio of D_1 and D_2 in three PM transformer configurations. The displacement ratios change even though the transformation ratio λ is kept constant to make up for the losses that increase with the increasing output flow Q. The magnitude of losses determine how significantly the displacement ratios have to change in order to provide the same transformation ratio λ as the output flow Q varies.

Orifice Throttling Loss

Figure 4.8-L1 shows the power loss due to throttling at the piston chamber exit. It shows that the throttling losses increase with the output flow for the PM transformers, but increase at a superlinear rate for the IHT.

The throttling loss results from the fact that the piston orifice area cannot be instantly changed to the full opening. The behavior of orifice area was modeled in Section 2.2.2. The piston chamber orifice flow was given by Eq. (2.35), which is reproduced here:

$$Q_{P,k}(t) = C_d A_{o,P,k}(t) \sqrt{\frac{2|P_{p,k}(t) - P_P(t)|}{\rho}} sgn(P_{P,k}(t) - P_P(t)) \tag{4.5}$$

where $P_P(t)$ is the pressure of the external port to which the piston chamber is connected

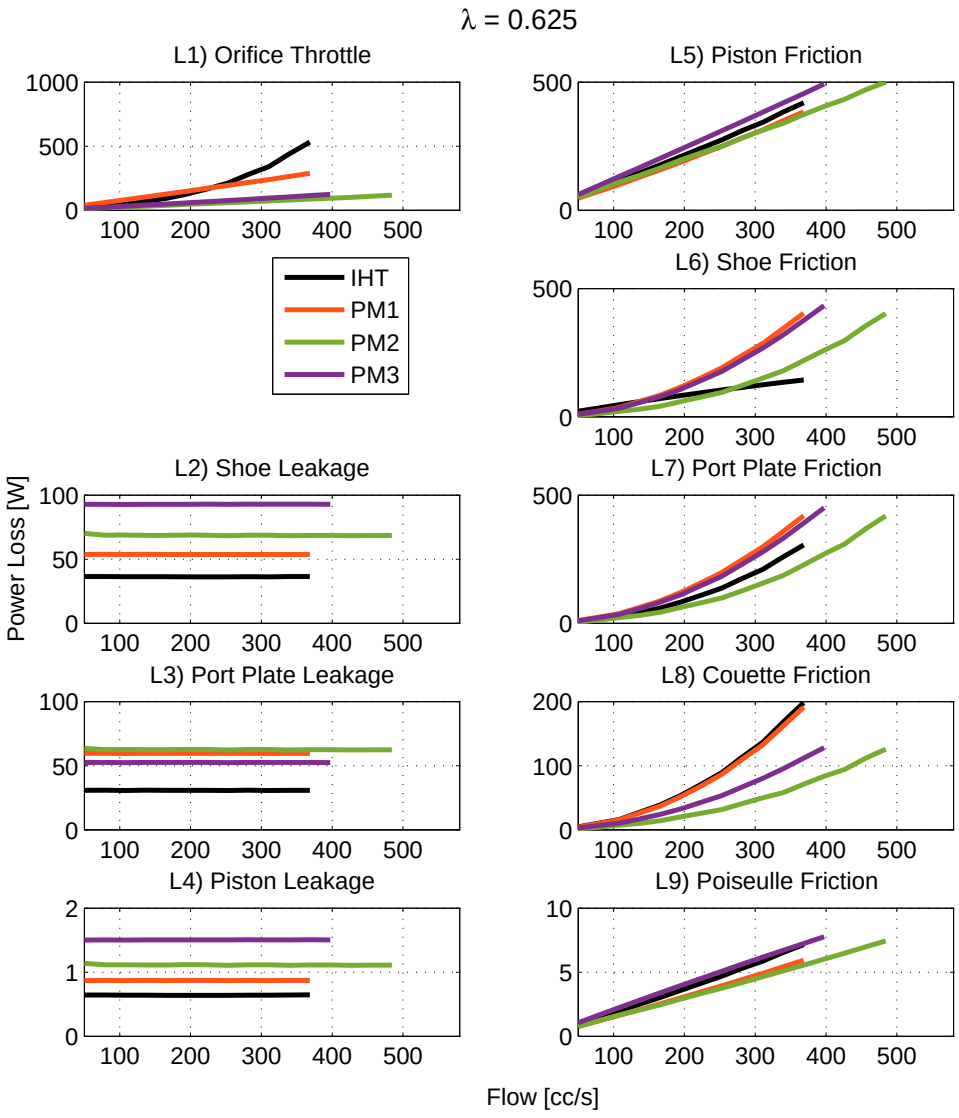

Figure 4.8: Loss trend for $\lambda = 0.625$, showing port throttling loss, leakage losses, and friction losses as the output flow varies

to, C_d is a coefficient of discharge for the orifice, ρ is the density of the hydraulic fluid, and $A_{o,P,k}(t)$ is the instantaneous discharge area of the orifice to the port P described in Section 2.2.2. The instantaneous power loss due to the throttling contributed by the k-th piston at the P-port is given by:

$$W_{throt,k} = (P_{p,k}(t) - P_P(t))Q_{P,k}(t) \tag{4.6}$$

the mean value is taken one shaft revolution during the steady-state for Fig. 4.8-L1. $(P_{p,k}(t) - P_P(t))$ is the pressure discrepancy between the piston chamber and the port.

Equations (4.5) and (4.6) can be examined either by imposing the the pressure condition or the flow condition. If the pressure condition is imposed, increasing $A_{o,P,k}$ does not necessarily decreases the throttling loss. If flow is imposed, however, the loss is decreased with increasing $A_{o,P,k}$. A common method to alleviate the throttling loss coming from the pressure discrepancy is to pre-compress the piston chamber pressure when the piston moves from low pressure port to the high pressure port, and to pre-decompress the piston chamber pressure when the piston moves in the other direction.

The throttling increasing linearly with the flow in PM transformers is unusual compared to what is expected from an axial piston pump or motor. This suggests that the throttling loss is dominated by the lack of piston chamber pre-compression and decompression due to the symmetric valve plate geometry considered. It was discussed in Section 3.3.2 that the symmetric valve plate geometry causes a large flow ripple in PM transformers. Figure 4.9 illustrates the behavior of a single piston flow observed at D_2 unit of PM-1 transformer with shaft speed $\omega = 200$ rad/s. Observe that as piston transitions from suction port to the discharge port around the shaft rotation at 0.85π rad, the piston chamber lags behind the port pressure change. The difference in the pressure during the transition, along with the flow ripple that happens at the same time contributes to the throttling loss as shown in the third subplot in the same figure illustrating the instantaneous throttle loss due to the piston being considered. The energy loss per cycle is the same, thus as flow increases with ω, the power loss increase linearly with ω. This results in the linearly increasing throttling loss seen in Fig. 4.8-L1.

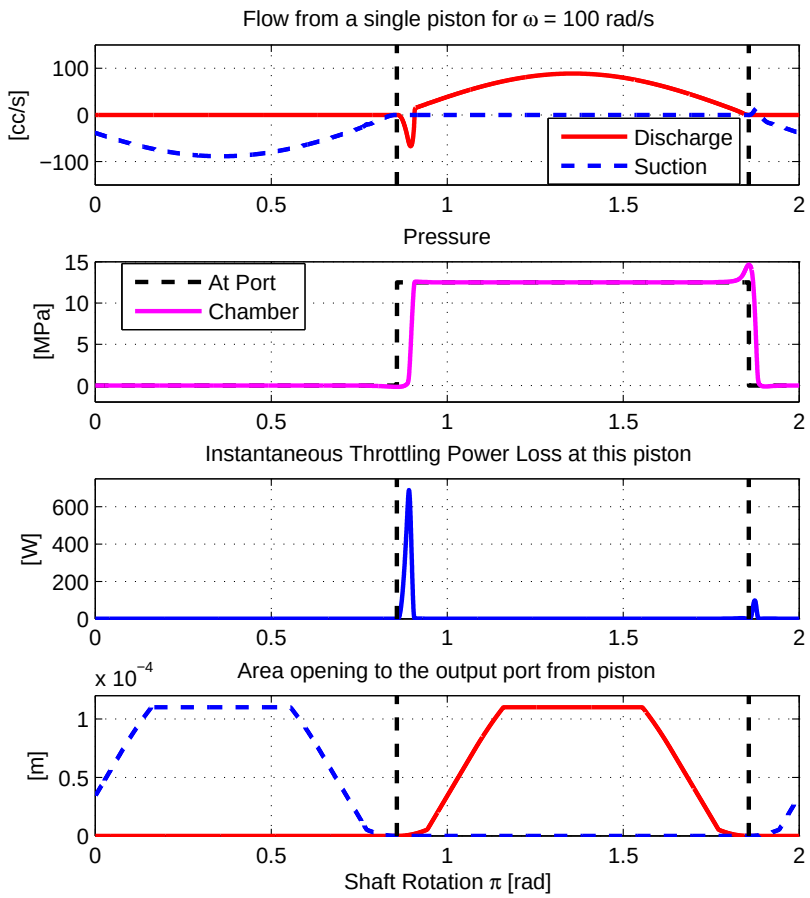

Figure 4.9: 1) Flow from a single piston in a D_2 unit of PM-1 transformer observed at its discharge port and suction port; 2) the pressure at the port and inside the single piston chamber being considered; 3) Instantaneous throttling power loss from a single piston; 4) A piston opening area to the ports

PM-1 shows quite a large throttling loss as the pressure difference across the upstream port and downstream port is larger for both D_1 and D_2 units compared to the other PM configurations, contributing to the larger pressure discrepancy as the pistons transition from one port to the other. For example, D_2 unit in PM-3 experiences the pressure differential between P_A to P_B as the piston transitions from one port to the other. In the meantime, D_2 unit in PM-1 faces the pressure differential between P_T to P_B.

For the IHT, the pre-compression does happen even with the symmetric valve plate geometry as piston transition from T port to B port where $P_B > P_T$. Moreover, the transition happens at non-TDC or non-BDC location where the flow is not at zero. Depending on whether $P_A > P_B$ or $P_A < P_B$, the pre-compression or pre-decompression will occur.

Figure 4.10 shows the flow observed at three ports of the IHT contributed by a single piston, along with the piston chamber pressure and port pressures, and the orifice area opening to the port from the single piston traveling at shaft speed of $\omega = 100$ rad/s for $\lambda = 0.625$. As the piston moves from the 'T' port to the 'B' port, notice the piston chamber pressure starts increasing before the port pressure makes a step change. Examining the third subplot in Fig. 4.10, the throttling loss is not dominated by the lack of piston chamber pre-compression, but rather comes from the port opening being too small for the kinematic flow to pass through, which causes the overshooting and undershooting of the piston chamber pressure as a piston transitions from one port to the other. As the valve plate angle θ is increasing with the output flow, the resulting throttling loss also increases with θ.

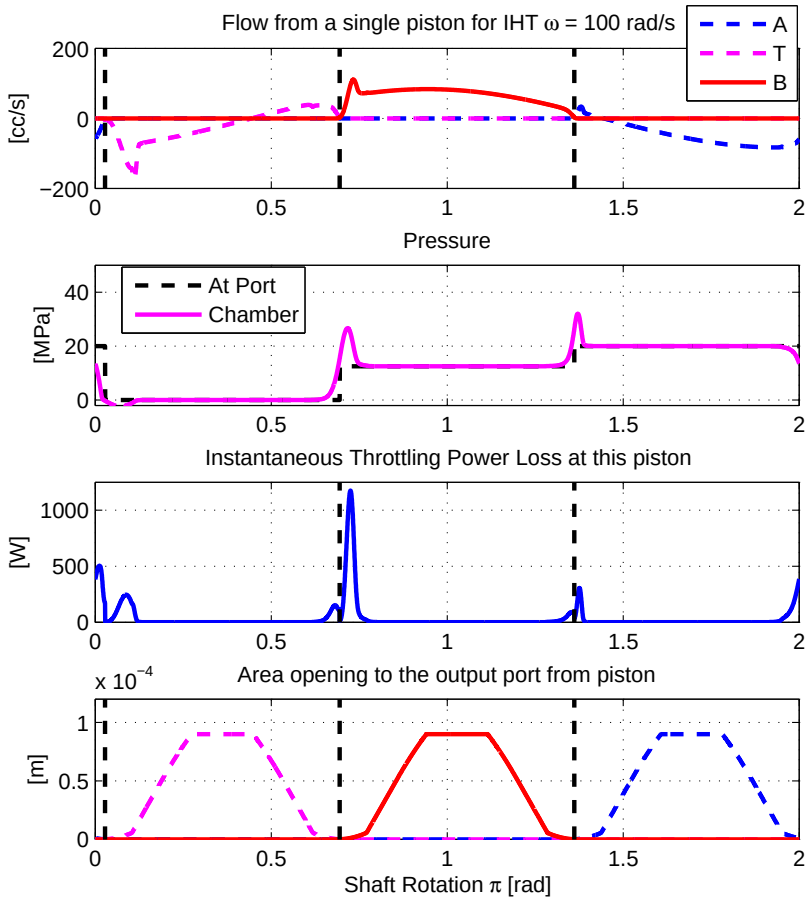

Figure 4.10: 1) Flow from a single piston in an IHT observed at three ports; 2) the pressure at the port and inside the single piston chamber being considered; 3) Instantaneous throttling power loss from a single piston; 4) A piston opening area to the ports

Leakage Losses

Figure 4.8-L2 through -L4 shows the power loss due to the flow leakage. In Section 2.3, three volumetric losses were considered: a leakage through the piston shoe, from the piston chamber to the case, and from the clearance between the port plate and the cylinder barrel.

Figure 4.8-L2 shows the power loss due to the flow leakage through the piston shoes. The order of losses are constant as the flow changes. The order is as follows: PM-3, PM-2, PM-1, and the IHT. The shoe leakage loss in Eq (2.44) is dependent on the port pressure. For a single piston shoe, the shoe acting with a higher port pressure will have larger power loss. If the piston shoe dimensions are the same, then unit with more number of pistons exposed to higher pressure will have larger losses. PM-3 shares the input pressure $P_A > P_B$ to two units, so there will be 2.5 pistons from each unit summing up to 5 total pistons exposed to the input pressure P_A, and 2.5 pistons exposed to $P_B < P_A$. PM-2, on the other hand, will have 5 pistons exposed to the output pressure $P_B < P_A$ while having 2.5 pistons exposed to the P_A. This puts power loss of PM-2 due to the shoe leakage to be lower than that of PM-3. In the same manner, PM-1 has 2.5 pistons exposed to P_A and 2.5 pistons exposed to P_B, having the lowest number of pistons pressurized among PM configurations. In case of IHT, even though there are 3 pistons exposed to P_A and 3 pistons exposed to P_B, the physical dimensions of each piston are much smaller than PM transformer as visualized in Fig. 4.1, placing the IHT in the last in terms of power loss due to the shoe leakage flow.

Figure 4.8-L3 is the power loss from the port plate leakage. Again, the order of losses are constant as the flow increases, but the order is different from Fig. 4.8-L2. Now losses are ordered such that PM-2 > PM-1 > PM-3 > IHT. From Eq. (2.48), the losses are dependent on the pressure condition on the cylinder barrel as well as the tilting condition of the barrel. The tilting condition depends on whether the unit is pumping or motoring, with motoring condition causing more loss than pumping condition. As configured, PM-2 has D_1 motoring with P_A and P_B, and D_2 pumping with P_T and P_B. PM-1 has D_1 motoring with P_A and P_T and D_2 pumping with P_T and P_B. Lastly, PM-3 has D_1 pumping (since displacement ratio is negative) with P_A and P_T and D_2 motoring at P_A and P_B. These conditions result in PM-2 with the most losses, followed by PM-1 and PM-3. The cylinder barrel in IHT balances itself better than the PM transformer does, which results in the least amount of power loss coming from port plate leakage.

Figure 4.8-L4 is the power loss caused by the leakage inside the piston chambers. The order of losses are the same as in Fig. 4.8-L2. This loss depends on the flow given by Eq (2.42), which again shows the dependency on the port pressure. It also depends on

the number of pistons being considered, along with the leakage path length. The order of losses are explained by the same reasoning as in Fig. 4.8-L2.

Friction Losses

Figure 4.8-L5 through -L9 shows the power loss due to the friction. In Section 2.4, five mechanical losses were considered: friction due to the contact force between each piston and its piston chamber, a friction between piston shoes and the swashplate, friction between the valve plate and the cylinder barrel, a Couette and Poiseuille friction between the piston and piston chamber. In general, the friction related power losses heavily depend on the shaft speed ω as the torque loss is multiplied by the shaft speed to obtain the power loss. The shaft speed are ordered as IHT = PM-1 > PM-3 > PM-2 from Fig. 4.7-e.

Figure 4.8-L5 shows the power loss from the piston friction. This loss is ordered in the following: PM-3 > IHT > PM-1 > PM-2, and increases linearly as output flow increases. Piston friction (Section 2.4.1) depends on shaft speed and number of pistons pressurized. PM-3 shows the highest loss despite having the slowest shaft speed, because more pistons are exposed to higher pressure. The pressure conditions described with Fig 4.8-L3 combined with the force balance that arises from the equations described in Section 2.4.1 describes the remaining configurations.

Figure 4.8-L6 presents the piston shoe friction power loss. The ordering is PM-1 > PM-3 > PM-2 > IHT at $Q > 275$ cc/s. For $Q < 275$ cc/s, the order of PM-2 and IHT changes. From Section. 2.4.4, the piston shoe friction depends on a coefficient of loss that is obtained from the geometrical parameters of the transformer. In obtaining the power loss, this coefficient is multiplied by ω^2. Thus this loss term follows the same ordering with the shaft speed of each unit for the PM transformers, in a quadratic manner. An IHT shows a smaller loss as the coefficient for the loss is more than twice smaller for IHT, making it appear as if the IHT does not have the quadratic relationship to the shaft speed.

Figure 4.8-L7 shows the port plate friction power loss, whose ordering is PM-1 > PM-3 > IHT > PM-2 for all flow range now, and shows the quadratic relationship for both PM transformers and IHT. The port plate friction loss (Section 2.4.5) is also obtained using a geometry based coefficient and thus follows the similar trend observed with the piston shoe friction. In this case however, the coefficient for PM is an order of magnitude smaller than that for IHT, and thus we see PM transformer power losses not much bigger than IHT compared to the difference observed in Fig. 4.8-L6.

Figure 4.8-L8 is the power loss due to the Couette friction. The ordering of power loss is IHT $\geq$ PM-1 > PM-3 > PM-2 for all flow. Couette friction power losses show a strong

quadratic relationship with ω for PM-1 and IHT, and a weaker quadratic relationship for PM-2 and PM-3. Couette friction was given in Section 2.4.2 and it depends heavily on the leakage length and the piston velocity. The key reasons for each unit having the losses relative to the other units are as follows. IHT and PM-1 both have swash plate angle at maximum. Thus has the longest leakage length. PM-3 at this transformation ratio has one displacement at -0.3 and the other at maximum. PM-2 has one displacement at 0.5 and the other at maximum, which results in larger leakage length that of PM-3, but it also has the lowest shaft speed, to offset the effect and makes PM-2 suffer the least from the Couette friction losses.

Lastly, Figure 4.8-L9 shows the power loss from a pressure driven loss acting on the surface area of the piston, a Poiseuille friction. The ordering of this loss is PM-3 $\geq$ IHT $>$ PM-1 $>$ PM-2 for all flow and shows a linear relationship with the output flow. Poiseuille friction presented in Section 2.4.3 is a pressure driven loss acting on the surface area of the piston. Thus, the surface area being pressurized and the number of pistons acting with the pressure matter the most. Thus, PM-3 and IHT show about the same losses while PM-1 and PM-2 sow the similar magnitude in losses. Power loss increases linearly with the output flow, as increasing output flow results in increasing ω that is used to calculate the power loss.

Loss Distribution within the Configuration

Figure. 4.11 recasts the information shown in Fig. 4.8 to present the loss distribution within each configuration. The legend items correspond to the power losses presented in Fig. 4.8. In all configurations, Fig. 4.8-L5, a friction arising from the contact force between the piston chamber and a piston, is a major contributor in the power loss. IHT and PM-1 has a large contribution of power loss coming from the throttling loss (Fig. 4.8-L1). PM transformers have a significant power loss from the piston shoe friction (Fig. 4.8-L6), due to having a larger piston diameter that ends up having more effective area being pressurized. Power losses from the port plate leakage (Fig. 4.8-L3), piston chamber leakage ((Fig. 4.8-L4), and Poiseuille friction (Fig. 4.8-L9) are the smallest contributors to the power loss for all configurations.

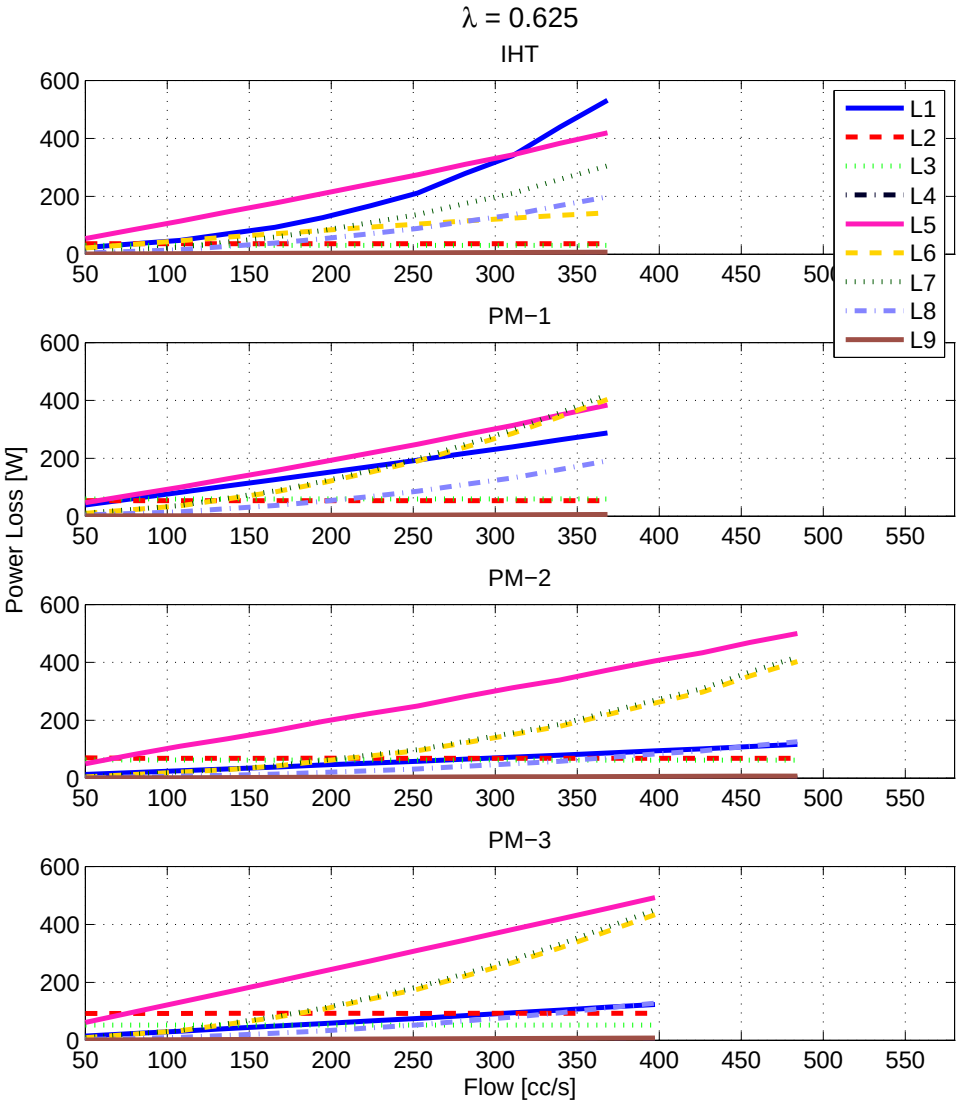

Figure 4.11: Loss trend for $\lambda = 0.625$ as the output flow varies showing losses within each transformer configurations. L1–L9 are the losses plotted in Fig. 4.8

4.3.2 Constant pressure transformation ratio $\lambda = 1.375$ with varying flow

Efficiency and Operating Parameters

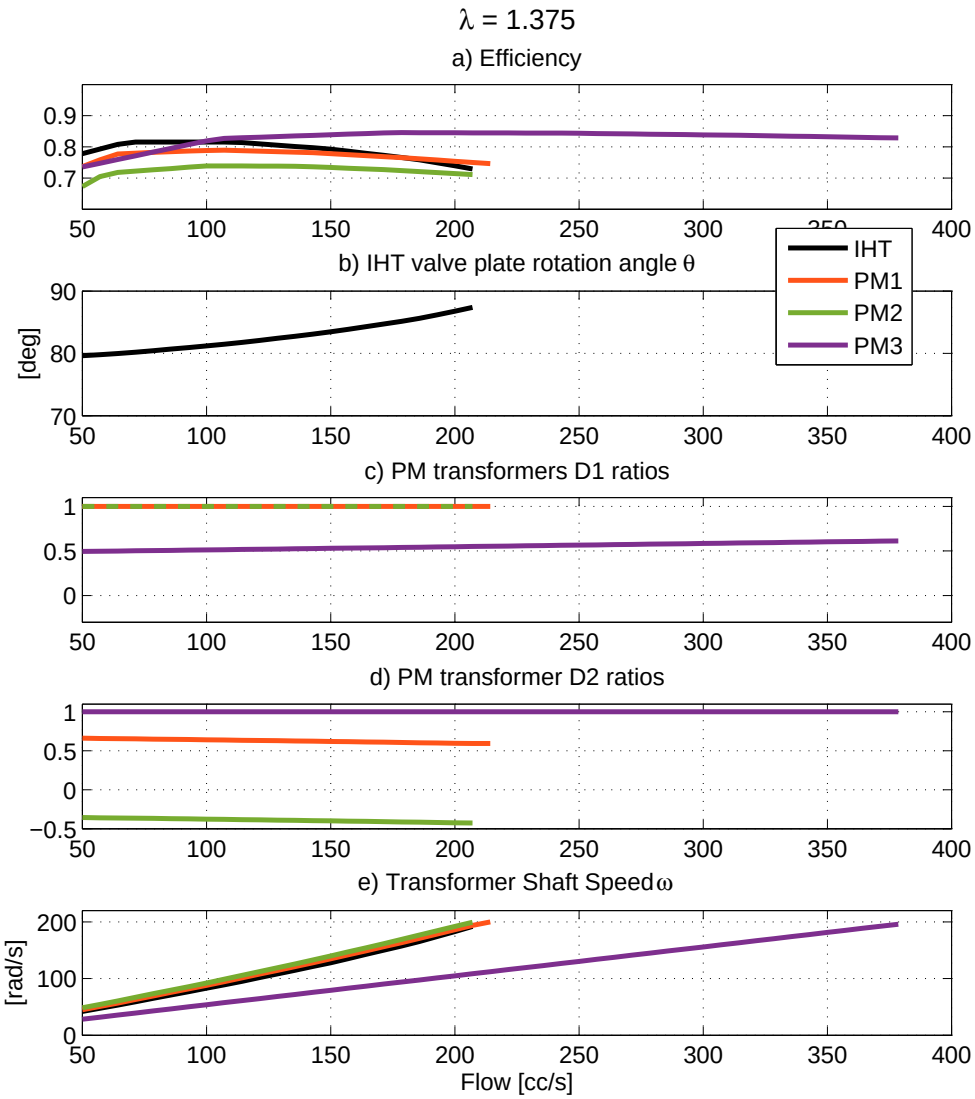

Figure 4.12: Loss trend for $\lambda = 1.375$, showing overall efficiency, displacement ratio, and shaft speed as the output flow varies

Figure 4.12-a shows the overall efficiency for the transformers being compared for transformation ratio λ at 1.375 as the output flow changes. IHT is the most efficient for $Q < 110$ cc/s and PM-3 is the most efficient for $Q > 110$ cc/s. Figure 4.12-e shows the shaft speed for each of the transformer configurations. Unlike in Fig. 4.7, now PM-3 can

provide the largest flow of 370 cc/s for the maximum shaft speed of 200 rad/s whereas the other configurations only provide the flow up to 220 cc/s at the same maximum shaft speed. PM-3 now shows the lowest shaft speed. Shaft speeds are ordered by: PM-2 > PM-1 > IHT > PM-3. The large output flow from PM-3 is possible as the D_2 unit that provides the output flow from the PM-3 is held at maximum displacement for all flow range being considered.

Figure 4.12-b shows the valve plate rotation angle θ for the IHT. Figure 4.12-c and 4.12-d show the displacement ratio of D_1 and D_2 in three PM transformer configurations. As in the previous case in Fig. 4.7-b, the valve plate angle has to increase to provide more flow with the presence of losses even as the transformation ratio λ is held constant. The displacement ratio of D_1 and D_2 in the PM transformer configurations also change as in Fig. 4.7-c and -d, to provide the larger flow holding the transformation ratio λ constant.

Orifice Throttling Loss

Figure 4.13-L1 shows the power loss due to orifice throttling at the piston chamber exits. The ordering, trend is the same with the observation made with Fig. 4.8-L1 except now PM-3 shows the least amount of power loss. As with the previous case, IHT and PM-1 show quite heavy throttle loss. Large throttle loss for PM-1 is attributed to the large pressure differential across the D_2 unit. PM-3 shows the least amount of power loss now due to the pressure differential across the ports being the smallest with $\lambda = 1.375$.

Leakage Losses

Figure 4.13-L2 through -L4 shows the power loss due to the flow leakage. The shoe and piston leakage follows the same trend observed in Section 4.3.1 for Fig. 4.13-L2 and Fig. 4.13-L4, but now PM-2 experiences more losses than PM-3. This is because with $\lambda > 1$, PM-2 now has more pistons exposed to the higher pressures than PM-3. Since the transformation ratio is held constant as output flow changes, the losses are constant across the horizontal axis.

Figure 4.13-L3 shows the port plate leakage, which now shows PM-3 having the largest power loss. At this transformation ratio, PM-3 has D_1 always motoring, and D_2 always pumping. These conditions are exactly opposite from Fig. 4.8-L3. On the other hand, PM-2 has D_1 always motoring, which is the same as in Fig. 4.8-L3, but the D_2 is now motoring (D_2 ¡ 0 can be observed from Fig. 4.12-d), as opposed to pumping. This changes the loss condition for PM-2 and PM-3 and results in their position changed on the loss plot.

Friction Losses

Figure 4.13-L5 through -L9 shows the power loss due to the friction for $\lambda = 1.375$ which are again all heavily dependent on ω. The shaft speed in decreasing order for all ranges of output flow observed in Fig. 4.12-e is: PM-2 > PM-1 > IHT > PM-3.

Figure 4.13-L5 shows the power loss from the piston friction. This loss is ordered in the following: PM-2 > IHT > PM-1 > PM-3, and increases linearly as output flow increases. Compared to Fig 4.8-L5, PM-2 and PM-3 changed their positions in the ordering of the power loss. As discussed, piston friction depends on pressure differential with the case pressure in each piston chamber and number of pistons pressurized. PM-2 now has the most number of pressure at high pressure, thus suffers the most from piston friction loss.

Figure 4.13-L6 presents the piston shoe friction power loss. The ordering is PM-2 > PM-1 > IHT > PM-3 for $Q < 220$ cc/s, which matches with the ordering of shaft speed observed in Fig. 4.12. For $Q > 220$ cc/s, only PM-3 can operate. As with Fig. 4.8-L6, PM configurations show a quadratic relationship whereas an IHT seems to be linear. This is again because the shoe friction depends on the a constant coefficient of friction, and the coefficient is significantly smaller for IHT, masking away the quadratic relationship between the power loss and ω.

Figure 4.13-L7 shows the port plate friction power loss, whose ordering is PM-2 > PM-1 > IHT > PM-3, again the same as the ordering of shaft speed ω. As with in Fig. 4.8-L7, the coefficient of friction between the valve plate and cylinder barrel is an order of magnitude smaller for the PM transformer compared to the IHT. Since there are two units in PM transformer, that coefficient difference is caught up in the magnitude of the power loss and all configurations show the quadratic relationship with ω.

Figure 4.13-L8 is the power loss due to the Couette friction, whose ordering is IHT > PM-1 > PM-2 > PM-3. Compared to Fig. 4.8-L8, the IHT and PM-2 have changed their positions in the ordering. Couette friction is dependent on leakage length and piston velocity, IHT, with swashplate always at maximum shows the largest Couette friction loss. PM-1 and -2 have similar leakage length due to having a similar magnitude of displacement ratio throughout the flow range. PM-3 shows the lowest loss because of its low shaft speed.

Lastly, Figure 4.13-L9 shows the Poiseuille friction for $\lambda = 1.375$. The ordering is PM-2 > PM-1 > IHT > PM-3 following the same trend with the ω ordering. This loss depends on the total surface area being pressurized and the number of pistons being pressurized. PM-2 shows the largest loss due to having the most number of pistons exposed to $P_B > P_A$. PM-3 has the lowest power loss due to it having the lowest shaft speed to offset the effect from it having many pistons exposed to the port pressures.

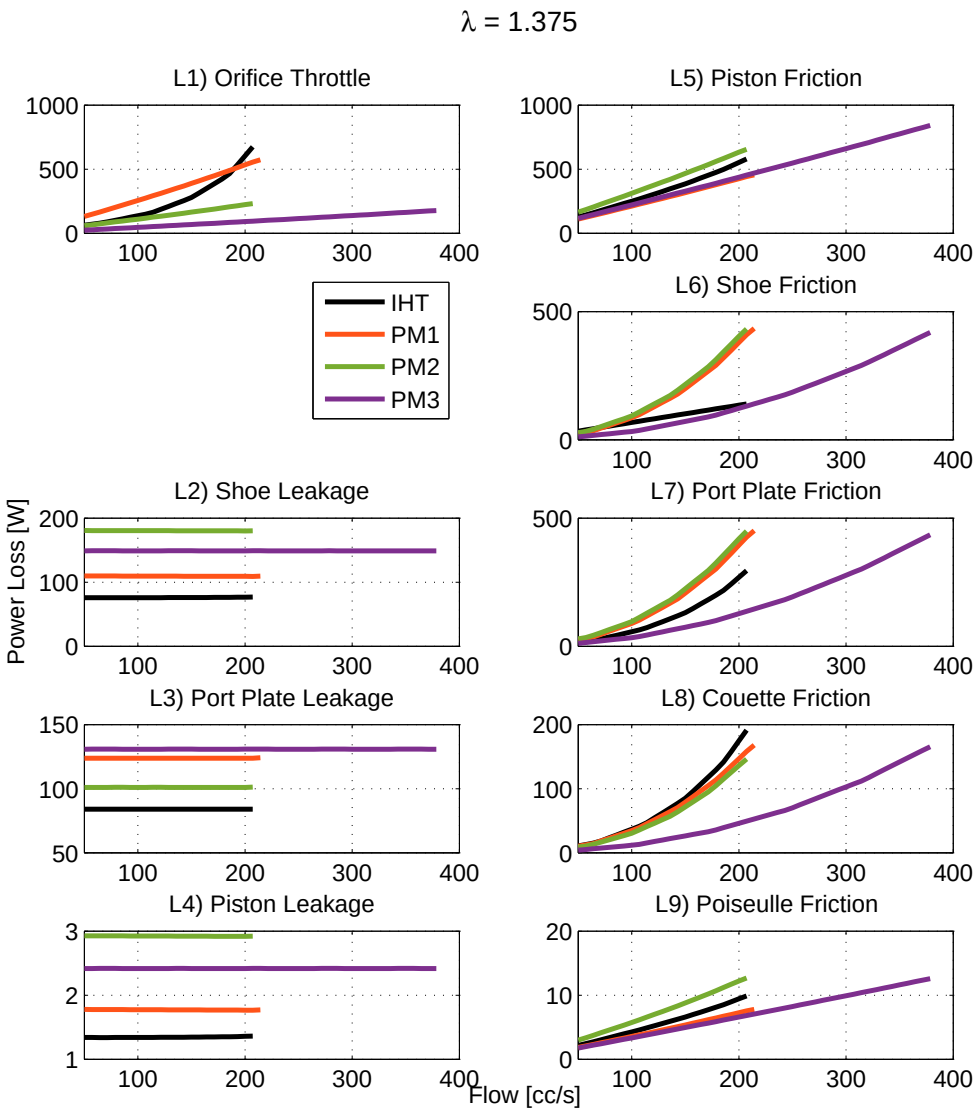

Figure 4.13: Loss trend for $\lambda = 1.375$, showing port throttling loss, leakage losses, and friction losses as the output flow varies

Loss Distribution within the Configuration

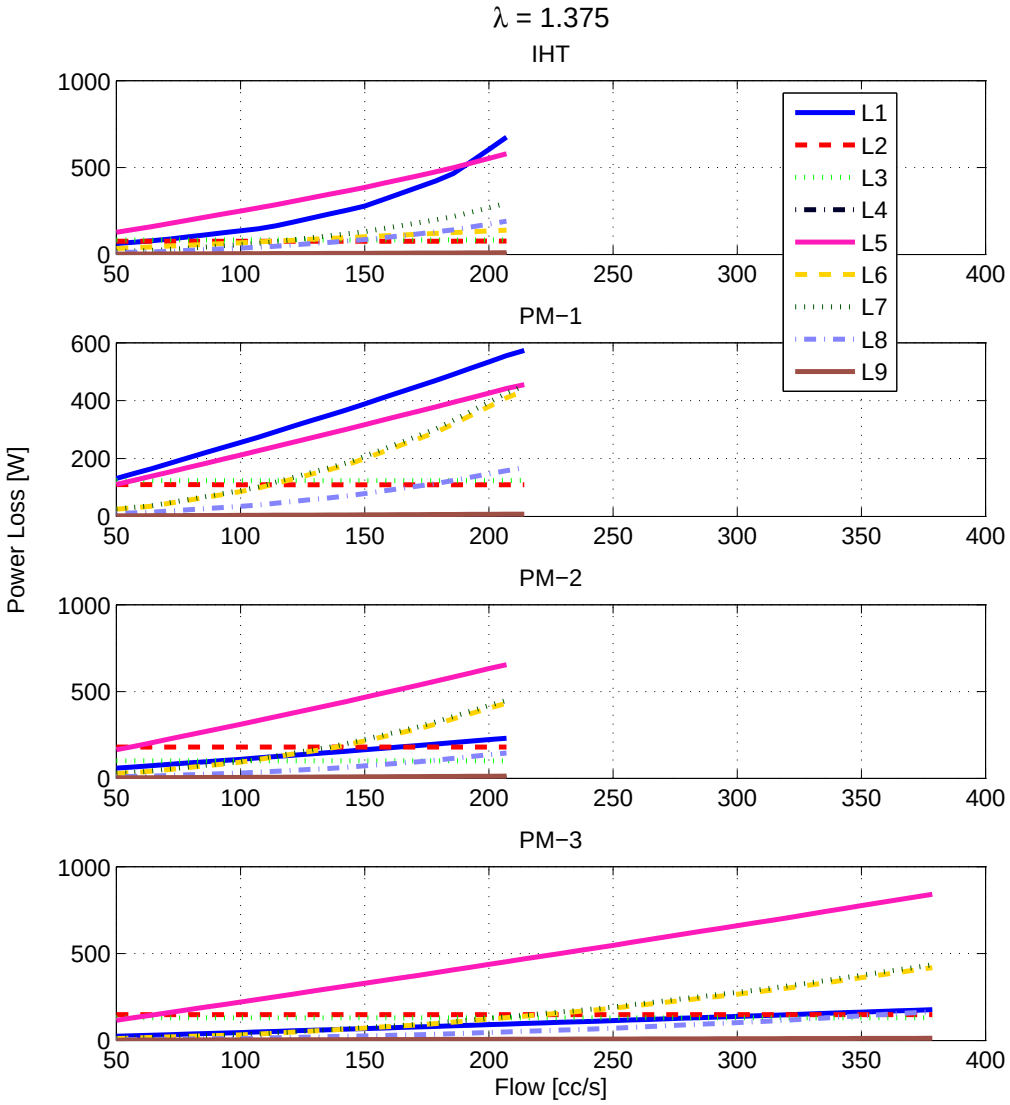

Figure 4.14: Loss trend for $\lambda = 1.375$ as the output flow varies showing losses within each transformer configurations. L1–L9 are the losses plotted in Fig. 4.13

Figure. 4.14 recasts the information shown in Fig. 4.13 to present the loss distribution within each configuration. No new observation is made beyond what was seen from Fig. 4.11. The piston friction loss dominates the power loss for all configurations. PM configurations has a large power loss coming from the piston shoe friction. PM-1 and IHT has a large throttling loss.

4.3.3 Constant output flow $Q = 330$ cc/s, varying pressure transformation ratio λ

Now we consider cases where the flow is held constant as the transformation ratio changes while the output flow is kept constant, starting with the case where flow is held at rather high at $Q = 330$ cc/s.

Efficiency and Operating Parameters

Figure 4.15-a shows the efficiency of transformer configurations as λ varies for the same output flow at 330 cc/s. PM-2 is the most efficient for $\lambda < 0.7$, and PM-3 is the most efficient for $\lambda > 0.7$. Figure 4.15-e shows the shaft speed for each of the transformer configurations. Unlike in Fig. 4.7-e and Fig. 4.12-e, the shaft speed is not linear with respect to the horizontal axis. The horizontal axis is now a pressure transformation ratio λ. For the most part, for IHT, PM-1, and PM-3, the shaft speed is held constant before it starts increasing as they approach the limit on their operating region. PM-2 shows a distinguishable trend for the shaft speed, with a concave down curve plotted with respect to varying λ. The shaft speeds are ordered by: PM-1 > PM-3 > IHT > PM-2 for $\lambda < 0.8$. For $\lambda > 0.8$ PM-2 surpasses PM-3 with the shaft speed.

Figure 4.15-b is the valve plate angle θ for the IHT. As it is expected with Fig. 2.5, increasing λ corresponds to increasing θ at the same output flow.

Figures 4.15-c and -d show the displacement ratio for D_1 and D_2 in PM transformers. While one of the displacement ratio is held at maximum, the other displacement ratio varies to realize the different transformation ratio λ. This behavior is as expected from Eq. (4.3). The PM-3, with its D_2 held at maximum for most of the λ, and the fact two units are used to draw a torque from the input pressure, allows it to have a wide operating region at high output flow.

Orifice Throttling Loss

Figure 4.16-L1 shows the orifice throttle loss for $Q = 330$ cc/s as the pressure ratio λ varies. IHT has the highest throttle loss for all λ being considered, followed by PM-1. For $\lambda < 0.75$, the PM-3 has higher throttle loss than PM-2, but for $\lambda > 0.75$ their position changes. The operating range for PM-2 does not extend much beyond the crossover point, but it can be inferred from extrapolating the trend that PM-2 would continue to have higher throttle loss than PM-3 as λ increases. The relationship between a throttling power loss and λ shows a strong quadratic relationship for an IHT, and weaker quadratic relationshup for PM-2, and PM-3. PM-1 one shows a linear relationship. In PM-1, the only change that

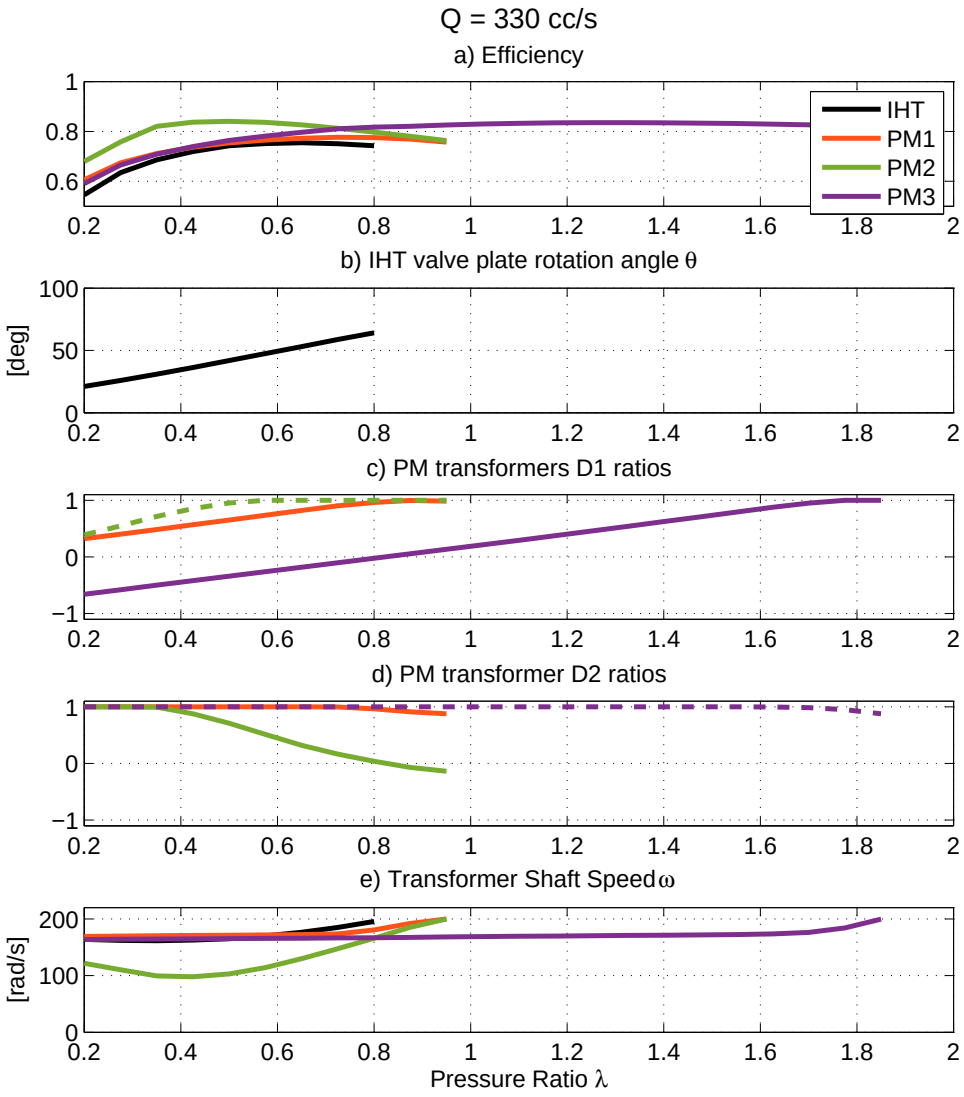

Figure 4.15: Loss trend for $Q = 330$ cc/s, showing overall efficiency, displacement ratio, and shaft speed as the pressure transformation ratio varies

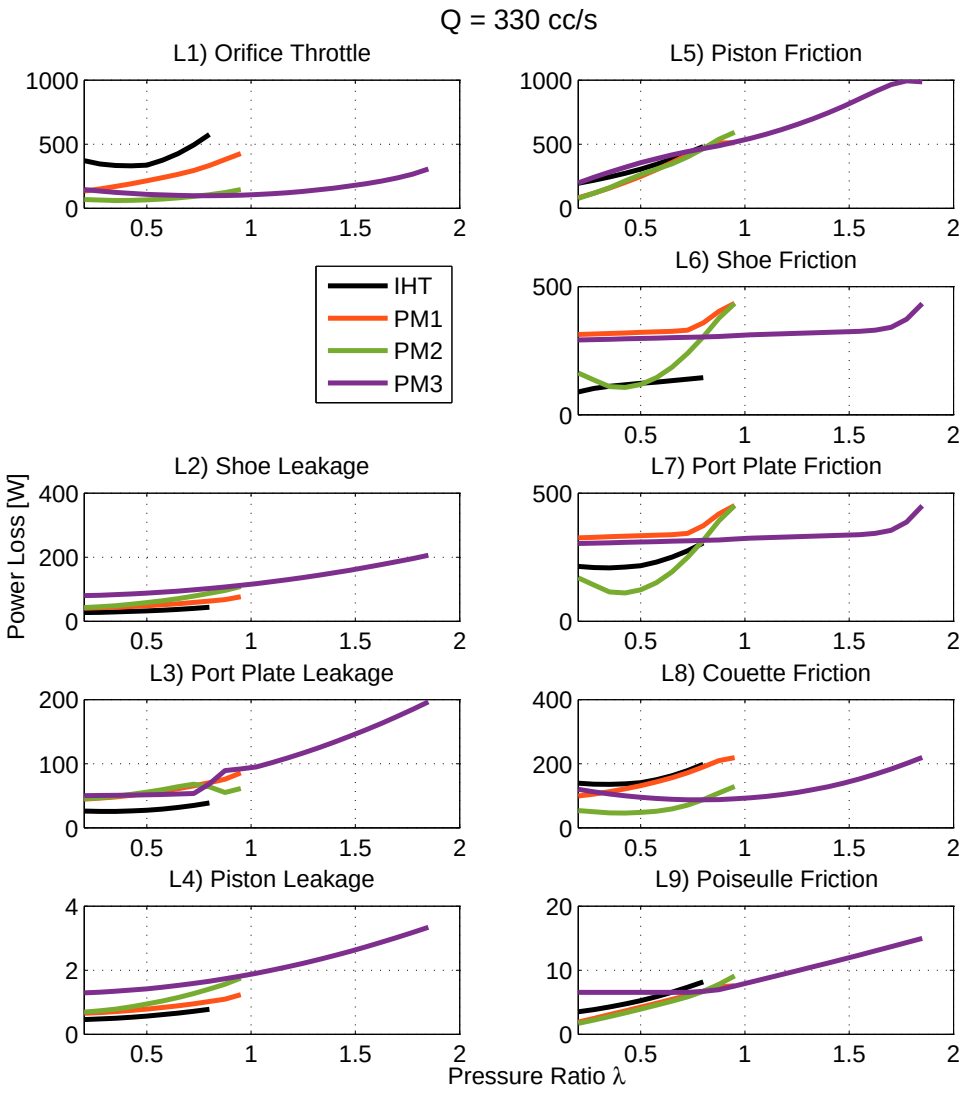

Figure 4.16: Loss trend for $Q = 330$ cc/s, showing port throttling loss, leakage losses, and friction losses as the pressure transformation ratio varies

occurs as λ increases is the pressure of outlet port in D_2 unit. As the pressure differential across D_2 gets larger, the pressure discrepancy between the piston chamber and the port that was described in Fig. 4.8-L1 also gets larger, attributing to the linearly increasing power loss with λ. The crossover between PM-2 and PM-3 is attributed the changing pressure conditions and magnitude of the pressure difference across the unit.

Leakage Losses

Figure 4.16-L2 through -L4 shows the power loss due to the flow leakage as λ changes for the same output flow. The power loss due to the shoe leakage and piston chamber leakage flows are shown on Fig. 4.16-L2 and Fig. 4.16-L4. As expected from Eq (2.44) and (2.42), these two losses depend on the magnitude of pressure acting on it, as well as the number of pistons pressurized. The linear relationship between the power loss and λ is attributed to the pressure dependency of these leakage flows. These two power losses are ordered PM-3 > PM-2 > PM-1 > IHT. PM-3 has the most number of pistons exposed to the high pressure, followed by PM-2 and PM-1. It can be seen that as output pressure increases, the PM-2 starts to have large power loss due to shoe and piston leakages. If PM-2 can operate beyond $\lambda = 1$, then it would surpass the PM-3 in power loss. The same reasoning as with Fig. 4.8-L3 explains the IHT showing the least amount of power loss. Even with 3 pistons pressurized at P_A and another 3 pistons pressurized at P_B, the piston chamber geometry for PM was scaled such that PM transformers will have larger piston diameter. As shoe and piston chamber leakage has a dependency on the diameter of the piston, IHT with a smaller diameter benefits from this geometry.

Figure 4.16-L3 shows the power loss from a port plate leakage. Its ordering is PM-2 > PM-1 > PM-3 > IHT for $\lambda < 0.78$ and PM-2 and PM-3 crosses each other at $\lambda = 0.78$ to swap their positions on the plot. The change over is because a PM-2 starts out as D_1 unit motoring but transitions to pumping after $P_B > P_A$. In the meantime, D_2 starts out pumping, but transitions to motoring as D_2 crosses zero as seen in Fig. 4.15-d. PM-3 undergoes similar transition with its units. D_1 starts out pumping, with $D_1 < 0$ and switches to motoring; D_2 starts motoring and transitions to pumping after $P_B > P_A$. This transition causes the PM-2 and PM-3 to cross each other. It was noted in Fig. 4.8-L3 how pumping and motoring affects the clearance parameter that enters into Eq (2.48) that models this leakage.

Friction Losses

Figure 4.16-L5 through -L9 are the power losses due to the friction losses for holding transformer output flow constant at $Q = 330$ cc/s as λ increases. As with the previous cases in Sec 4.3.1 and 4.3.2, the power loss due to friction shows a heavy dependency on the shaft speed of the transformers, whose ordering is: PM-1 > PM-3 > IHT > PM-2, with PM-2 showing a distinct concave down curve with λ.

Figure 4.16-L5 presents the power loss due to the contact friction inside the piston chamber that was modeled in Section 2.4.1. It shows a liner relationship with λ and goes PM-3 > IHT > PM-2 $\geq$ PM-1 for $\lambda < 0.8$. IHT cannot operate for $\lambda > 0.8$, and PM-2 shows the largest loss for $\lambda > 0.8$. The piston friction is explained by the combination of shaft speed and number of pistons pressurized. As λ increases, PM-2 with output shared port connection will have more pistons exposed to higher pressure and thus surpasses PM-3 in power loss. It is worthwhile to note that PM-2 operates at significantly lower speed than other configurations when $\lambda < 0.8$, which is one contributing factor to PM-2 being very efficient in bucking pressure.

Figure 4.16-L6 and -L7 show the power loss from a piston shoe friction. Both losses depend on ω^2 as with previous sections, so the ordering follows what was observed with Fig. 4.15-e. The difference in the magnitude of IHT between Fig. 4.16-L6 and Fig. 4.16-L7 is due to the difference in the ratio between the coefficient of friction for a PM transformer and IHT for these two losses. An IHT has much larger coefficeint of friction than PM for the port plate friction, whereas an IHT has much smaller coefficient for the piston shoe friction, masking the square relationship with ω. This was discussed in Sections 4.3.1 and 4.3.2.

Couette friction, shown in Fig. 4.16-L8, depends on the displacement ratio and piston velocity, and is the highest for IHT because an IHT has its swashplate always at maximum. PM-1 is has equally large power loss because one of the units is held at maximum swashplate angle while other unit approaches the maximum angle as λ increases. PM-3 and -2 have smaller displacement ratios than the other two and thus show smaller power losses.

Finally, the power loss due to Poiseuille friction losses are plotted in Fig. 4.16-L9. It depends on the total surface area of pistons being pressurized. PM-3 starts with higher losses because of the shared port in P_A, but as λ increases, PM-2 surpasses PM-3 as more the total surface area becomes bigger and bigger.

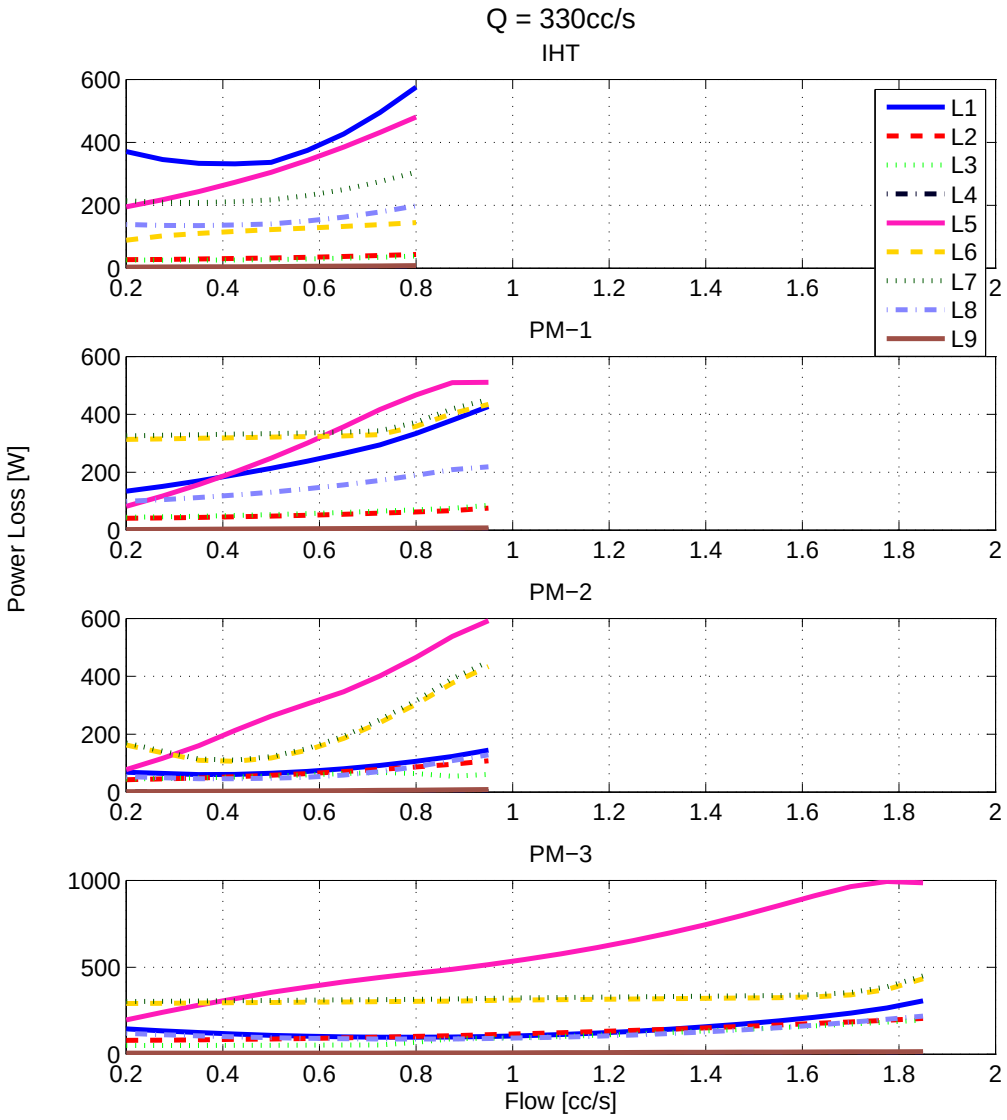

Figure 4.17: Loss trend for $Q = 330$ cc/s as the pressure transformation ratio varies showing losses within each transformer configurations. L1–L9 are the losses plotted in Fig. 4.16

Loss Distribution within the Configuration

Figure 4.17 shows the power loss presented in Fig. 4.16 grouped by the transformer configuration. The loss distribution within the configuration is the same as it was observed in Fig. 4.11 and 4.14.

4.3.4 Constant output flow $Q = 100$ cc/s, varying pressure transformation ratio λ

Efficiency and Operating Parameters

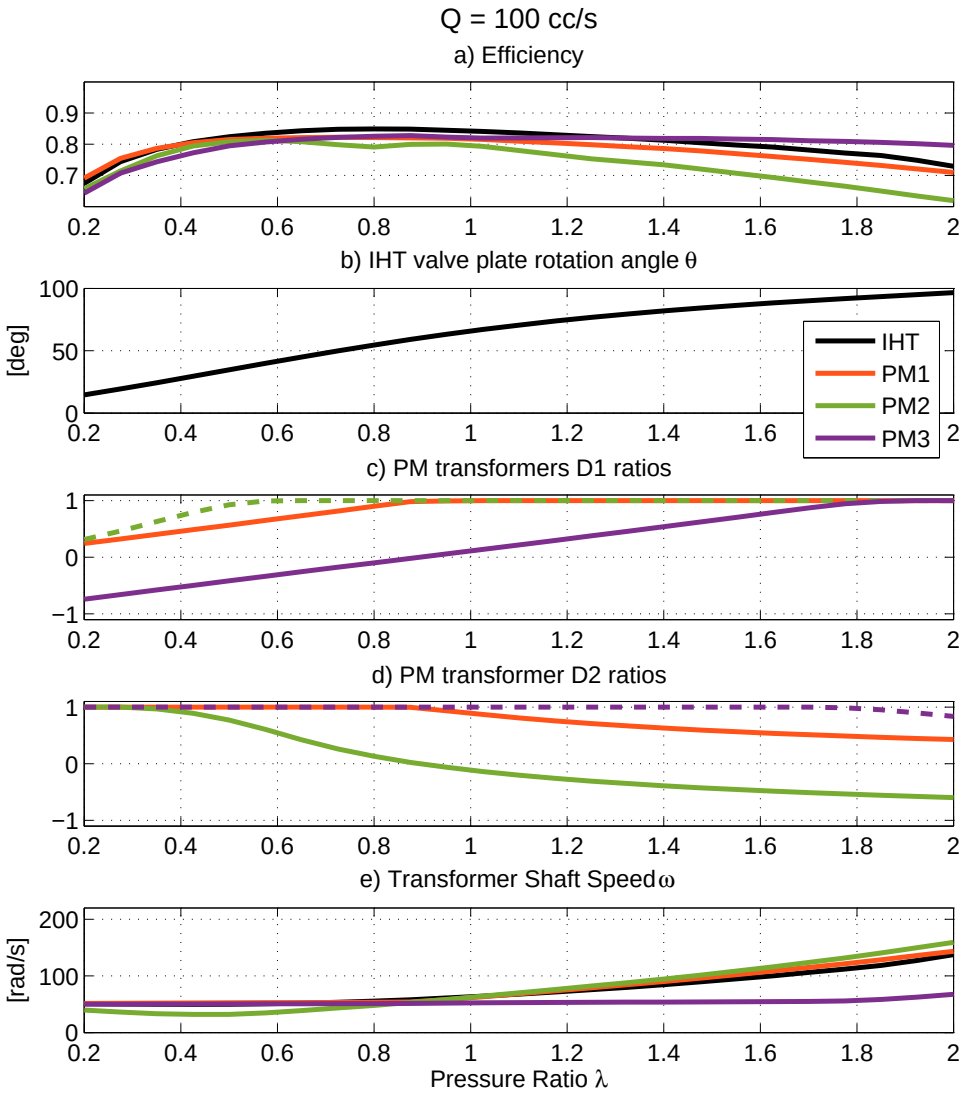

Figure 4.18: Loss trend for $Q = 100$ cc/s, showing overall efficiency, displacement ratio, and shaft speed as the pressure transformation ratio varies

Figure 4.18-a shows the efficiency of transformer configurations as λ varies while holding the output flow at 100 cc/s. PM-1 is the most efficient for $\lambda < 0.4$. IHT is the most efficient for $0.4 < \lambda < 1.3$, and PM-3 is the most efficient for $\lambda > 1.4$. With a low output

flow, all transformers can operate up to $\lambda = 2$. The shaft speeds plotted in Fig. 4.18-e shows that none of the transformer configurations has reached the maximum shaft speed of 200 rad/s at $\lambda = 2$. The shaft speed is ordered as PM-1 > PM-3 > IHT > PM-2 for $\lambda < 0.8$, and

PM-2 is the most efficient for $\lambda < 0.7$, and PM-3 is the most efficient for $\lambda > 0.7$. Figure 4.18-e shows the shaft speed for each of the transformer configurations. Unlike in Fig. 4.7-e and Fig. 4.12-e, the shaft speed is not linear with respect to the horizontal axis. The horizontal axis is now a pressure transformation ratio λ. For the most part, for IHT, PM-1, and PM-3, the shaft speed is held constant before it starts increasing as they approach the limit on their operating region. PM-2 shows a distinguishable trend for the shaft speed, with a concave down curve plotted with respect to varying λ. The shaft speeds are ordered by: PM-1 > PM-3 > IHT > PM-2 for $\lambda < 0.85$. For $\lambda > 0.85$, it is PM-2 > PM-1 > IHT > PM-3. PM-3 has a constant shaft speed for $\lambda < 1.8$, beyond that point, shaft speed starts increasing, but it is still much lower than any other configurations.

Figure 4.18-b is the valve plate angle θ for the IHT, showing that increasing λ corresponds to increasing θ in the same manner as in Fig. 4.15-b.

Figures 4.18-c and -d show the displacement ratio for D_1 and D_2 in PM transformers. While one of the displacement ratio is held at maximum, the other displacement ratio varies to realize the different transformation ratio λ. This is the same observation as in Figs 4.15-c and -d. For PM-1, D_1 is held at maximum until $\lambda \leq 0.9$, and D_2 is held at maximum when $\lambda > 0.9$. PM-2 has D_2 unit going over center, whereas PM-3 has D_1 unit going over center.

Orifice Throttling Loss

Figure 4.19-L1 shows the power loss due to the orifice throttling at piston chamber exit. No new trend is observed beyond what has been already established in Sections 4.3.1–4.3.4, except that PM-2 start to have a large throttling loss as λ increases. The D_2 unit in PM-2 configuration has one port connected to $P_T = 0$ and the other port connected to P_B that increases as λ increases. As discussed with Fig. 4.8-L1, this results in larger and larger pressure discrepancy between the piston chamber and the output port during the valve plate transition and result in large throttling loss. Likewise, a PM-1 shows high loss due to high pressure differential at piston exit when $\lambda > 1$. Moreover D_2 unit has a swashplate not at maximum, which causes the effective dead volume to increase, which in return, causes higher throttling loss that is even larger than that of IHT.

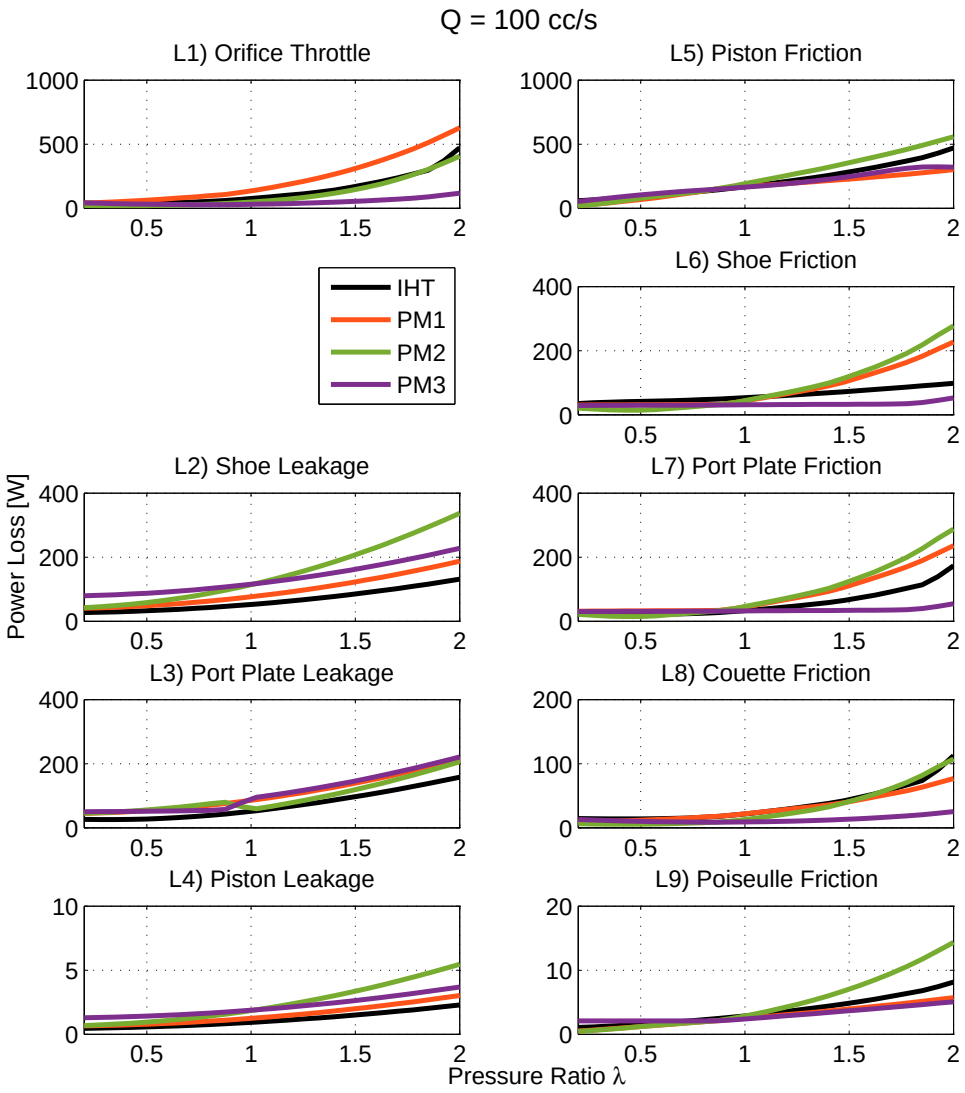

Figure 4.19: Loss trend for $Q = 100$ cc/s, showing port throttling loss, leakage losses, and friction losses as the pressure transformation ratio varies

Leakage Losses

Figure 4.19-L2 through -L4 present the power loss due to leakage flows. No new observation is made except that now, all transformer can operate up to $\lambda = 2$.

The power loss due to the shoe leakage and piston chamber leakage flows are shown on Fig. 4.19-L2 and Fig. 4.19-L4. Up until $\lambda = 1$, PM-3 has the highest loss, followed by PM-2, PM-1, and IHT respectively. In Fig. 4.16-L2 and Fig. 4.16-L4, it was suggested that PM-2 surpass PM-3 in these power losses if PM-2 can operate for the wider range of λ. For $\lambda > 1$, PM-2 does show the highest power loss. This is due to the change in pressure conditions at the ports. At $\lambda = 1$, PM-2 and PM-3 will have same number of pistons pressurized at the same pressure level. For $\lambda < 1$, PM-3 has more number of pistons pressurized at higher pressure, and for $\lambda > 1$, PM-2 has more number of pistons pressurized at higher pressure.

The port plate leakage follows the same trends as with Fig. 4.16-L3. PM-2 starts out as D_1 unit motoring but transitions to pumping after $P_B > P_A$. At the same time, D_2 starts out pumping, but transitions to motoring as D_2 crosses zero as seen in Fig. 4.18-d. PM-3 undergoes similar transition with its units. D_1 starts out pumping, with $D_1 < 0$ and switches to motoring; D_2 starts motoring and transitions to pumping after $P_B > P_A$. This transition causes the PM-2 and PM-3 to cross each other. In all cases considered thus far, IHT does show an advantage in leakage losses.

Friction Losses

Figure 4.19-L5 through -L9 show the friction related losses. No new observation is made beyond those already made in previous sections, especially in Figs 4.16-L5 through -L9. PM-2 shows the highest piston chamber friction losses and Poiseuille friction losses at higher λ as more pistons are being pressurized. Shoe friction and port plate friction shows the square relationship with respect to shaft speed ω. Couette friction is high for the unit with higher swashplate angle and faster shaft speed.

Loss Distribution within the Configuration

Figure 4.20 shows the power loss presented in Fig. 4.19 grouped by the transformer configuration. With a small output flow, we observe that PM-2 and PM-3 suffer large power loss from the piston shoe leakage (Fig. 4.19-L2. We also see as in Fig. 4.19-L1 that the throttling loss becomes a major loss item in a PM-2 configuration as output port pressure increases. The rest of the the loss distribution within each configuration is the same as it was observed in Fig. 4.11, 4.14 and 4.17.

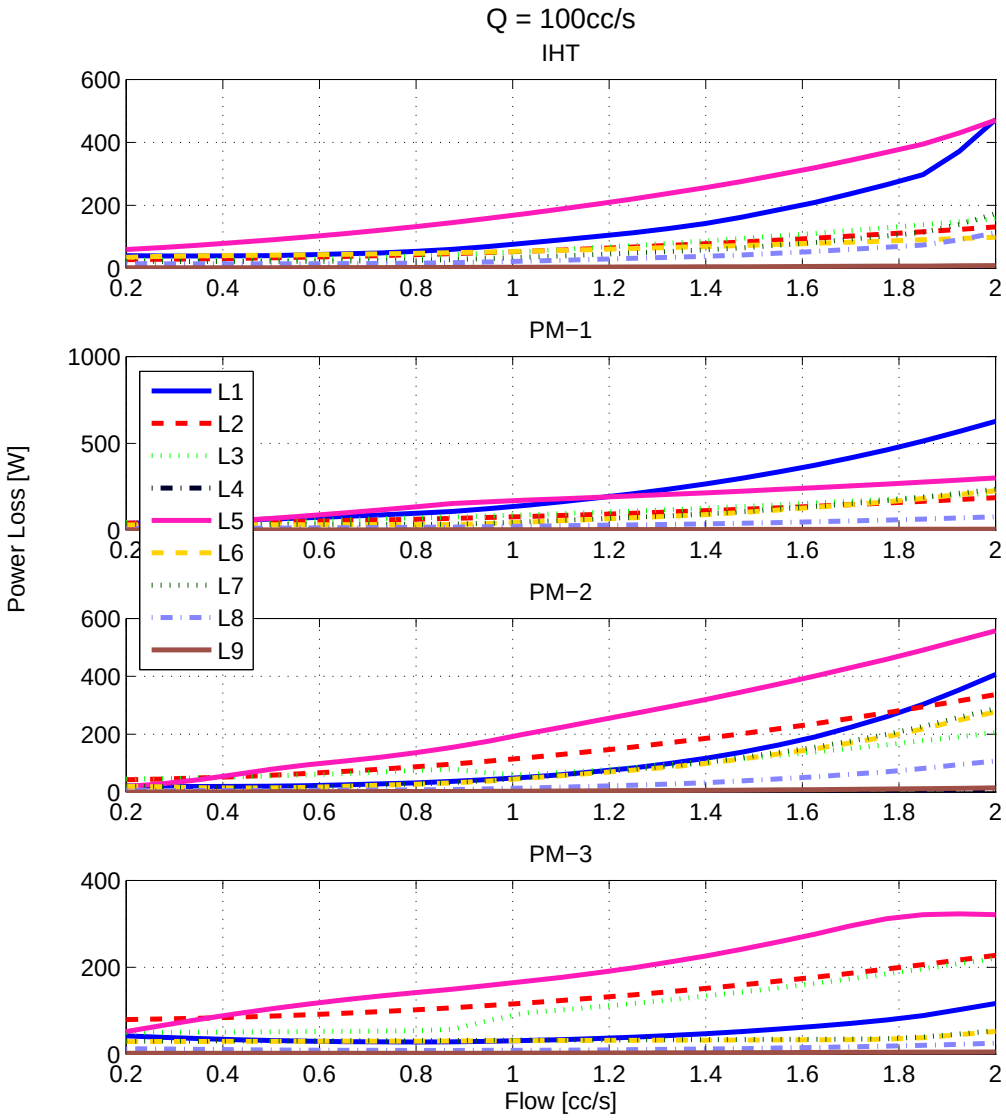

Figure 4.20: Loss trend for $Q = 100$ cc/s as the pressure transformation ratio varies showing losses within each transformer configurations. L1–L9 are the losses plotted in Fig. 4.19

4.4 Configuration Mode Switching Idea for Efficiency

The idea of allowing the PM transformer configuration to switch proposed in Section 3.1.3 will also have benefits to efficiency. If the transformer is allowed to switch among the modes to pick the regions with the best efficiency, then the resulting transformer will be more efficient. One such example is shown in the top subplot of Fig. 4.21, which was created by simply picking the configuration with the highest efficiency at each operating point from Figs. 4.2–4.4. The resulting figure not only has a wide region with high efficiency operation but also has wider operable region. For example, utilizing PM-2 allows the transformer to operate at higher flow rate when λ is low. On the other hand, utilizing PM-3 allows the transformer to operate at higher flow rate when λ is high. The bottom subplot in Fig. 4.21 shows which mode is utilized to arrive at the combined contour. Compared with an IHT in Fig. 4.5, this combined efficiency contour has much wider region with high efficiency, and wider operating region.

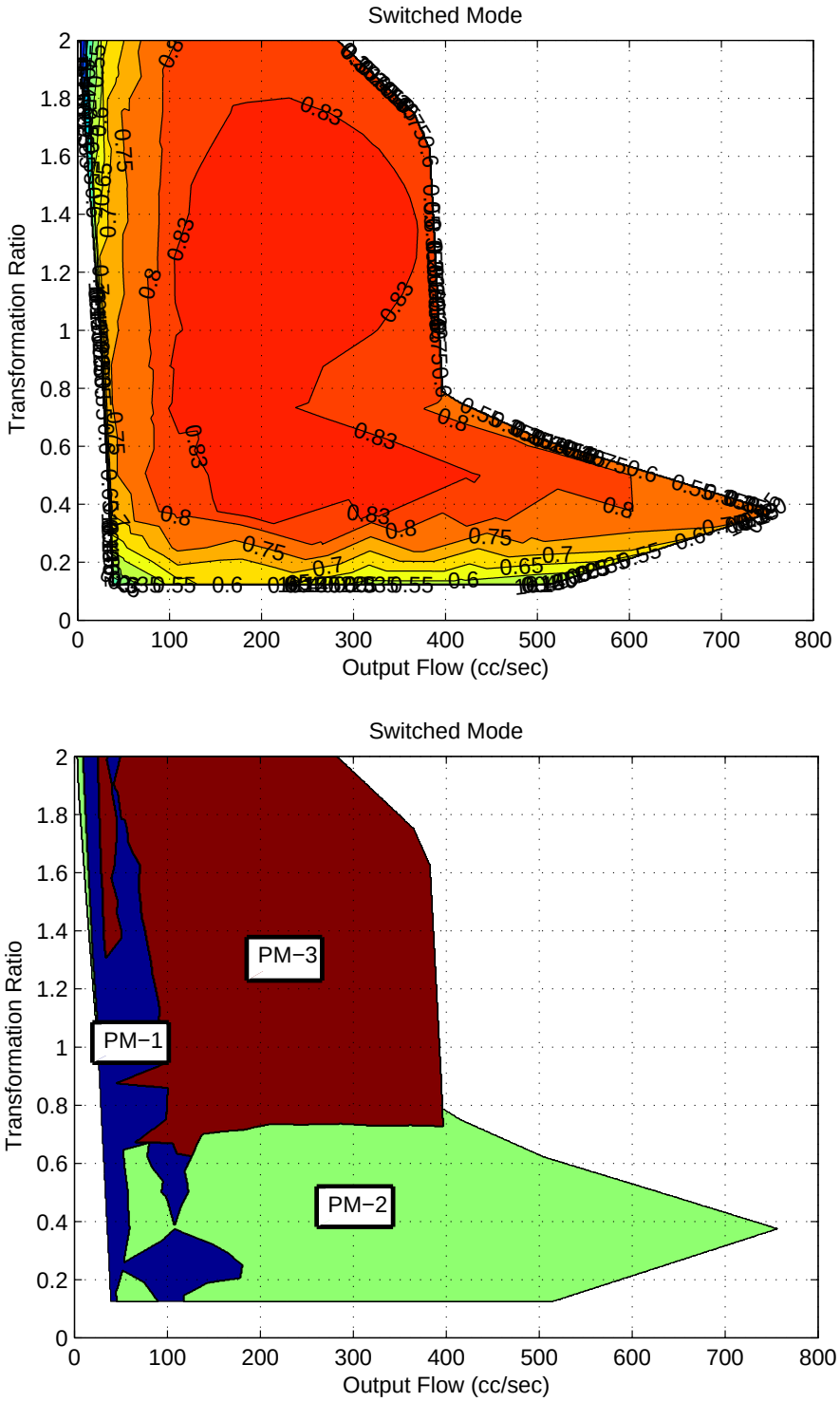

Figure 4.21: Top: Potential Efficiency Contour if mode switching is allowed to select the most efficient configuration; Bottom: Mode selection corresponding to the efficiency contour

4.5 Chapter Summary

In this chapter, the efficiency comparison was made between PM transformers and IHT. Utilizing the models developed in Chapter 2, the efficiency contours for three PM configurations and IHT were generated. PM transformer was sized according to the sizing method presented in Sections 3.1. The similarities in peak efficiencies were observed, and the differences in the operating region were noted.

Utilizing the subcomponent loss models, the differences in loss distribution were observed for 4 different sets of operating lines, either holding the pressure ratio λ constant while varying the output flow or holding the output flow constant while varying the pressure ratio λ. An IHT has a significant throttling loss coming from its rotatable valve plate design. PM transformers have a large piston shoe friction losses coming from their large piston diameters. The loss for PM-1 is dominated by the throttling loss, whereas for PM-2 and PM-3, the loss is dominated by the piston chamber friction.

For PM transformer, allowing the configuration mode switch can allow PM transformer to be more efficient and have wider operating region. In Chapter 3, the same idea is proposed to make a more compact transformer. Configuration mode switching can potentially bring more compact and efficient PM transformer. In the next chapter, the prototype developed as a result of analyses performed in this chapter and Chapter 3 will be presented.

Chapter 5

Prototype Switched Mode Transformer

From the analysis in Chapter 3 and 4, it was determined that the research potential exists with a PM transformer, especially if the basic configurations in Fig. 2.3 can be switched in real time operation to benefit both sizing and efficiency. Compared with an IHT, PM transformer has better flow ripple characteristics, and using the same axial piston design, the efficiency is comparable to that of an IHT. The mode switching allows the PM transformer to operate in its most efficient region, and where it can provide the maximum flow. Thus, a switched mode PM transformer was chosen as the transformer design to be implemented for this dissertation.

This chapter is organized as follows. In Section 5.1, the prototype transformer is presented. Methods to realize the idea of switching among different configurations is documented in Section 5.3. The testbench is presented in Section 5.4. Lastly in Section 5.5, an experimental efficiency data is obtained from this prototype and compared against the model developed in Chapter 2.

5.1 Prototype Hydraulic Transformer

The prototype transformer consists of two rotating groups, each having a displacement of 3.15 cc/rev. Figure 5.1 shows the CAD modeling of the prototype. The barrels are on common shaft, which is contained within the transformer. Two rotating groups are facing away from each other with their swashplates located towards the middle of the unit. This in turn places the port connections to be located towards each ends of the transformer. Each rotating group has 7 pistons, and the swashplate angles are variable and can go-over

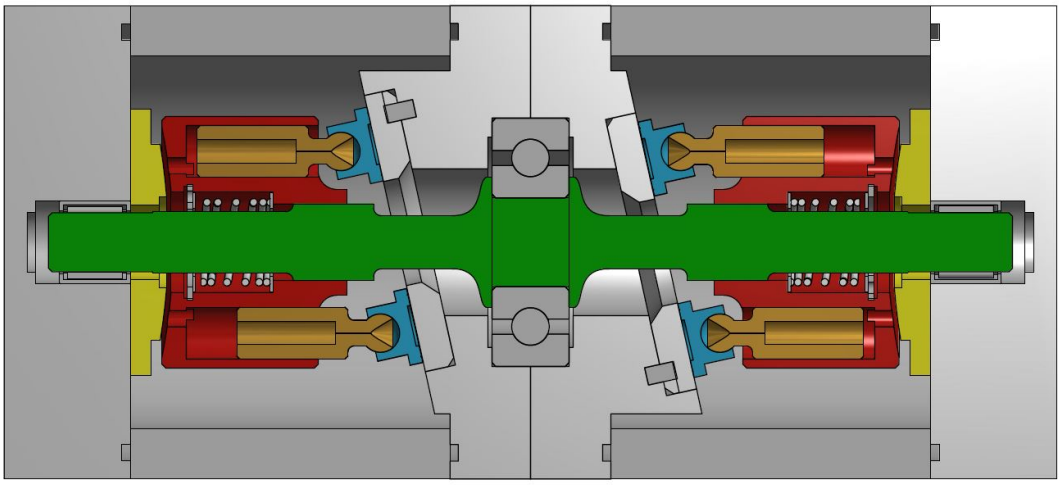

Figure 5.1: CAD model of the prototype hydraulic transformer, swashplate actuation mechanisms are not depicted in this model

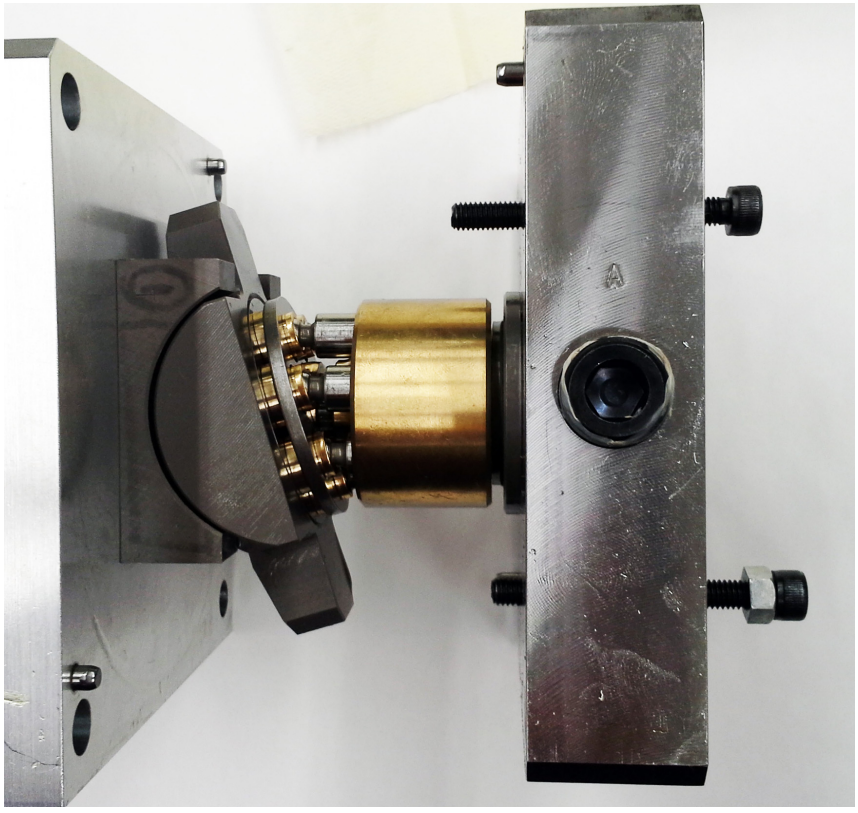

Figure 5.2: Actual prototype disassembled to show the swashplate, piston barrel, valve plate, the port block, and two manual adjustment screws that were replaced by a stepper motor and hydraulic piston

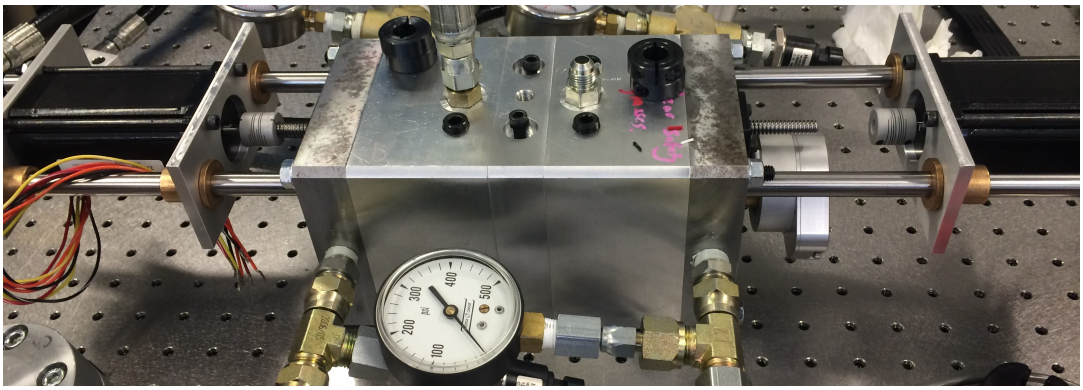

Figure 5.3: Actual prototype assembly

center to achieve the displacement ratios between -1 and 1. Note the CAD model does not depict the mechanisms for the swashplate variation. The base unit, as donated by Takako industries had manual displacement adjustments through screw adjustments as shown in Fig. 5.2.

To allow computer control of the displacement ratios, one of these manual screws were replaced with screw bearings driven by stepper motors (Anaheim Automation 23L Series) rated at 5A with 48V supply as shown in Fig. 5.4. These motors in turn are driven by micro-step driver (Anaheim Automation MBC05641) and communicate with the experiment station through a DAQ board (Humusoft MF634). The other of these manual screws were replaced with hydraulic pistons triggered by solenoid switches. When the stepper motor is advancing towards the swashplate, the piston is turned off. When the stepper motor is retracting back, the piston is turned on to push the swashplate back. This balancing act between the stepper motor and hydraulic piston allows the full automatic control of the swashplate actuation. Figure 5.3 is a picture of the actual prototype assembly. An optical encoder (US Digital), also shown in the picture, is added to allow the measurement of the transformer shaft speed.

5.2 Swashplate Actuation

An inner loop controller is designed to allow displacement ratios to be specified as the control inputs, which will be presented in Ch 6 and 7. The stepper motors have a limit on the acceleration. While the stepper motor is capable of providing a fast shaft speed rotation, it will stall if the acceleration is too high, for both an open-loop and closed-loop command. The inner loop controller is designed such that it limits the rate of the acceleration while providing the velocity command to the stepper motor to track the

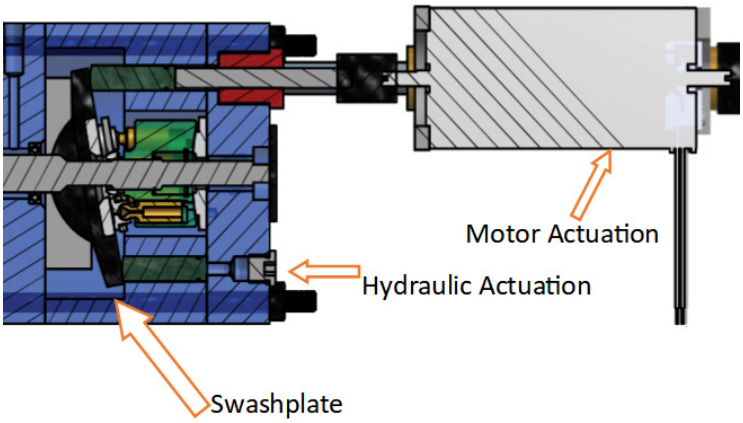

Figure 5.4: CAD drawing illustrating the stepper motor and hydraulic piston utilized for the automatic control of the swashplate

control inputs to the transformer.

Figure. 5.5 shows the block diagram of this control approach. A first order filter is used to smooth any sharp change in the desired displacement that may cause the stepper motors to be stalled:

$$G_f(s) = \frac{1}{\tau s + 1} \tag{5.1}$$

where τ is a time-constant for this first order filter that ranges between 0.02 to 0.04 in experiments. After passing the desired displacement command through this first order filter, an error in providing desired displacement input for the transformer is calculated and fed into a controller a proportional controller $C(s) = K_p$. The generated signal is a velocity command, which goes through another feedback loop, that takes an error between desired velocity command and the actual velocity command sent to the stepper motor. The velocity error goes through another proportional controller $C_{in}(s) = K_a$, whose output is an acceleration command that is limited with a saturation function, then is integrated to provide a velocity command to the stepper motor, modeled as $G(s)$.

$$G(s) = \frac{1}{s} \tag{5.2}$$

The limitation with the stepper motor acceleration turned out to be the single most limiting factor in swashplate actuation bandwidth.

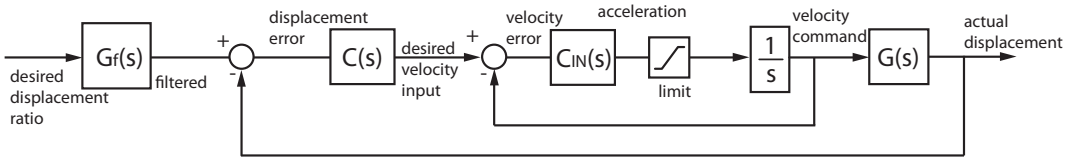

Figure 5.5: Inner loop control translating desired displacement to actual displacement with additional first order filter

5.3 Switched Mode Transformer

As pointed out in Chapters 3 and 4, allowing the PM transformer to switch among the 3 configurations are beneficial for sizing and efficiency of the transformer.

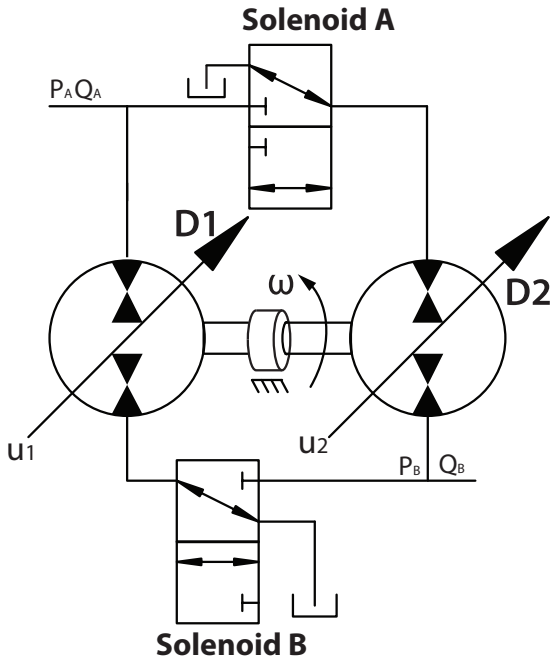

Figure 5.6: Hydraulic schematic for mode switching transformer with its solenoid valves

In order to realize such switching mechanism, two 3-way solenoid-operated directional spool valves (Sun Hydraulics DMDA-MBN) are placed at both sides of the transformer in Fig. 5.6. Using these two valves enables this prototype transformer to be become one of the three configurations without having to physically re-plumb the port connections. At the default position where none of the solenoid valves are triggered, the transformer is configured in PM-1 configuration, with the shared line connected to the return line. If solenoid B is triggered, the transformer becomes PM-2 configurations, with the shared output port. Lastly, if solenoid A is triggered, the transformer is in PM-3 configuration

with the input port shared between two units. This is summarized in Table. 5.1. If both A and B are triggered, then the transformer becomes a set of two motors whose shafts are connected to each other.

Table 5.1: Solenoid valve commands necessary to realize different PM configurations

	Solenoid A	Solenoid B
PM-1	OFF	OFF
PM-2	OFF	ON
PM-3	ON	OFF

A preliminary experiment was performed to demonstrate the switching ability of the transformer. In the experiment the transformer was connected to a needle valve set to a fixed orifice area, with an input pressure of 500 psi (3.5 MPa). Swashplates on both units are held constant at the maximum, while Solenoid valves A and B are triggered respectively to change the transformer configuration among PM-1, PM-2, and PM-3. Eqs. (2.18)–(2.21) describes the pressure transformation ratio λ with respect to the displacement D_1 and D_2 of lossless transformer, which is reproduced here for reading convenience:

$$\lambda = \begin{cases} \frac{D_1}{D_2} & \text{for PM-1} \\ \frac{D_1}{D_1+D_2} & \text{for PM-2} \\ \frac{D_1+D_2}{D_2} & \text{for PM-3} \end{cases} \tag{5.3}$$

Above equations indicate that for the lossless transformer, operating the transformer in PM-3 results in λ approaching 2, while PM-2 results in λ approaching 0.5. In case of PM-1, λ approaches 1. If the transformer switches its configuration mode as expected, then the output pressure will change following Eq (5.3).

Figure 5.7 shows the result from the preliminary experiment. As the mode was switched among PM-1, PM-2, and PM-3 repeatedly, it can be seen that output pressure changes according to Eq. (5.3). The deviations from the expected λ come from the losses in the transformer. Algorithms to automate this switching to maximize the operating efficiency will be discussed in Chapter 8.

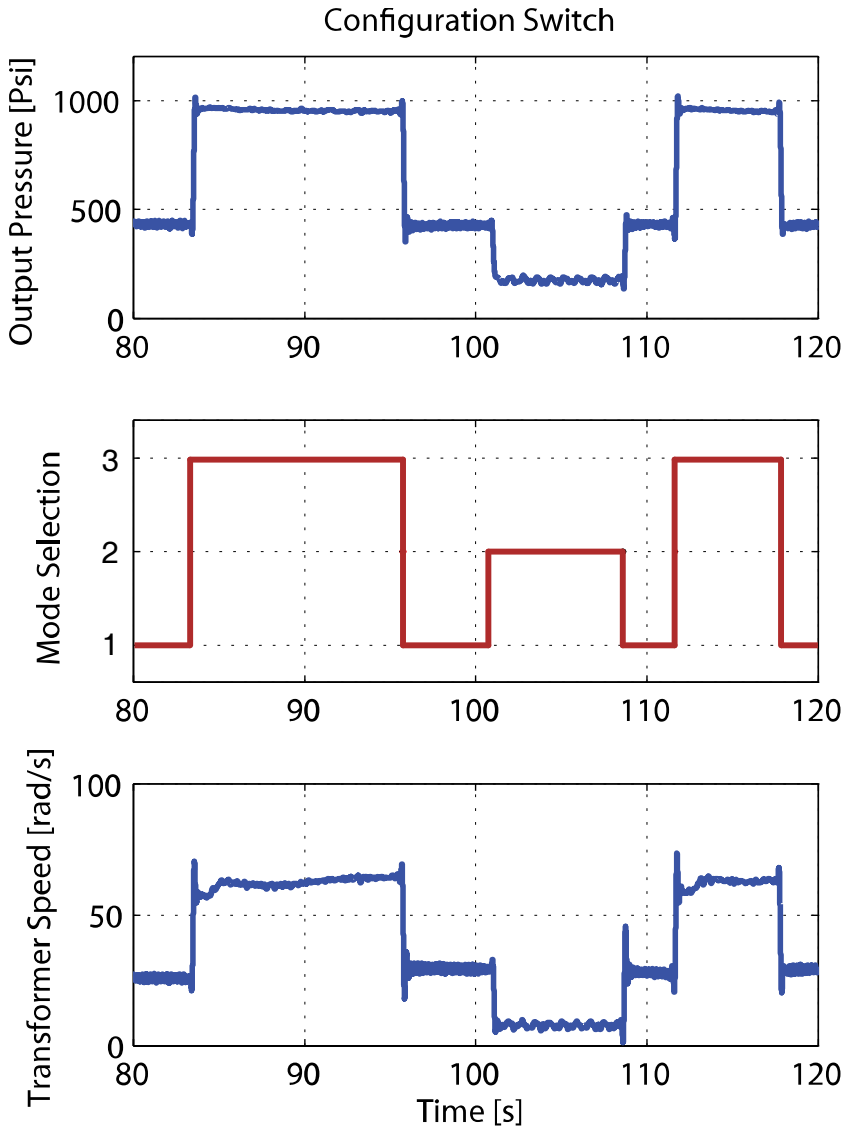

Figure 5.7: Open loop mode switching with both displacements held at max, Top: Output pressure of the transformer; Middle: a configuration mode command sent to the transformer Bottom: transformer shaft speed

5.4 Testbench

With the prototype hydraulic transformer, a testbench was developed such that the transformer can be connected to a various hydraulic actuators for the controller developments that will be presented in Chapters 6– 8.

Figure 5.8 is the picture of the testbench, and Fig. 5.9 shows the hydraulic schematic. In the testbench, there are solenoid valves denoted 'A' and 'B' that are used for the switched mode transformer as discussed in Section 5.3. A valve 'C' is placed to serve as a directional valve for the actuator to be connected, and a valve 'D' is placed such that one end of the actuator can be connected to the common pressure rail directly if desired. Valves 'C' and 'D' were not utilized in the controller developments in this dissertation.

Various pressure and flow measurements are available. Two flow sensors (AW Gear Meters JV30KG) measure the flow to port A of the transformer Q_A, and the flow coming out of the transformer Q_B. Pressure measurements are available for P_A, P_B, and P_T of the transformer (Honeywell MLH03KPS01A or MLH500PSB01A). Note that if the valve 'D' is utilized, then the P_T measurement will show the CPR pressure.

Quick connect couplings are placed on the downstream of the transformer such that various load types can be quickly swapped. This testbench can be connected to a needle valve, a hydraulic motor, or a hydraulic cylinder.

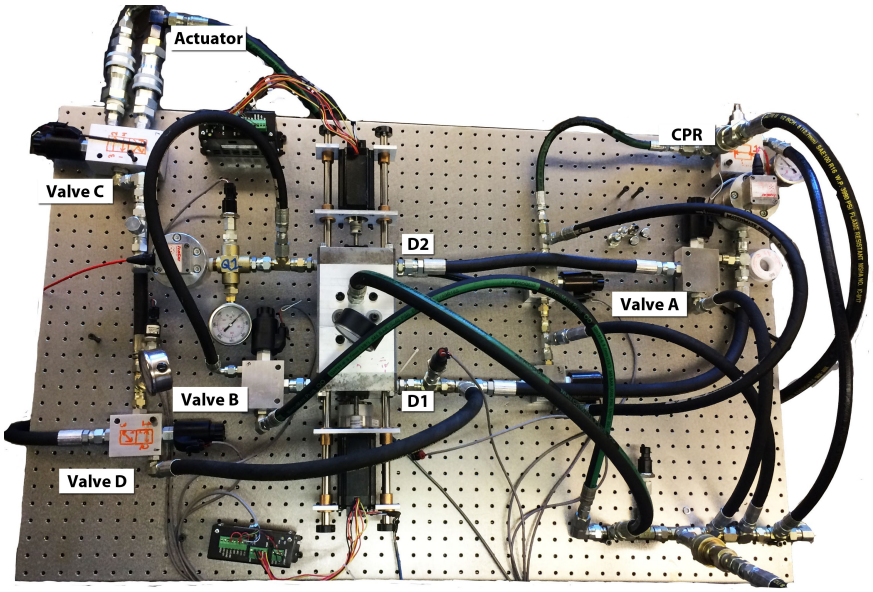

Figure 5.8: Top view picture of the prototype hydraulic transformer testbench

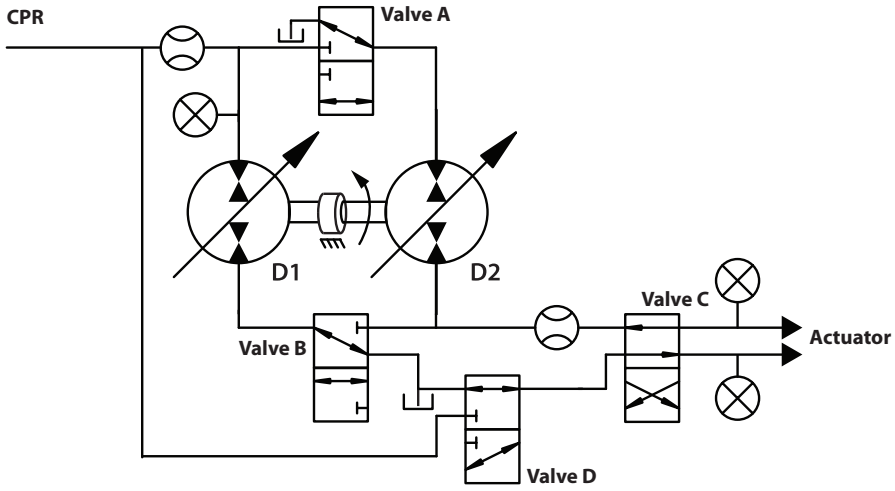

Figure 5.9: Hydraulic Schematic for the testbench

5.5 Prototype Operating Characteristics

This section will present the measured operating characteristics of the prototype transformer, compared with the simulation using the model built in Chapter 2.

In the experiment, one of the two displacements was held at maximum, while the other was varied by ratio increment of 0.2. For a given set of displacements, the needle valve was adjusted to obtain the steady state operating data point to space the shaft speed by increment of approximately 20 radian per second, with maximum speed at 200 radian per second, which is the rated maximum operating speed given by the manufacturer of this prototype transformer. Due to the limitations of the needle valve, there were some data points that could not be obtained even though transformer is capable operating at that region (ie. maximum needle valve opening is too small or too big to obtain a data point). The data points were taken for steady-state operating conditions to determine input power and output power.

Input power is given as by the hydraulic power at port A that derives the cylinder and the output power is given by the hydraulic power at port B which goes to the attached needle valve.

$$\begin{aligned} W_{in} &= -(P_A - P_T)Q_A \\ W_{out} &= (P_B - P_T)Q_B \end{aligned} \tag{5.4}$$

To ensure that the prototype operates as anticipated by the dynamic loss models developed in Chapter 2, a simulation was performed to be compared with the experiment. In the simulation, the experimental conditions were imposed to obtain the data points for

the same operating points at the steady state to obtain simulated input power and output power.

5.5.1 Efficiency

The efficiency is the ratio of power input and output of the transformer given by:

$$\eta = \frac{W_{out}}{W_{in}} \tag{5.5}$$

Left-hand side plots in Figure 5.10 shows an experimental efficiency contours obtained from the prototype transformer attached to an adjustable needle valve and supply pressure of 1000 psi.

It could be seen that PM-1,-2,-3 all have different operating regions where they achieve the highest efficiency. This trend is in accordance with the efficiency results obtained by using the model from Chapter 4. However, because of the small geometry of this prototype, a mechanical loss is quite large, contributing to the peak efficiency only reaching to about 70%. Roughly speaking, this means that each unit in the transformer by itself reaches only about 84% efficiency for PM-1. However, as it will be shown in Chapter 9, this transformer is still able to show a significant efficiency improvement over using a throttling valve. Although it could have brought in even more efficiency improvement if the prototype was more efficient.

Right-hand side plots in Figure 5.10 is the efficiency contours obtained from simulating the prototype transformer for the same testing conditions used to generate contours in Fig. 5.10. Because the needle valve in simulation does not have a physical limitation in delivering the appropriate opening area to obtain steady state operating points, the simulated contours fill more area than experimental contours. The trend shown by simulation matches well with what is observed with the experiments.

Figure. 5.11 compares the experimental efficiency and simulated efficiency for each of the data point that corresponds to a specific load flow and pressure transformation ratio. Across all the data points being considered, the RMS of the difference in efficiencies is only 4%, showing a good match between the experiments and simulations.

Figure 5.12 shows the combined efficiency map from picking the best mode among three configurations. The resulting efficiency map has a wider region showing the peak efficiency. An algorithm to take advantage of this switched mode will be explored in Chapter 8

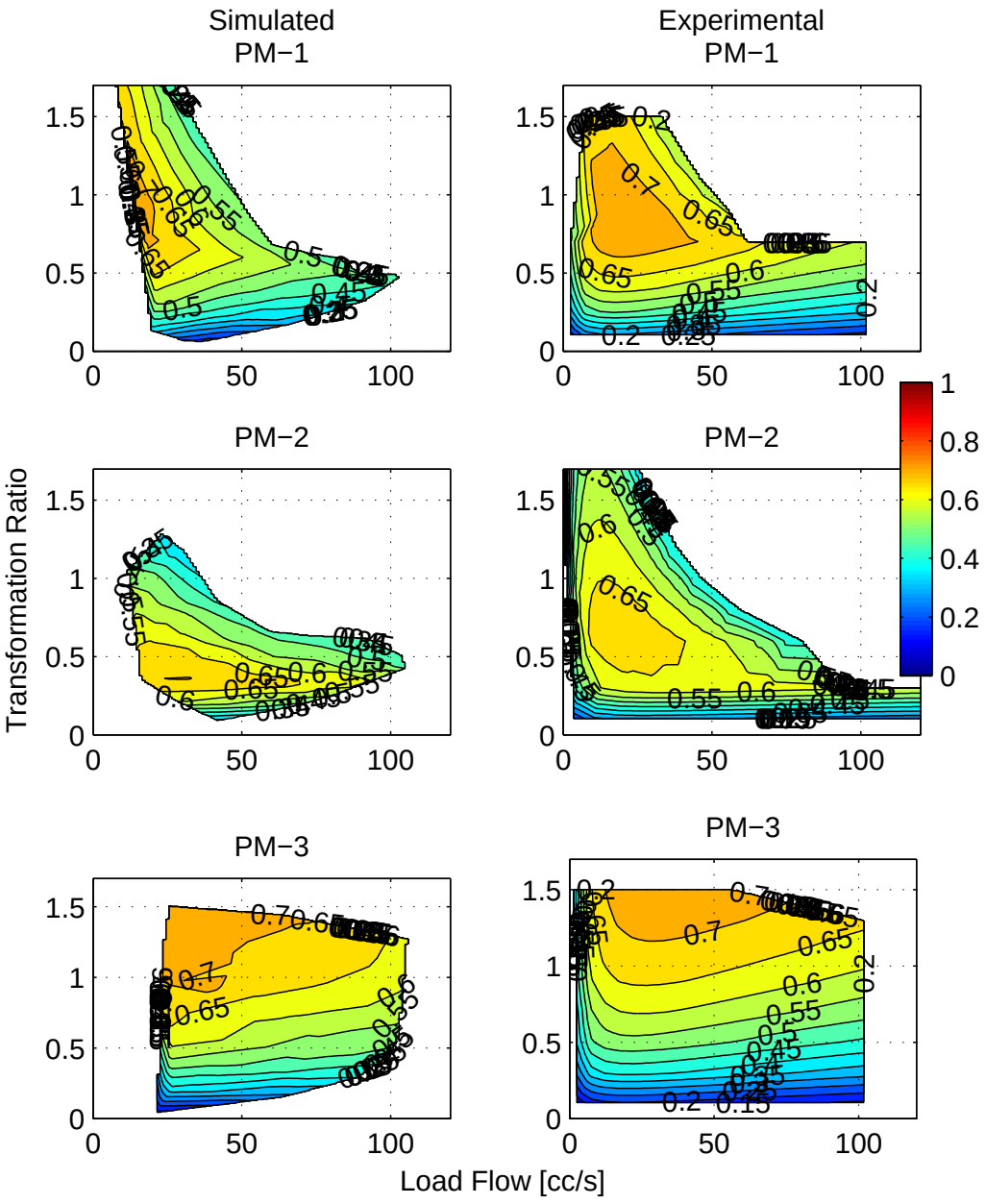

Figure 5.10: Prototype Experimental Efficiency Contour with Simulated

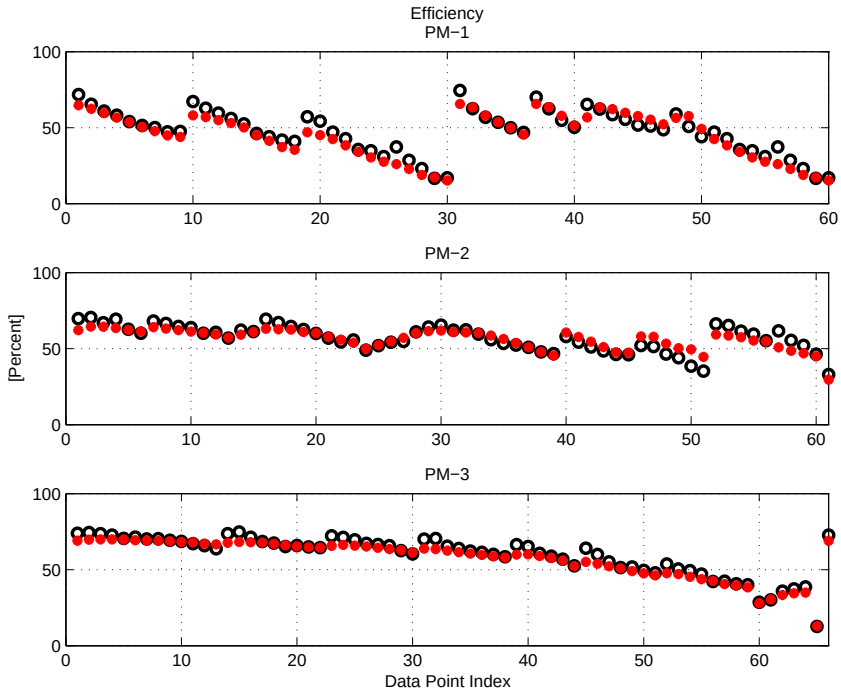

Figure 5.11: Comparison of Experimental data points against simulated ones for efficiency

5.5.2 Power Loss

Power loss is defined to be the difference in magnitude of the power input and output noted in Eq. (5.4):

$$W_{loss} = W_{in} - W_{out} \tag{5.6}$$

Left-hand side plots in Figure 5.13 shows a contours of experimental power loss in the transformer obtained from the prototype transformer. As with the efficiency contours, there are some data points that could not be obtained due to the limitation with the needle valve used in the experiment. The power loss shows a strong relationship with an increasing load flow, which corresponds to an increasing shaft speed. In the meantime, the pressure dependency is observed to be not as strong as relationship. The power loss in the prototype hydraulic transformer is dominated by mechanical losses.

Right-hand side plots in Figure 5.13 shows a contours of power loss generated by the simulation, it shows the same trend as observed with the experiments. The good match between the model and experimental results were beneficial in the controller optimization that will be presented in Chapter 8. The data points are spread out evenly across the output flow Q_B for each set of D_1 and D_2 utilized. With the losses, increasing ω results in decrease in λ for the given set of D_1 and D_2. Thus, with respect to λ, the data points

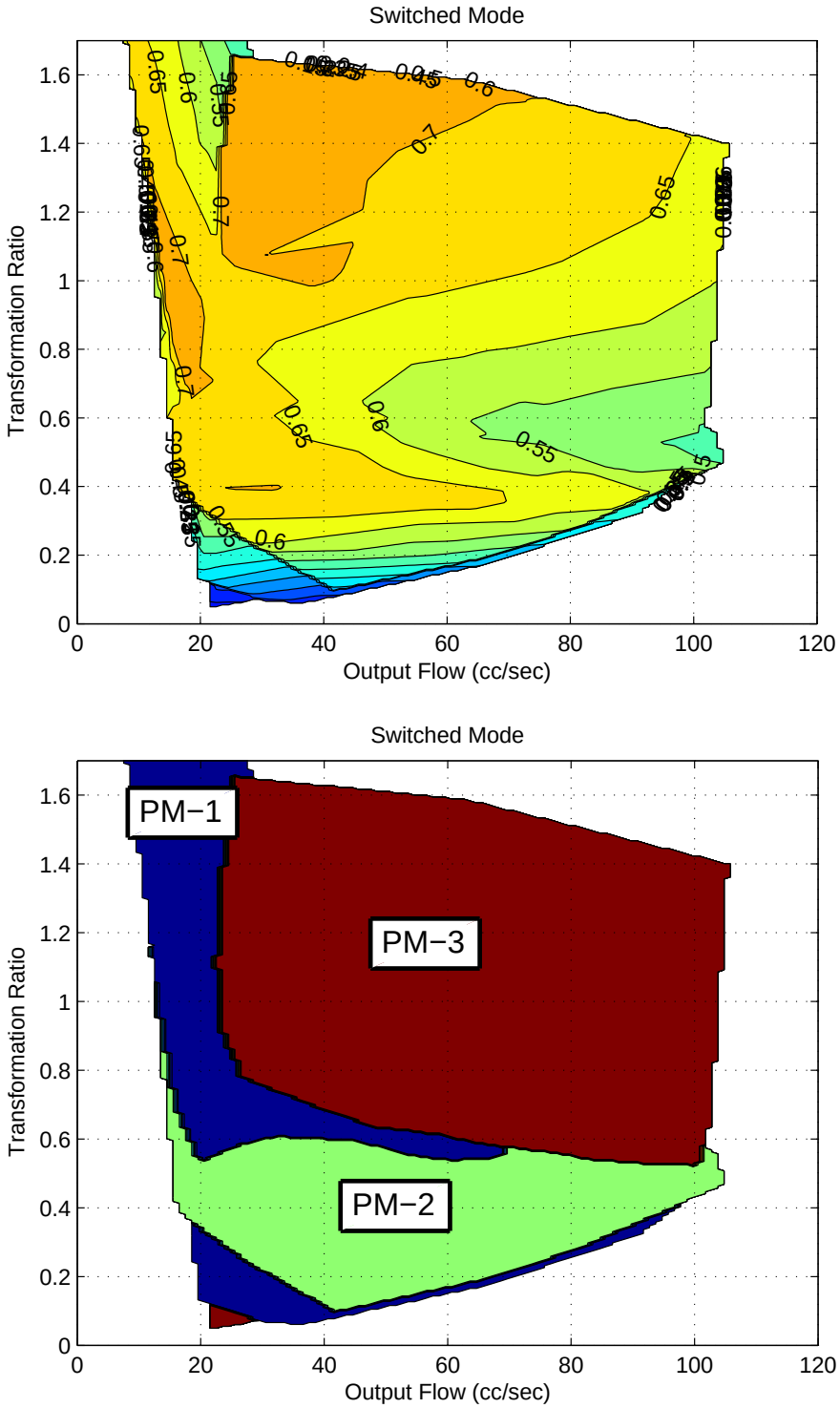

Figure 5.12: Top: Potential Efficiency Contour if mode switching is allowed to select the most efficient configuration; Bottom: Mode selection corresponding to the efficiency contour

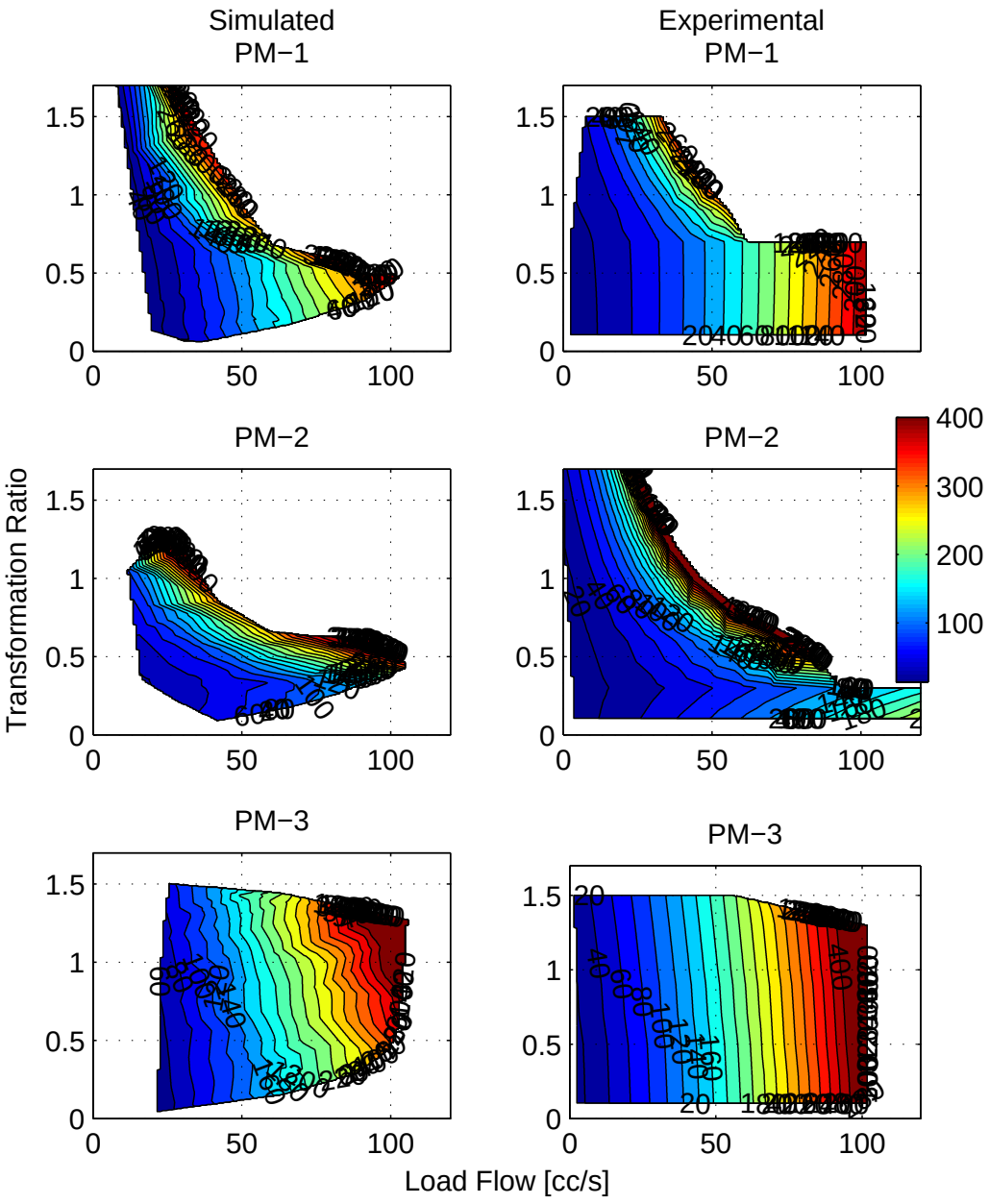

Figure 5.13: Prototype experimental power loss contour with simulated one

are distributed such that it droops down as Q_B increases.

Figure 5.14 shows the experimental data points compared against simulated data points comparing the power loss for all three configurations. The RMS in anticipating the power loss is 27 W, again showing a good match between the experiment and simulation.

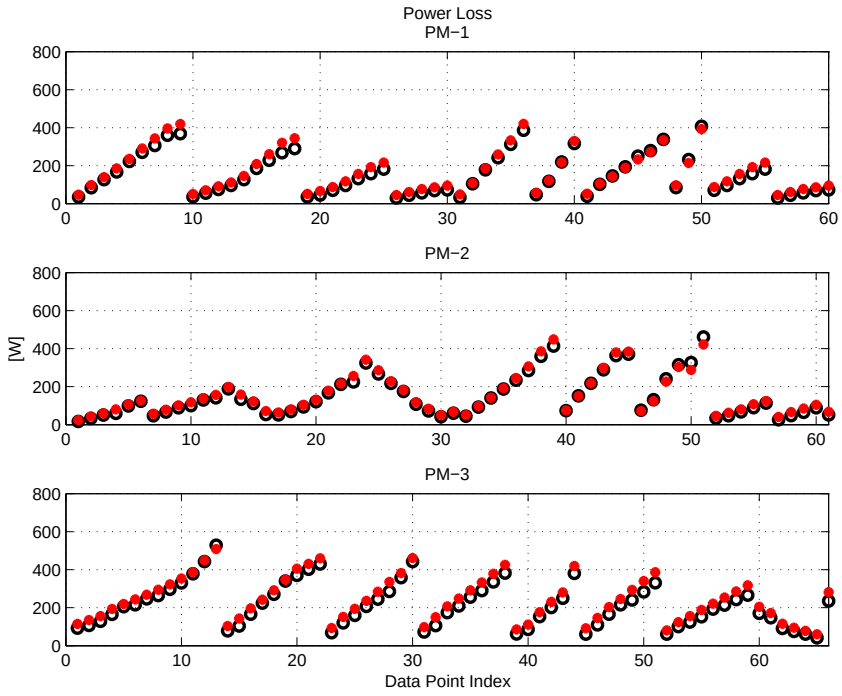

Figure 5.14: Comparison of Experimental data points against simulated ones for power loss

5.6 Chapter Summary

This chapter presented the prototype that was developed as a result of analyses conducted in Chapter 3 and 4. The prototype is capable of switching among configurations modes to take advantage in efficiency and sizing, and the testbench can be connected to any hydraulic loads. The controller was developed to automate the swashplate actuation using stepper motors. The operating characteristics of this prototype showed a good match between experiments and simulations. The peak efficiency of the transformer is measured around 70%, due to a large mechanical losses. The next chapters will present a controller developed with this prototype.

Chapter 6

Trajectory Controller using Hydraulic Transformer

If a hydraulic transformer is to replace existing throttling valves in hydraulic systems, it needs to have a good control performance, at least on par with the existing systems. As the first step in developing a controller for hydraulic transformer, we present the trajectory tracking controller for a cylinder driven by our prototype hydraulic transformer in this chapter.

As observed in Chapter 1, many previous works on hydraulic transformers focus on a component design aspect, with few works discuss the control aspect. Werndin and Palmberg [87, 88] presented design concepts necessary to control the IHT to drive a hydraulic cylinder to follow a reference trajectory. They used a model based estimator and a feedforward control in parallel with a PI controller and presented satisfactory simulated results. However, no experimental validation on this framework is presented. Vael et al. (2003) [84] discussed various possible hydraulic circuit options that could be utilized for experimentation of IHT on an excavator testbed. However, only qualitative analysis is presented, without simulation or experimental results. Shen et al. (2014) [79] presented a controller to drive a cylinder attached to the IHT. They utilized a fuzzy control theory to address the challenge with IHT's nonlinear behavior and experimentally proved the effectiveness of their algorithm. The results revealed that the response of the system was slow and suggested advanced control algorithm to be employed to optimize the control.

Ahn and Ho [31] presented a robust controller based on disturbance observer for regulating the position of a hydraulic cylinder driven by a PM transformer. They demonstrate the effectiveness of their controller over PID controller for a cylinder driven by a hydraulic transformer in the presence of load disturbance, parameter uncertainty, and sensor noise.

The tracking results are satisfactory in simulation, but no experimental data is provided. On their following work [32], they add three directional control valves to aid the operation of the hydraulic transformer connected to a cylinder. Depending on the position of those valves, 8 different operating modes are identified and an algorithm to determine the operating mode is presented. An analysis of energy consumption for different types of load is presented, but again the results are only in simulation.

Ikeo et al. [80] developed a controller for the injection molding machine driven by a hydraulic transformer. For the application shown, a cylinder drive pattern is separated into one that requires velocity control of the cylinder, and the other one requiring force control of the cylinder. Feedback control is applied to design a PI controller based on the internal model principle from a mathematical model of velocity and force control system. Good experimental results are shown for given velocity and pressure reference signals. However, the experimental results are shown only for one step signal rather than a continuous trajectory. Also, the pumping unit of the transformer has a fixed displacement in their setup. With the maximum displacements of the two units being the same, this results in a transformer only capable of reducing the pressure.

In this chapter, a trajectory tracking controller is developed and experimentally validated as the first step in developing a control algorithm for a hydraulic transformer driven system described in Section 6.1 and Section 6.2. In order to enable a hydraulic actuator to precisely track the desired trajectory, a passivity-based back-stepping control strategy is utilized in Section 6.3.1. Using the natural energy storage function in [56] instead of the commonly quadratic function in the definition of the Lyapunov function is delivers better tracking and is robust to the feedback noise. In Section 6.3.2, methods to control transformer to provide the required flow while regulating the shaft speed of the transformer is presented. Shaft speed regulation will used to optimize efficiency and to avoid transformer stalling as will be discussed in Chapter 8. Since both displacements are variable with $D_{1,max} = D_{2,max}$, the proposed controller is capable of boosting pressures as well. Moreover, the proposed controller can be adapted to all three traditionally configured transformers that differ by port connections. The controller performance is experimentally validated in Section 6.4. These results also appeared in [55].

6.1 System Description

For this controller, a hydraulic cylinder connected to a hydraulic transformer in 3 different configurations is considered as in Figs. 6.1-6.3. In the circuit shown in Fig. 6.1, a PM transformer is used in place of a servo valve to control the flow rate into the cylinder

chamber carrying a vertical mass load. By controlling the displacement ratio of a D_2 in the PM transformer, velocity and the position of the cylinder can be regulated. To recover the gravitational potential to the supply line while the load is being lowered, the pump/motor can go over-center. By controlling the displacement ratio of the D_1, the shaft speed of the transformer can be controlled by varying the power/torque valance within the transformer. If more power is injected into the transformer than what is required by the load trajectory, the transformer shaft will accelerate. If there exists such excess power in the transformer, this extra energy can be recovered back to the supply pressure line. Fig. 6.2 and 6.3 and illustrate the cylinder system configured with PM-2 and PM-3 respectively. In all three configurations, the displacements of both units are adjusted to simultaneously satisfy the flow requirement and the energy/torque balance of the transformer. This feature will be used to prevent a transformer from stalling in a low-speed region and to operate the transformer at the most optimal speed (discussed in Section 8.3).

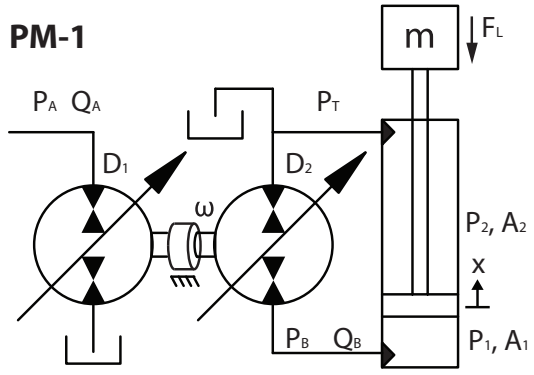

Figure 6.1: Schematic of hydraulic transformer for trajectory tracking controller: PM-1 connected to a cylinder

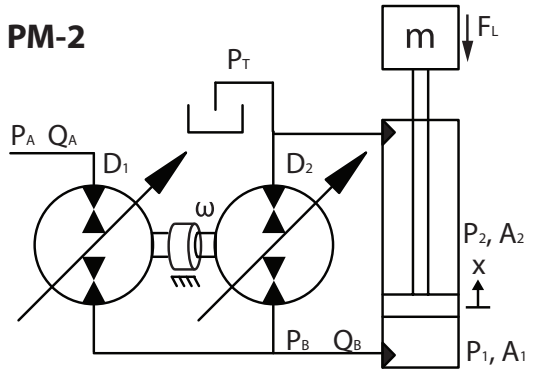

Figure 6.2: Schematic of hydraulic transformer for trajectory tracking controller: PM-2 connected to a cylinder

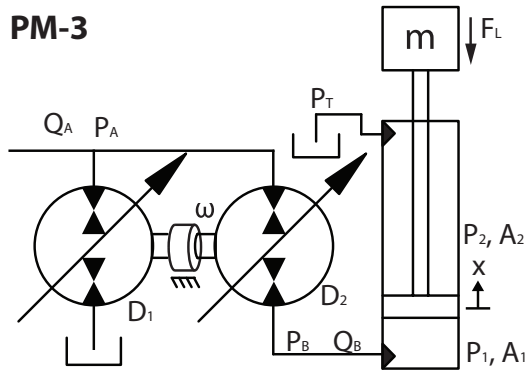

Figure 6.3: Schematic of hydraulic transformer for trajectory tracking controller: PM-3 connected to a cylinder

6.2 System Dynamics

The inertia dynamics of the hydraulic cylinder considered are:

$$m\ddot{x} = -b\dot{x} + P_1(t)A_1 - P_2A_2 + F_L \tag{6.1}$$

where m is the mass of the cylinder rod and load, x is the vertical position of the cylinder load mass, A_1 and A_2 are respectively the cap side and rod side areas of the hydraulic actuator, b is the viscous friction coefficient, and $F_L(t)$ is a load force that encapsulates any external load including gravity, environment forces, and un-modeled dynamics.

The dynamics of the cap-side pressure P_1 are given by the compressibility of the fluid in the cylinder and hose:

$$\dot{P}_1 = \frac{\beta(P_1)}{V_{10} + A_1x}(Q_B - A_1\dot{x}) \tag{6.2}$$

where Q_B is the flow rate into the cap side chamber to be provided by the transformer, V_{10} is the volume in the cap side chamber and hose when the actuator is at the position $x = 0$, and $\beta(P_1)$ is the pressure dependent bulk modulus [20]. The rod side is connected to the lower common pressure rail so, $P_2 = P_T$, which is assumed to be constant.

The cap side flow is supplied (or absorbed) by the hydraulic transformer which consists of a pair of variable displacement hydraulic pump/motors. The pump/motors are connected mechanically. Two of the ports, one from each pump/motor, are connected together as well. The transformer dynamics are governed by the common rotational inertia J and the torque applied by the pump/motors. The input, output, and tank ports are labeled as A, B, and T. By permuting the port connections, the three configurations in

Figs. 6.1-6.3 can be obtained. Each configuration will have different flow capability and efficiency characteristics as discussed in Chapter 3. The transformer rotational speed (ω) dynamics, flow at port A (Q_A), flow at port B (Q_B), and (ideal) pressure transformation ratio (λ) for the three configurations are given by:

PM-1 (Fig. 6.1):

$$\begin{aligned} J\dot{\omega} &= (P_A - P_T)\frac{D_{1,max}}{2\pi}u_1 + (P_B - P_T)\frac{D_{2,max}}{2\pi}u_2 - B_t\omega - T_{loss} \\ Q_A &= -\omega \cdot \frac{D_{1,max}}{2\pi}u_1 + Q_{leak'} \\ Q_B &= \omega \cdot \frac{D_{2,max}}{2\pi}u_2 - Q_{leak} \\ \lambda(u_1, u_2) &= \frac{D_{1,max}u_1}{D_{2,max}u_2} \left(:\approx \frac{P_B - P_T}{P_A + P_T}\right) \end{aligned} \tag{6.3}$$

PM-2 (Fig. 6.2):

$$\begin{aligned} J\dot{\omega} &= (P_A - P_B)\frac{D_{1,max}}{2\pi}u_1 + (P_T - P_B)\frac{D_{2,max}}{2\pi}u_2 - B_t\omega + T_{loss} \\ Q_A &= -\omega \cdot \frac{D_{1,max}}{2\pi}u_1 + Q_{leak'} \\ Q_B &= \omega \cdot \left(\frac{D_{1,max}}{2\pi}u_1 + \frac{D_{2,max}}{2\pi}u_2\right) - Q_{leak} \\ \lambda(u_1, u_2) &= \frac{D_{1,max}u_1}{D_{1,max}u_1 + D_{2,max}u_2} \end{aligned} \tag{6.4}$$

PM-3 (Fig. 6.3):

$$\begin{aligned} J\dot{\omega} &= (P_A - P_T)\frac{D_{1,max}}{2\pi}u_1 + (P_A - P_B)\frac{D_{2,max}}{2\pi}u_2 - B_t\omega + T_{loss} \\ Q_A &= -\omega \cdot \left(\frac{D_{1,max}}{2\pi}u_1 + \frac{D_{2,max}}{2\pi}u_2\right) + Q_{leak'} \\ Q_B &= \omega \cdot \frac{D_{2,max}}{2\pi}u_2 - Q_{leak} \\ \lambda(u_1, u_2) &= \frac{D_{1,max}u_1 + D_{2,max}u_2}{D_{2,max}u_2} \end{aligned} \tag{6.5}$$

where $D_{1,max}$ and $D_{2,max}$ are the maximum volumetric displacements of the pump/motor units in m^3/rev, u_1 and $u_2 \in [-1, 1]$ are control inputs which are the normalized displacements. Previously Eqs. 2.18–2.21, D_1 and D_2 themselves were variable. In this chapter, we separate the displacement ratios such that $D_1 = D_{1,max}u_1$ and $D_2 = D_{2,max}u_2$. B_t is the coefficient of the viscous friction loss. $Q_{leak'}$, Q_{leak} and T_{loss} are the lumped volumetric loss

at the A and B ports and the mechanical loss inside the transformer due to friction. These losses are generally configuration, pressure and speed dependent as discussed in Chapter 3. As with Chapter 2, sign convention is defined such that for a positive displacement unit $D_{1,max} > 0$ or $D_{2,max} > 0$, a positive shaft speed $\omega > 0$ defines a port flow $Q < 0$ to be flow going into the transformer and $Q > 0$ to be flow coming out of the transformer. λ is the input to output flow transformation ratio, which, in steady-state, is also the output to input pressure transformation ratio when losses are absent. These are the utilization of average model obtained in Section 2.1.

6.3 Control Strategy

The control objective is for the actuator position $x(t)$ to track a reference trajectory $x_d(t)$ subjected a load F_L, while regulating the hydraulic transformer speed at $\omega_d(t)$.

In all 3 configurations in Figs. 6.1-6.3, P_A and P_T are the high and low pressures of the common pressure rails which are assumed constant. Overrunning load and cavitation are assumed not to occur as would be the case when the gravity load is sufficiently large, and speed is sufficiently slow. Otherwise, a directional control valve can be added between the transformer and the actuator. In the proposed approach, the desired velocity, force, pressure of the actuator, and finally the required flow to the actuator are successively defined and controlled via passivity backstepping. Unlike feedback linearization or backstepping that uses a generically defined quadratic Lyapunov function [53] where active cancellation of specific terms are needed, the passivity-based approach uses a natural energy inspired Lyapunov function such that the cancellation is done automatically due to the structural property of the system. This results in improved performance, robustness against model uncertainties, and fewer gains to tune [56].

In addition to specifying the required flow (Q_B) to control the cylinder motion, the net torque (U_{total}) on the transformer will also be specified. The required flow to the cylinder and the net torque are then simultaneously satisfied by decomposing these requirements into appropriate settings for the two displacements of the hydraulic transformer. This is visualized in Fig. 6.4

6.3.1 Cylinder Flow Requirement

In this subsection, we design required Q_B in Eq. (6.2) such that $x(t) \to x_d(t)$, where x_d, $\dot{x}_d$, $\ddot{x}_d$, and $\dddot{x}_d$ are assumed to be smooth and available. The passivity approach in [56], summarized below, is taken for this purpose. The readers are referred to [56] for details.

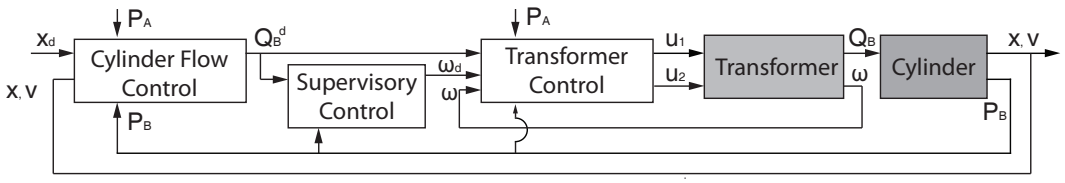

Figure 6.4: Control Scheme for Trajectory Control using Hydraulic Transformer

Let $e := x - x_d$ be the tracking error and define the reference velocity, and the reference velocity error as

$$r := \dot{x}_d - \lambda_p e \tag{6.6}$$

$$e_v := \dot{x} - r = \dot{e} + \lambda_p e \tag{6.7}$$

where $\lambda_p > 0$. Then, by designing the desired pressure to be:

$$P_d := \frac{1}{A_1}(m\dot{r} + br - F_L + A_2 P_2 - K_p e - K_{v1} e_v) \tag{6.8}$$

where $K_p > 0$, and $K_{v1} > 0$, the reference velocity error dynamics become:

$$m\dot{e}_v = -K_p e - K_v e_v + A_1 \tilde{P} \tag{6.9}$$

where $\tilde{P} := P_1 - P_d$ and $K_v = K_{v1} + b$. With the Lyapunov (or storage) function

$$\begin{aligned} W_{mech} &:= \frac{1}{2} m e_v^2 + \frac{1}{2} K_p e^2 \\ \dot{W}_{mech} &= -K_v e_v^2 - \lambda_p K_p e^2 + \tilde{P} A_1 e_v \end{aligned} \tag{6.10}$$

the mechanical system can be seen to be passive with respect to the supply rate $\tilde{P} A_1 e_v$.

Next, pressure dynamics is taken into account by augmenting the Lypaunov (or storage) function W_{mech} with the pressure error energy: $V_1(x) W_V(\tilde{P}, P_d)$ where $V_1(x) := (V_{10} + A_1 x)$,

$$W_V(\tilde{P}, P_d) := \int_{P_d}^{P_d + \tilde{P}} \left[e^{g(P_d + \tilde{P}, P')} - 1 \right] dP' \tag{6.11}$$

is the volumetric pressure error energy density associated with compressing the fluid from pressure P_d to $P_d + \tilde{P}$ with

$$g(P_d + \tilde{P}, P_d) := \int_{P_d}^{P_d+\tilde{P}} \frac{dP'}{\beta(P')} \tag{6.12}$$

and $\beta(P')$ is the bulk modulus at pressure P' (see [56] for details). Hence, the augmented Lyapunov function is:

$$W_{total} = \frac{1}{2}me_v^2 + \frac{1}{2}K_p e^2 + V_1(x)W_V(\tilde{P}, P_d) \tag{6.13}$$

Using the property [56]:

$$\frac{d}{dt}\left[(V_1(x)W_V(\tilde{P}, P_d)\right] = \left[\tilde{P} + W_V(\tilde{P}, P_d)\right] Q_B - \tilde{P}A_1\dot{x} - V_1(x)\left[e^{g(P_1,P_d)} - 1\right]\dot{P}_d$$

and writing $Q_B = Q_d + \tilde{Q}$, we have:

$$\begin{aligned}
\dot{W}_{total} &= -K_v e_v^2 - \lambda_p K_p e^2 + \tilde{P}Ae_v + \tilde{P}Q_B - \tilde{P}A\dot{x} \\
&\quad + W_V(\tilde{P}, P_d)Q_B - V_1(x)[e^{g(P_1,P_d)} - 1]\dot{P}_d \\
&= -K_v e_v^2 - \lambda_p e^2 + \tilde{P}\left[Q_d - A_1 r - \frac{V_1(x)}{B(P_1, P_d)}\dot{P}_d\right] \\
&\quad + W_V(\tilde{P}, P_d)Q_d + \tilde{P}\underbrace{\left[1 + \frac{W_V(\tilde{P}, P_d)}{\tilde{P}}\right]}_{>0}\tilde{Q}
\end{aligned} \tag{6.14}$$

where $B(P, P_d)$ is defined from

$$[e^{g(P_1,P_d)} - 1] = \frac{1}{B(P_1, P_d)}\tilde{P}. \tag{6.15}$$

By successively applying Eq. (6.6) and Eq. (6.8),

$$\dot{P}_d = \frac{1}{A_1}\left[m(\dddot{x}_d - \lambda_p\ddot{e}) - \dot{F}_L - K_p\dot{e} - K_v\dot{e}_v\right] \tag{6.16}$$

$$= \underbrace{\frac{1}{A_1}\left[m\dddot{x}_d - \dot{F}_L\right]}_{\dot{P}_{d1}} + f(e, e_v, \tilde{P}) \tag{6.17}$$

where $f(e, e_v, \tilde{P}) = \alpha_e e + \alpha_{ev}e_v + \alpha_P\tilde{P}$ for some α_e, α_{ev}, α_P.

Now compensating only for the terms related to the trajectory, Q_d is designed to be:

$$Q_d = A_1 r + \frac{V_1(x)}{\beta(P_d)} \dot{P}_{d1} \tag{6.18}$$

where $r(t)$ is the reference velocity defined in Eq. (6.6) and $\dot{P}_{d1}$ is given in Eq. (6.17). Using this term:

$$\dot{W}_{total} \leq -K_v e_v^2 - \lambda_p e^2 + \tilde{P}\left[1 + \frac{W_V(\tilde{P}, P_d)}{\tilde{P}}\right]\tilde{Q} - \tilde{P}\frac{V_1(x)}{\beta(P_d)} f(e, e_v, \tilde{P}) + \underbrace{\left(\mu(P_1, P_d)V(x)\dot{P}_d + \epsilon(P_1, P_d)\,|Q_d|\right)}_{\kappa}\tilde{P}^2 \tag{6.19}$$

where $\mu(P_1, P_d) > 0$, $\epsilon(P, P_d) > 0$ satisfy:

$$\mu(P_1, P_d)|\tilde{P}| \geq |[1/B(P_1, P_d) - 1/\beta(P_d)]|$$
$$\epsilon(P_1, P_d) \geq W_V(\tilde{P}, P_d)/\tilde{P}^2$$

Note that the term $\tilde{P}A_1 e_v$ from the mechanical system Eq. (6.14) has been canceled out automatically by the term from the pressure error dynamics.

Finally, since it can be shown that $\left[1 + W_V(\tilde{P}, P_d)/\tilde{P}\right] > 0$, we design $\tilde{Q} = -\lambda_3 \tilde{P}$ such that the overall control law for desired flow into the piston chamber is:

$$Q_B^d = A_1 r + \frac{V_1(x)}{\beta(P_d)} \dot{P}_{d1} - \lambda_3 \tilde{P} \tag{6.20}$$

Using the notation V_β to denote $\frac{V_1(x)}{2\beta(P_d)}$ gives rise to

$$\dot{W}_{total} \leq -\begin{pmatrix} e & e_v & \tilde{P} \end{pmatrix} \mathcal{M}_{pass} \begin{pmatrix} e \\ e_v \\ \tilde{P} \end{pmatrix} \tag{6.21}$$

where

$$\mathcal{M}_{pass} := \begin{pmatrix} \lambda_p K_p & 0 & \alpha_e V_\beta \\ 0 & K_v & \alpha_{ev} V_\beta \\ \alpha_e V_\beta & \alpha_{ev} V_\beta & \bar{\lambda}_3 - \kappa + 2\alpha_P V_\beta \end{pmatrix}$$

with $\bar{\lambda}_3 = \lambda_3(1 + \frac{W_V(\tilde{P}, P_d)}{\tilde{P}})$. Thus, for $\lambda_3 > 0$ sufficiently large, $\mathcal{M}_{pass}$ is positive definite and $(e, e_v, \tilde{P})$ converge to $(0, 0, 0)$ exponentially. This implies that the bounded un-modeled

disturbance would only cause bounded effects.

Despite the analysis being a little involved, the control law in (6.20), (6.6), (6.7), (6.16) and (6.17) is quite straightforward. Moreover, inaccuracies or ignorance in the estimation of $\dot{P}_{d1}$ and $\beta(P_d)$ in Eq. (6.20), could be treated as disturbances with negligible effects after proper controller tuning.

6.3.2 Transformer Control

Transformer Speed Control

Since the displacements of both pump/motors in the hydraulic transformer can be manipulated, an additional control objective other than controlling the cylinder motion can be specified. Here, we impose that the transformer speed should track an arbitrary profile $\omega_d(t)$. $\omega_d(t)$ can be designed to prevent stalling or to optimize the operating efficiency of the transformer.

From (6.3)-(6.5), the speed dynamics of the three transformer configurations can be written as:

$$J\dot{\omega} = U_{total} - B_t\omega + T_L \tag{6.22}$$

where

$$U_{total} = \begin{cases} (P_A - P_T)\dfrac{D_{1,max}}{2\pi}u_1 + (P_T - P_B)\dfrac{D_{2,max}}{2\pi}u_2 & \text{PM-1} \\ (P_A - P_B)\dfrac{D_{1,max}}{2\pi}u_1 + (P_T - P_B)\dfrac{D_{2,max}}{2\pi}u_2 & \text{PM-2} \\ (P_A - P_T)\dfrac{D_{1,max}}{2\pi}u_1 + (P_A - P_B)\dfrac{D_{2,max}}{2\pi}u_2 & \text{PM-3} \end{cases} \tag{6.23}$$

is the total torque acting on the transformer by the pump/motor units. Given the reference shaft speed for transformer $\omega_d(t)$, an appropriate U_{total} is needed to drive the transformer speed ω to the desired speed. Here we use a simple PI control with feedforward compensation:

$$\begin{aligned} \dot{\tilde{\omega}}_I = \tilde{\omega} &:= \omega - \omega_d \\ U_{total} &= J\dot{\omega}_d - K_{pt}\tilde{\omega} - K_{It}\tilde{\omega}_I + B_t\omega_d \end{aligned} \tag{6.24}$$

With the above controller, the error dynamics is

$$J\dot{\tilde{\omega}} = -\underbrace{(K_{pt} + B_t)}_{\bar{K}_{pt}}\tilde{\omega} - (K_{It}\tilde{\omega}_I - T_L) \tag{6.25}$$

The I control works as an estimator for the torque loss T_L:

$$\dot{\hat{T}}_L = K_{It}\dot{\tilde{\omega}}_I \tag{6.26}$$

Assuming this unaccounted torque loss does not change with respect to the time or varies slowly such that $\dot{T}_L = 0$ then

$$\begin{aligned} \hat{T}_L - T_L &= \tilde{T}_L \\ \dot{\hat{T}}_L &= \dot{\tilde{T}}_L \end{aligned} \tag{6.27}$$

With this, the resulting dynamics becomes

$$J\dot{\tilde{\omega}} = \bar{K}_{pt}\tilde{\omega} - \underbrace{(\underbrace{K_I\tilde{\omega}_I}_{\hat{T}_L} - T_L)}_{\tilde{T}_L} \tag{6.28}$$

We can write the resulting dynamics in following manner:

$$\begin{bmatrix} \dot{\tilde{T}}_L \\ \dot{\tilde{\omega}} \end{bmatrix} = \underbrace{\begin{bmatrix} 0 & K_{It} \\ -\frac{1}{J} & -\frac{\bar{K}_{pt}}{J} \end{bmatrix}}_{A} \begin{bmatrix} \tilde{T}_L \\ \tilde{\omega} \end{bmatrix} \tag{6.29}$$

From the linear quadratic Lyapunov theory, for $A \in \mathbb{R}^{n\times n}$, there exists a $P = P^T \in \mathbb{R}^{n\times n}$ that solves the Lyapunov equation $A^TP + PA = -Q$ where $Q = Q^T \in \mathbb{R}^{n\times n}$.

With $Q = \begin{bmatrix} \frac{2}{J} & 0 \\ 0 & \frac{2}{J} \end{bmatrix}$:

$$P = \begin{bmatrix} \frac{JK_{It}+\bar{K}_{pt}^2+1}{J\bar{K}_{pt}K_{It}} & 1 \\ 1 & \frac{JK_{It}+1}{\bar{K}_{pt}} \end{bmatrix} \tag{6.30}$$

Since K_{It}, $\bar{K}_{Pt} > 0$, $J > 0$, and $P > 0$, this system is globally asymptotically stable, showing that $[\tilde{T}_L, \tilde{\omega}]^T \to 0$ exponentially.

A classical control design method such as a pole placements could be utilized to place the controller poles at desired location.

Displacement Input Distribution

Here, we determine u_1 and u_2 to work simultaneously to provide the desired torque in Eq. (6.24) and the desired flow Q_B in Eq. (6.20).

For each transformer configuration, u_1 and u_2 could be solved simultaneously using the flow equations in Eqs. (6.3)-(6.5) and Eq. (6.23) as follow:

PM-1:

$$\begin{bmatrix} u_1 \\ u_2 \end{bmatrix} = \begin{bmatrix} 0 & \omega \cdot \frac{D_{2,max}}{2\pi} \\ (P_A - P_T)\frac{D_{1,max}}{2\pi} & (P_T - P_B)\frac{D_{2,max}}{2\pi} \end{bmatrix}^{-1} \begin{bmatrix} Q_B^d \\ U_{total} \end{bmatrix} \tag{6.31}$$

PM-2:

$$\begin{bmatrix} u_1 \\ u_2 \end{bmatrix} = \begin{bmatrix} \omega \cdot \frac{D_{1,max}}{2\pi} & \omega \cdot \frac{D_{2,max}}{2\pi} \\ (P_A - P_B)\frac{D_{1,max}}{2\pi} & (P_T - P_B)\frac{D_{2,max}}{2\pi} \end{bmatrix}^{-1} \begin{bmatrix} Q_B^d \\ U_{total} \end{bmatrix} \tag{6.32}$$

PM-3:

$$\begin{bmatrix} u_1 \\ u_2 \end{bmatrix} = \begin{bmatrix} 0 & \omega \cdot \frac{D_{2,max}}{2\pi} \\ (P_A - P_T)\frac{D_{1,max}}{2\pi} & (P_A - P_B)\frac{D_{2,max}}{2\pi} \end{bmatrix}^{-1} \begin{bmatrix} Q_B^d \\ U_{total} \end{bmatrix} \tag{6.33}$$

Notice that mechanical and volumetric losses were ignored in these expressions. These could be compensated with additional terms to improve performance.

6.4 Experimental Trajectory Tracking Results

The controller in Section 6.3 has been experimentally implemented on the pitch axis of the robotic device shown in Fig. 6.5, connected to the prototype transformer shown in Chapter 5. The transformer in all three configurations in Figs. 6.1-6.3 have been tested. System physical parameters are summarized in Table 6.1, and the controller gains are summarized in Table 6.2. Although the orientation of the hydraulic cylinder in Fig. 6.5 does vary, the variation is small, allowing us to estimate the effective mass and damping coefficient of the actuator as constants.

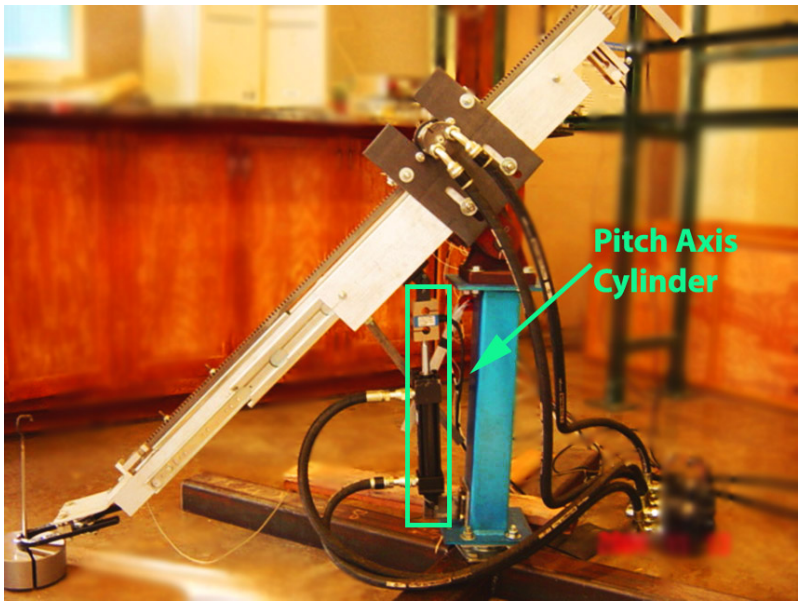

Figure 6.5: Transformer based control is tested on the pitch axis of this experimental setup.

Table 6.1: Experimentation parameters for trajectory tracking control

Parameter	Notation	Value
Cylinder mass	m	100 kg
Load	F_L	-981 N
Viscous damping	b	5000 $N/m \cdot s$
Piston Cap Area	A_1	11.87 cm^2
Piston Rod Area	A_2	5.1 cm^2
Supply (gauge) pressure	P_A	5.5 MPa
Return (gauge) pressure	P_T	0 MPa
Transformer Displacement	D_1,D_2	3.15 cc/rev
Transformer Inertia	J	2×10^{-5} kg·m^2

Table 6.2: Control gains used for the trajectory control

Gain	Symbol	Value
Transformer Proportional gain	K_{pt}	80
Transformer Integral gain	K_{It}	1600
Position feedback gain	K_p	20
Reference velocity error gain	K_v	10
Velocity error dynamics gain	λ_p	1×10^{-10}
Pressure feedback gain	λ_3	10

6.4.1 Cylinder trajectory tracking

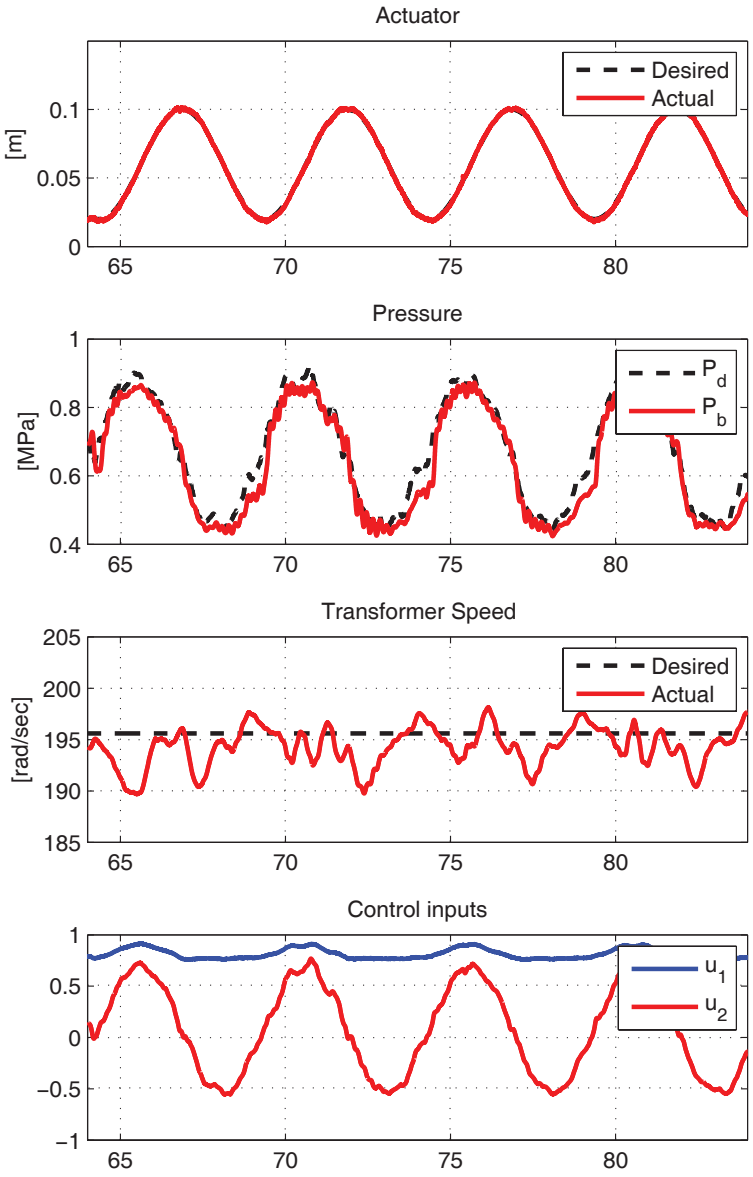

Figure 6.6: Low frequency (0.2 Hz) large amplitude (0.04 m) trajectory tracking for PM-1

First, the controller is tested with two different sinusoidal trajectories on the PM-1 setup (Fig. 6.1). One trajectory has a higher amplitude (0.04 m) and lower frequency (0.4π rad/s, or 0.2 Hz), and the other has a lower amplitude (0.015 m) and higher frequency (0.7π rad/s, or 0.35 Hz). The transformer speed is to be regulated at 196 rad/s and 167 rad/s. Results for these two cases are shown in Fig. 6.6 and Fig. 6.7 respectively and RMS errors in position, pressure and transformer speed are shown in Tab. 6.3. The performance with both trajectories is similar. RMS motion errors of less than 1 mm and transformer

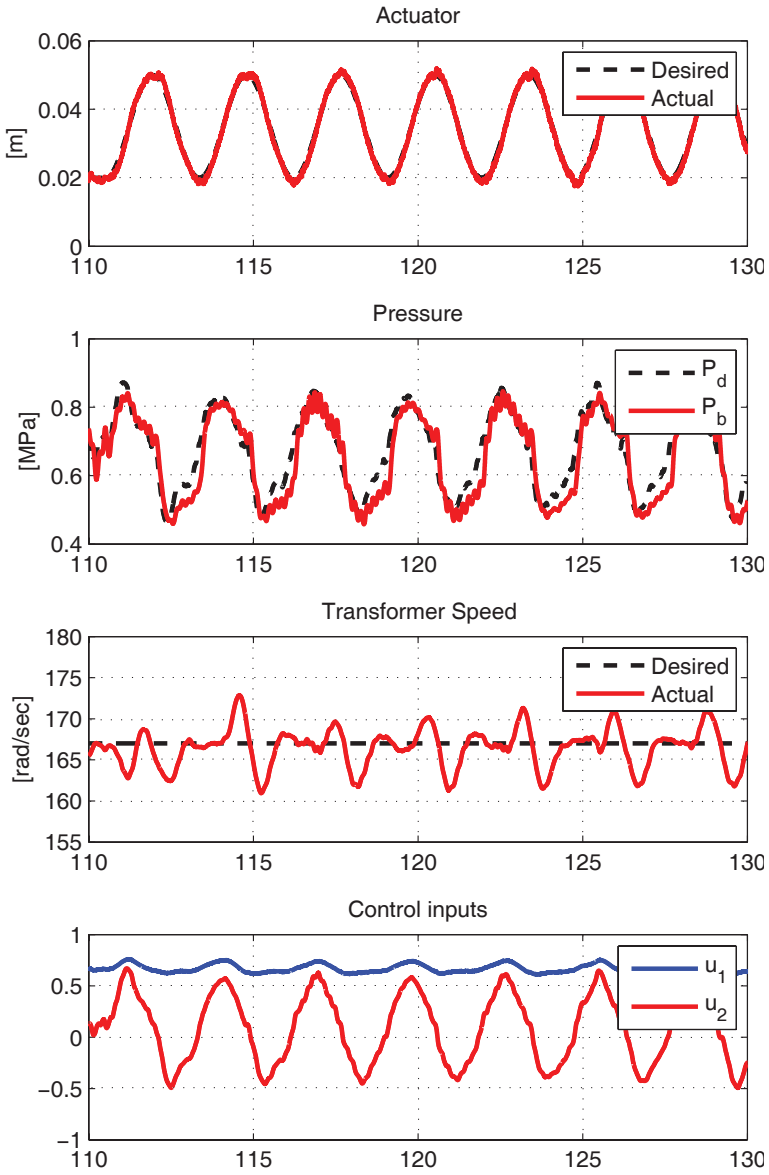

Figure 6.7: High frequency (0.35 Hz), small amplitude (0.015 m) trajectory tracking for PM-1

speed errors of less than 1.3% are achieved for both trajectories.

Table 6.3: Fast and slow sinusoidal trajectory tracking with fixed transformer speed on PM-1. RMS errors in position, pressure and transformer speed.

	e [mm]	$\tilde{P}$ [MPa]	$\tilde{\omega}$ [rad/s]
Slow (0.2 Hz)	0.88	0.041	2.31
Fast (0.35 Hz)	0.9	0.0480	2.45

6.4.2 Transformer speed tracking

Next, the controller is tested with a smoothed trapezoidal motion trajectory on the PM-1, 2, 3 setups while the desired transformer operating speed is varied arbitrarily. Tracking results are plotted on Figs 6.8-6.10. RMS errors are summarized in table 6.4. The RMS motion errors are within 1 mm for all three configurations whereas the transformer speed errors are slightly larger than the case when the desired speed is a constant. While the performances of all 3 configurations are very similar, PM-1 and PM-3 have slightly better motion control performance than PM-2, whereas PM-1 and PM-2 have slightly better transformer speed control performance than PM-3.

These experiments demonstrate that the proposed control algorithm can be used to simultaneously control the trajectory and the transformer operating speed. The latter will be used in Chapter 8 to optimize the transformer operation.

Table 6.4: Trapezoidal trajectory tracking with varying desired transformer speed on PM-1, PM-2, PM-3. RMS errors in position, pressure and transformer speed.

	e [mm]	$\tilde{P}$ [MPa]	$\tilde{\omega}$ [rad/s]
PM-1	0.804	0.0786	4.09
PM-2	0.866	0.0816	4.03
PM-3	0.813	0.0566	5.06

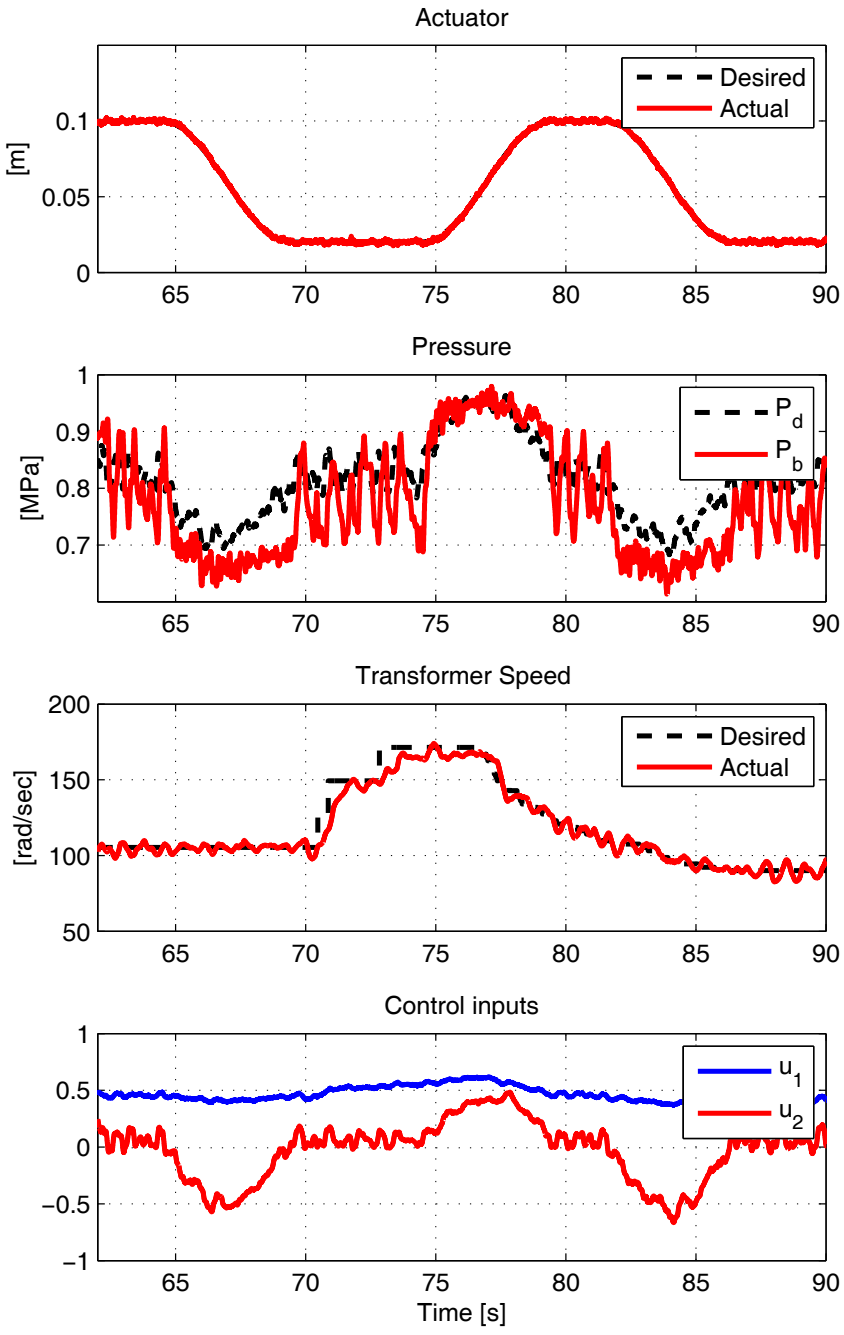

Figure 6.8: Trapezoidal trajectory tracking with variable desired transformer speed for PM-1

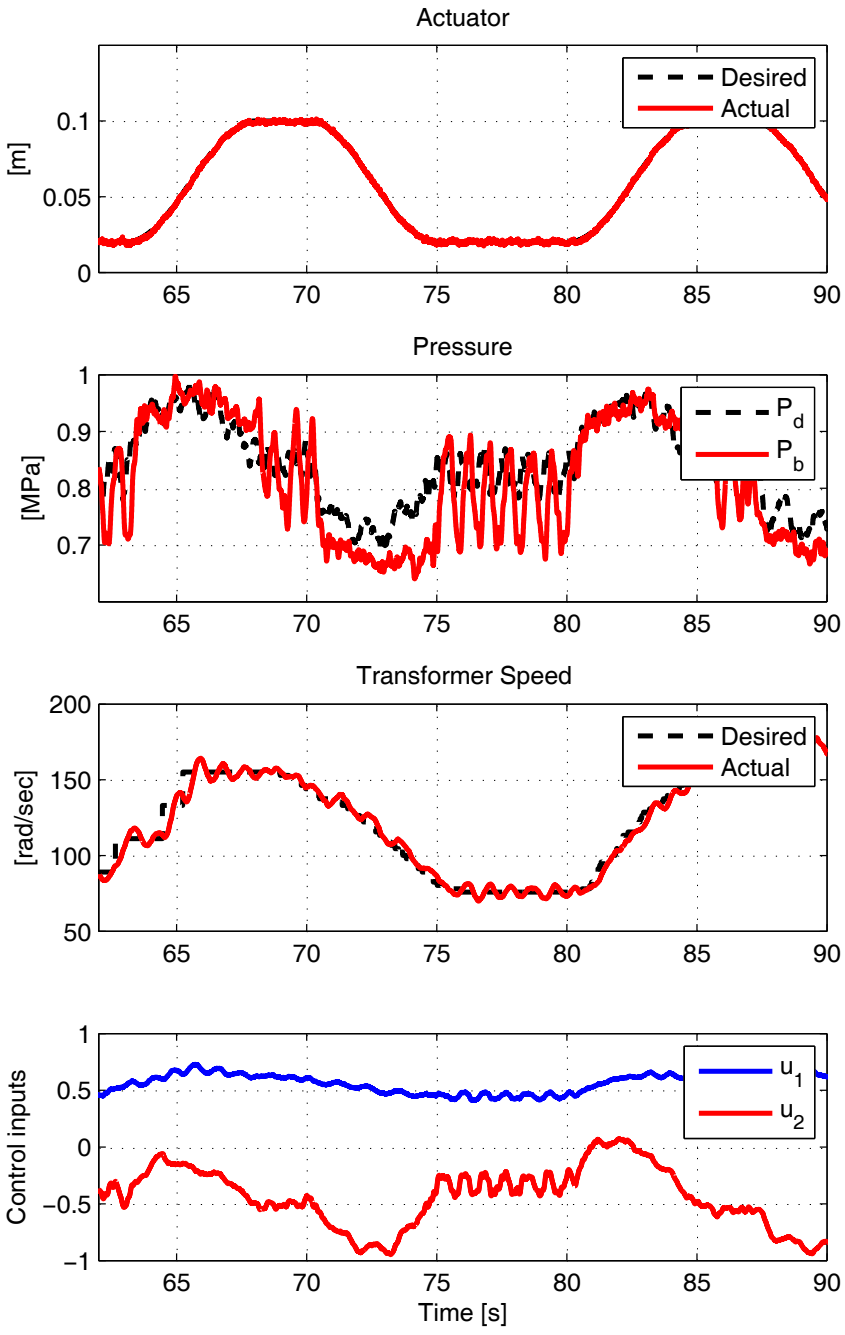

Figure 6.9: Trapezoidal trajectory tracking with variable desired transformer speed for PM-2

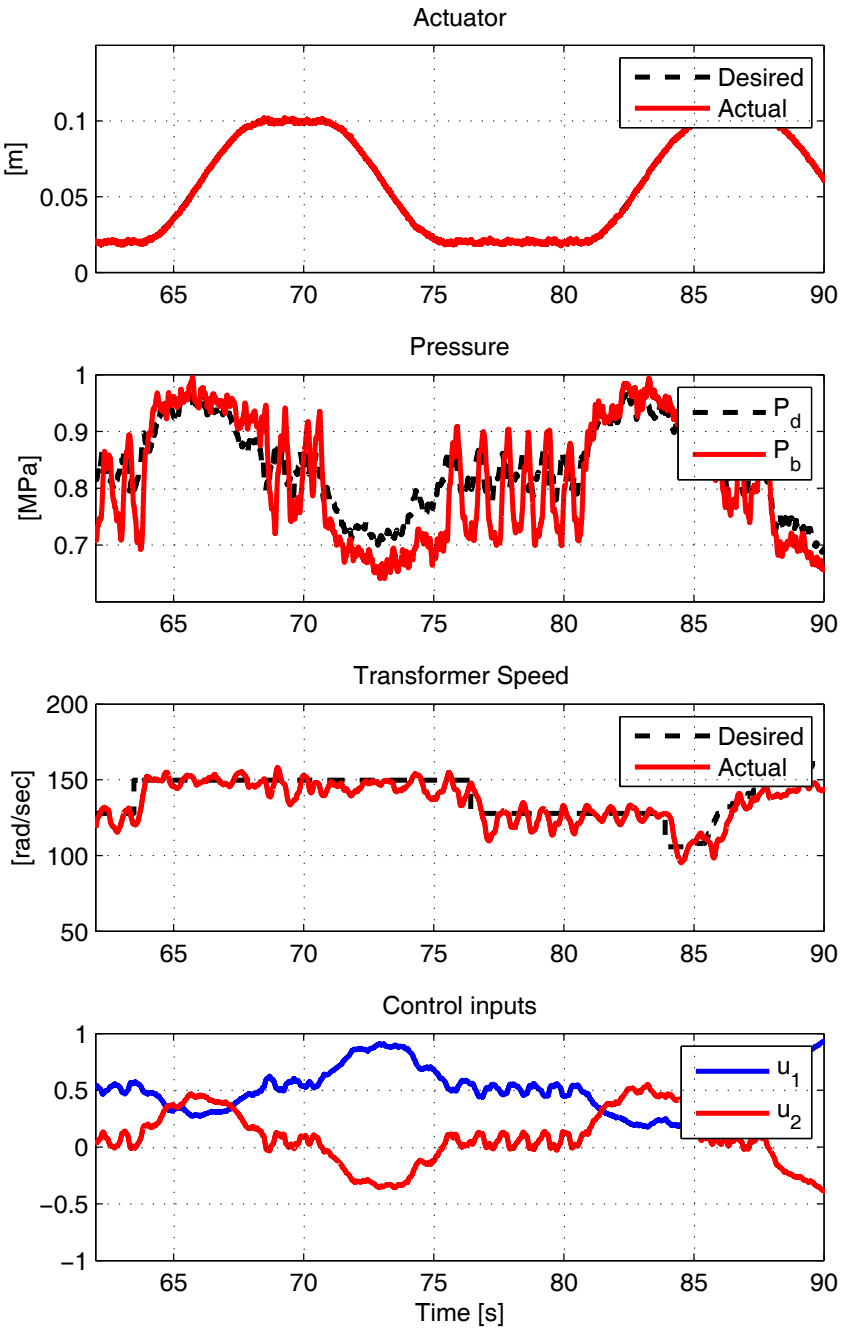

Figure 6.10: Trapezoidal trajectory tracking with variable desired transformer speed for PM-3

6.4.3 Effect of Parameter Uncertainty

Effects of uncertainty in the effective mass and damping coefficient are tested. Instead of using the best-known parameters in Tab. 6.1, other parameters in Tab. 6.5 are used in the controller instead. Control gains are, however, kept the same. Results with the PM-1 configuration are summarized in Tab. 6.5 and select cases are plotted in Fig. 6.11. As expected, uncertainties in mass and damping values result in a larger error, and the position error tends to have a bias. However, in all cases but one, the RMS position error does not increase by more than 1.7 mm, and in all cases, the RMS transformer speed error does not increase by more than 0.8 rad/s. To improve on these errors, an adaptive control scheme that estimates the mass and the damping coefficient (or similarly, by adding an integral action) can be a fruitful avenue for further investigation.

Table 6.5: Tracking results for various assumed effective mass and damping coefficient: RMS errors in position e, pressure $\tilde{P}$ and transformer speed $\tilde{\omega}$.

m [kg]	b $[N/m \cdot s]$	e [mm]	$\tilde{P}$ [MPa]	$\tilde{\omega}$ [rad/s]
50	0	5.4719	0.4199	3.4705
70	0	2.3840	0.2050	3.7217
100	500	1.1518	0.0993	4.4237
100	5000	0.7150	0.0474	3.8671
120	0	1.2775	0.1820	3.9412
120	50	1.4120	0.1989	4.1105
120	5000	0.9451	0.1476	4.6690

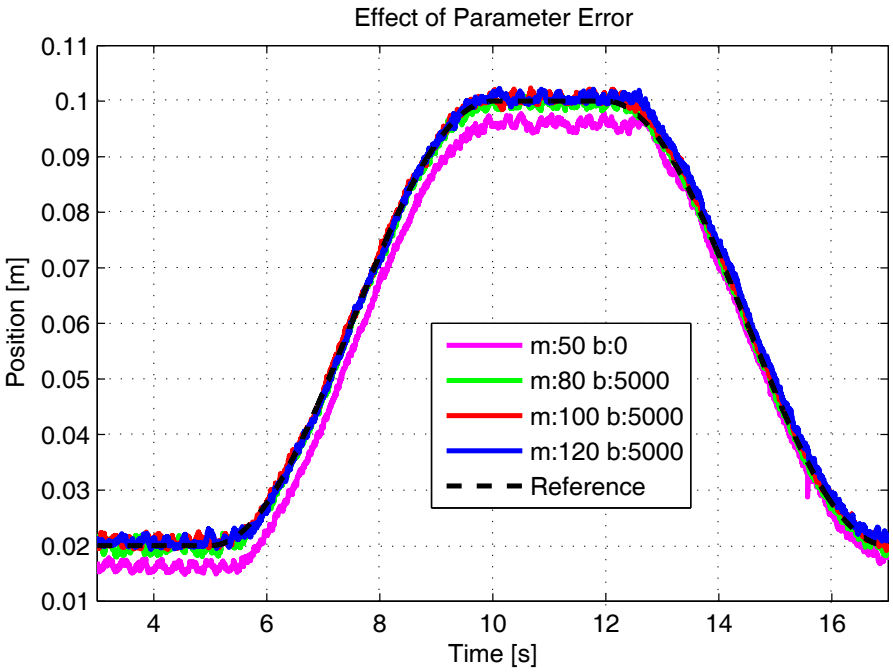

Figure 6.11: Trajectory tracking results ran with various different parameter values deviating away from the true value results in more error

6.5 Chapter Summary

This chapter presented a controller for a hydraulic cylinder driven by a PM transformer such that the cylinder tracks a predefined trajectory and the transformer speed is regulated at its desired value. The controller, which was designed based upon the passivity property of the hydraulic actuator and a recently discovered natural energy storage functions [56], can be applied to all three configurations of the transformer in Figs. 6.1-6.3. Experimental results show satisfactory cylinder trajectory and transformer speed regulation performance. All three transformer configurations have similar control performance and achieve RMS position errors of less than 1 mm. With these experimental results, this chapter shows that good trajectory tracking performance can be achieved using hydraulic transformers.

The desired transformer speed has been arbitrarily defined in this chapter, the reference speed can be determined to improve efficiency and to avoid stalling. Chapter 8 will demonstrate how to operate the transformer at its most efficient region to improve efficiency. This will involve transformer speed optimization, consideration of energy regeneration capability of a hydraulic transformer, and active switching of the transformer among the three configurations.

Chapter 7

Human Power Amplifier Control using Hydraulic Transformer

In this chapter, another application for validating the control performance of a system driven by a hydraulic transformer is presented. A Human Power Amplifier shown in Fig. 7.1 is utilized in this chapter. A number of previous students in our lab have worked on this machine in the past [59, 27]. However, they all utilized a servo valve control to achieve the control objective, just as any other hydraulic system. In this dissertation, we replace one of the servo valves with a hydraulic transformer to demonstrate that an advanced control methodologies for a complex system can be delivered by a hydraulic transformer.

This chapter is organized as follow. An introduction of the human power amplifier, along with a detailed literature review of previous works on human power amplifier and similar system are presented in Section 7.1 to highlight the novelty presented by this dissertation. System models and control objectives are stated in Section 7.2. The reformulation of the force control problem into a coordination control problem is presented in Section 7.3. Shape system coordination control and locked system guidance are presented in Sections 7.4 and 7.5 respectively. Controls of the hydraulic valve and transformer are presented in Section 7.6. Closed loop passivity is discussed in Section 7.7. Experimental results are given in Section 7.8. Section 7.9 contains concluding remarks.

7.1 Human Power Amplifier

The goal of the human power amplifier (HPA) is to enable a human operator to physically interact with the machine as if it is an extension of his/her body while amplifying the applied human effort. The control objective is similar to that of a wearable exoskeleton

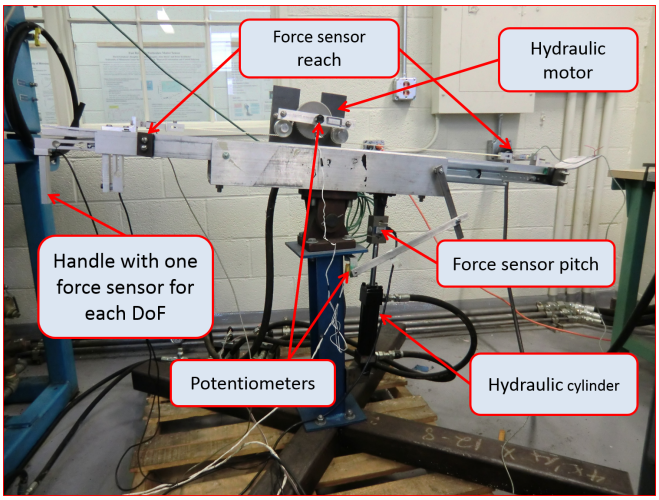

Figure 7.1: Picture of the Human Power Amplifier

except that the operator uses the machine as a tool that he/she can hold onto or let go off whenever he/she desires. In both cases, because of the physical connection to the machine, direct haptic and motion feedback are provided to the operator for intuitive operation while reducing the physical efforts required.

Since the HPA interacts physically with both the human operator and its physical environment, coupling stability and safety of both human and physical environments are paramount. One approach to improving safety is to impose on the control such that the machine behaves like an energetically passive device (with an appropriate power scaling) to its human and the physical environments (formal definition will be provided in section 7.2.3). An energetically passive system is one that only stores and dissipates (scaled) energy but does not generate the energy of its own. Since most physical environments and humans can also be considered energetically passive systems [33], the physical interactions with these environments are guaranteed to be stable by the passivity theorem which states that the coupling between a passive and a strictly passive system is necessarily stable [85, 22]. Even with active environments, the coupled system can only become unstable if the environments generate an infinite amount of energy.

The HPA, shown in Fig. 7.1, being considered has two degrees of freedom and is hydraulically actuated in order to be powerful and compact. An issue with hydraulic actuation, however, compared to electric motors, is that its force/torque is not directly controlled but are the result of pressure dynamics which are in turn controlled by the flows into the actuators.

Although the objective of an HPA is to amplify the applied human force, it is shown

in [57] that a direct approach to controlling the actuator force leads to positive velocity feedback which is not robust in the presence of uncertainty, slow sampling or feedback noise. As an alternative, a virtual velocity coordination approach was proposed in [58]. In this approach, a hydraulic actuator is modeled as a combination of an ideal velocity source and a nonlinear spring; the latter captures the compressibility effects of the fluid medium. Instead of controlling the actuator to track the desired force directly, the controller coordinates the velocities of the system and of a fictitious virtual mass whose dynamics are influenced by the hydraulic actuator and the human force. The control law for achieving coordination is accomplished via a passive decomposition [49, 50, 51] into a shape system and a locked system. This approach is more robust as the controller structure itself enforces the passivity property. The control law, which determines the flow command, was ultimately executed using a high bandwidth servo-valve. This approach was applied to a hydraulically actuated patient transfer device in [34].

In this dissertation, the control of hydraulic HPA is extended beyond the previous work in [58] in several ways. Firstly, in [58], the control was developed for each individual degree-of-freedom assumed to be decoupled from each other. Here, the fully coupled dynamics of a multi-DoF HPA are considered. Secondly, we develop human-machine shared control strategies by rendering useful passive dynamics to assist the human to execute specific tasks more easily. In particular, guidance for moving in preferable directions, such as to follow a contour, is achieved by incorporating the Passive Velocity Field Controller (PVFC) [60]; and obstacle avoidance is achieved by incorporating potential fields [45] to prohibit the machine from entering prohibited zones. These assistive dynamics are imposed while allowing the HPA to remain energetically passive. Thirdly, in [58], the hydraulic actuator is modeled as a combination of an ideal kinematic actuator and an empirically defined "nonlinear spring" that represents the fluid compressibility; and a linear affine parameterization based control was developed. In this dissertation work, this model is replaced by a physical model of the fluid compressible energy which properly accounts for the volume variation in the actuator as well as the pressure dependent bulk modulus (if so desired) [56]. The use of this model results in a more robust, nonlinear passivity based shaped system control. Finally, and most importantly for this dissertation work, unlike in [58] where high bandwidth, but energetically inefficient, servo valves are used for the flow control, one of the actuators in this dissertation is controlled by a prototype hydraulic transformer presented in Chapter 5. The experimental results will demonstrate that utilizing the hydraulic transformer is possible for this application.

Among the exoskeletons in the open academic literature (Dollar and Herr [24] and

Bogue [17] presented review papers), the Berkeley Lower Extremity Exoskeleton (BLEEX) [44] and the Hybrid Assistive Leg (HAL) [42, 41] are the most prominent and represent two ends of the spectrum. HAL is electrically driven and is targeted for performance augmentation and for rehabilitation. BLEEX is hydraulically actuated and targets mainly able-bodied persons. HAL uses electromyography (EMG) sensing to interpret human intention, but BLEEX uses only motion sensors on the exoskeleton in order to impart positive feedback. Since EMG sensing is susceptible to accurate sensor placements and skin conditions, the approach that only uses motion sensors is simpler and more robust. This approach is also adopted by several other research groups [66, 73, 47]. However, motion sensing alone cannot distinguish between human applied force and external environment forces that are not explicitly modeled, including uncertain gravitational loads. Effects due to these external load would be amplified unintentionally by the control law. To work around with this issue, Kazerooni et al. [44], and Lv and Gregg [66] pre-determine the amounts of weight-bearing assistance to be provided (i.e., not estimated from sensing on the go) and treat them differently from scaling of inertial effects. Similarly, in Kong and Tomizuka [47], the joint torque estimator in the fictitious gain controller requires a knowledge of the gravitational potential energy function.

In our hydraulic HPA, an intermediate approach is taken in that the human applied force is measured by a force handle. Since the point of interaction is well defined at the handle, the human intent, distinct from the applied environment forces, can be determined accurately. Inertia effects and gravitational loads and other environment forces can then be compensated in a uniform manner by "simply" scaling the applied human force to achieve the similar effects of fictitious gain in Kong and Tomizuka [47], and of admittance or energy shaping in Nagarajan et al. [73] and Lv and Gregg [65].

The close attention paid to the hydraulic actuation in this dissertation is in contrast to most academic exoskeletons that use electric motor actuation. Those that are hydraulically actuated (e.g., Kazerooni et al. [44] and Cao et al. [18]) are controlled by throttling valves and do not address the critical issue of pressure dynamics that ultimately produce the actuation force. An exception is a recent paper by Chet at al [19] on a 1-DoF hydraulic exoskeleton in which the valve controlled hydraulics are treated in details in a cascade motion control structure with direct force tracking.

Preliminary results in this chapter appeared in [54] and in [27, 52] where single DoF passivity based force amplification control and multiple DoF assistive dynamics rendering were first presented respectively. This dissertation presents the multi-DoF, passivity-based, human power amplifier control with assistive dynamics in a comprehensive and complete

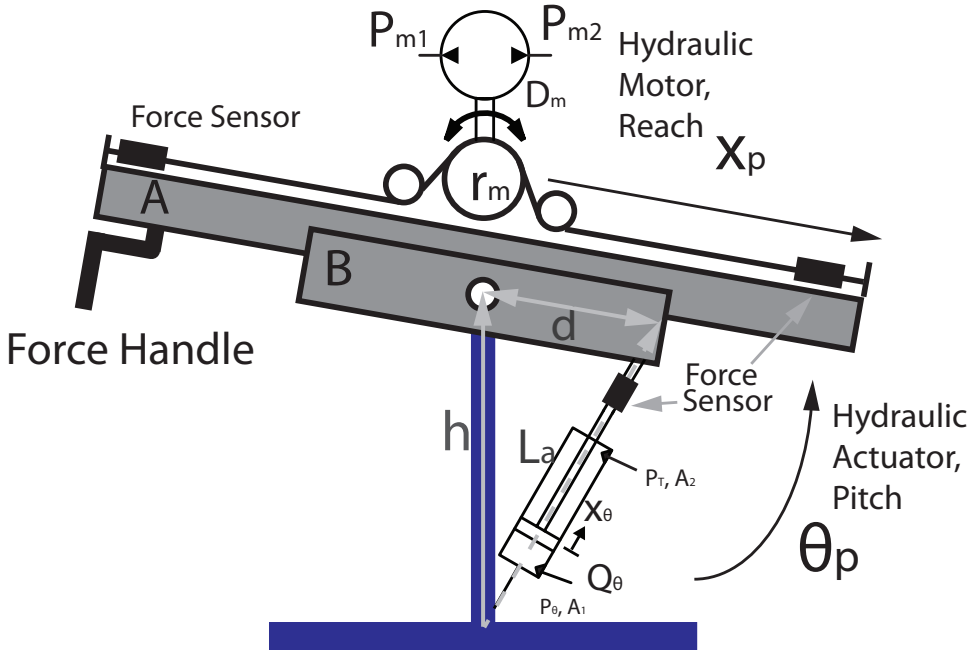

Figure 7.2: Schematic of the Human Power Amplifier

manner. All of these were driven by a prototype hydraulic transformer to demonstrate the control performance of the hydraulic transformer-driven system. This chapter includes detailed proofs and analysis, a thorough discussion of energetic passivity, and extensive experimental validations.

7.2 System Description and Control Objectives

The human power amplifier (HPA) being considered (Figs. 7.1-7.2) has two degrees of freedom (DoF) in the form of a beam (A) that can translate (reach motion) relative to another beam (B) and rotate (pitch) about a pivot. The generalized coordinates are $q = [\theta_p, x_p]^T$ where θ_p describes the angular position of the pitch movement and x_p describes the linear position of the reach movement. The pitch (angular) motion is actuated by a linear hydraulic actuator whereas the reach (linear) motion is actuated by a hydraulic motor via a pulley-and-belt mechanism. The linear forces applied by the hydraulic actuator and by the pulley-and-belt are measured by force sensors. The human operates the HPA via a handle instrumented with a 2-DoF force sensor.

7.2.1 Mechanical System

The dynamics of the HPA are given by:

$$M_p(q)\ddot{q} + C_p(\dot{q}, q)\dot{q} = F_{human} + F_{env} + F_a \tag{7.1}$$

where $M_p(q) \in \Re^{2X2}$ is the symmetric and positive definite inertia matrix, $C_p(\dot{q}, q) \in \Re^{2X2}$ is the Coriolis matrix such that $\dot{M}_p(q) - 2C_p(\dot{q}, q)$ is skew-symmetric; F_{human} is the generalized torque/force; F_{env} is the force exerted by the environment, including gravitational force; F_a is the generalized actuator force/torque given as:

$$F_a = \begin{bmatrix} T_\theta \\ F_x \end{bmatrix} = \begin{bmatrix} J_A(\theta_p)F_\theta \\ \frac{1}{r_m}T_x \end{bmatrix} \tag{7.2}$$

where T_θ and F_x are the torque and force applied to the pitch and reach directions. They are related to the the pitch hydraulic cylinder force F_θ and the reach hydraulic motor torque T_x by the Jacobian $J_A(\theta_p)$ given by:

$$J_A(\theta_p) = \frac{h \cdot d \ \sin(\theta_p)}{\sqrt{h^2 + d^2 - 2 \cdot h \cdot d \ \cos(\theta_p)}}$$

and the pulley radius r_m. The generalized pitch and reach motions are related to the linear velocity of the hydraulic cylinder and the angular velocity of the hydraulic motor by:

$$\dot{x}_\theta = J_A(\theta_p)\dot{\theta}_p; \quad r_m\dot{\theta}_x = \dot{x}_p \tag{7.3}$$

Pitch and reach motions (θ_p and x_p) are monitored via encoders; and their velocities are obtained via dirty differentiation. The actuator forces F_θ and F_x and the human force F_{human} are measured via force sensors. The environment force F_{env}, however, is not measured.

7.2.2 Hydraulic System

In our setup, the pitch hydraulic cylinder is controlled via a prototype hydraulic transformer [29]; whereas the reach hydraulic motor is controlled via a servo-valve (Fig. 7.3). The servo-valve has high control bandwidth, but it uses throttling as a means of control, which is very energy inefficient. Hydraulic transformers do not use throttling to control flow so they are naturally more efficient. However, their control bandwidths tend to be lower. This setup allows us to study the control performance of the more efficient hydraulic

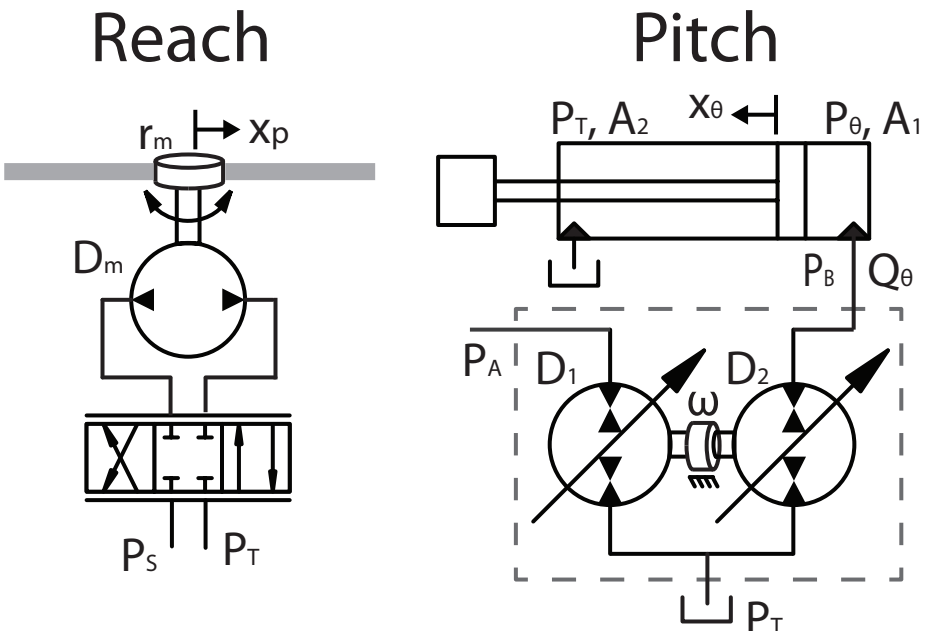

Figure 7.3: Schematic of the Hydraulics. Left: Reach hydraulic motor controlled by a servo-valve. Right: Pitch hydraulic cylinder controlled by a prototype hydraulic transformer.

transformer relative to the high bandwidth, low efficiency, servo valve.

Reach actuation

The reach axis hydraulic motor torque is:

$$F_x = \frac{1}{r_m} T_x = \underbrace{(P_{m1} - P_{m2})}_{P_x} \frac{D_m}{2\pi r_m} \tag{7.4}$$

where D_m is the fixed displacement of the motor, $P_x = P_{m1} - P_{m2}$ is the pressure differential across the two ports of the motor. The pressure dynamics for the two sides of the hydraulic motor are:

$$\dot{P}_{m1} = \frac{\beta}{V_{m1}} \left(Q_{m1} - \frac{D_m}{2\pi} \frac{\dot{x}_p}{r_m} \right)$$
$$\dot{P}_{m2} = \frac{\beta}{V_{m2}} \left(-Q_{m2} + \frac{D_m}{2\pi} \frac{\dot{x}_p}{r_m} \right)$$

where V_{m1}, V_{m2} are the fixed fluid volumes in the motor and the hoses, β is the fluid's bulk modulus. Flow Q_{m1}, Q_{m2} are the cap-side input and rod-side return flows from/to the servo valve, which in general, will be proportional to the valve command u_x and dependent on the individual volume pressures P_{m1} and P_{m2}.

The servo-valve is assumed to be matched, symmetric and critically lapped. With the assumption that $Q_{m1} = Q_{m2} =: Q_x$, which would be valid when the load is constant, the dynamics of the pressure difference becomes:

$$\dot{P}_x = \frac{\beta}{\bar{V}_m}\left(Q_x - \frac{D_m}{2\pi}\frac{\dot{x}_p}{r_m}\right) \tag{7.5}$$

where $\bar{V}_m = (V_{m1}^{-1} + V_{m2}^{-1})^{-1}$ is the effective fluid volume of the motor. Furthermore, it can be shown that $P_{m1} + P_{m2} = P_s - P_T$, so that the servo-valve flow equation becomes:

$$Q_x = \begin{cases} u_x K_q \sqrt{P_s - P_T - P_x} & \text{if } u_x \geq 0 \\ u_x K_q \sqrt{P_s - P_T + P_x} & \text{if } u_x < 0 \end{cases} \tag{7.6}$$

where K_q is a valve coefficient and u_x is the valve command. Since F_x is measured directly and is related to P_x in (7.4), the formulation in (7.4)-(7.6) avoids the need for pressure sensors for measuring P_{m1} or P_{m2} when the net reach force F_x is measured.

In the experiment, Q_θ and Q_x are respectively controlled by a prototype transformer presented in Chapter 5 and a servo valve.

Pitch actuation

The pitch hydraulic cylinder is connected to the output of a hydraulic transformer as shown in Fig. 7.3 where the cap-side is connected to the transformer output with pressure P_B and the rod side is connected to the tank with constant pressure P_T, assumed to be atmospheric. It is assumed that the gravity load (in F_{env}) is sufficiently large such that over-running load and cavitation will not occur for the operations considered in this paper. Otherwise, a 4-way directional control valve can be inserted between the transformer and cylinder to prevent these conditions from occurring.

The pitch hydraulic torque T_θ is given by (Fig. 7.3):

$$T_\theta = J(\theta_p)F_\theta = J(\theta_p)(A_1 P_\theta - A_2 P_T) \tag{7.7}$$

where A_1 and A_2 are the cap side and piston side areas, $P_\theta = P_B$ and P_T are the supply and tank pressures on the cap and rod sides of the actuator. The pressure dynamics are given by:

$$\dot{P}_\theta = \frac{\beta}{V_1(x_\theta)}\left[Q_\theta - A_1 J_A(\theta_p)\dot{\theta}_p\right] \tag{7.8}$$

where Q_θ is the flow input to the cap side chamber,

$$V_1(x_\theta) = V_{10} + A_1 x_\theta \tag{7.9}$$

is the fluid volume in the cap-side chamber and the hose dependent on the linear displacement of the cylinder x_θ, β is the fluid bulk modulus.

The input flow Q_θ is the output flow of the hydraulic transformer. Ignoring friction and leakage, the dynamics and output flow of the tank shared transformer, or PM-1 configuration, as shown in Fig. 7.3 are given by:

$$\begin{aligned} J\dot{\omega} &= (P_A - P_T)\frac{D_{1,max}}{2\pi}u_1 + (P_T - P_B)\frac{D_{2,max}}{2\pi}u_2 =: U_{total} \\ Q_\theta &= \omega \cdot \frac{D_{2,max}}{2\pi}u_2 \end{aligned} \tag{7.10}$$

where J is the inertia of the transformer, $D_{1,max}$ and $D_{2,max}$ are the maximum displacements of the pump/motor units of the transformer, u_1 and $u_2 \in [-1, 1]$ are the control inputs which are the displacement ratios, $P_A = P_s$ is the constant supply pressure, $P_B = P_\theta$ is the output pressure, P_T is the tank pressure.

The transformer can be configured in other ways by the two pump/motor units sharing the input port or the output port, with advantages in pressure boosting or pressure bucking respectively. The dynamics of these are given in Eqs. (2.18)–(2.21). In this chapter, we focus on the tank shared configuration in Fig. 7.3 but the controls developed in this chapter can be easily adapted to the other configurations as seen in Section 6.3.2

7.2.3 Control Objectives

The control inputs of the HPA are the reach axis servo-valve input u_x and the pitch axis transformer inputs u_1, u_2. The goals are to enable the generalized actuator force F_a to:

1. Exert $\rho > 0$ times the applied human force F_{human} so that the human would feel that he/she is interacting with an inertia and an environment force that are attenuated by $(\rho + 1)$ times;

2. Apply assistive dynamics to provide task specific guidance, such as to follow a preferred contour and/or to avoid obstacles.

To enhance safety, the human power amplifier is to behave, in its interactions with the human and physical environments, like an energetically passive system with a power scaling of $\rho + 1 > 1$: i.e. there exists $c^2 > 0$, s.t. for all human force $F_{human}(\cdot)$ and

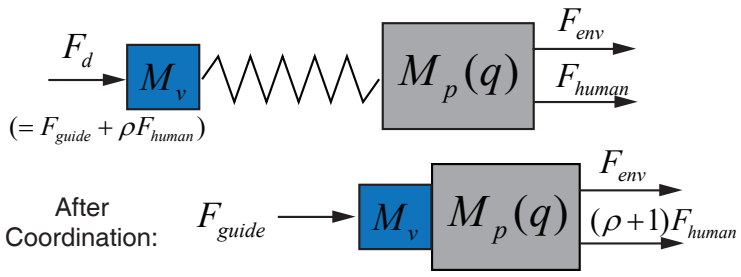

Figure 7.4: Hydraulic human power amplifier coupled with a virtual inertia via the fluid spring. They become a common mechanical tool after coordination.

environment force $F_{env}(\cdot)$, and for all time $t > 0$,

$$\int_0^t \underbrace{\left[(\rho+1)\dot{q}^T F_{human} + \dot{q}^T F_{env}\right]}_{\text{supply rate}} d\tau \geq -c^2 \tag{7.11}$$

Here, the supply rate consists of $(\rho+1)\dot{q}^T F_{human}$ and $\dot{q}^T F_{env}$ which are the scaled power exerted by the human and the physical environment. (7.11) expresses that c^2 is the maximum net scaled energy that the human and physical environment can extract from the HPA.

These objectives will be satisfied, in comparison with (7.1), if $F_a = F_d$ given by:

$$F_d = \rho F_{human} + F_{guide} \tag{7.12}$$

and F_{guide} which installs the guidance dynamics is passive:

$$\int_0^t \dot{q}^T F_{guide}\, d\tau \leq -c_1^2.$$

The challenges are that F_a is only indirectly controlled by the pressure dynamics.

7.3 Virtual Coordination Control Approach

Instead of directly controlling the actuator force F_a to track the desired force F_d in (7.12) as in [57], the virtual coordination approach in [58] converts the problem into one of coordinating the velocities of two coupled mechanical systems. Besides avoiding the need for positive velocity feedback, this approach can also be interpreted physically as an interconnection of passive components. The controller can exploit the intrinsically passive structure to make the system more robust and safer to operate.

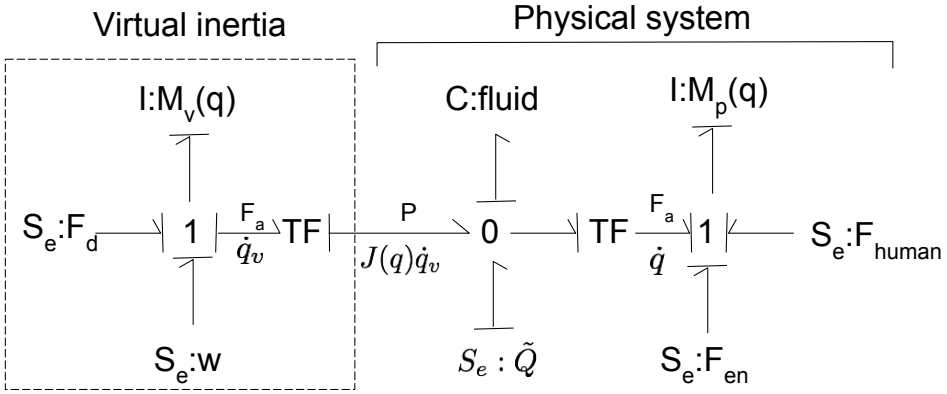

Figure 7.5: Bond graph of the hydraulic human power amplifier interacting with a virtual inertia and additional control effort w and control flow $\tilde{Q}$.

The compressible fluid in the hydraulic cylinder and motor actuators can be interpreted as 2-port springs, with a mechanical port (connected to the inertia M_p of the HPA) and a fluid port. The fluid port is connected, via a kinematic transformation, to a small virtual inertia $M_v \in \Re^{2\times 2}$ which is, in turn, acted on by the desired force F_d as given by (7.12). Figure 7.4 illustrate this physical interconnection and Fig. 7.5 is the bond graph representation. Hence, the dynamics of a virtual inertia M_v (implemented as part of the controller) and the flow into the hydraulic actuators are:

$$M_v \ddot{q}_v = F_d - F_a + w \tag{7.13}$$

$$Q = \begin{bmatrix} Q_\theta \\ Q_x \end{bmatrix} = \underbrace{\begin{bmatrix} A_1 J_A(\theta_p) & 0 \\ 0 & \frac{D_m}{2\pi r_m} \end{bmatrix}}_{\bar{J}(q)} \dot{q}_v + \tilde{Q} \tag{7.14}$$

where $q_v = [\theta_v, x_v]^T$ is the generalized coordinate for the virtual inertia, F_a is the generalized actuator force, Q are the flows to the actuators, and w and $\tilde{Q}$ are the additional control to achieve coordination.

If the virtual inertia M_v and the actual inertia $M_p(q)$ are perfectly coordinated such that $\dot{q}_v(t) \equiv \dot{q}(t)$ (i.e. they become a single rigid inertia), then comparing (7.1) and (7.13), and with w defined such that $w \to 0$ when coordinated, the resulting dynamics become:

$$M_L(q)\ddot{q} + C_p(q,\dot{q})\dot{q} = (\rho + 1)F_{human} + F_{env} + F_{guide} \tag{7.15}$$

where $M_L(q) = M_v + M_p(q)$ is the apparent inertia. Hence the required human force

amplification is fulfilled and after coordination $\dot{q}_v(t) \equiv \dot{q}(t)$, the closed loop system is energetically passive as defined in (7.11). The rest of the control effort would be to i) define the additional hydraulic flow $\tilde{Q}$ to ensure that this coordination indeed occurs, ii) define F_{guide} properly, iii) define the valve and transformer control inputs to achieve the desired flows Q, and iv) to ensure that the passivity property (7.11) is satisfied even during the transient.

7.3.1 Passive Decomposition into locked and shape systems

The coupled system of (7.1) and (7.13) is given by

$$\begin{aligned} M_p(q)\ddot{q} + C_p(\dot{q}, q)\dot{q} &= F_{human} + F_{env} + F_a \\ M_v\ddot{q}_v &= F_d - F_a + w \end{aligned} \tag{7.16}$$

where the generalized coordinates for the physical system are $q = [\theta_p, x_p]^T$ and for the virtual system are $q_v = [\theta_v, x_v]^T$. Since we are interested in the coordination between $\dot{q}$ and $\dot{q}_v$, i.e, $V_E := \dot{q} - \dot{q}_v \to 0$ and in ensuring that the desired dynamics in (7.15) are not disturbed by the coordination control, the passive decomposition transformation [49, 50, 51] is used:

$$\begin{bmatrix} V_L \\ V_E \end{bmatrix} = \underbrace{\begin{bmatrix} I - \phi(q) & \phi(q) \\ I & -I \end{bmatrix}}_{S(q)} \begin{bmatrix} \dot{q} \\ \dot{q}_v \end{bmatrix} \tag{7.17}$$

where $\phi(q) = [M_p(q) + M_v]^{-1} M_v$ and $M_L(q) = M_p(q) + M_v$ is the so-called *locked* system inertia. Since V_E corresponds to the relative speed, it is referred to as the *shape system* velocity, and as $V_L = \dot{q} = \dot{q}_v$ when $V_E = 0$, V_L is referred to as the *locked system* velocity. It is in fact the velocity of the center of mass of the combined virtual and actual system. The system dynamics in the *shape* and *locked* system coordinates are:

$$M_L(q)\dot{V}_L + C_L(q, \dot{q})V_L + C_{LE}(q, \dot{q})V_E = F_d + F_{env} + F_{human} + w \tag{7.18}$$

$$M_E(q)\dot{V}_E + C_E(q, \dot{q})V_E + C_{EL}(q, \dot{q})V_L = F_a + \underbrace{\phi(F_{env})}_{F_{E1}} + \underbrace{\phi(F_{human}) - (I - \phi)(F_d + w)}_{F_{E2}} \tag{7.19}$$

where the transformed *locked* and *shape* systems' inertias are (see [49] for a similar derivation):

$$M_L(q) = M_p(q) + M_v \tag{7.20}$$

$$M_E(q) = (I - \phi(q))^T M_v (I - \phi(q)) \tag{7.21}$$

$$\begin{bmatrix} C_L(q,\dot{q}) & C_{LE}(q,\dot{q}) \\ C_{EL}(q,\dot{q}) & C_E(q,\dot{q}) \end{bmatrix} = S^{-T} \begin{bmatrix} M_p(q) & 0 \\ 0 & M_v \end{bmatrix} \frac{d}{dt}(S^{-1}) + S^{-T} \begin{bmatrix} C(\dot{q},q) & 0 \\ 0 & 0 \end{bmatrix} S^{-1} \tag{7.22}$$

Note that the *locked* and *shape* systems are coupled through the $C_{LE}(q,\dot{q})V_E$ and $C_{EL}(q,\dot{q})V_L$ terms. Defining the decoupling control as:

$$\begin{aligned} w &= C_{LE}(q,\dot{q})V_E \\ F_a &= F_{a1} + C_{EL}(q,\dot{q})V_L \end{aligned} \tag{7.23}$$

and the decoupled system dynamics become:

$$M_L(q)\dot{V}_L + C_L(q,\dot{q})V_L = F_d + F_{env} + F_{human} \tag{7.24}$$

$$M_E(q)\dot{V}_E + C_E(q,\dot{q})V_E = F_{a1} + F_{E1} + F_{E2} \tag{7.25}$$

where F_{E1} and F_{E2} are defined in (7.19).

The passive decomposition transformation $S(q)$ in (7.17) is defined with the property that:

$$\frac{1}{2}V_L^T M_L(q) V_L + \frac{1}{2}V_E^T M_E(q) V_E = \frac{1}{2}\dot{q}^T M_p(q)\dot{q} + \frac{1}{2}\dot{q}_v^T M_v \dot{q}_v \tag{7.26}$$

i.e., the kinetic energy of the system is preserved if $M_L(q)$ and $M_E(q)$ are considered the inertias of the locked and shape systems. This gives rise to the result that (7.24) and (7.25) can be considered individual passive mechanical systems as shown in the Proposition 7.1 below:

Proposition 7.1 *The inertia matrices $M_L(q)$ and $M_E(q)$ in* (7.20)-(7.21) *are positive definite, and the matrices,*

$$\dot{M}_L(q) - 2C_L(q,\dot{q}); \qquad \dot{M}_E(q) - 2C_E(q,\dot{q}) \tag{7.27}$$

are skew-symmetric. Hence, the systems (7.24) *and* (7.25) *satisfy the passivity properties:*

$\exists c_L, c_E$ s.t. $\forall\ t \geq 0$ and all inputs,

$$\int_0^t V_L^T(\tau)(F_d(\tau) + F_{env}(\tau) + F_{human}(\tau)) \cdot d\tau \geq -c_L^2$$
$$\int_0^t V_E^T(\tau)\left(F_{a1}(\tau) + F_{E1}(\tau) + F_{E2}(\tau)\right) \cdot d\tau \geq -c_E^2$$

Furthermore, no mechanical power is required for the decoupling control (7.23)*, i.e.*

$$0 = V_L^T C_{LE}(q, \dot{q}) V_E + V_E^T C_{EL}(q, \dot{q}) V_L$$

Proof *$M_L(q)$ and $M_E(q)$ are positive definite is a direct consequence of* (7.26) *and $S(q)$ being non-singular.*

From direct computation and $\dot{M}_p - 2C_p(q, \dot{q})$ being skew-symmetric, it can be shown that:

$$\begin{bmatrix} \dot{M}_L(q) & 0 \\ 0 & \dot{M}_E(q) \end{bmatrix} - 2 \begin{bmatrix} C_L(q, \dot{q}) & C_{LE}(q, \dot{q}) \\ C_{EL}(q, \dot{q}) & C_E(q, \dot{q}) \end{bmatrix}$$

is skew-symmetric. The skew-symmetry of the matrices in (7.27)*, and $C_{LE}(q, \dot{q}) = -C_{EL}^T(q, \dot{q})$ are direct consequences. The latter shows that decoupling requires no energy.*

By differentiating the locked and shape system energies

$$W_L = \frac{1}{2} V_L^T M_L(q) V_L; \qquad W_E = \frac{1}{2} V_E^T M_E(q) V_E$$

and making use of (7.27)*, we have*

$$\dot{W}_L = V_L^T [F_d + F_{env} + F_{human}].$$

Hence, on integration,

$$W_L(t) - W_L(0) = \int_0^t V_L^T [F_d + F_{env} + F_{human}] \cdot d\tau.$$

Making use of $W_L(t) > 0$, the required passivity property is obtained with $c_L^2 = W_L(t = 0)$. Similar results for the shape system are obtained by differentiating W_E.

To achieve the control objective the shape system dynamics have to be regulated and F_{guide} has to be designed to preserve the energetic passivity of the system. From the locked system dynamics, it can be inferred that the combined system moves only under the influence of the amplified human force and other environmental forces. In the following sections, we design F_{guide} in Eq. (7.13) to provide useful dynamics to assist the human

operator in his/her task. An earlier attempt to implement useful dynamics for HPA can be found in [27].

7.4 Shape System Control - Coordination

Combining Eqs.(7.4),(7.5),(7.7),(7.8),(7.23),(7.25), the shape system dynamics are:

$$M_E(q)\dot{V}_E + C_E(\dot{q}, q)V_E = F_{a1} + F_{E1} + F_{E2} \tag{7.28}$$

$$F_a = F_{a1} + C_{EL}(q, \dot{q})V_L = \bar{J}(q)P \tag{7.29}$$

$$\dot{P} = B_v(q)\left(Q - \bar{J}^T(q)\dot{q}\right) \tag{7.30}$$

where F_{E2} contains measureable or known terms and F_{E1} is potentially unknown as defined in (7.19) and

$$B_v(q) := \begin{bmatrix} \beta/V_1(x_\theta) & 0 \\ 0 & \beta/\bar{V}_m \end{bmatrix}, \quad \bar{J}(q) := \begin{bmatrix} J(\theta_p)A_1 & 0 \\ 0 & \frac{D_m}{2\pi r_m} \end{bmatrix}$$

Since the flow Q is statically related to the the valve u_x in (7.55) and transformer inputs u_1 and u_2 in (7.10), we can assume that Q is the command input.

7.4.1 Flow control input Q

The shape system flow input will be given by:

$$Q = \bar{J}(q)\dot{q}_v + B_v^{-1}(q)\dot{P}_d - \Lambda_p\tilde{P} \tag{7.31}$$

where $\tilde{P} = P - P_d$ is the pressure error, and the desired pressure and actuator force are:

$$P_d = \bar{J}^{-1}(q)F_{a,d} + \begin{bmatrix} P_T A_2/A_1 & 0 \end{bmatrix}^T \tag{7.32}$$

$$F_{a,d} = C_{EL}(\dot{q}, q)V_L - \Lambda V_E - \hat{F}_{E1} - F_{E2} \tag{7.33}$$

$\hat{F}_{E1}$ is an estimate of F_{E1}. $\Lambda_p = \text{diag}(\lambda_{p,\theta}, \lambda_{p,x})$, and Λ are positive definite gain matrices.

The estimate for the external force, $\hat{F}_{E1}$, is obtained from the adaptation algorithm,

$$\dot{\hat{F}}_{E1} = \sigma V_E + \dot{F}_{E1} \tag{7.34}$$

where $\dot{F}_{E1}$ is the best estimate of the derivative of F_{E1} and $\sigma > 0$.

Notice that the flow input (7.31) is consistent with the interaction with the virtual mass in (7.14) with $\tilde{Q} = B_v^{-1}(q)\dot{P}_d - \Lambda_p \tilde{P}$.

7.4.2 Derivation and analysis

To derive the control law (7.31)-(7.33), notice that the desired pressure in Eq. (7.32) will generate the following shape velocity dynamics:

$$M_E(q)\dot{V}_E + C_E(\dot{q}, q)V_E = -\Lambda V_E - \tilde{F}_{E1}(t) + \tilde{F}_a \tag{7.35}$$

where $\tilde{F}_a = F_a - F_{a,d}$ is the error in delivering the desired force in (7.33). Consider a Lyapunov function consisting of the shape system kinetic energy and F_{E1} estimation error energy:

$$W_1 = \frac{1}{2}V_E^T M_E V_E + \frac{1}{\sigma}\tilde{F}_{E1}^T \tilde{F}_{E1} \tag{7.36}$$

Its time derivative is given by:

$$\dot{W}_1 = -V_E^T \Lambda V_E - V_E^T \tilde{F}_{E1}(t) + \frac{\tilde{F}_{E1}^T}{\sigma}(\dot{\hat{F}}_{E1} - \dot{F}_{E1}) + V_E^T \tilde{F}_a \tag{7.37}$$

The proposed adaptation algorithm in Eq. (7.34) gives rise to:

$$\dot{W}_1 = -V_E^T \Lambda V_E + V_E^T \tilde{F}_a \tag{7.38}$$

If $\dot{F}_{E1}$ is not available, an extra term $-V_E \tilde{F}_{E1} \frac{\dot{F}_{E1}}{\sigma}$ will be present. However, if $F_{E1}(t)$ is slowly varying such that $\dot{F}_{E1}/\sigma$ is small, this term can be ignored.

The force error could be written in terms of pressure error using $\tilde{F}_a = \bar{J}(q)\tilde{P}$. To account for the pressure error, the Lyapunov function is augmented to become:

$$W_2 = W_1 + V_1(x_\theta) W_V(\tilde{P}_\theta) + \frac{\bar{V}_m}{2\beta}\tilde{P}_x^2 \tag{7.39}$$

where $\tilde{P} = [\tilde{P}_\theta, \tilde{P}_x]$ and the additional terms correspond to the pressure error energy for the pitch and reach axes respectively. $\tilde{W}_V(\tilde{p})$ is the volumetric pressure error energy density associated with compressing the fluid from pressure p_d to $p_d + \tilde{p}$ as defined in [56]. For constant bulk modulus β, it is independent of p_d and is given by:

$$\tilde{W}_V(\tilde{p}) := \beta \left[e^{\frac{\tilde{p}}{\beta}} - \left(1 + \frac{\tilde{p}}{\beta}\right) \right]. \tag{7.40}$$

The pressure error energy terms for the pitch and reach axes take different forms because

the fluid volume for the rotary (reach) actuator does not change with the rotary motion whereas the fluid volume for the cylinder actuator (pitch) does change with cylinder movement according to (7.30). However, from Taylor expansion of (7.40), they are similar in that:

$$V_1(x_\theta)\tilde{W}_V(\tilde{P}_\theta) \approx V_1(x_\theta)\frac{\tilde{P}_\theta^2}{2\beta} + H.O.T.$$

Proposition 7.2 *The pitch and reach pressure error energy functions satisfy:*

$$\begin{aligned}&\frac{d}{dt}\left[V_1(x_\theta)\tilde{W}_V(\tilde{P}_\theta) + \frac{\bar{V}_m}{2\beta}\tilde{P}_x^2\right]\\ =&\tilde{P}^T\left[\begin{bmatrix}1+\frac{W_v}{\tilde{P}_\theta} & 0\\ 0 & 1\end{bmatrix}Q - \bar{J}^T(q)\dot{q} - \begin{bmatrix}\frac{V_1(x_\theta)}{B(\tilde{P}_\theta)} & 0\\ 0 & \frac{\bar{V}_m}{\beta}\end{bmatrix}\dot{P}_d\right]\end{aligned} \tag{7.41}$$

where

$$\frac{1}{B(\tilde{P}_\theta)} = \frac{e^{\tilde{P}_\theta/\beta}-1}{\tilde{P}_\theta} \approx \frac{1}{\beta} + \frac{\tilde{P}_\theta}{2\beta} + H.O.T. \tag{7.42}$$

and $(1+\tilde{W}_V(\tilde{P}_\theta)/\tilde{P}_\theta) > 0$.

Proof *By direct computation and using* (7.30), (7.9) *and* (7.3), *we have*

$$\begin{aligned}\frac{d}{dt}\left[V_1\tilde{W}_V\right] &= \left[\tilde{P}+\tilde{W}_V\right]Q_\theta - \tilde{P}A_1\dot{x}_\theta - \tilde{P}\frac{V_1(x_\theta)}{B(\tilde{P}_\theta)}\dot{P}_{d,\theta}\\ \frac{d}{dt}\left[\frac{\bar{V}_m}{2\beta}\tilde{P}_x^2\right] &= \tilde{P}_x\left(Q_x - \frac{\bar{V}_m}{\beta}\dot{P}_{d,x} - \frac{D_m}{2\pi r_m}\dot{x}_p\right)\end{aligned}$$

The desired relation (7.41) *is an organization of these.*

Remark 7.1 *Proposition 7.2 shows that the hydraulic cylinder and motor system is a passive 3-port system with a hydraulic port, a mechanical port, and a port relating to desired pressure. Interestingly, the hydraulic port supply rate for the hydraulic cylinder is* $Q_\theta\tilde{P}_\theta(1+\tilde{W}_V/\tilde{P})$ *instead of the more conventional* $Q_x\tilde{P}_x$ *for the hydraulic motor. The difference is due to the fluid volume being constant in the hydraulic motor but varying in the hydraulic cylinder. For details, please see [56].*

We are now ready to define the flow input Q. From (7.41), if we approximate

$$1+\tilde{W}_V/\tilde{P}_\theta \approx 1; \quad B(\tilde{P}_\theta) \approx \beta$$

(the approximation errors are of the order $\tilde{P}_\theta$), the flow input:

$$Q_1 = \bar{J}^T(q)\dot{q}_v + B_v(q)\dot{P}_d$$

would generate a term $-\tilde{P}^T\bar{J}^T(q)V_E = -V_E^T\tilde{F}_a$ to cancel out the force error term in (7.38). Let

$$Q = Q_1 - \Lambda_p\tilde{P}$$

where the second term with $\Lambda_p = \text{diag}(\lambda_{p,\theta}, \lambda_{p,x})$ being positive definite will be used to compensate for the approximation error. Then,

$$\dot{W}_2 = -V_E^T\Lambda V_E + \tilde{P}^T\begin{bmatrix} 1+\frac{W_v}{\tilde{P}_\theta} & 0 \\ 0 & 1 \end{bmatrix}\Lambda_p\tilde{P}$$
$$+ \tilde{P}_\theta\left[\frac{1}{\beta} - \frac{1}{B(\tilde{P}_\theta)}\right]V_1(x_\theta)\dot{P}_{d,\theta} + \tilde{W}_V(\tilde{P}_\theta)Q_{1,\theta}$$

Note that the last two terms are quadratic in $\tilde{P}_\theta$. Thus, with $\lambda_{p,\theta}$ (possibly time-varying) in Λ_p sufficiently large, we have for some $\lambda_{p1} > 0$,

$$\dot{W}_2 \leq -V_E^T\Lambda V_E - \lambda_{p1}\|\tilde{P}\|^2.$$

Applying Babalat's lemma, this analysis shows that $V_E \to 0$ and $\tilde{P} \to 0$.

Theorem 7.1 *With the input flow control law and the environment force estimator* (7.31)-(7.34)*, assuming that $\dot{F}_{E1}$ is well estimated, the velocity coordination error $V_E = \dot{q} - \dot{q}_v \to 0$ and the pressure error $\tilde{P} = P - P_{a,d} \to 0$ asymptotically. Furthermore, $V_L \to \dot{q}$, i.e. the locked system velocity converges to velocity of the HPA.*

Remark 7.2

1. *With the natural energies of the hydraulic actuators in the Lyapunov function* (7.39)*, the shape system control results in a natural passive interconnection between the mechanical system and the hydraulic system. The experimental study in [56] reveals that this method requires fewer parameter tuning (than conventional arbitrarily defined quadratic terms in $\tilde{P}$) and has better performance especially in the presence of measurement noise.*

2. *The natural energy function used in* (7.39) *assumes that the bulk modulus β is a constant. The general form of pressure dependent bulk modulus [56], can also be used.*

3. *Although the control is written in terms of pressure feedback, it can be implemented using the actuator force sensing (as is the case in our experiments).*

7.5 Locked system control - Guidance F_{guide}

With $F_d = \rho F_{human} + F_{guide}$, the locked system dynamics are given by (7.24):

$$M_L(q)\dot{V}_L + C_L(q,\dot{q}) = F_{guide} + (\rho+1)F_{human} + F_{env} \tag{7.43}$$
$$F_{guide} = F_{PVFC} + F_{OA}$$

Here, two types of guidance are considered for the design of F_{guide}: 1) with F_{PVFC}, the HPA is guided towards a preferred direction of motion encoded with a velocity field; 2) with F_{OA}, the HPA is prevented from entering prohibited regions. The former will be provided using a passive velocity field controller (PVFC) [60, 49] and the latter will be provided via an artificial potential field. In both cases, the guidance dynamics will have intrinsic passivity properties to enhance system safety.

7.5.1 Passive Velocity Field Control (PVFC)

A general approach to task guidance is to encode the task as the desired velocity field $q \mapsto V(q)$ which specifies the desired velocity at each configuration. Instead of using the time to specify the desired motion, task encoding as velocity fields specifies the best motion direction given the current position. For HPA applications, there is likely preferred path of motion for completing the task. Path/contour following can be naturally coded this way where the flow of the velocity field converges to the preferred path. An example velocity field is shown in Fig. 7.6 which guides the tip of the HPA to converge to and follow a circular path in the Cartesian workspace.

In this dissertation, the Passive Velocity Field Control (PVFC) is used to incorporate passive dynamics into the locked system (7.24) to guide the operator to follow a scaled copy of the desired velocity field $V(q)$ while the controller itself does not generate or dissipate energy. In the absence of any human or environmental input, the PVFC controller will cause the locked system velocity $V_L(t) \to \bar{\delta}(t)V(q(t))$ where $\bar{\delta}^2(t)$ is proportional to the current amount of kinetic energy in the system. The human operator (or the environment) can increase or decrease the speed by injecting or absorbing energy. In this way, it is possible to provide path guidance without violating passivity.

The PVFC design procedure, described in details in [60], is summarized below.

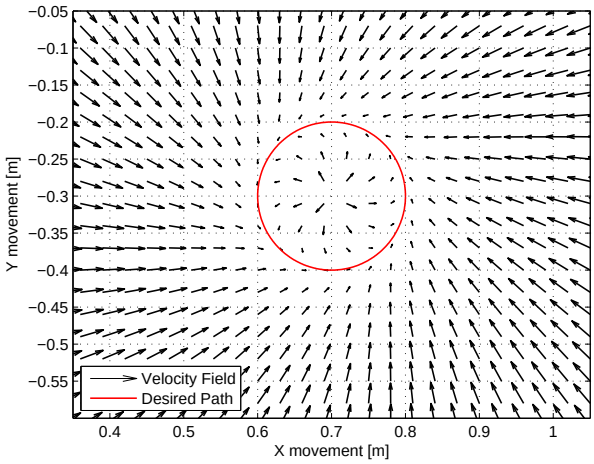

Figure 7.6: Velocity field in the Cartesian workspace for the tip of the HPA tracing a circle.

Augmented locked system

To define PVFC, we first augment the locked system dynamics with a 1-DoF fictitious flywheel dynamics:

$$\underbrace{\begin{bmatrix} M_L(q) & 0 \\ 0 & M_F \end{bmatrix}}_{\bar{M}(\bar{q})} \begin{bmatrix} \dot{V}_L \\ \ddot{q}_F \end{bmatrix} + \underbrace{\begin{bmatrix} C_L(q,\dot{q}) & 0 \\ 0 & 0 \end{bmatrix}}_{\bar{C}(\bar{q},\dot{\bar{q}})} \underbrace{\begin{bmatrix} V_L \\ \dot{q}_F \end{bmatrix}}_{\dot{\bar{q}}} = \underbrace{\begin{bmatrix} F_{PVFC} \\ \tau_F \end{bmatrix}}_{\bar{T}} + \begin{bmatrix} F_{OA} + (\rho+1)F_{human} + F_{env} \\ 0 \end{bmatrix} \quad (7.44)$$

where M_F is the fictitious flywheel inertia, scalars q_F, $\dot{q}_F$ and τ_F are its angle, speed and input torque, $\bar{q} = [q^T, q_F]^T \in \Re^3$, $\bar{M}(\bar{q}) \in \Re^{3\times3}$ and $\bar{C}(\bar{q},\dot{\bar{q}}) \in \Re^{3\times3}$ are the configuration, inertia and Coriolis matrix of the augmented system, $\bar{T}$ is the control that couples the fictitious flywheel with the locked system.

In order to control and utilize the fictitious flywheel, the desired velocity field $V : q \in \Re^2 \mapsto V(q) \in \Re^2$ needs to be augmented as:

$$\bar{V}(\bar{q}) = \begin{bmatrix} V(q)^T & V_F(q) \end{bmatrix}^T \in \Re^3 \quad (7.45)$$

such that the kinetic energy of the augmented system is constant when the augmented

field is tracked. This can be accomplished by ensuring that for all $q \in \Re^2$,

$$\bar{E} = \frac{1}{2}\bar{V}^T(\bar{q})\bar{M}(q)\bar{V}(\bar{q})$$

where $\bar{E}$ is a sufficiently large constant. In other words, the desired flywheel velocity field is given by:

$$V_F(q) = \sqrt{\frac{2}{M_F}\left(\bar{E} - \frac{1}{2}V(q)^T M_L(q)V(q)\right)} \tag{7.46}$$

Coupling Control

With the augmented locked system and velocity field, the coupling control $\bar{T}$ in (7.44) is designed as

$$\bar{T} = \Omega(\bar{q}, \dot{\bar{q}})\dot{\bar{q}} \tag{7.47}$$

where $\Omega(\bar{q}, \dot{\bar{q}}) \in R^{3\times 3}$ is skew-symmetric and defined as:

$$\Omega(\bar{q}, \dot{\bar{q}}) = \frac{1}{2\bar{E}}(\bar{w}\bar{P}^T - \bar{P}\bar{w}^T) + \gamma(\bar{P}\bar{p}^T - \bar{p}\bar{P}^T) \tag{7.48}$$

where

$$\bar{P}(\bar{q}) := \bar{M}(\bar{q})\bar{V}(\bar{q}); \quad \bar{p}(\bar{q}, \dot{\bar{q}}) := \bar{M}(\bar{q})\dot{\bar{q}}$$
$$\bar{w}(\bar{q}, \dot{\bar{q}}) := \bar{M}(\bar{q})\dot{\bar{V}}(\bar{q}) + \bar{C}(\bar{q}, \dot{\bar{q}})\bar{V}(\bar{q})$$

Here, $\bar{P}(\bar{q})$ is the desired momentum field, $\bar{p}(\bar{q}, \dot{\bar{q}})$ is the actual momentum, $\bar{w}(\bar{q}, \dot{\bar{q}})$ is the covariant derivative of the desired momentum field and γ is a feedback gain.

Roughly speaking, the first skew-symmetric term in (7.48) generates the feedforward coupling for tracking a scaled copy of $\bar{V}(\bar{q})$, and the second skew-symmetric term in (7.48) generates the error feedback. The fact that $\Omega(\bar{q}, \bar{\dot{q}})$ is skew symmetric means that the power generated by the coupling torque is 0 since $\dot{\bar{q}}^T\bar{T} = \dot{\bar{q}}^T\Omega(\bar{q}, \dot{\bar{q}})\dot{\bar{q}} = 0$.

With the PVFC in (7.44)-(7.48), the augmented locked system dynamics become:

$$\bar{M}(\bar{q})\ddot{\bar{q}} + \bar{Y}(\bar{q}, \dot{\bar{q}})\dot{\bar{q}} = \begin{bmatrix} F_{OA} + (\rho+1)F_{human} + F_{env} \\ 0 \end{bmatrix} \tag{7.49}$$

where $\bar{Y}(\bar{q}, \dot{\bar{q}}) = \bar{C}(\bar{q}, \dot{\bar{q}}) - \Omega(\bar{q}, \dot{\bar{q}})$. It has the following properties.

Theorem 7.2 *$\bar{M}(\bar{q})$ and $Y(\bar{q},\dot{\bar{q}})$ in (7.49) satisfy:*

$$\dot{\bar{M}}(\bar{q}) - 2Y(\bar{q},\dot{\bar{q}}) \quad \textit{is skew-symmetric.}$$

Eq.(7.49) has the passivity that: there exists c_{PVFC} such that for all inputs, and any $t > 0$,

$$\int_0^t V_L^T[(\rho+1)F_{human} + F_{env} + F_{OA}]d\tau \geq -c_{PVFC}^2$$

Furthermore, when $(\rho+1)F_{human} + F_{env} + F_{OA} = 0$, let $\delta := sign(\gamma)\sqrt{\frac{\dot{\bar{q}}^T\bar{M}(\bar{q})\dot{\bar{q}}}{2\bar{E}}}$. Then, δ is a constant and $\dot{\bar{q}} \to \delta\bar{V}(\bar{q}(t))$ (and therefore $\dot{q} \to V(q)$) exponentially except for the initial condition of $\dot{\bar{q}}(t=0) = -\bar{V}(\bar{q}(t=0))$.

Proof *Since $\Omega(\bar{q},\dot{\bar{q}})$ and $\dot{\bar{M}} - 2C_L$ are skew-symmetric, $\dot{\bar{M}} - 2Y$ is skew-symmetric.*

The passivity property can be obtained using the kinetic energy of the augmented system as a storage function and the fact that $\dot{\bar{M}} - 2Y$ is skew-symmetric:

$$W_{PVFC} = \frac{1}{2}\dot{\bar{q}}^T\bar{M}(\bar{q})\dot{\bar{q}}$$
$$\dot{W}_{PVFC} = V_L[(\rho+1)F_{human} + F_{env} + F_{OA}]$$

so that the desired passivity property is obtained on integration and with $c_{PVFC}^2 = W_{PVFC}(t=0)$.

When $(\rho+1)F_{human} + F_{env} + F_{OA} = 0$, then W_{PVFC} is constant so that δ is also a constant. Let $e_\delta := \dot{\bar{q}} - \delta\bar{V}(\bar{q})$. Using the Lyapunov function,

$$W_\delta := \frac{1}{2}e_\delta^T\bar{M}(\bar{q})e_\delta$$

it can be shown (see [60] for details) that

$$\dot{W}_\delta(t) \leq -4\gamma\delta\bar{E}\cdot\mu(0)W_\delta(t)$$

where

$$\mu(t) = \frac{1}{2}\left[1 + \frac{\bar{V}(\bar{q}(t))\bar{M}(\bar{q}(t))\dot{\bar{q}}(t)}{2\delta\bar{E}}\right].$$

Hence, $e_\delta \to 0$ exponentially from any initial condition except when $\mu(t=0) = 0$ or $\dot{\bar{q}}(0) = -\bar{V}(\bar{q}(0))$.

Thus, as the kinetic energy of the system increases (with input by the human operator or the environment), the speed at which the desired velocity is tracked will also increase.

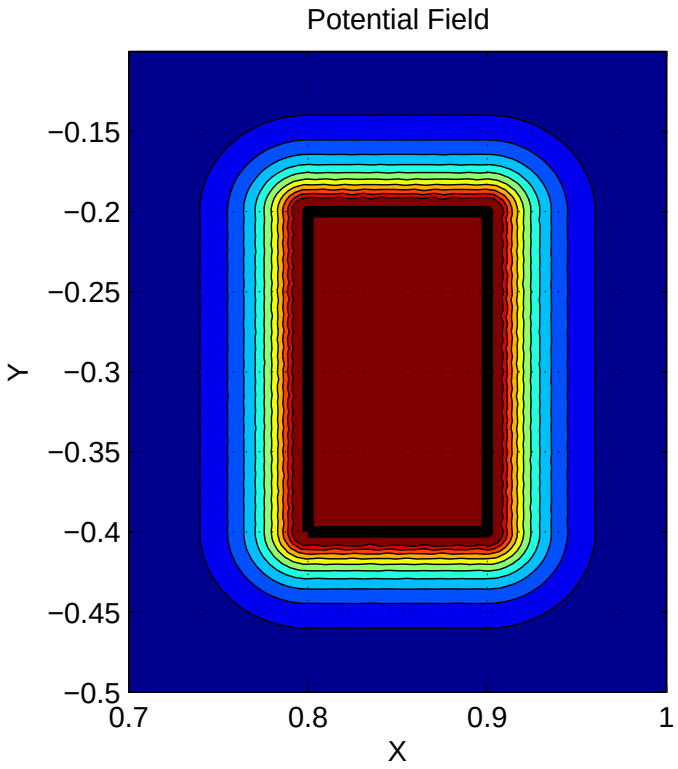

Figure 7.7: An example potential field for a rectangular obstacle in Cartesian (workspace) coordinates.

7.5.2 Obstacle Avoidance

To prevent the machine from entering the prohibited area in the workspace to protect itself or other objects, artificial potential fields [45] are used to provide the operator tactile feedback to repel the machine from running into the obstacle.

The potential field is designed to be a non-negative continuous and differentiable function that increases towards the obstacle. Its effect should be limited to the obstacle's vicinity to avoid undesirable effects elsewhere.

For a point obstacle at m in the Cartesian workspace of the tip of HPA, the field is defined as:

$$U_p(q,m) = \begin{cases} U_d\, e^{-k_{oa}\Lambda(q,m)} & \Lambda(q,m) \leq \Lambda_0 \\ 0 & \Lambda(q,m) > \Lambda_0 \end{cases} \tag{7.50}$$

where $\Lambda(q,m)$ is the Cartesian distance of the tip of HPA with generalized coordinate q to an obstacle at m. k_{oa}, U_d and Λ_o are parameters that define the decay rate, magnitude, and the domain size of the field. The discontinuity of (7.50) is negligible if k_{oa} is sufficiently large compared to Λ_o. It is extended to a region $\mathcal{B}$ with boundaries by integrating individual

U_p's at points along the boundaries: i.e.

$$U_{oa}(q) = \int_{m \in \partial \mathcal{B}} U_p(q, m)\, ds$$

Figure 7.7 shows an example for a rectangular obstacle region.

The obstacle avoidance guidance force is the negative derivative of $U_{oa}(q)$:

$$F_{OA} = -\left(\frac{\partial}{\partial q} U_{oa}(q)\right)^T \tag{7.51}$$

In summary, the guidance control $F_{guide} \in \Re^2$ is the combination of PVFC in (7.47) and obstacle avoidance in (7.51):

$$\begin{bmatrix} F_{guide} \\ M_F \ddot{q}_F \end{bmatrix} = \Omega(\bar{q}, \dot{\bar{q}})\dot{\bar{q}} + \begin{bmatrix} F_{OA} \\ 0 \end{bmatrix}. \tag{7.52}$$

7.6 Hydraulic Flow Control

The desired hydraulic flow $Q = [Q_p, Q_x]^T$ is specified to achieve coordination in the shape system control in (7.31)-(7.34). Note that the decoupling w in (7.23) and F_{guide} for the locked system are used in (7.33) as part of F_{E2} defined in (7.19). To achieve the desired flow Q, the commands to the hydraulic transformer (for the pitch axis) and to the servo-valve (for the reach axis) are needed.

7.6.1 Transformer control - Pitch

The displacements, u_1, u_2 of both pump/motor units of the hydraulic transformer used in this study are used simultaneously to control the flow Q_p via (7.10). This redundancy also allows the transformer speed ω to be controlled so as to optimize efficiency (with a supervisory control) and to avoid difficulties with low-speed operation due to stiction [53]. In this study, the desired transformer speed ω_d are arbitrarily specified for simplicity.

To specify u_1 and u_2, we first define the desired hydraulic torque U_{total} in (7.10) to control the transformer speed with a proportional-integral (PI) + feedforward controller as in Section 6.3.2:

$$\begin{aligned} \dot{\tilde{\omega}}_I &= \tilde{\omega} := \omega - \omega_d \\ U_{total} &= J\dot{\omega}_d - K_{pt}\tilde{\omega} - K_{It}\tilde{\omega}_I + B_t\omega_d \end{aligned} \tag{7.53}$$

with K_p, K_I being positive constants. The convergence of this controller is proved in Section 6.3.2.

Following Section. 6.3.2, the displacement inputs u_1 and u_2 are obtained by solving for Q_p and U_{total} in (7.10):

$$\begin{bmatrix} u_1 \\ u_2 \end{bmatrix} = \begin{bmatrix} 0 & \omega \cdot \frac{D_{2,max}}{2\pi} \\ (P_A - P_T)\frac{D_{1,max}}{2\pi} & (P_T - P_B)\frac{D_{2,max}}{2\pi} \end{bmatrix}^{-1} \begin{bmatrix} Q_\theta^d \\ U_{total} \end{bmatrix} \tag{7.54}$$

where $P_B = P_\theta$. To avoid singularity when $\omega = 0$, ω can be replaced by ω_d in Eq. (7.54).

7.6.2 Valve control - reach

The servo-valve command u_x to achieve the reach axis flow requirement Q_x in Eq. (7.31) is obtained from Eq. (7.6):

$$u_x = \begin{cases} \frac{Q_x}{K_q\sqrt{P_s - P_x}} & \text{if } u_x \geq 0 \\ \frac{Q_x}{K_q\sqrt{P_s + P_x}} & \text{if } u_x < 0 \end{cases} \tag{7.55}$$

Since P_θ and P_x can be obtained from the force sensor measurements via (7.4) and (7.7), pressure sensors are not necessary to implement (7.54) or (7.55).

Note that the flow for each DoF could be provided either by a transformer or a valve. Besides the fact that only one prototype transformer is available in our laboratory, an added benefit of controlling one DoF with a valve and the other with a transformer is that the control performance with these control devices can be compared.

7.7 Closed Loop Passivity Property

In this section, we study the energetic passivity property of the HPA under the proposed control. Assuming that the human and physical environments are strictly energetically passive with respect to supply rates $-\dot{q}^T F_{human}$ and $-\dot{q}^T F_{env}$ which are physical power *inputs* from the HPA, then coupling stability with these environments will be guaranteed if the HPA satisfies the energetic passivity property defined in (7.11), i.e. for some c^2,

$$\int_0^t \dot{q}^T[(\rho + 1)F_{human} + F_{env}]d\tau \geq c^2. \tag{7.56}$$

Note that the human and physical environment interact via the physical system's velocity $\dot{q}$, not the locked system velocity V_L. Hence the locked system passivity property in Theorem 7.2 is not sufficient.

For the locked system (7.43) with F_{guide} in (7.52), using the storage function,

$$W_{lock} := \frac{1}{2}\dot{\bar{q}}^T \bar{M}(\bar{q})\dot{\bar{q}} + U_{oa}(q)$$

we have:

$$\dot{W}_{lock} = V_L^T \left[(\rho+1)F_{human} + F_{env}\right] + \left(\frac{\partial}{\partial q}U_{oa}\right) V_E$$

Thus, after V_E has converged to 0 so that $V_L = \dot{q}$, we have the desired energetic passivity property (7.11).

In the transient, if for some finite bound $M < \infty$,

$$-\int_0^t V_E^T \underbrace{\left[(\rho+1)F_{human} + F_{env} + F_{OA}\right]}_{F_{ext}} d\tau < M \tag{7.57}$$

then, (7.11) is also achieved. Condition (7.57) is satisfied if $V_E(\cdot) \in L_1$ and F_{ext} is bounded.

Unfortunately, in the shape system control, because F_{E1} in (7.33) has to be estimated, Theorem 7.1 only guarantees that $V_E \to 0$ but not necessarily exponentially, hence, theoretically, V_E may not be L_1.

To strengthen the enforcement of the passivity property (7.11), either the shape system control or the locked system control can be modified as follows.

Theorem 7.3 *The closed loop passivity property* (7.11) *is observed with either of the following control modifications:*

1. *F_{guide} for the locked system in* (7.43) *is modified with additional damping:*

$$F_{guide} = F_{PVFC} + F_{OA} - \lambda_L V_L \tag{7.58}$$

such that: there exists $M < \infty$ s.t. for all $t \geq 0$,

$$-\int_0^t \left\{V_E^T F_{ext} + \lambda_L \|V_L\|^2\right\} \cdot \; d\tau < M \tag{7.59}$$

2. *Let $F_{ext} = [F_{ext,\theta}, F_{ext,x}]^T$. $F_{a,d}$ in* (7.33) *for the shape system is modified with a robust feedback term:*

$$F_{a,d} = C_{EL}(\dot{q}, q)V_L - \Lambda V_E - \hat{F}_{E1} - F_{E2} - F_{pass,\theta} \cdot \mathrm{sgn}(V_{E,\theta}) - F_{pass,x} \cdot \mathrm{sgn}(V_{E,x}) \tag{7.60}$$

where $V_E = (V_{E,\theta}, V_{E,x})^T$ and $F_{pass,\theta/x}(\tau)$ is chosen s.t. $F_{pass,\theta/x}(\tau) > |F_{ext,\theta/x}(\tau)|$.

Proof *With the locked system modification* (7.58)*,*

$$\dot{W}_{lock} = (\dot{q} - V_E)^T \left[(\rho+1)F_{human} + F_{env} - \lambda_L V_L\right] - F_{OA}V_E$$

On integration and using the condition (7.59)*,* (7.11) *is obtained.*

With the shape system modification (7.60)*, notice first that convergence of* V_E *is not compromised, since the modification introduces the negative term,* $-F_{pass,\theta}|V_{E,\theta}| - F_{pass,x}|V_{E,x}|$ *to the derivative of Lyapunov function* $\dot{W}_1$ *in* (7.38)*.*

Using the total system energy $W_{total} = W_{lock} + W_2$ *where* W_2 *is defined in* (7.39)*,* $\dot{W}_2$ *is modified to be:*

$$\begin{aligned}\dot{W}_2 &\leq \dot{q}^T \left[(\rho+1)F_{human} + F_{env}\right] + F_{ext,\theta}V_{E,\theta} + F_{ext,x}V_{E,x} \\ &\quad - F_{pass,\theta}|V_{E,\theta}| - F_{pass,x}|V_{E,x}| \\ &\leq \dot{q}^T \left[(\rho+1)F_{human} + F_{env}\right]\end{aligned}$$

so that the desired passivity property is preserved.

The integral (7.57) can be thought of as extraneous energy generation that may cause passivity to be violated. Both control modifications in Theorem 7.3 dissipate energy either in the locked system or in the shape system. Passivity is preserved if the extraneous energy generation does not exceed the extra dissipation by a finite amount. In this regard, the locked and shape system modifications can also be combined with less stringent gains to achieve the needed net dissipation. Similarly, an imperfect convergence of V_E can also be compensated this way. Furthermore, friction, which is inevitable in physical systems, may provide sufficient dissipation already that additional damping is not necessary.

7.8 Experimental Results

The controller proposed in this chapter has been experimentally implemented on a 2-DoF Human Power Amplifier (HPA). The physical parameters are listed in Table 7.8. For the pitch axis, the prototype hydraulic transformer shown in Chapter 5 was used. For the reach axis, the servo-valve was used (MTS series 252), which is rated at 9.5 L/min (2.5 gal/min) and has a bandwidth of 250 Hz. The shape system coordination control parameters are summarized in Table. 7.2.

Table 7.1: Physical parameters of the HPA

Parameter	Symbol	Value
Inertia Matrix	$M_p(q)$	$\text{diag}([2.5 + 7 \cdot x_p^2 \text{ kg} \cdot \text{m}^2, 7 \text{ kg}])$
Virtual inertia	M_v	$0.1 M_p(x_p = 0)$
Piston area	A_1	$1.187 \cdot 10^{-3}$ m^2
Motor Displacement	D_m	12.9 cc/rev
Transformer Displacement	D_1,D_2	3.15 cc/rev
Transformer Inertia	J	2×10^{-5} kg·m^2

7.8.1 Force amplification

We first examine the force amplification aspect with amplification factor $\rho = 7$ and with guidance control turned off ($F_{guide} = 0$).

Table 7.2: Shape system control parameters

Gain	Symbol	Value
V_E gain	Λ	$\text{diag}([110, 110])$
Pressure feedback gain - pitch	$\lambda_{p,\theta}$	$1 \cdot 10^{-10}$
Pressure feedback gain - reach	$\lambda_{p,x}$	$1 \cdot 10^{-10}$
Estimation	σ	5000

Figures 7.8–7.11 show the experimental results for the 4 different operating conditions. In each of the figure, the torque tracking is shown for the pitch axis, and the force tracking is shown for the reach axis. Velocity coordinations are also plotted to show the coordination control in Section 7.4 is working as intended.

Figure 7.8 shows the case when the HPA is opposing some load being applied to it. Figure 7.9 shows the case where the mass was loaded and unloaded rapidly. A rapid change in torque delivered is observed. Figure 7.10 shows the case when the HPA is freely moving without hitting any obstacles or being under some external load. Lastly, Fig. 7.11 shows the case when the operator used the HPA to repeatedly contact the hard surface. Repeated contact occurred in the pitch direction for the first 30 seconds, and in the reach direction for the remainder of the experiment.

Overall, the measured actuator force F_a and the desired force (ρF_{human}, $\rho = 7$), as well as the actual velocity $\dot{q}$ and the velocity of the virtual mass $\dot{x}_v$ match quite well for both the pitch and reach axes. The absolute torque/force errors are of the order of 8Nm and 2N for the pitch and reach degrees of freedom, and the coordination errors are of the

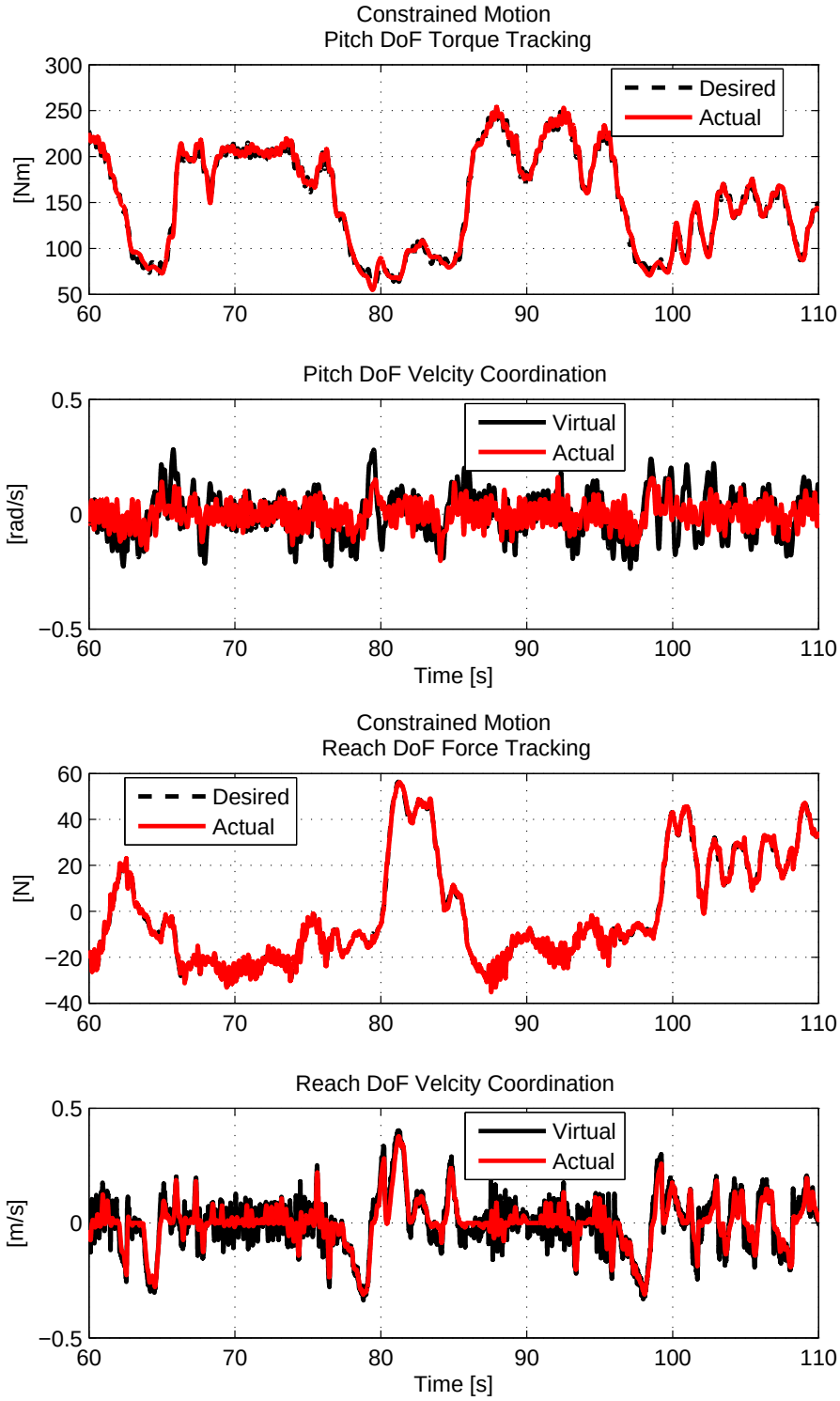

Figure 7.8: Constrained motion. Top: pitch torque and angle; bottom: reach force and displacement. The RMS pitch torque error is 5.5 Nm; RMS pitch coordination error is 0.076 rad/s. The RMS reach force error is 1.24 N; RMS reach coordination error is 0.047 m/s.

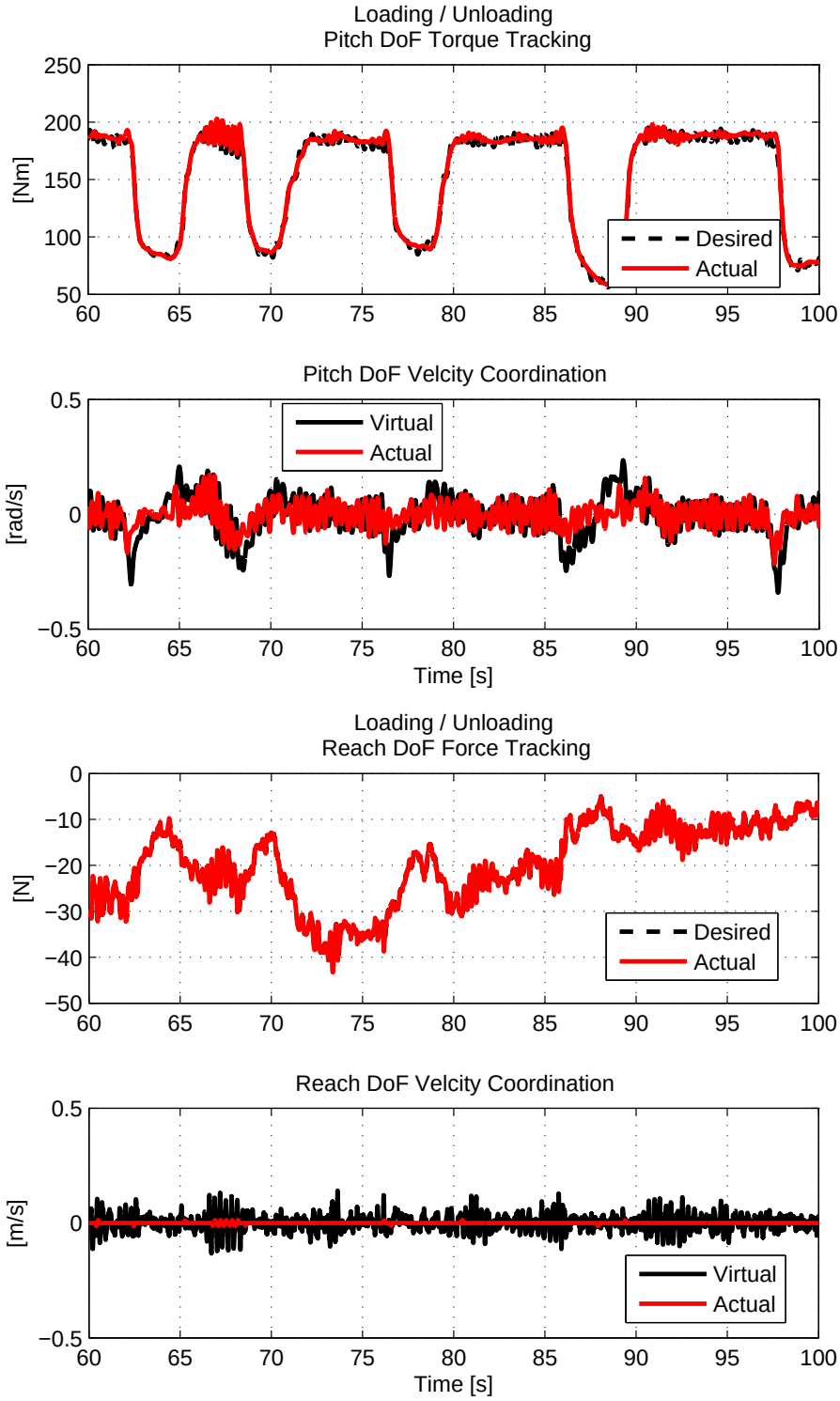

Figure 7.9: Loading/Unloading task. Top: pitch torque and angle; bottom: reach force and displacement. The RMS pitch torque error is 4.97 Nm; RMS pitch coordination error is 0.056 rad/s. The RMS reach force error is 0.73 N; RMS reach coordination error is 0.036 m/s.

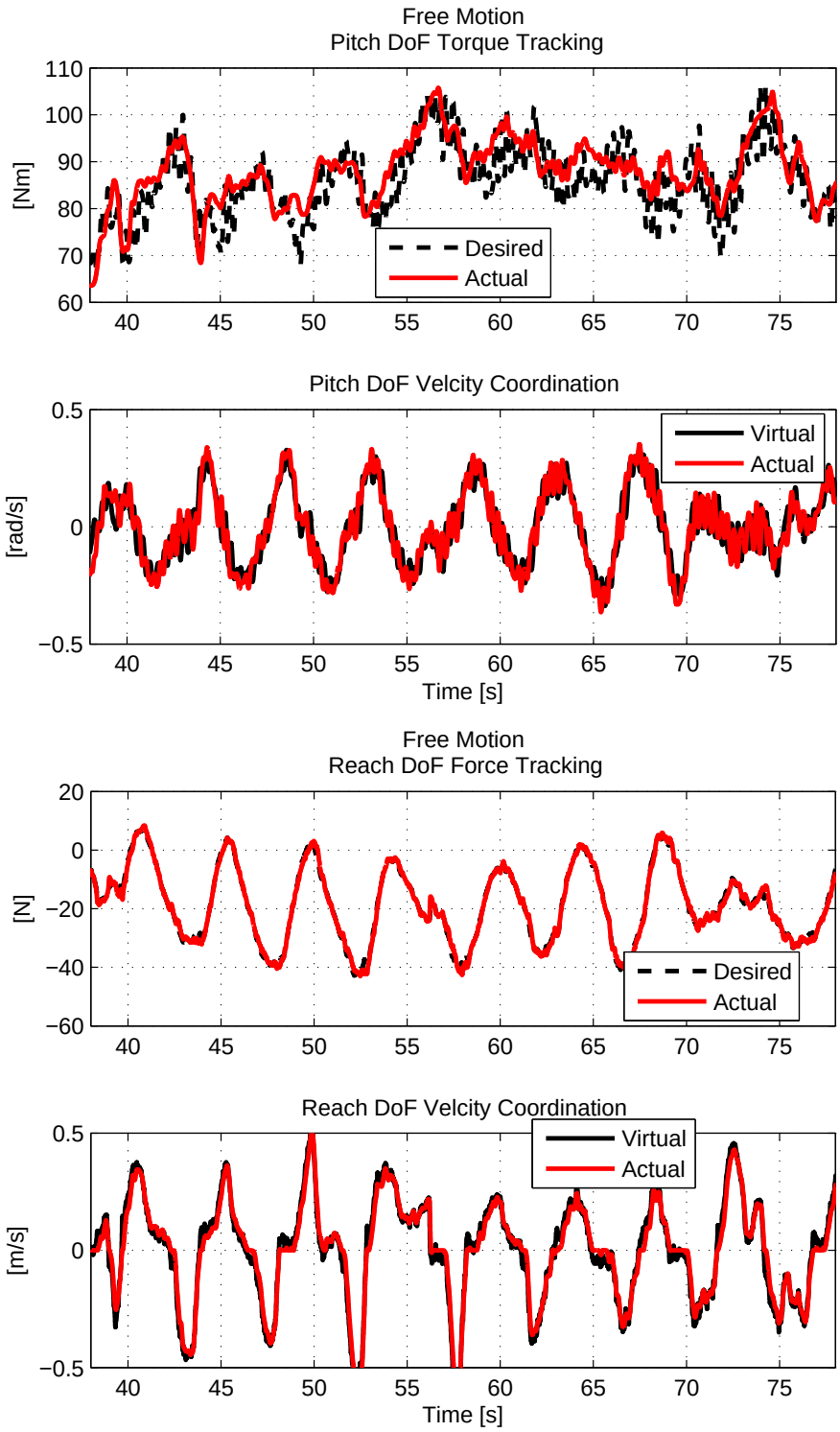

Figure 7.10: Unconstrained motion. Top: pitch torque and angle; bottom: reach force and displacement. The RMS pitch torque error is 5.38 Nm; RMS pitch coordination error is 0.061 rad/s. The RMS reach force error is 1.20 N; RMS reach coordination error is 0.034 m/s.

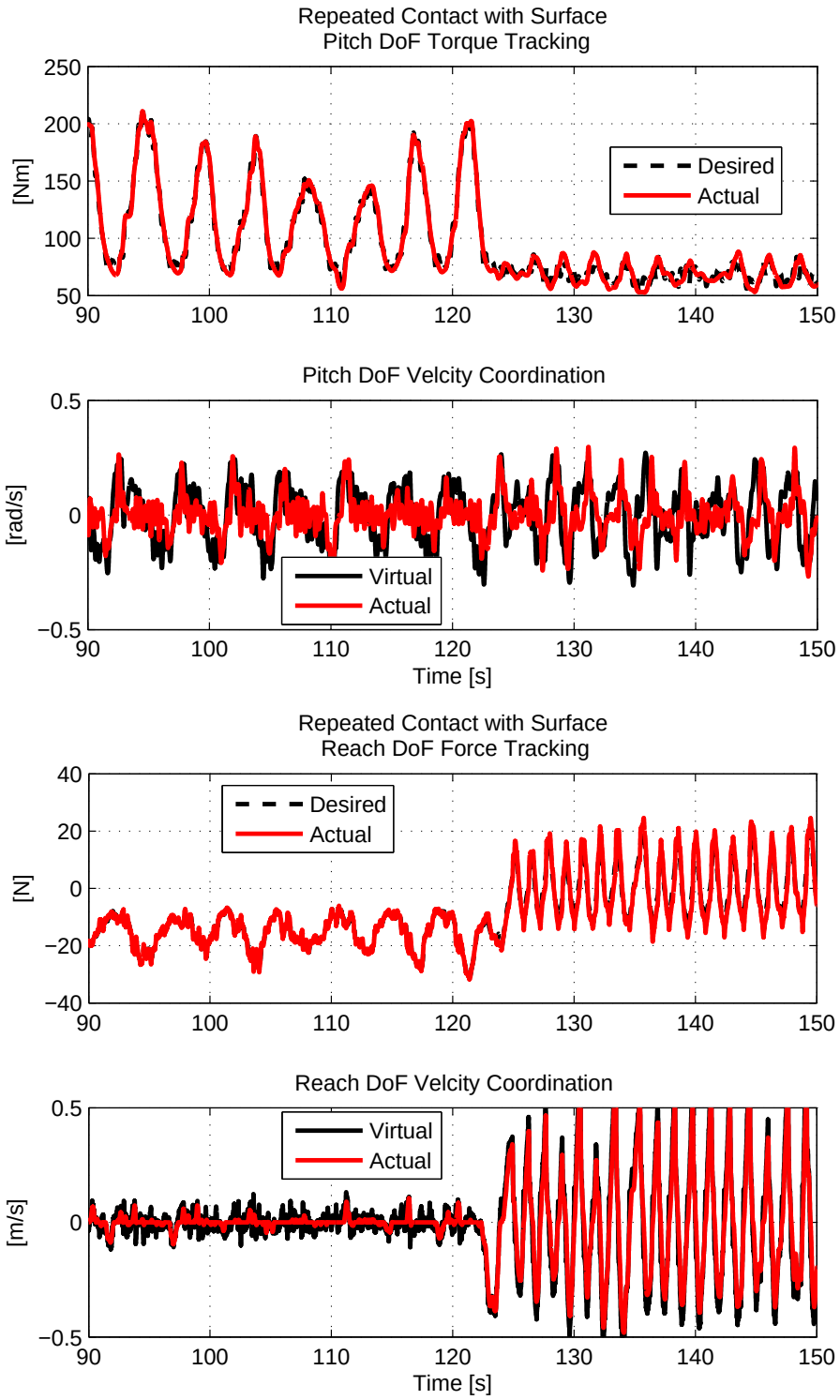

Figure 7.11: Repated Contact with Surface. Top: pitch torque and angle; bottom: reach force and displacement. The RMS pitch torque error is 5.83 Nm; RMS pitch coordination error is 0.12 rad/s. The RMS reach force error is 1.98 N; RMS reach coordination error is 0.049 m/s.

order of 0.1 rad/s and 1 m/s. At $\rho = 7$ and moment arm of $\sim 1m$, the torque/force errors correspond to approximately $1.1N$ and $0.3N$ of human force input for the pitch and reach DoF respectively. The levels of performance are adequate for the application of both axes. However, as percentages of absolute torque/force or velocities, the servo-valve controlled reach axis, performs better than the hydraulic transformer controlled pitch axis. This is especially prominent in Fig. 7.10 where the desired force/torque and velocities are smaller.

Figure 7.12 shows, for the case in Fig. 7.8, that the hydraulic transformer control was able to track the desired pressure P_d and the transformer shaft speed ω_d.

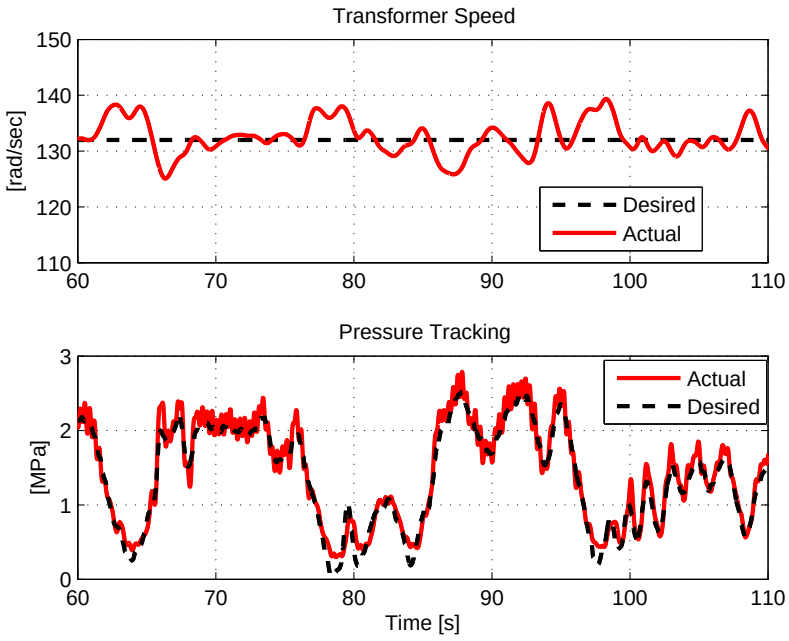

Figure 7.12: Hydraulic transformer control performance: Top: Actual (ω) vs desired (ω_d) transformer shaft speed; bottom: Pressure tracking (P_θ vs. $P_{d,\theta}$).

7.8.2 Guidance

Assistive guidance dynamics are examined next. In the following experiments, F_{guide} as described in Section 7.5 is activated. Control parameters used for the guidance control are summarized in Table 7.8.2.

In an experiment with PVFC activated, the velocity field shown in Fig. 7.6 was used such that the HPA converges to and moves around a circle. The human operator simply pushed the HPA in its natural movement without paying much attention to tracing the circle or even looking at the HPA. Figure 7.13 shows the resultant movements of the HPA tip, superimposed with the desired velocity field $V(q)$ from two initial conditions. The tip

Table 7.3: PVFC and Obstacle Avoidance (OA) Parameters

PVFC Parameters	Symbol	Value
Virtual Flywheel	M_F	2 kg-m^2
Augmented Energy	$\bar{E}$	30 J
Obs. Avoidance Parameters		
Obstacle Gain	k_{oa}	50 m^{-1}
Field scaling	U_d	36 J

of the HPA moved towards the circle directly (a characteristic of velocity field encoding compared to timed trajectory planning) and around the circle in the anti-clockwise direction. Figure 7.14 shows the actual augmented velocity vs scaled desired augmented velocity for each DoF including the virtual flywheel. The augmented velocity field $\bar{V}(\bar{q})$ was indeed tracked up to the scaling according to the square root of the instantaneous kinetic energy.

Finally, Fig. 7.15 shows the experimental results for the obstacle avoidance control. A potential field was generated to create a virtual wall for the rectangular region in the top right corner of the Cartesian workspace. The figure shows that the obstacle avoidance control was successful in prohibiting the HPA from entering the rectangle despite the effort by the human operator. Figure 7.16 shows the force and velocity coordination for each DoF when the obstacle avoidance is active. In the reach DoF, it can be seen that the operator is repeatedly trying to advance the HPA in a positive direction, but the actuator exerts force in the opposing direction. The operator will feel the machine is preventing the user from entering the prohibited region. The velocity coordination still well coordinated as the obstacle avoidance occurs.

7.9 Chapter Summary

In this chapter, a fully coupled multi-DoF hydraulic human power amplifier was controlled to demonstrate another potential application for the hydraulic transformer.

This device allows the human to operate the machine as a passive mechanical tool such that the machine's inertia and any external loads are perceived to be smaller. In addition, the control incorporates passive guidance dynamics in the form of passive velocity field control (PVFC) and artificial potential fields to perform specific tasks while avoiding obstacles. The control law structure observes and makes use of the intrinsic passivity properties of both the mechanical and hydraulic components. The force control requirement to

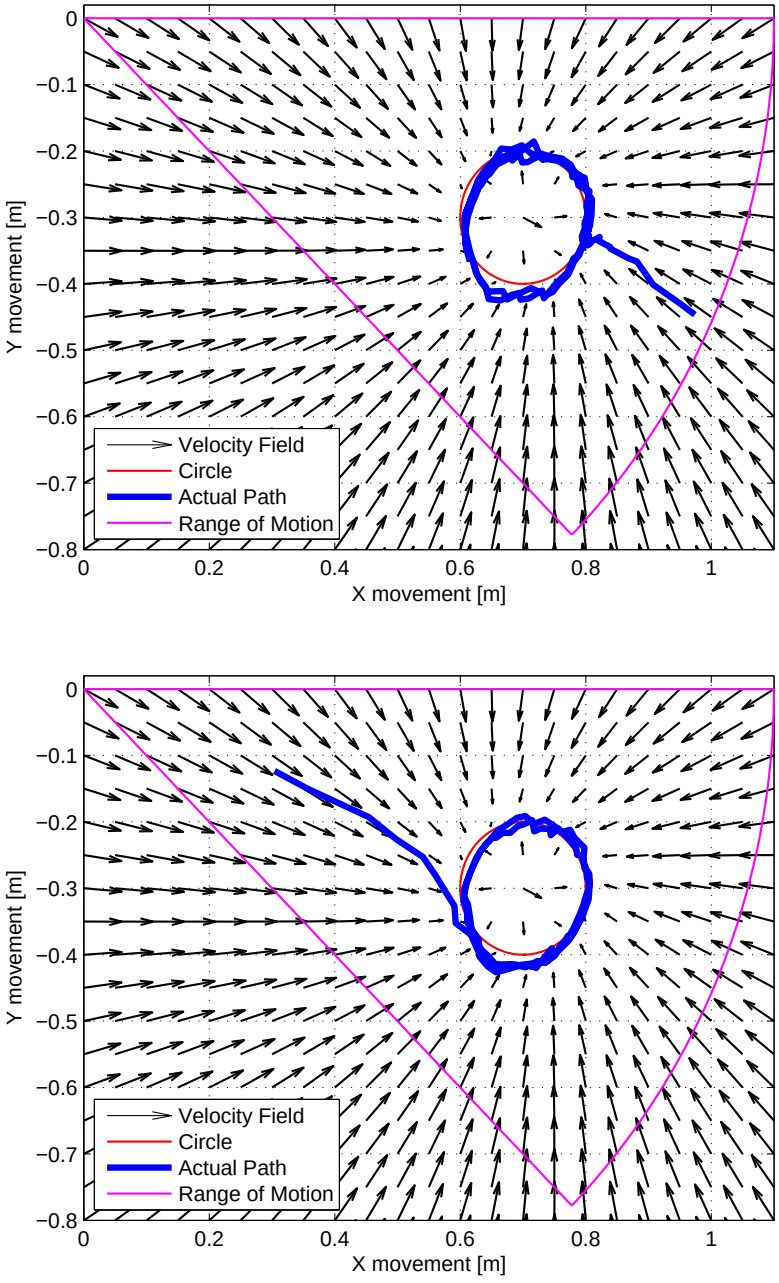

Figure 7.13: Movements of the tip of the HPA in Cartesian workspace coordinates superimposed with the desired velocity field. The magenta sector prescribes the allowable workspace.

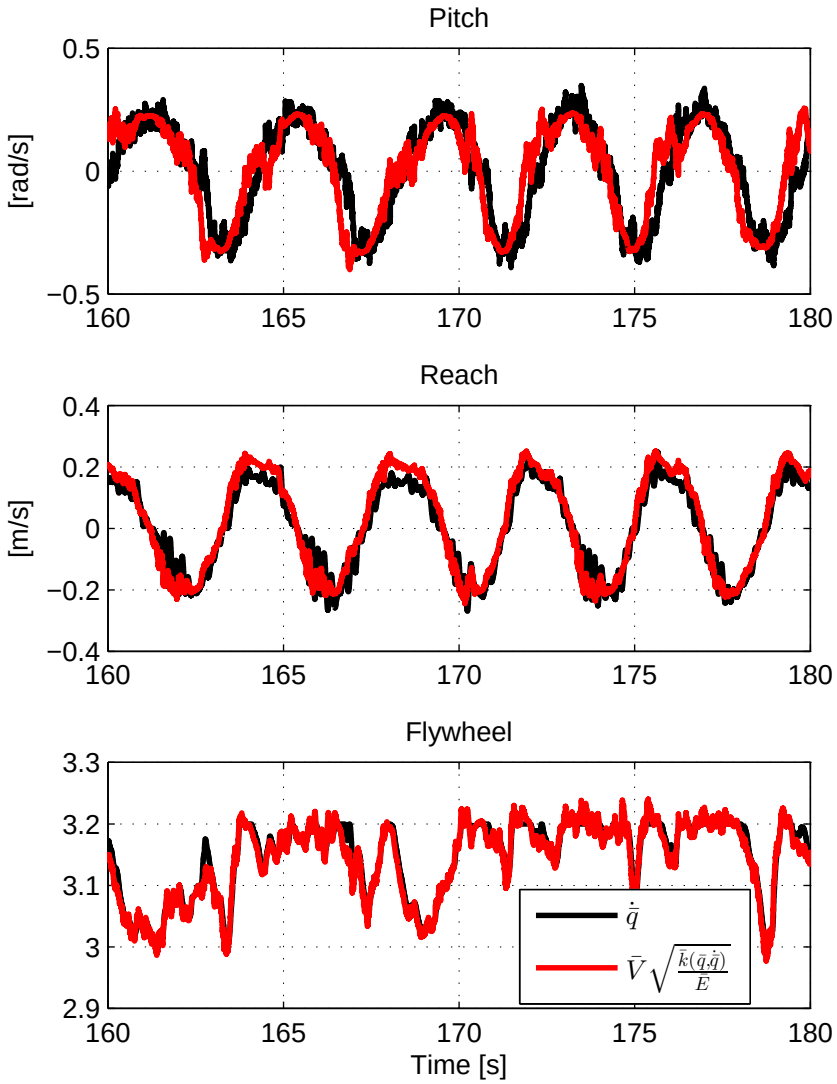

Figure 7.14: Actual augmented velocity ($\dot{\bar{q}}$) vs scaled desired augmented velocity $\delta\bar{V}(\bar{q})$ under PVFC. Top: pitch [rad/s], Middle: reach [m/s], Bottom: fictitious flywheel [rad/s]. RMS errors are pitch: 0.23 rad/s, reach: 0.065 m/s, fictitious flywheel: 0.04 rad/s.

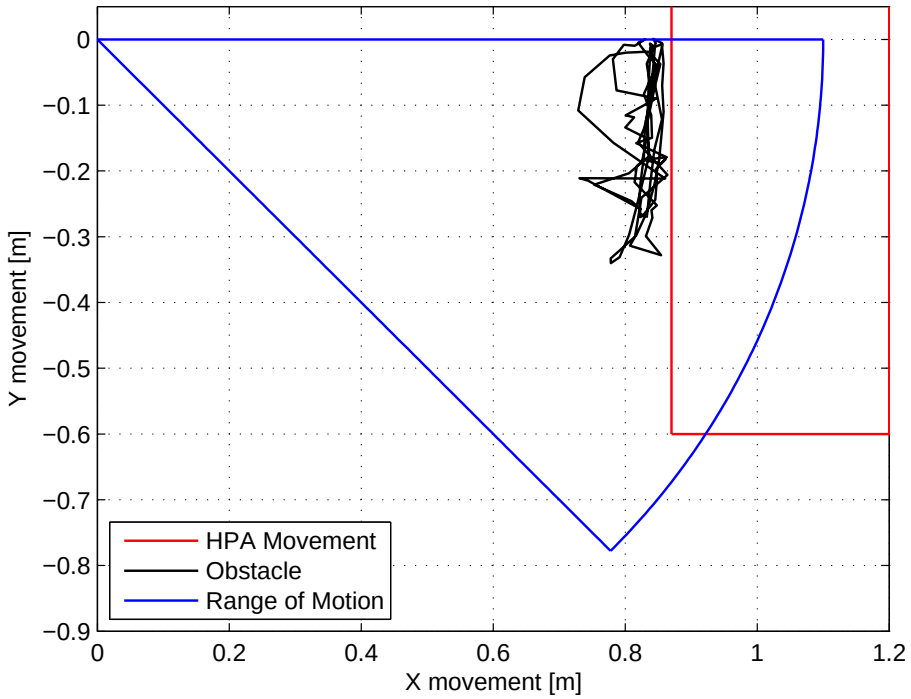

Figure 7.15: Movements of the tip of the HPA in Cartesian workspace coordinates with Obstacle Avoidance control activated. The blue sector prescribes the allowable workspace, and the red rectangle is the virtual obstacle created

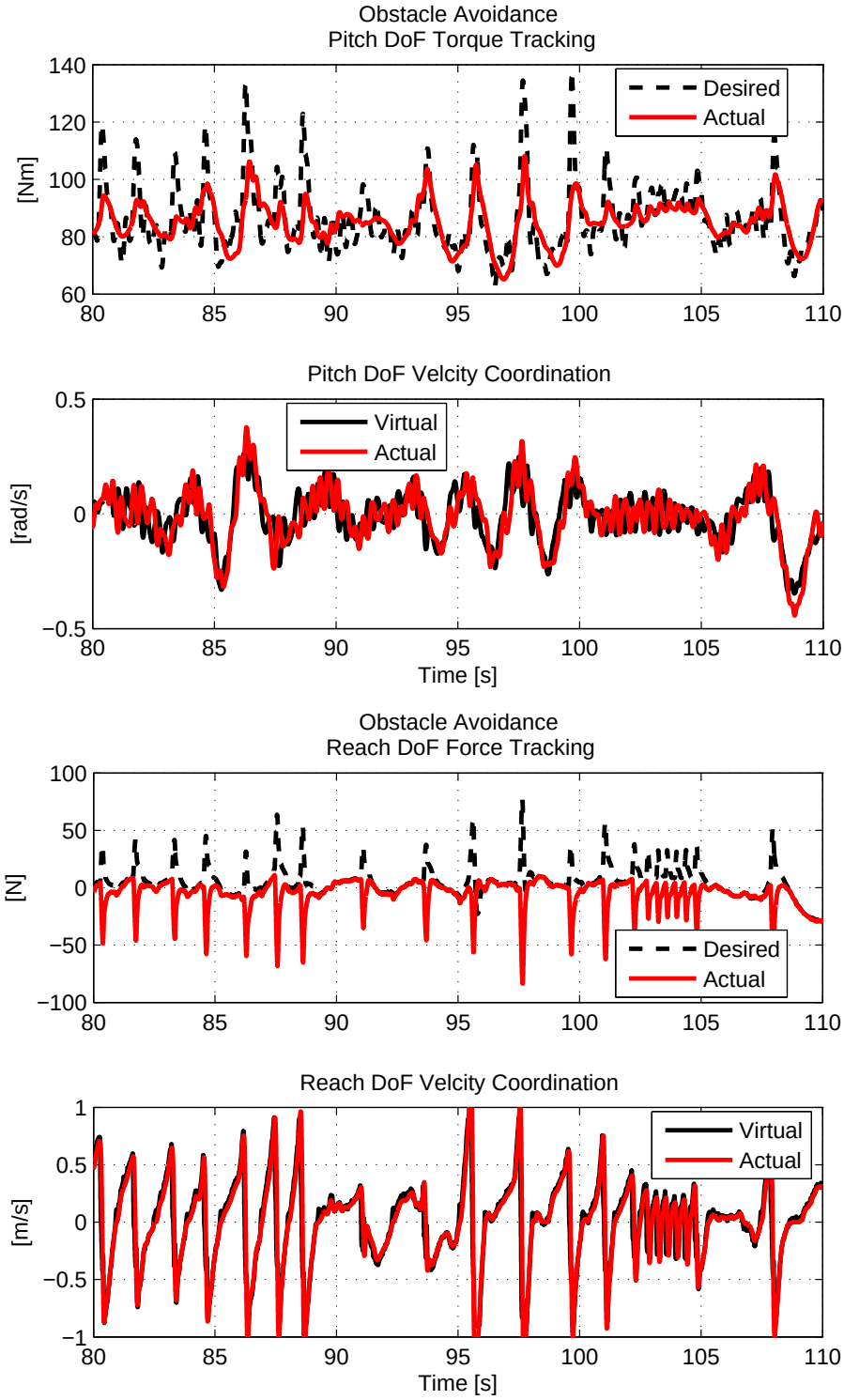

Figure 7.16: Obstacle Avoidance. Top: pitch torque and angle; bottom: reach force and displacement. Velocity coordination is still happening even as the actuator force deviates away form the desired force. The RMS pitch torque error is 8.87 Nm; RMS pitch coordination error is 0.08 rad/s. The RMS reach force error is 24.2 N; RMS reach coordination error is 0.14 m/s.

amplify human force and apply guidance dynamics is converted into one of coordinating the velocities of virtual inertia and of the actual system. This results in a closed loop system that is passive with respect to a scaled human and environment power input.

Experimental results demonstrated good force tracking and velocity coordination performance with either a hydraulic transformer utilized, as well as effective task guidance. The fact that one of the DoFs was driven by a hydraulic transformer shows another application for the hydraulic transformer driven system and shows that advanced control algorithms can be implemented using transformers.

Along with the results in Chapter 6, this chapter successfully proves that utilizing a hydraulic transformer does not need to make a sacrifice in delivering a desired control performance, even for a complex system that employs several advanced control approaches. In the next chapter, we will explore the energy savings of using hydraulic transformers.

Chapter 8

Optimal Control to Maximize Efficiency

Chapter 6 and Chapter 7 demonstrated with motion and force control that utilizing a hydraulic transformer does not require a sacrifice in accurate control performance. However, these previous chapters did not explore some other aspects. Even though the prototype switched mode transformer presented in Chapter 5 was capable of switching its configuration mode during the operation, the control results were all shown for a fixed configuration mode. Also, even though the transformer controller is capable of tracking any desired shaft speed, the optimal methods to determine the desired speed were not discussed. Lastly, they only provided the tracking results and did not mention efficiency of the experiments. This was due to the challenges faced with existing lab equipments in delivering needed appropriate operating conditions to demonstrate the efficiency of systems driven by hydraulic transformers.

In this chapter, a Hardware-In-the-Loop testbed that solves the challenges with the experimental operating conditions are presented. An algorithm to take advantage of the ability of the transformer controller and determine the optimal desired speed is presented and its energy savings will be demonstrated. Also, the method to determine the optimal configuration mode to operate the transformer will be developed to further increase the energy savings of utilizing the hydraulic transformer.

This chapter is organized as follow. Section 8.1 presents a Hardware-In-the-Loop testbed that was developed to address the challenges in experimentally validating the efficiency of hydraulic transformer driven systems. Section 8.2 presents the definition of 'efficiency' that is used for the efficient control analysis. Section 8.3 explores what needs to be done to the shaft speed given the transformer configuration in order to maximize the

efficiency. Section 8.4 develops an algorithm to automatically determine what is the most efficient transformer configuration mode that brings the maximum efficiency. Finally, the chapter summary is presented in Section 8.5

8.1 Hardware In-The-Loop Testbed

8.1.1 Motivation for HIL system

In order to demonstrate the efficiency of the hydraulic transformers, it is necessary to have a load pressure that corresponds to the pressure transformation ratio of at least ($\lambda = 0.3$) such that the transformer is operating at an acceptable efficiency for an input pressure of 1000 psi.

However, in experimentally validating the control performance and efficiency of transformers, it became apparent that experimental setups shown in Section 6.4 and Section 7.8 cannot generate the operating condition for the transformer that would show reasonable efficiency. The existing setup simply could not bring the output pressure above 1.03 MPa (150 psi), which resulted in the hydraulic transformer being as inefficient as utilizing a throttling valve. More importantly, even though the hydraulic transformer can be applied to any hydraulic systems under a variety of situations, it is not cost-effective to have multiple testbeds to experimentally demonstrate them. Consequently, a controller could only be tested for limited cases and efficiency results were not reported.

A Hardware-In-the-Loop (HIL) testbed is a convenient solution for the aforementioned challenges. In an HIL system, the actual machine is replaced with a dynamic simulation executed in software, while the hydraulic component to be tested is presented physically with the pressure and flow conditions as in the actual machine. Figure 8.1 illustrates this concept for the prototype mode switching transformer. This allows a hydraulic component to be tested for a variety of operating scenarios without having to physically obtain the hardware.

Several other HIL testbeds had been constructed by various research groups to overcome similar challenges in investigating the hydraulic system. For example, Zhang et al. [92] developed an HIL testbed to develop a controller for a hydraulic earthmoving vehicle, addressing the challenge in reproducing the digging cycles. Du et al. [25] developed a hydrostatic dynamometer for testing hydraulic hybrid vehicles, capable of emulating a variety of driving conditions and vehicle characteristics.

An HIL testbed for the hydraulic transformer has been developed to test the performances of hydraulic transformer controlled systems. Each degree of freedom can be tested

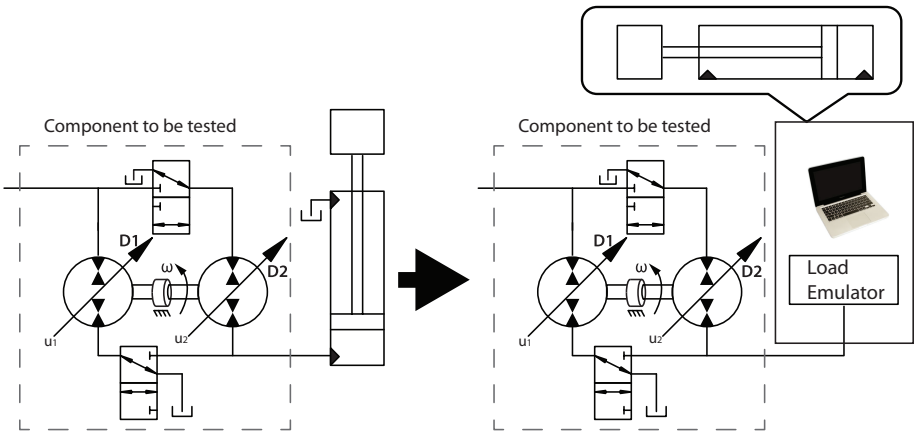

Figure 8.1: HIL Concept. The connected load is replaced with a computer simulation generating the pressure condition while the component to be tested remains

one at a time without needing the physical actuators or inertial loads. The same testbed can also be used to test the transformer in different machine configurations and duty cycles by simply reprogramming the dynamic simulation. This testbed was designed to have a simple construction and can emulate both resistive and overrunning loads.

8.1.2 Components of HIL System Architecture

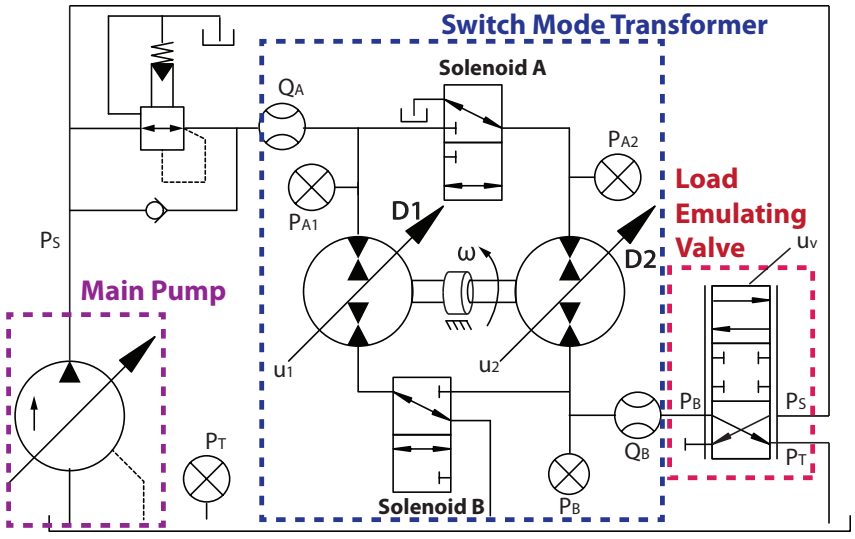

Figure 8.2: HIL Circuit for testing Switch Mode Transformer

The hydraulic schematic of the HIL Testbed for the hydraulic transformer is shown in Fig. 8.2. The system is powered by the main pressure compensated pump which provides

the constant pressure P_S at 16 MPa (2320 psi) to the load emulating valve and a pressure reducing valve that is placed before the hydraulic transformer.

As described in Chapter 5, pressure (P) sensors (Honeywell MLH03KPS01A or MLH500PSB01A) and flow (Q) sensors (AW Gear Meters JV30KG) are placed at various places as shown in Fig. 8.2. The transformer shaft speed ω is measured with an optical encoder. The transformer controller determines the displacement control inputs u_1 and u_2 to alter $D_1 = D_{1,max}u_1$ and $D_2 = D_{2,max}u_2$ which in turn deliver the desired flow Q_B^d to the actuator while maintaining the shaft speed at the desired ω_d as shown in Chapter 6.

In the HIL testbed, a load emulating valve (LEV) is utilized in place of the hydraulic actuator. A Moog 760 series servo valve (rated 9.5 LPM at 3000 psi or 20.7 MPa), connected to the main pump prior to the pressure reducing valve and to tank, is used for this purpose. One outlet port is connected to the transformer output while the other port is blocked. As will be described in Section 8.1.5, the servo valve command u_v is used to create an appropriate pressure condition for the transformer that mimics the actual load condition.

The fact that the LEV is connected to a supply pressure P_S (16 MPa $\approx$ 2320 psi)) is higher than the input port pressure of the transformer P_A (6.9 MPa $\approx$ 1000 psi) allows this HIL system to emulate both resistive and overrunning loads just using one main pump. This configuration is advantageous as only one main pump is needed to power the whole testbed as opposed to having separate pumps for emulating load and running a hydraulic transformer.

8.1.3 Data and Signal Flow in the HIL Testbed

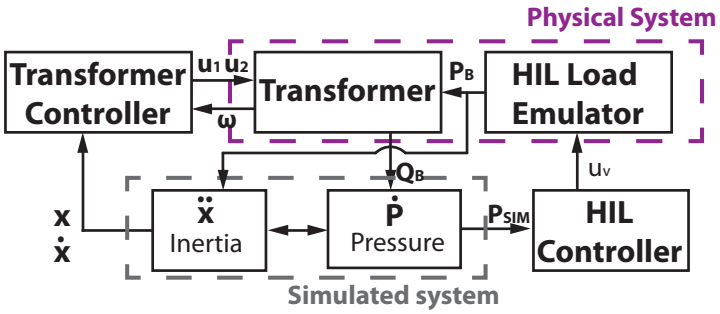

Figure 8.3: HIL Control Scheme

Fig. 8.3 shows the block diagram illustrating the data flow within the testbed. The output flow Q_B from the transformer is measured and is provided to simulate the pressure dynamics $\dot{P}$, creating a simulated pressure P_{SIM} in return. In case of a hydraulic actuator

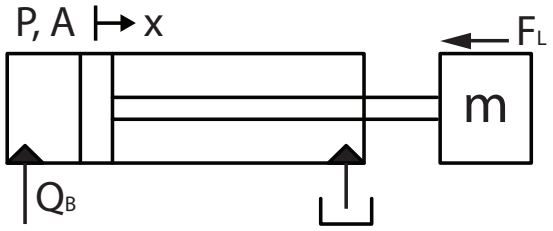

Figure 8.4: Example cylinder being simulated

shown in Fig. 8.4, the pressure dynamics of the capside chamber which is to be (virtually) connected to the transformer is given by:

$$\dot{P}_{SIM} = \frac{\beta}{V_0 + Ax}(Q_B - A\dot{x}) \tag{8.1}$$

where V_0 is the volume in the capside chamber and hose when the actuator is at the position $x = 0$, and β is the bulk modulus of the fluid. Integrating $\dot{P}_{SIM}$ yields a P_{SIM} which is fed into a HIL controller to determine the LEV control u_v to match the actual pressure P_B with P_{SIM}.

The measured pressure P_B in turn drives the simulated inertia dynamics, $\ddot{x}$:

$$m\ddot{x} = -b\dot{x} + \underbrace{P_B(t)}_{measured} A + F_L \tag{8.2}$$

where m is the mass of the cylinder and rod to be simulated, A is the cap side area of the hydraulic actuator, b is the viscous friction coefficient, and F_L is the load force that would encapsulate any external load including gravity and environment forces. Integrating $\ddot{x}$ yields the velocity $\dot{x}$ and the position x which are used in (8.1). Note that this simulated inertia dynamics take the measured pressure. This is useful, for an example, for accounting for any movement change due to pressure dynamics associated with transformer mode switch.

The pressure dynamics $\dot{P}$ and the inertia dynamics $\ddot{x}$ in (8.1)-(8.2) can be set to simulate any desired actuator type with specified loading conditions, generating appropriate motion and mechanical load. If desired, the simulated system dynamics could simply be replaced by a duty cycle information providing the desired pressure and flow traces.

Finally, the transformer controller takes the feedback of the above information to determine the transformer control inputs u_1 and u_2 to achieve the desired flow for the (emulated) load and the desired torque for the (actual) transformer speed regulation.

8.1.4 Transformer Controller

The same transformer controller as in Section. 6.3.2 is utilized to provide the desired flow Q_B^d for the given task and the desired torque T^d to track the desired shaft speed.

$$\begin{aligned} \dot{\tilde{\omega}}_I &= \tilde{\omega} := \omega - \omega_d \\ T^d &= J\dot{\omega}_d - K_{pt}\tilde{\omega} - K_{It}\tilde{\omega}_I + B_t\omega_d \end{aligned} \tag{8.3}$$

T^d is distributed between two control inputs accordingly:

PM-1:

$$\begin{bmatrix} u_1 \\ u_2 \end{bmatrix} = \begin{bmatrix} 0 & \omega \cdot \frac{D_{2,max}}{2\pi} \\ (P_A - P_T)\frac{D_{1,max}}{2\pi} & (P_T - P_B)\frac{D_{2,max}}{2\pi} \end{bmatrix}^{-1} \begin{bmatrix} Q_B^d \\ T^d \end{bmatrix}$$

PM-2:

$$\begin{bmatrix} u_1 \\ u_2 \end{bmatrix} = \begin{bmatrix} \omega \cdot \frac{D_{1,max}}{2\pi} & \omega \cdot \frac{D_{2,max}}{2\pi} \\ (P_A - P_B)\frac{D_{1,max}}{2\pi} & (P_T - P_B)\frac{D_{2,max}}{2\pi} \end{bmatrix}^{-1} \begin{bmatrix} Q_B^d \\ T^d \end{bmatrix}$$

PM-3:

$$\begin{bmatrix} u_1 \\ u_2 \end{bmatrix} = \begin{bmatrix} 0 & \omega \cdot \frac{D_{2,max}}{2\pi} \\ (P_A - P_T)\frac{D_{1,max}}{2\pi} & (P_A - P_B)\frac{D_{2,max}}{2\pi} \end{bmatrix}^{-1} \begin{bmatrix} Q_B^d \\ T^d \end{bmatrix}$$

8.1.5 Load Emulating Valve Controller

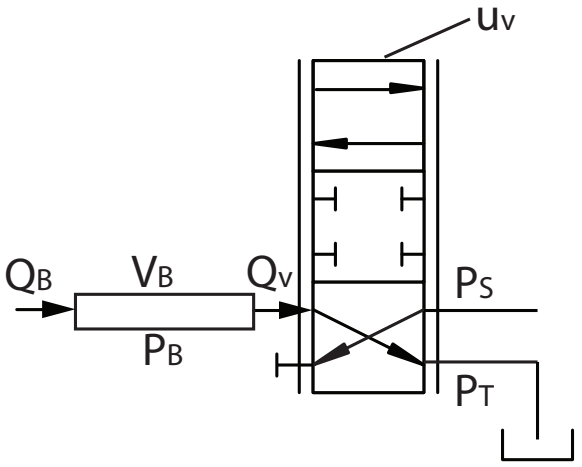

Figure 8.5: Load emulating valve shown with its control volume

The most important aspect of the HIL testbed is the load emulating valve (LEV) reproduced in Fig. 8.5, which will provide the desired loading condition through pressure. For $u_v > 0$, the flow is released to the tank (as shown in the figure) and for $u_v < 0$, the flow is taken from the main pump to increase pressure. The flow Q_v traveling across the valve

from the transformer output to be exposed to P_T or P_S is given by the supply pressure or the tank pressure:

$$Q_v = \begin{cases} k_v u_v \sqrt{P_B - P_T}, & \text{for } u_v > 0 \\ k_v u_v \sqrt{P_S - P_B}, & \text{for } u_v < 0 \end{cases} \tag{8.4}$$

(assuming $P_S > P_B > P_T$) where $k_v = 1.25 \cdot 10^{-8} m^3/(V \cdot \sqrt{Pa})$ is the valve coefficient, and $u_v \in [-10, 10]$ V is the analog voltage command to the valve to be designed. The valve is rated at 9.5 LPM at 20.7 MPa. Even with the very low pressure drop at 1.4 MPa, the valve is able to provide more than 100 cc/s of flow, which matches the output flow provided by the transformer with output displacement of 3.15cc/s spinning at 200 rad/s.

For the controller design, consider the pressure dynamics within the hose that lies between the hydraulic transformer and the LEV:

$$\dot{P_B} = \frac{\beta}{V_B}(Q_B - Q_v) \tag{8.5}$$

where V_B is the volume of the hose between the transformer and the LEV, Q_B is the flow out of the transformer that is measured, and Q_v is the flow command to be designed. Define pressure error as $e = P_B - P_{SIM}$. Defining the desired valve port flow Q_v^d as:

$$Q_v^d = \left(1 - \frac{V_B}{V_0 + Ax}\right) Q_B - \frac{V_B}{V_0 + Ax} A\dot{x} + K_p e + K_I e_I \tag{8.6}$$

where $\dot{e}_I = e$ and K_p and K_I are the proportional and integral gains. To show that the desired pressure P_{SIM} can be achieved for the HIL testbed, consider the Lyapunov function:

$$\begin{aligned} W &= \frac{1}{2}\frac{V_B}{\beta} e^2 + \frac{1}{2} K_I e_I^2 \\ \dot{W} &= e(Q_B - Q_v) - e\frac{V_B}{V_0 + Ax}(Q_B - A\dot{x}) + eK_I e_I \end{aligned} \tag{8.7}$$

With Q_v given by (8.6),

$$\dot{W} = -K_p e^2 \tag{8.8}$$

which shows that for $K_p > 0$, $K_I > 0$, $e \to 0$ and P_B will track P_{SIM}, providing the simulated pressure.

Table 8.1 summarizes the parameters used for this controller. In summary, the LEV controller is a PI controller with feed-forward information coming from the measured flow out the transformer. Figure 8.6 shows the control schematic for this controller.

Table 8.1: HIL control parameters

Parameter	Symbol	Value
Proportional gain	K_p	0.5×10^{-5}
Integral gain	K_I	2×10^{-5}
Hose volume	V_B	1.5×10^{-4} m^2

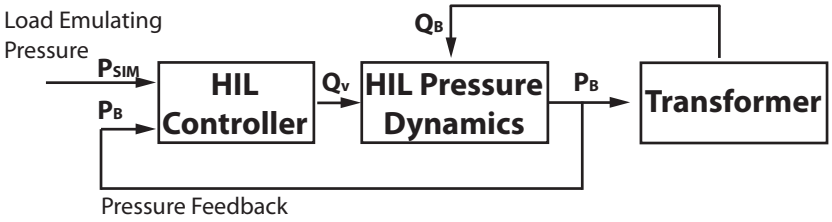

Figure 8.6: Control scheme for load emulating valve

8.1.6 Experimental Results for HIL testbed

Pressure Tracking Results

To validate the flow command to track desired pressure given in Eq (8.6), the transformer displacements were held steady while only the desired pressure loading condition was varied. This type of experiment can be used to analyze the steady-state operation of the hydraulic transformer under various loading conditions.

Fig. 8.7 shows the step pressure response for a 0.345 MPa (50 psi) step pressure command. Negligible overshoot with 10 ms rise time is observed. Fig. 8.8 shows various responses of the same step size, showing the similar response with the previous figure.

Figure 8.9 shows a response to the chirp signal while Fig. 8.10 shows the same response zoomed in at select frequencies (3 Hz, 5 Hz, and 10 Hz). The reference chirp signal, an amplitude of 0.345 MPa (50 psi), started as 0.01Hz at $t = 0$ and approached 10 Hz at $t = 50$. Phase lag of 36 degrees was observed at the peak frequency. At low frequency and around 3 Hz, the phase lag is negligibly small. Thus, it will be safe to claim this testbed can be operated satisfactorily under 3 Hz load profile. Careful tuning of the parameters along with better valve identification will lead to even better performance. As transformer itself has a limited bandwidth due to the swashplate actuation, HIL testbed is more than capable of simulating the loads for the transformer.

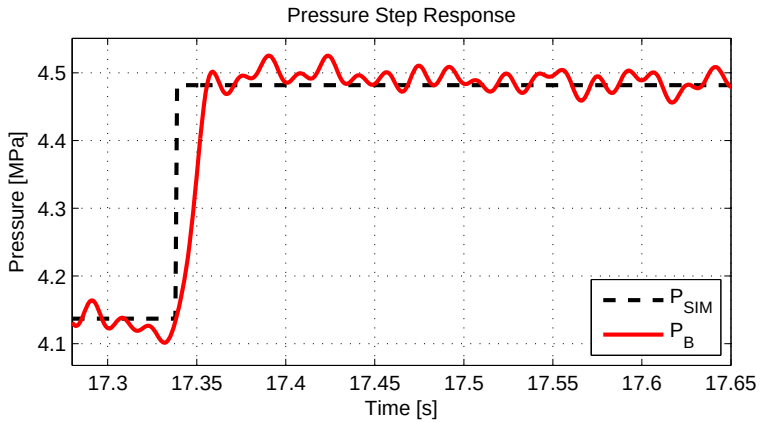

Figure 8.7: Pressure step response for a single step of 0.345 MPa (50 psi)

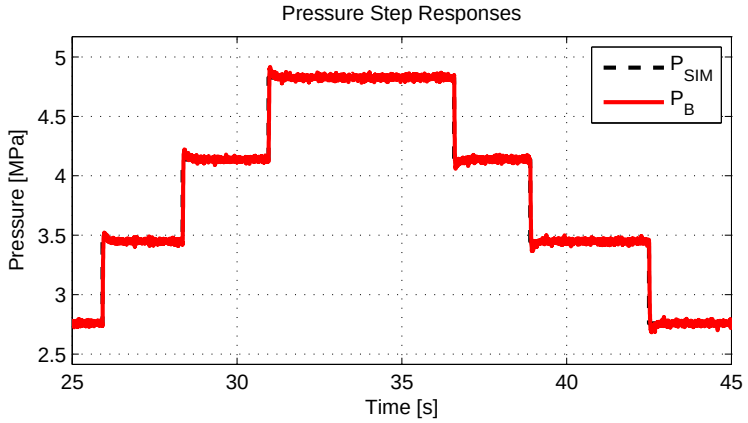

Figure 8.8: Pressure step response for various steps of 0.345 MPa (50 psi)

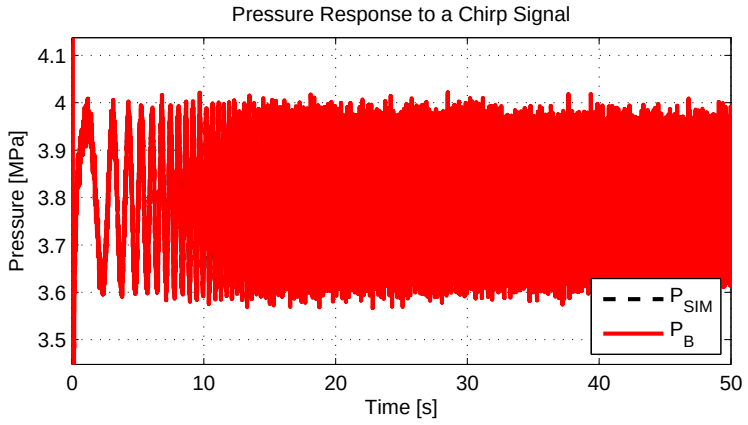

Figure 8.9: Chirp signal response from 0.01Hz to 10Hz

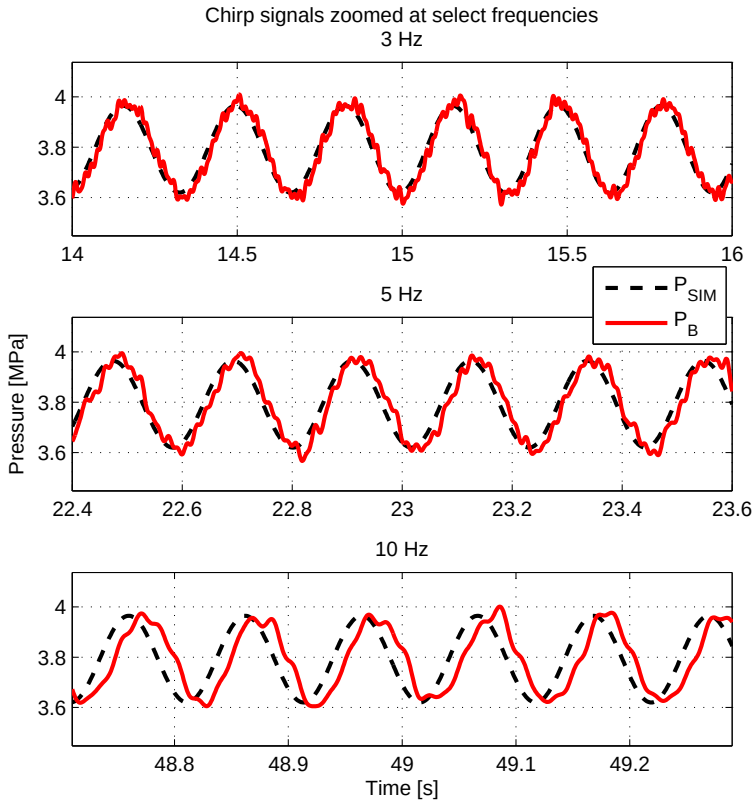

Figure 8.10: Chirp signal zoomed in at select frequencies for 6 cycles

Flow and Pressure Tracking Results

An operating condition where a LEV and transformer are simultaneously controlled is shown in Fig. 8.11. For this implementation, a cylinder with vertical gravity load following a filtered trapezoidal trajectory was studied with the switched mode transformer operating in 3 different modes. Controller determining the transformer displacement commands is taken from Chapter 6. Transformer mode switch is manually triggered for this experiment.

In this operating mode, HIL provides a loading condition to which trajectory tracking controller decides the transformer control inputs to be implemented. As described, the trajectory is generated by simulation using the measured flow and pressure. It is observed that trajectory tracking is still satisfactory even as the operating mode switch causes some sharp change of dynamics. In the meantime, pressure is tracking the simulated pressure P_{SIM} satisfactorily. These results show HIL testbed can be used in a satisfactory manner to study the prototype transformer at any desired pressure condition without having to obtain such load physically.

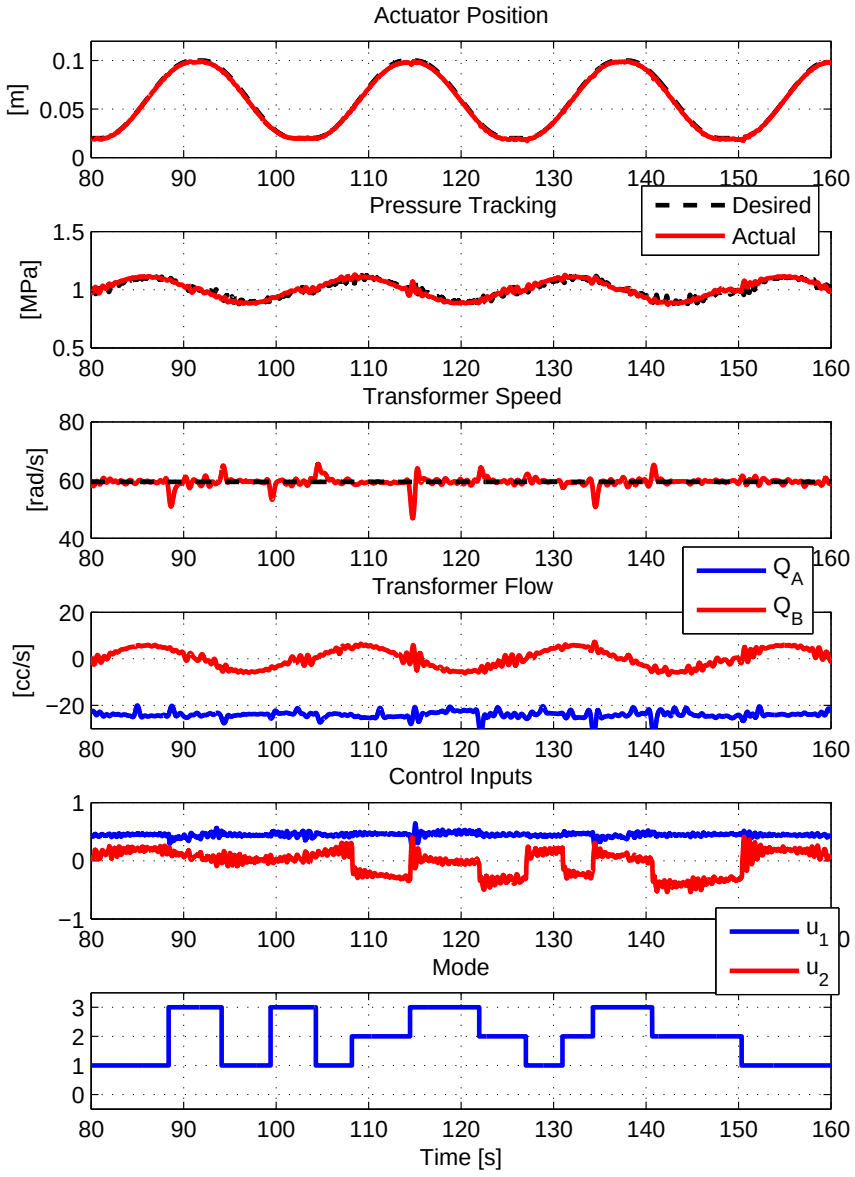

Figure 8.11: Simulated cylinder tracking result

8.2 Definition of the Transformer Efficiency

In evaluating the transformer operation, the efficiency can be calculated either for the efficiency of the unit itself or the efficiency of the combined transformer and actuator system. The difference in these definitions comes from what is defined as input and output power.

8.2.1 Component Efficiency

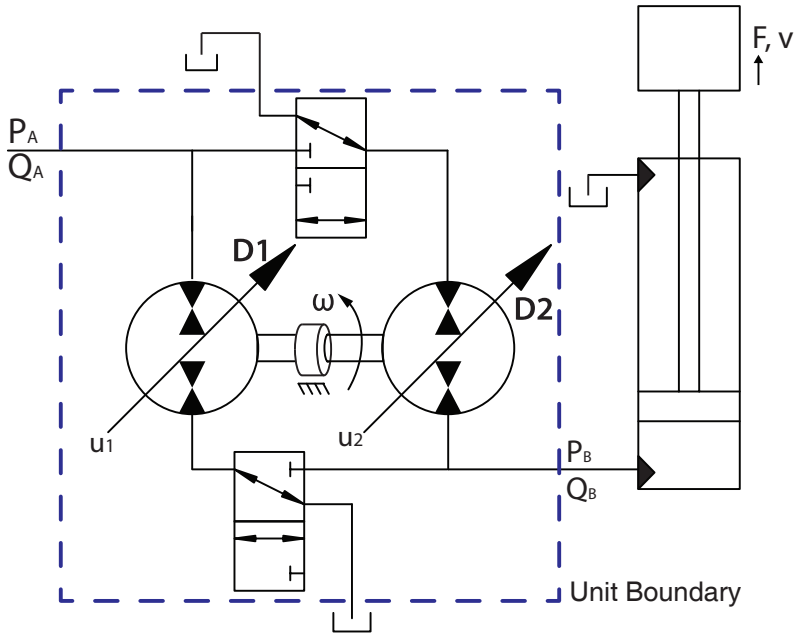

Figure 8.12: The boundary used for determining the 'component' efficiency of the transformer, it encapsulates only the transformer

The component efficiency reveals the relationship between power flow entering the transformer and existing the transformer. In this definition, the only power flow of interest are the fluid power flowing along the three ports, as shown in Fig. 8.12. Unlike in Chapter 4, the power flow of potential energy stored within the compressed fluid is not considered in this definition since we only have measurements of flow and pressure, and also to remain consistent with the industry standard in defining hydraulic pump/motor efficiency as found in ISO 4409.

With a relatively small displacement (3.15 cc/rev each side) at maximum speed of 200 rad/s, the maximum output flow is 200 cc/s for PM-2, which has both of the PM units contributing to the output flow. With this level of flow, the inclusion of pressure

compressible energy term $W_V(P, P_T)$ as in Eq. (4.1) only results in difference of ≈ 3.5 W for $P_B = 6.9$ MPa and $Q_A = 200$ cc/s. Omission of the compressed energy does not have a significant impact in the total power.

The fluid power at P-port can be obtained from pressure P_P and volumetric flow rate Q_P of the port:

$$\mathscr{P}_{f,P} = (P_P - P_T)Q_P \tag{8.9}$$

where Q_P being positive indicates the flow is exiting the unit and P_P is gauge pressure referenced against ambient pressure. The total fluid power input $P_{f,i}$ and total fluid power output $P_{f,o}$ of the unit are defined as follows:

$$\mathscr{P}_{f,i} = -C_{f,i}(\mathscr{P}_{f,A}) - C_{f,i}(\mathscr{P}_{f,B}) \tag{8.10}$$

$$\mathscr{P}_{f,o} = C_{f,o}(\mathscr{P}_{f,A}) + C_{f,o}(\mathscr{P}_{f,B}) \tag{8.11}$$

where $C_{f,i}$ and $C_{f,o}$ are indicator functions of the form:

$$C_{f,i}\left(\mathscr{P}_{f,P}\right) = \begin{cases} \mathscr{P}_{f,P} & \text{if } \mathscr{P}_{f,P} < 0 \\ 0 & \text{else} \end{cases} \tag{8.12}$$

$$C_{f,o}\left(\mathscr{P}_{f,P}\right) = \begin{cases} \mathscr{P}_{f,P} & \text{if } \mathscr{P}_{f,P} > 0 \\ 0 & \text{else} \end{cases} \tag{8.13}$$

In order words, $C_{f,i}$ will only count the work that is fed into the transformer and $C_{f,o}$ only counts the work coming out from the transformer.

Utilizing Eq. (8.10) and Eq. (8.11), the power loss of the transformer is defined to be the difference between and input and output power:

$$\text{Transformer Power Loss} = \mathscr{P}_{f,i} - \mathscr{P}_{f,o} \tag{8.14}$$

For an example, with $\mathscr{P}_{f,i}$ = -50 W and $\mathscr{P}_{f,o}$ = 50 W, then there is no power loss. In case where $\mathscr{P}_{f,o}$ = 30 W, than the W_{loss} = 20 W, meaning we are losing 20 W of power.

In order to analyze the unit efficiency of the transformer over a trajectory, the fluid energy over the time of interest rather than power at a single point in time needs to be considered. The total input energy and output energy for the transformer unit is simply the net integrated fluid power given as:

$$\begin{aligned} \mathscr{E}_{f,i} &= \int_{t_1}^{t_2} \mathscr{P}_{f,i}(t)dt \\ \mathscr{E}_{f,o} &= \int_{t_1}^{t_2} \mathscr{P}_{f,o}(t)dt \end{aligned} \tag{8.15}$$

The component efficiency η_u for a given trajectory implemented with the transformer is determined as the fraction of the total output energy with respect to the total input energy:

$$\eta_u = \frac{\mathscr{E}_{f,o}}{\mathscr{E}_{f,i}} \tag{8.16}$$

8.2.2 Cycle Efficiency

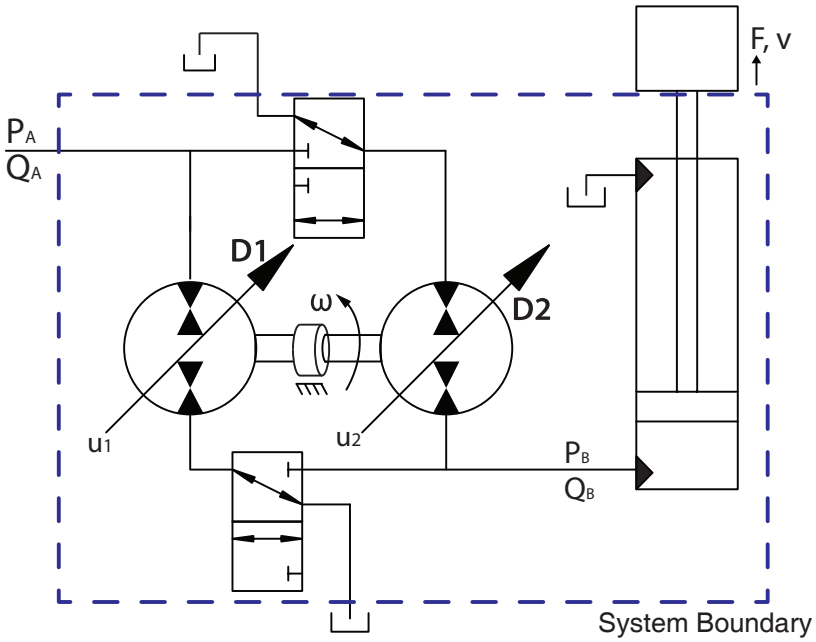

Figure 8.13: A system boundary in determining 'cycle' efficiency now the boundary encapsulates the actuator as well as the transformer

In evaluating the efficiency of the system that has a transformer within it, the boundary of analysis needs to be set such that the actuator being driven is included. In the system where common pressure rail drives the transformer and attached load, the power flows of interest are the fluid power to the 'A' port and 'T' port of the transformer, and the mechanical power output from the actuator, as shown in Fig. 8.13.

The fluid power into the system is defined as:

$$\mathscr{P}_{f,i} = -(P_A - P_T)Q_A \tag{8.17}$$

Note the absence of an indicator function as the net power will be used in the calculation. Any regenerative energy sent back to the common pressure rail through port 'A' will have an effect of reducing the net consumed fluid energy, to increase the system efficiency. In this definition, it is possible to have zero net consumed energy or have efficiency higher than 100%.

The power from the actuator, for a linear actuator shown in Fig. 8.13, is defined as:

$$\mathscr{P}_a = F_a(t)v_a(t) \tag{8.18}$$

The power output from the system contributed by the actuator is defined as:

$$\mathscr{P}_{a,o} = C_{a,o}(\mathscr{P}_a) \tag{8.19}$$

where $F_a(t)$ and $v_a(t)$ are the force and velocity of the cylinder actuator connected to the transformer. If a rotary actuator is connected, they will be replaced with torque $T_a(t)$ and rotational speed $\omega_a(t)$ of the actuator. $C_{a,o}$ is the indicator function of the form:

$$C_{a,o}(\mathscr{P}_a) = \begin{cases} \mathscr{P}_a & \text{if } \mathscr{P}_a > 0 \\ 0 & \text{else} \end{cases} \tag{8.20}$$

If the actuator is under overrunning load such that no positive work is needed to drive the cylinder, then power output of the system in consideration will be zero. Thus, the net output energy is determined by the integrated positive mechanical power output. In the meantime, the input energy will be the integrated fluid power input.

$$\begin{aligned} \mathscr{E}_i &= \int_{t_1}^{t_2} \mathscr{P}_{f,i}(t)dt \\ \mathscr{E}_o &= \int_{t_1}^{t_2} \mathscr{P}_{a,o}(t)dt \end{aligned} \tag{8.21}$$

Then, the total cycle efficiency η_{sys} for a given trajectory implemented in the transformer can be determined as the fraction of the total output energy with respect to the total input energy:

$$\eta_{sys} = \frac{\mathscr{E}_{f,o}}{\mathscr{E}_{f,i}} \tag{8.22}$$

8.3 Optimal Transformer Shaft Speed

The transformer controllers designed in Chapters 6 and 7 are capable of regulating the shaft speed ω to any desired speed ω_d. However, in the experiments presented in these previous chapters, the transformer shaft speed was arbitrarily set to some constant speed that meets the maximum demand for the trajectory being considered, or the power amplification being considered. This method of setting the shaft speed is similar to using a throttling valve to control the system, as the excess energy is wasted just spinning the transformer when the load demand is lower than that what the transformer can provide at the given shaft speed. In this section, a method to optimally choose the desired shaft speed ω_d will be presented to ensure efficient operation of transformer driven system.

8.3.1 Approach

Using the model developed in Chapter 2, an optimization can be performed a priori to obtain the optimal shaft speed for sets of pressure and flow. The process is to find the shaft speed that will minimize the power loss of the transformer while meeting the pressure and flow demand at the steady-state, and not have any of the displacement commands exceed the physical limitation of the swashplate actuation to meet the demand. This optimization can be summarized as follow:
For a given transformer configuration mode,

$$\begin{aligned} \min_{\omega} \quad & \text{Transformer Power Loss} \\ \text{subject to} \quad & P_B = P_d \\ & Q_B = Q_B^d \\ & |u_1| < 1 \\ & |u_2| < 1 \\ & \omega \geq \underline{\omega} \\ & J\dot{\omega} = 0 \end{aligned} \tag{8.23}$$

where $\underline{\omega} > 0$ is the lower limit on the ω_d to be designed to prevent transformer spinning too slow, which can cause a stalling due to stiction. Transformer power loss is given by Eq. (8.14).

8.3.2 Optimal Shaft Speed

The resulting optimal shaft speed and power loss corresponding to those speeds for each operating mode are shown in Fig. 8.14 for a transformer supply pressure of 6.9 MPa ($\approx$ 1000 psi). The gaps in the contour plots are attributed to the fact that the given transformer mode cannot operate in that region meeting the constrains in Eq. (8.23). Since the prototype transformer is mechanically inefficient, the expected losses correlate closely with the desired shaft speed. For a PM-1, the vertical trend in the desired speed at positive flow for at low P_d starts to have a sloping trend for as λ increases. This corresponds to the situation where D_2 has to decrease. Since the output is only coupled to D_2 in PM-1 (Eq. (2.18)), decrease in D_2 will have to be compensated by increase in shaft speed ω to deliver the same output flow as P_d increases. The other trends are explained in the similar manner.

During an actual transformer operation, the desired flow and pressure condition as determined by the controller will be fed into these contours to determine the most efficient shaft speed to be used for the transformer operation. The controller schematic for tracking a cylinder trajectory is illustrated in Fig. 8.15.

8.3.3 Energy Savings in Trajectory Tracking Control

Figure 8.16 presents an experimental result where a cylinder following a sinusoidal trajectory with an attached mass is studied. The same controller gains from Section 6.3 and Section 8.1.5 were used. The experiment was ran only utilizing a PM-1 configuration, with the transformer shaft speed kept constant at $\omega = 110$ rad/s to be able to deliver the maximum Q_B^d for the trajectory control. As mentioned earlier, this is not an efficient way to operate a transformer as excess power is wasted to spin the transformer. In this particular trajectory, 37% system efficiency is measured, with 3163 J of energy consumed through the cycle.

Table 8.2: Efficiency improvement through the shaft speed optimization

Operating	Component Efficiency		Cycle Efficiency		Net Energy Consumed	
Condition	Experiment	Model	Experiment	Model	Experiment	Model
Constant ω_d	27.2%	27.8%	37%	38.7%	2977 J	2846 J
Optimized ω_d	45%	41.8%	62%	66.3%	1731 J	1619 J

Figure 8.17 shows the same trajectory as in Fig. 8.16, but now the ω_d is varying according to the optimization results shown in Fig. 8.14. It can be observed that shaft speed increases as the flow demand increases and is kept at a set low threshold when flow

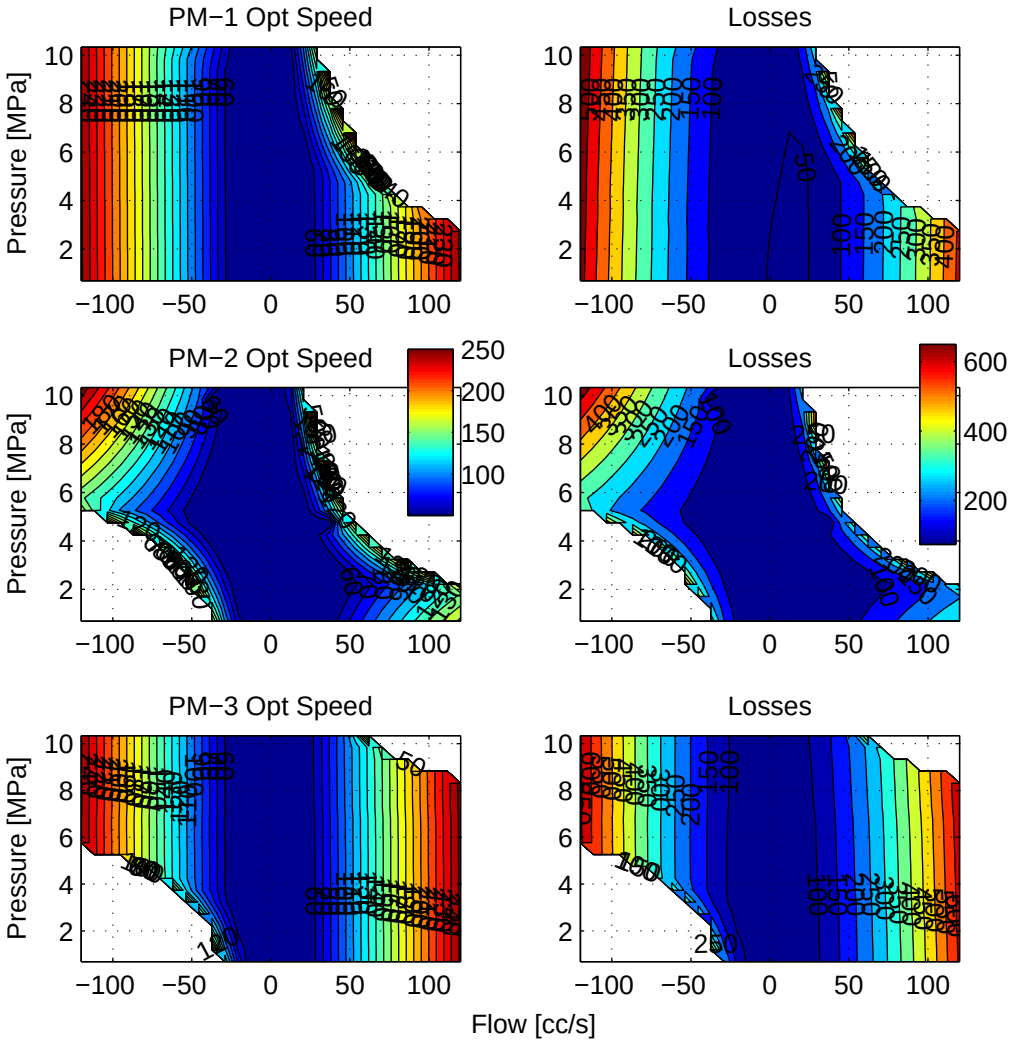

Figure 8.14: Left: the optimal shaft speed ω_d for the desired output flow Q_B^d and pressure P_d for three PM configurations driven by 6.9 MPa pressure; Right: an expected power loss for three PM configurations if transformer is running at the optimal ω_d

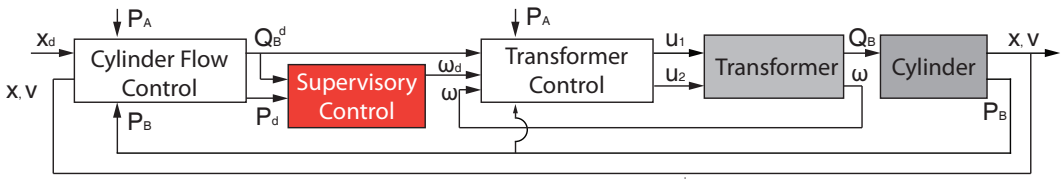

Figure 8.15: Control Scheme for trajectory Control using hydraulic Transformer with a supervisory control. A supervisory controller takes the desired pressure and flow to determine the optimal desired shaft speed ω_d

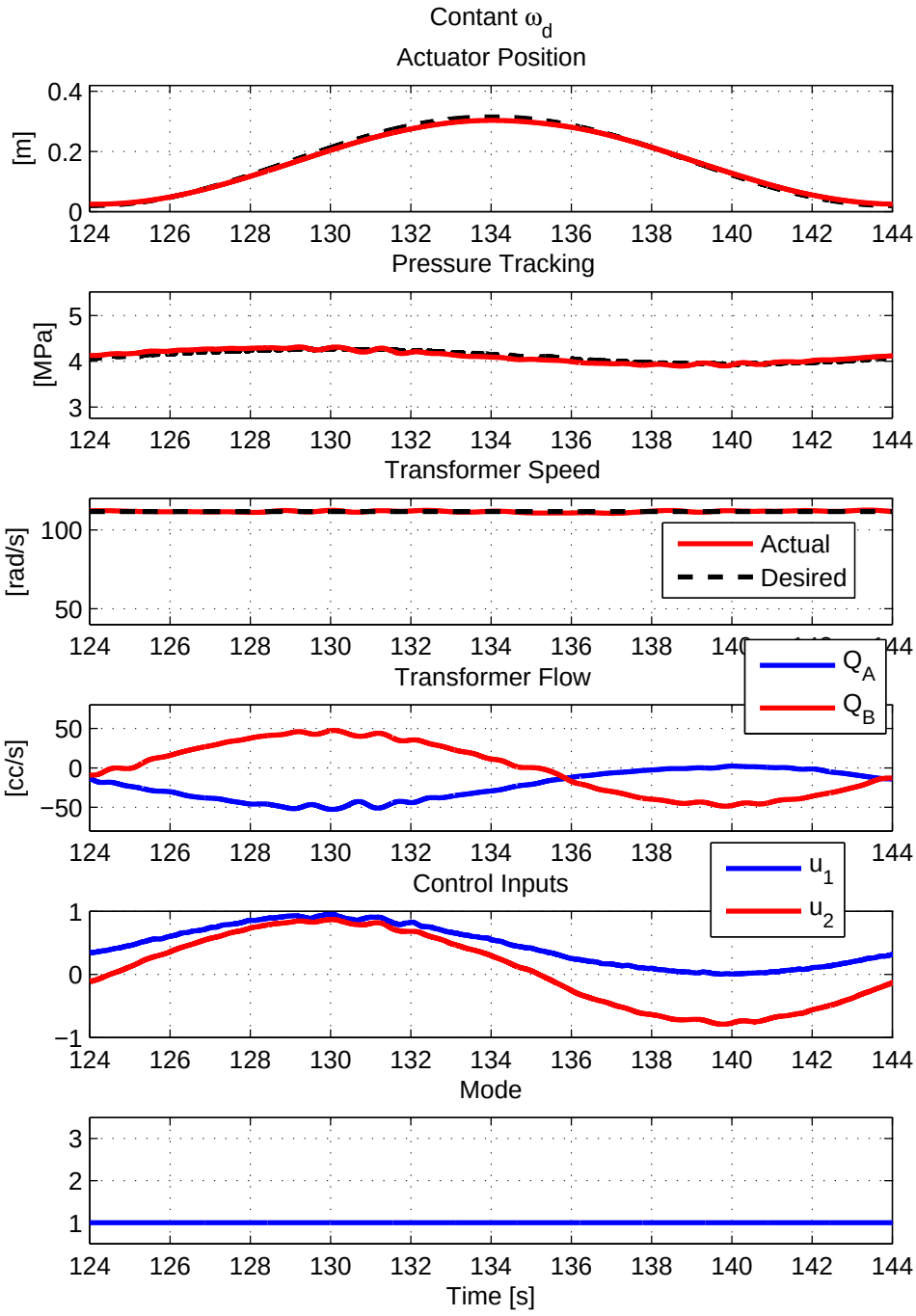

Figure 8.16: Trajectory tracking performed by PM-1 at constant shaft speed demand: 37% cycle efficiency, and 27.2% component efficiency observed. The model expected 38.7% cycle efficiency and 27.8% component efficiency

demand is not high. Displacement inputs tend to be maximum for the most of the cycle, which is beneficial as variable displacement units have the highest efficiency when the swashplate angle is at the maximum. For this cycle, the measured system efficiency was 65%, with 1852 J of energy consumption through the cycle. This means 41.5% reduction in energy consumption is possible by regulating the transformer to operate at most efficient shaft speed. Table 8.2 summarizes this this improvement

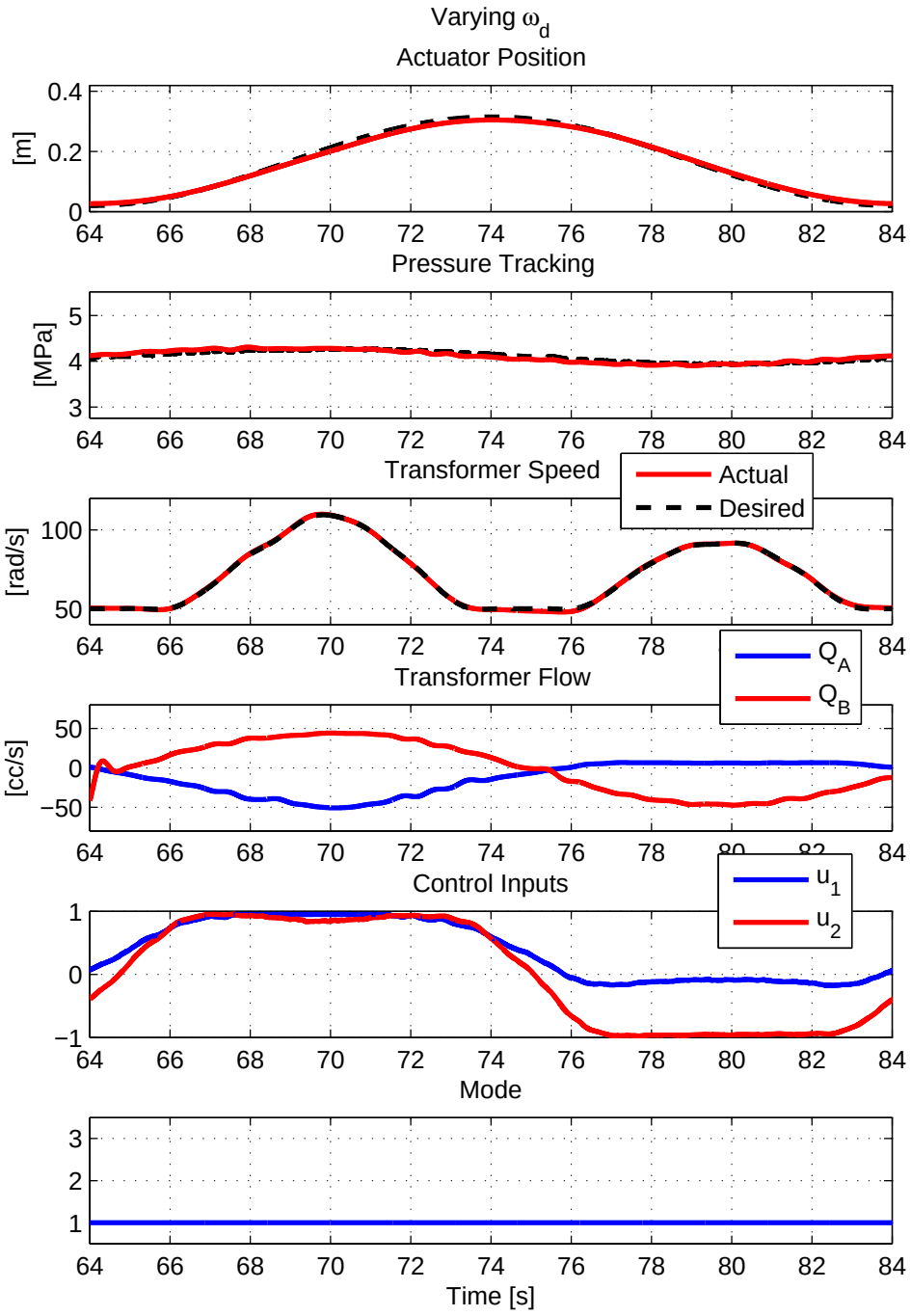

Figure 8.17: Trajectory Tracking with Optimized Shaft Speed Demand: 62% cycle efficiency, with 45% component efficiency. The model expected 66.3% cycle efficiency and 41.8% component efficiency

8.4 Optimal Operating Mode

Utilizing the results visualized in Fig. 8.14 that shows the optimal operating speed and expected power loss for each configuration mode, the supervisory control algorithm can be expanded one step further to determine the most optimal mode for given set of pressure and flow. Eq. (8.23) is updated such that the optimization is now with respect to the both the shaft speed ω and the configuration mode.

$$\begin{aligned} \min_{\omega,\,\text{Mode}} \quad & \text{Transformer Power Loss} \\ \text{subject to} \quad & P_B = P_d \\ & Q_B = Q_B^d \\ & |u_1| < 1 \\ & |u_2| < 1 \\ & \omega \geq \underline{\omega} \\ & J\dot{\omega} = 0 \end{aligned} \tag{8.24}$$

In order to obtain the optimal mode, we utilize the result from the previous section where the best shaft speed and expected power loss across the transformer for given the set of desired flow and pressure condition were found. Comparing the expected power loss L_1, L_2, L_3 from three configurations as shown in right side of Fig. 8.14, the optimal mode will have the least amount of expected power loss in the transformer.

$$\text{Mode} = \begin{cases} 1 & \text{if } \min(L_1, L_2, L_3) = L_1 \\ 2 & \text{if } \min(L_1, L_2, L_3) = L_2 \\ 3 & \text{if } \min(L_1, L_2, L_3) = L_3 \end{cases} \tag{8.25}$$

The supervisory control in turn is updated to produce not only the optimal shaft speed for a given operating configuration mode but also the optimal operating mode as well. Figure 8.18 is an updated control scheme reflecting this algorithm.

Figure 8.19 shows the contour of operating modes for any set of desired flow and pressure at the actuator attached to the transformer. If one were to operate based on this mode map, the optimal shaft speed and associated power loss at each operating points can be visualized with contours shown in Fig. 8.20. The resulting contour shows the similar trend as in Fig. 5.12. PM-3 is the best mode for an operating region with high flow and high pressure, PM-2 is the best mode for high flow but with low pressure, and the

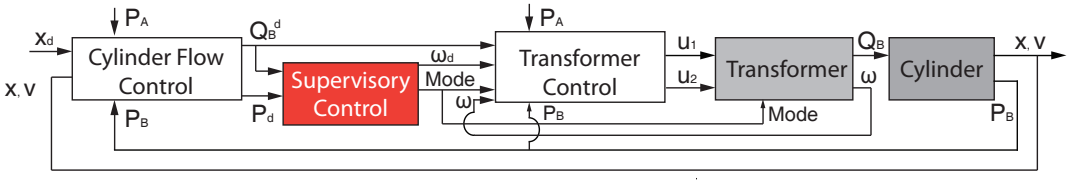

Figure 8.18: Control scheme for trajectory control using hydraulic transformer with a supervisory control also determining the operating mode

PM-1 fills the rest of the region. Note that contours generated in Chapter 4 were for a much larger unit (total displacement was 31.4 cc/rev, as opposed to 6.30 cc/rev from the prototype switched mode transformer) and thus shows different optimal operating modes from Fig. 4.21.

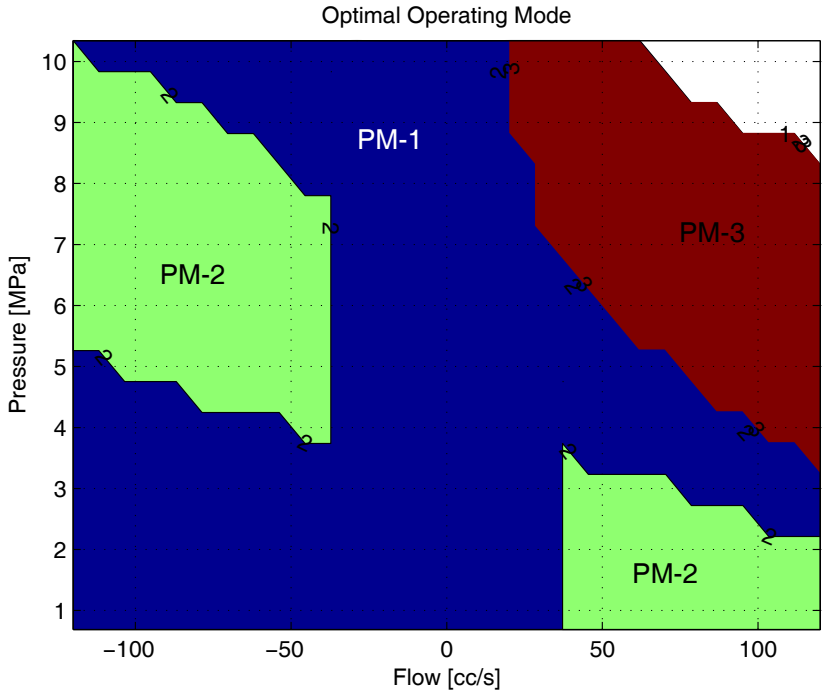

Figure 8.19: Contour of optimal operating mode for desired flow and pressure of the transformer

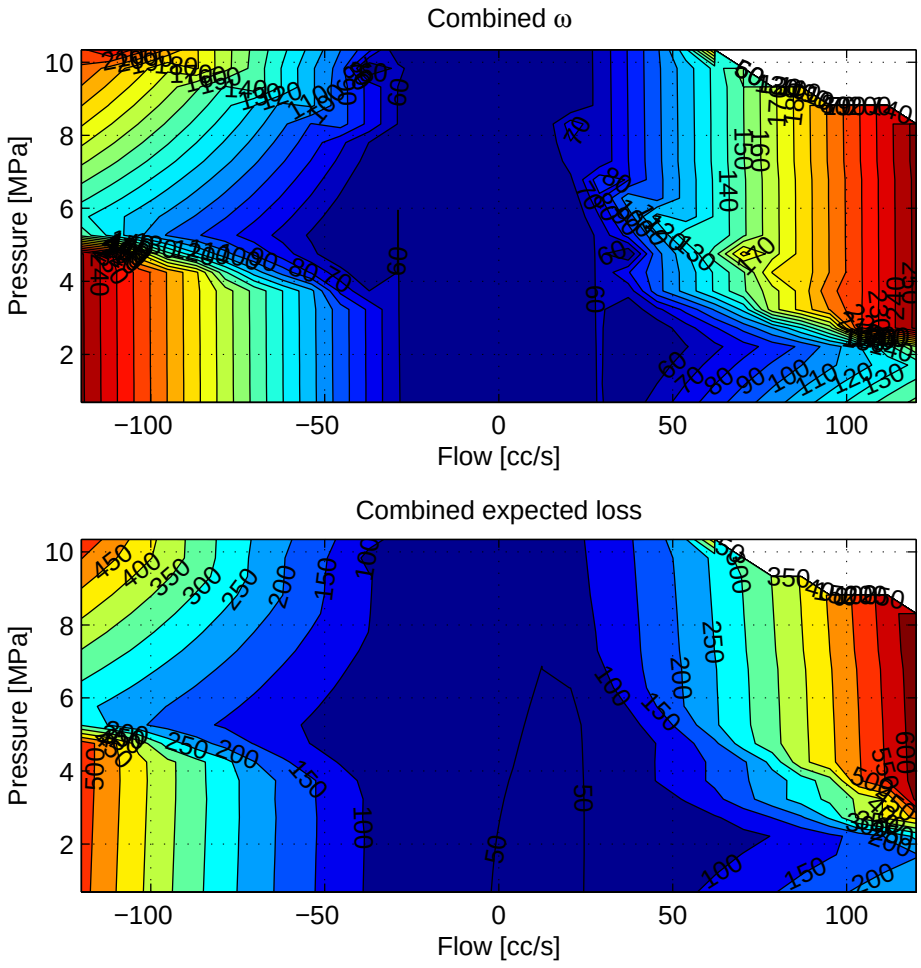

Figure 8.20: Top: Combined optimal ω_d (rad/s) following the optimal mode in Fig. 8.19; Bottom: Expected power loss (W) in the transformer by operating in optimal modes according to Fig. 8.19

8.4.1 Energy Savings with Mode Switching

Using the same trajectory as before, the trajectory tracking scenario was run on HIL testbed, allowing the transformer to automatically determine the optimal mode as seen in Fig. 8.19. The result is plotted on Fig. 8.22, showing 46.72% component efficiency and 62.9% system efficiency. The improvement in efficiency is rather subtle. This can be explained by Fig. 8.21, which shows the trace of pressure and flow for this cycle on top of the contour for the optimal mode. It can be seen that the trace only slightly reaches into PM-2 region only slightly, making the improvement less dramatic.

Table 8.3: Efficiency improvements through shaft speed optimization and mode switch

Operating Condition	Component Efficiency		Cycle Efficiency		Net Energy Consumed	
	Experiment	Model	Experiment	Model	Experiment	Model
Constant ω_d	27.2%	27.8%	37%	38.7%	2977 J	2846 J
Optimized ω_d	45%	41.8%	62%	66.3%	1731 J	1619 J
Mode Switch & Optimized ω_d	46.72%	45.0%	62.9%	68.2%	1706 J	1573 J

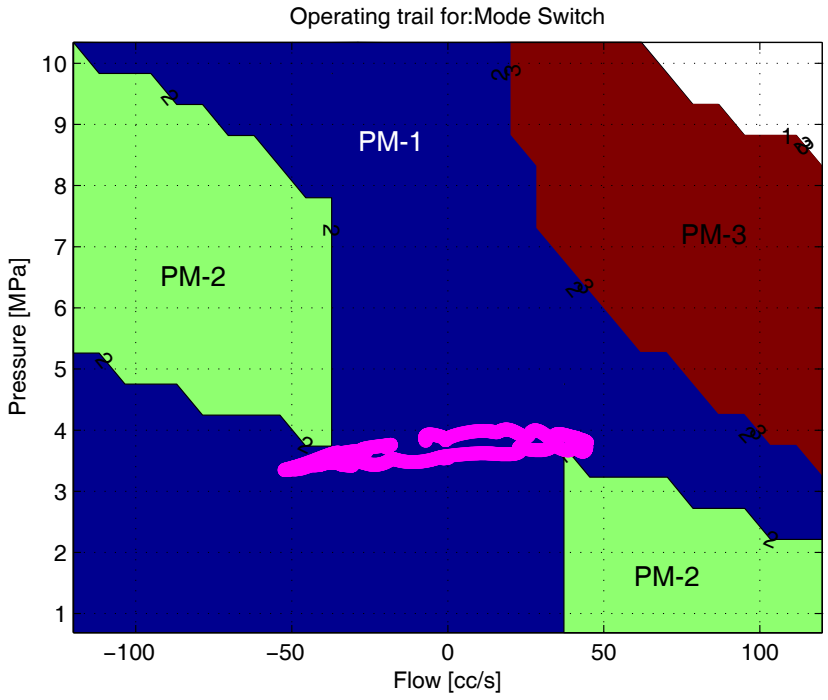

Figure 8.21: Pressure and Flow trace of trajectory tracking profile in Fig. 8.22, it only slightly reaches into the PM-2 mode

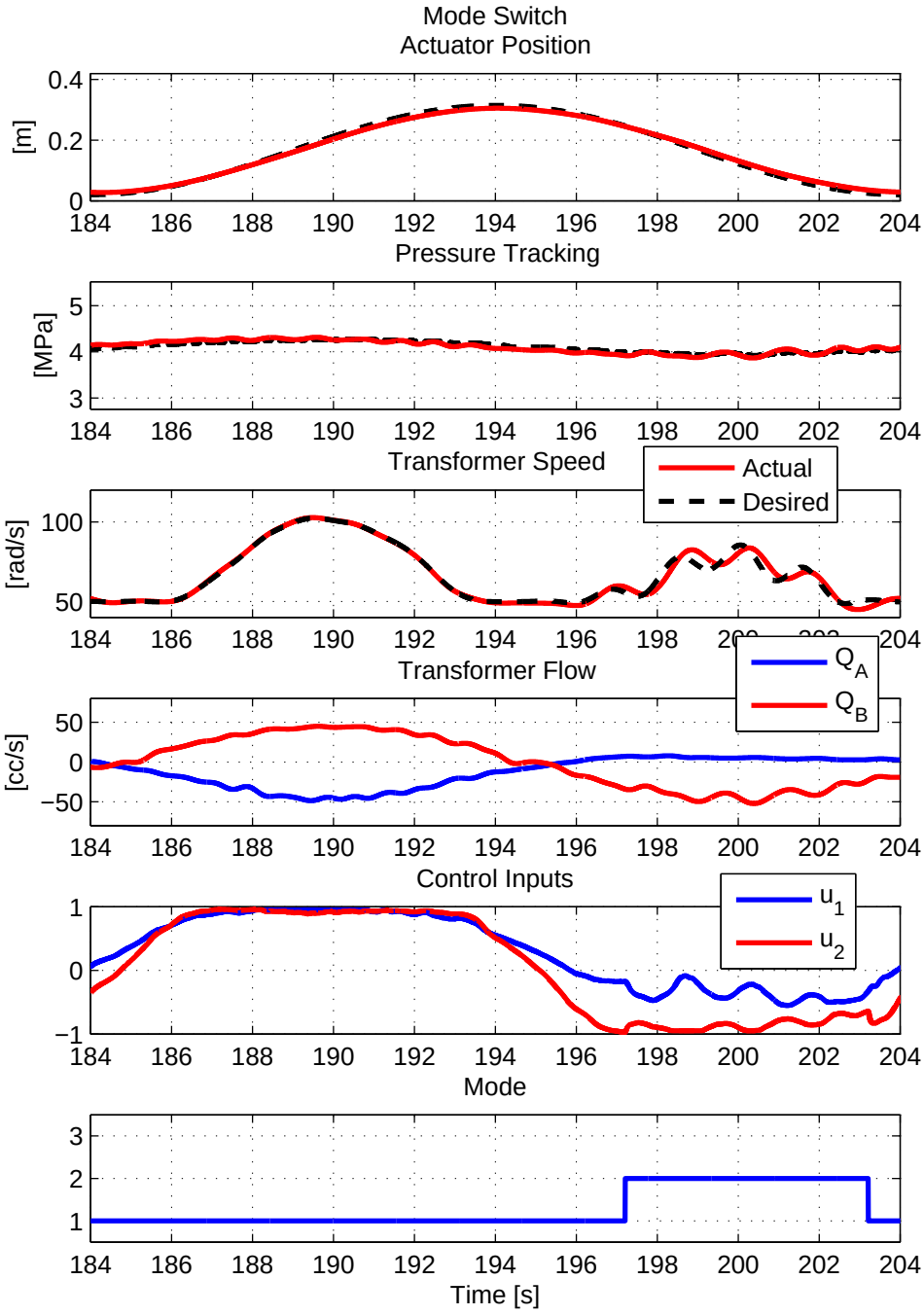

Figure 8.22: Trajectory Tracking with optimal shaft speed and optimal mode switch; Observed: 62.9% cycle efficiency, 46.72% component efficiency; Model expected: 68.2% cycle efficiency, 45.0% component efficiency

8.4.2 Another Example with Lower Pressure Profile

The same trajectory but with different loading condition is utilized to demonstrate the effectiveness of mode switching for the trajectory tracking control. Fig. 8.23 shows this new condition, with the trace lowered down along the pressure level, resulting in the trajectory going deeper into the region where PM-2 is the most efficient. Figure 8.24 shows this trajectory ran with a single operating mode (in PM-1 only), which resulted in 28.9% component efficiency and 37.8% system efficiency. In the meantime, Fig. 8.25 shows the result with mode switching results. Component efficiency is measured at 32.2%, whereas the system efficiency is measured at 43.2%. This finding is summarized in Table 8.4. In summary, optimizing the transformer shaft speed and configuration indeed improve the efficiency of the transformer driven system. In this particular example, more than double the cycle efficiency is measured.

Table 8.4: Efficiency improvements through shaft speed optimization and mode switch, for another trajectory with lower pressure demand

Operating Condition	Component Efficiency		Cycle Efficiency		Net Energy Consumed	
	Experiment	Model	Experiment	Model	Experiment	Model
Constant ω_d	18.2%	18.6%	21.4%	22.4%	3188 J	3046 J
Optimized ω_d	28.9%	27.7%	37.8%	38.5%	1772 J	1740 J
Mode Switch & Optimized ω_d	32.2%	30.3%	43.2%	43.5%	1580 J	1569 J

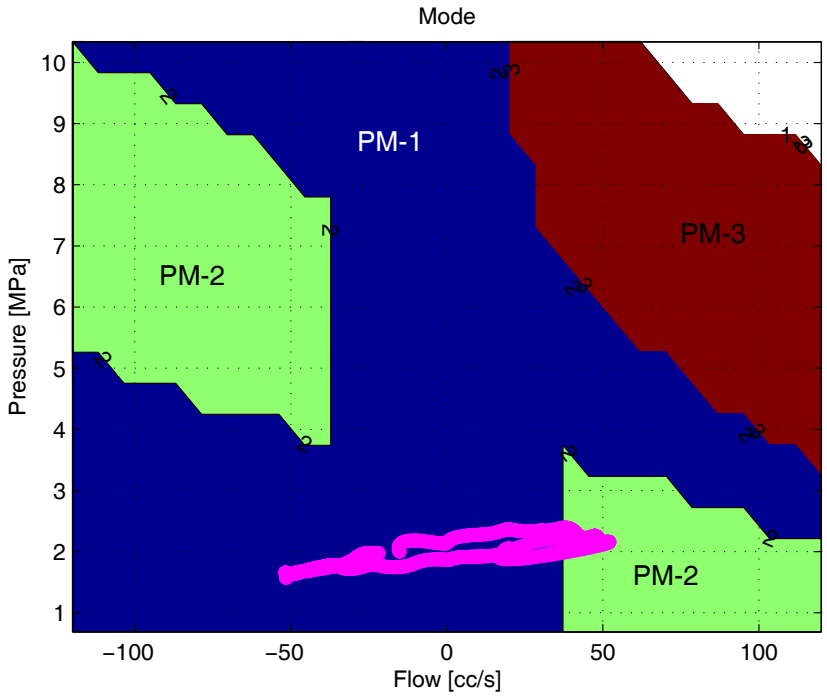

Figure 8.23: Pressure and flow trail for a trajectory with lower pressure demand

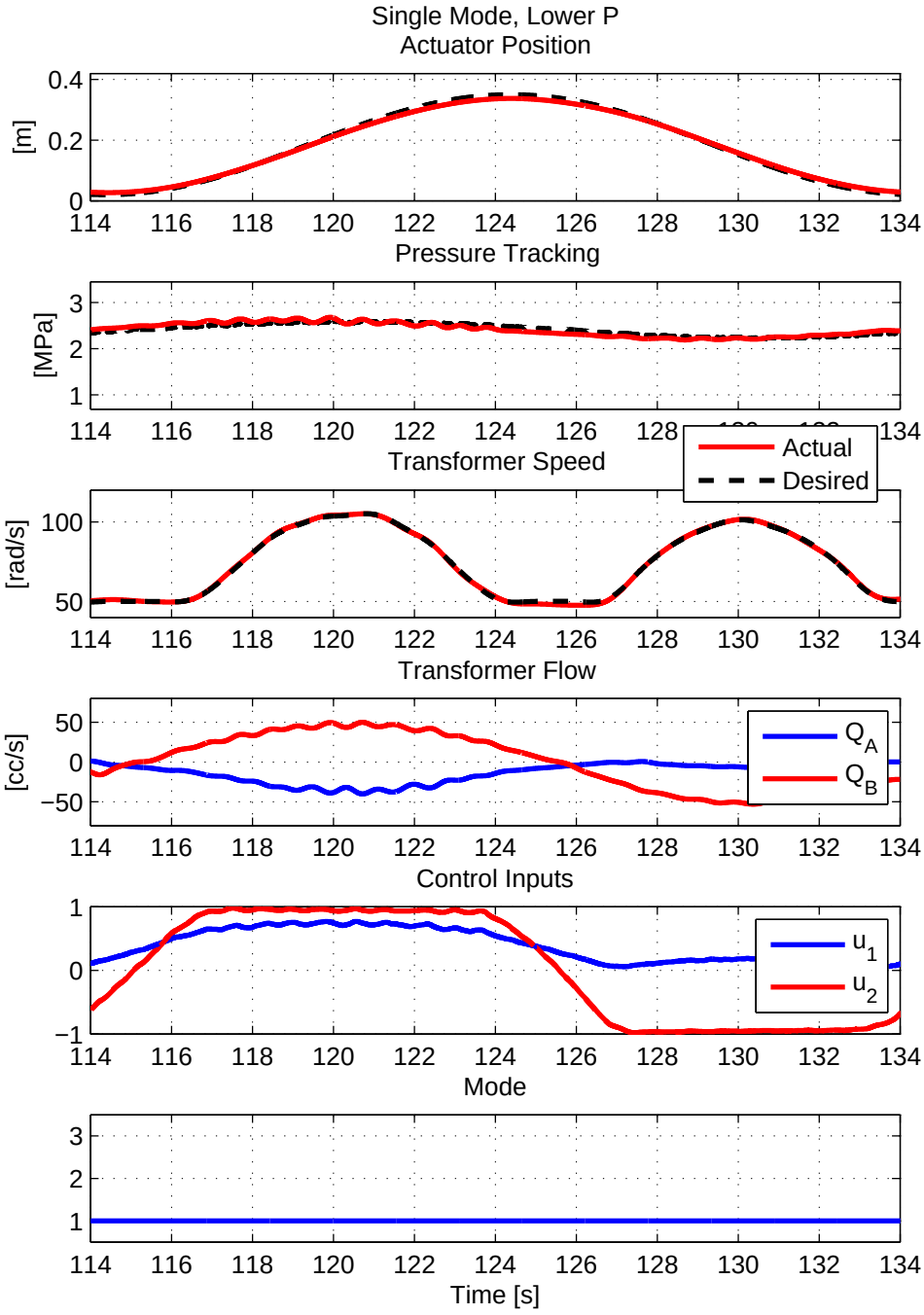

Figure 8.24: Trajectory tracking with an optimal shaft speed but a constant Mode: 37.8% cycle efficiency, and 28.9% component efficiency observed. The model expected 38.5% cycle efficiency and 27.7% component efficiency

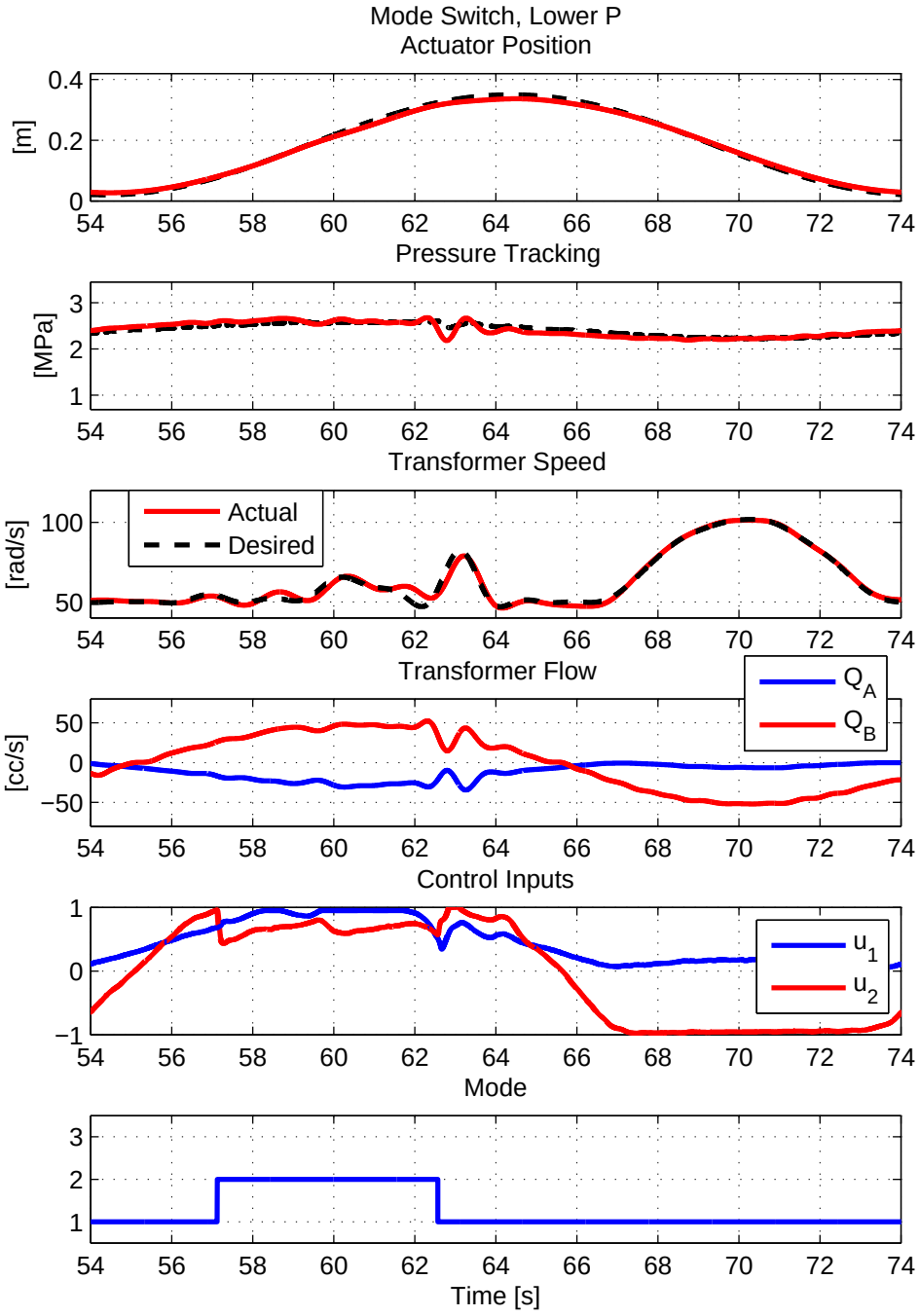

Figure 8.25: Trajectory tracking with an optimal shaft speed and with a optimal mode switch: 43.2% cycle efficiency, and 32.2% component efficiency. The model expected 43.5% cycle efficiency and 30.3% component efficiency

8.4.3 Switching Penalty

In implementing the automatic mode switch algorithm, there might be a condition where the desired pressure and flow combination ends up very close to the boundary of each mode. Figure 8.27 illustrates one such case. In this operating scenario, a sinusoidal flow demand with an amplitude of 55 cc/s was directly provided to the transformer, with the constant pressure condition of 5.5 MPa (800 psi) to explore whether transformer can track an arbitrary flow demand at constant pressure. Observe that the operating mode switches from PM-2 to PM-1 without any trouble around $t = 99$ sec. However, when it starts to switch into PM-3 around $t = 103$ sec, the desired configuration rapidly switches back and forth between PM-1 and PM-3, well beyond the bandwidth of stepper motors that actuate swashplates in this prototype transformer. Both stepper motors failed noted by the displacement commands saturation around $t = 105$ sec. This experiment ended with failure in tracking the desired condition.

Figure 8.26 zooms into the region from $t = 103$ sec to $t = 104$ where rapid switch between PM-1 and PM-3 starts to happen. The top plot shows the expected loss for the desired flow and pressure condition, and the bottom plot shows the resulting operating mode. PM-2 cannot operate in this pressure range, and thus the loss map only shows expected the loss for PM-1 and PM-3. The difference in expected loss between two available modes is rather subtle, and it can be seen that two available lines cross each other many times. Since the supervisory control is designed to simply pick the mode with the least expected loss, each instance of two curves crossing each other results in a command to switch the mode. In the time window being considered in Fig. 8.26, controller is asking the transformer to switch mode 9 times in just 1 second.

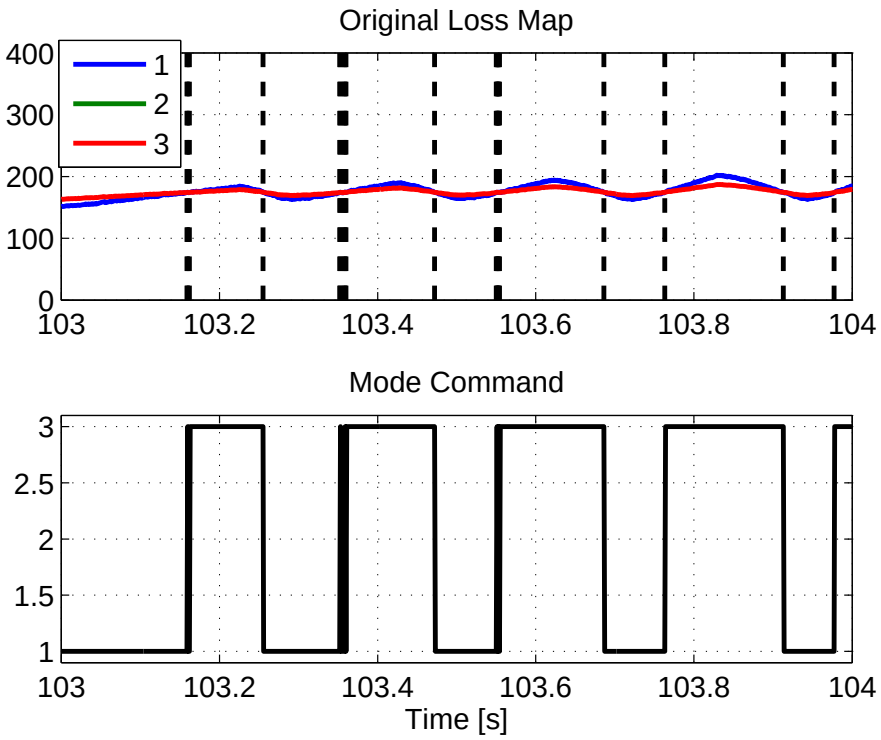

Figure 8.26: Top: Expected power loss the supervisory control is using to determine the operating mode; Bottom: Resulting mode command after comparing expected losses for available modes

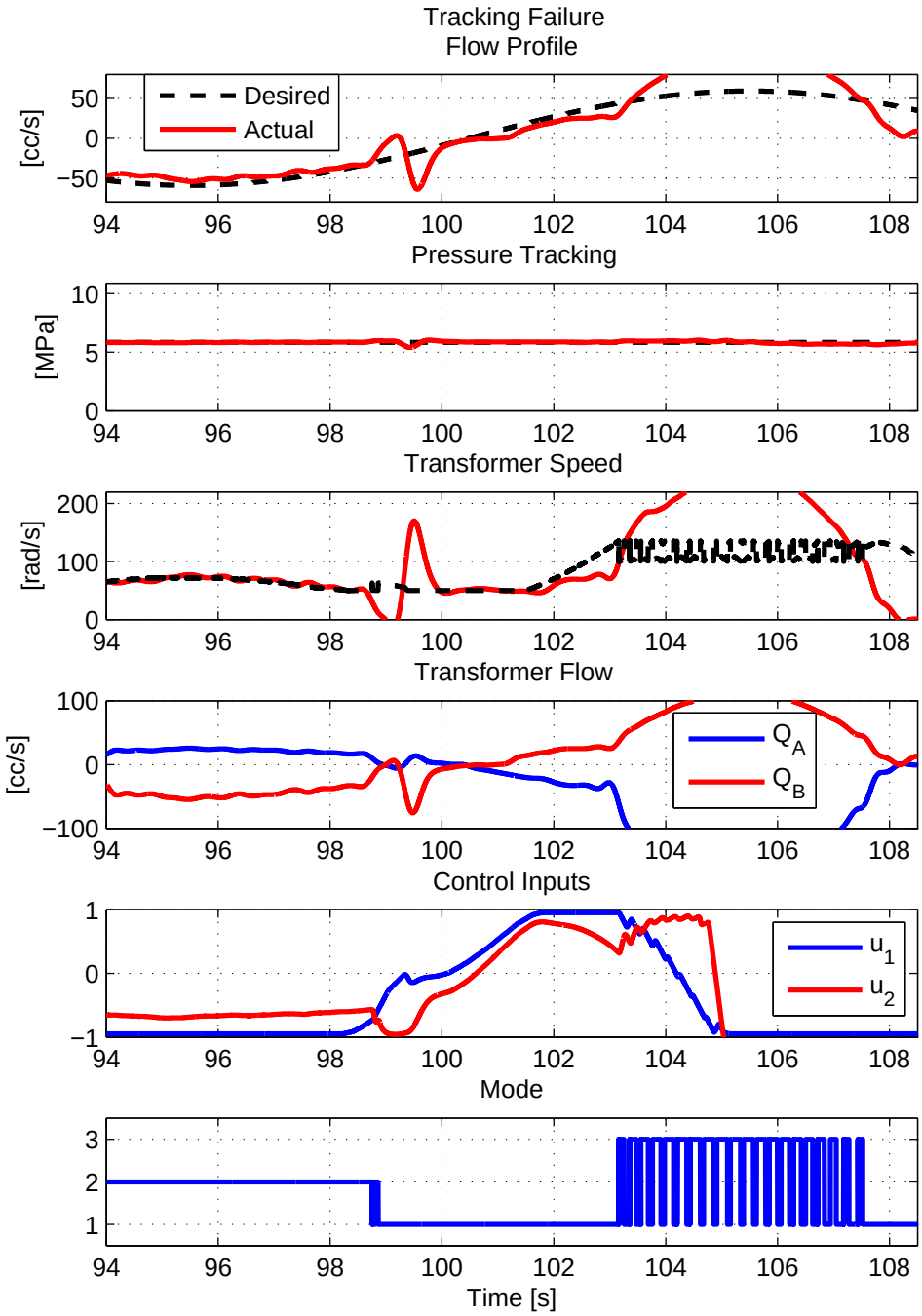

Figure 8.27: Flow tracking at constant pressure demand without switching penalty applied to the controller. Starting at t = 103 sec, a mode is switched rapidly back and forth between two modes

Mode switching algorithm needs to be modified to prevent failures in Fig. 8.27 where rapid mode switch causes the swashplate actuation to saturate and stall. To address this problem, a penalty is given to the mode switch by assigning a cost of switching to the loss map the supervisory control is using to determine the optimal mode. A time-based penalty shall be given such that the cost of switching is severe if not enough time has elapsed since the the last mode switch event, and decreases as more time has elapsed since the last mode switch. The magnitude of the penalty is set to scale with respect to the desired output power. One such cost function is given as:

$$\mathscr{C} = M(P_d Q_B^d) \exp(-p \cdot t_p) \tag{8.26}$$

where M is the magnitude of the penalty to be given with respect to the desired output power. p is the scaling factor in determining how fast the time-dependent penalty will decay, and t_p is the time elapsed since the last mode switch event.

This penalty will be given to modes that are not currently in operation, in the following manner:

$$C_L(L_m, \mathscr{C}) = \begin{cases} L_m & \text{if currently in PM-}m\text{ mode} \\ L_m + \mathscr{C} & \text{else} \end{cases} \tag{8.27}$$

The mode selection algorithm is updated to compare the losses with appropriate penalty applied to modes not currently being operated

$$\text{Mode} = \begin{cases} 1 & \text{if } \min(C_L(L_1,\mathscr{C}), C_L(L_2,\mathscr{C}), C_L(L_3,\mathscr{C})) = C_L(L_1,\mathscr{C}) \\ 2 & \text{if } \min(C_L(L_1,\mathscr{C}), C_L(L_2,\mathscr{C}), C_L(L_3,\mathscr{C})) = C_L(L_2,\mathscr{C}) \\ 3 & \text{if } \min(C_L(L_1,\mathscr{C}), C_L(L_2,\mathscr{C}), C_L(L_3,\mathscr{C})) = C_L(L_3,\mathscr{C}) \end{cases} \tag{8.28}$$

Figure 8.29 shows the same trajectory as in Fig. 8.27, where 55 cc/s sinusoidal flow is demanded with a constant pressure load of 5.5 MPa (800 psi). An empirically determined values $M = 0.5 P_d Q_B^d$, $p = 0.25$ 1/sec were used for the penalty function. Around $t = 44$ sec, the transformer now successfully switches to PM-3 and stays in that mode rather than rapidly going back and forth between PM-1 and PM-3. Figure 8.28 shows the loss map supervisory control referenced for this cycle. It can be seen that with the penalty applied, supervisory control considers PM-1 to be not more efficient than PM-3 to trigger a configuration switch. The resulting effect of applying the penalty to other configurations is adding a hysteresis in determining the mode switch.

As demonstrated in this particular duty cycle, adding a penalty in mode switch prevents the operating condition that rapidly switches between two modes at the boundary condition and ensures successful tracking of the control.

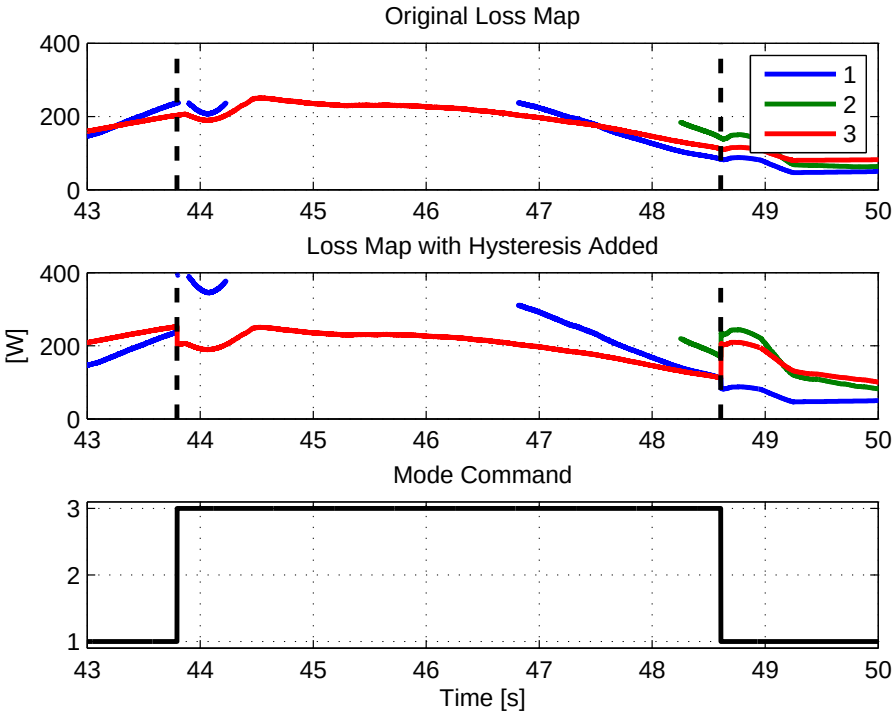

Figure 8.28: Top: Expected power loss with the penalty of switching applied. The supervisory control is using this plot determine the operating mode; Bottom: Resulting mode command after comparing expected losses for available modes

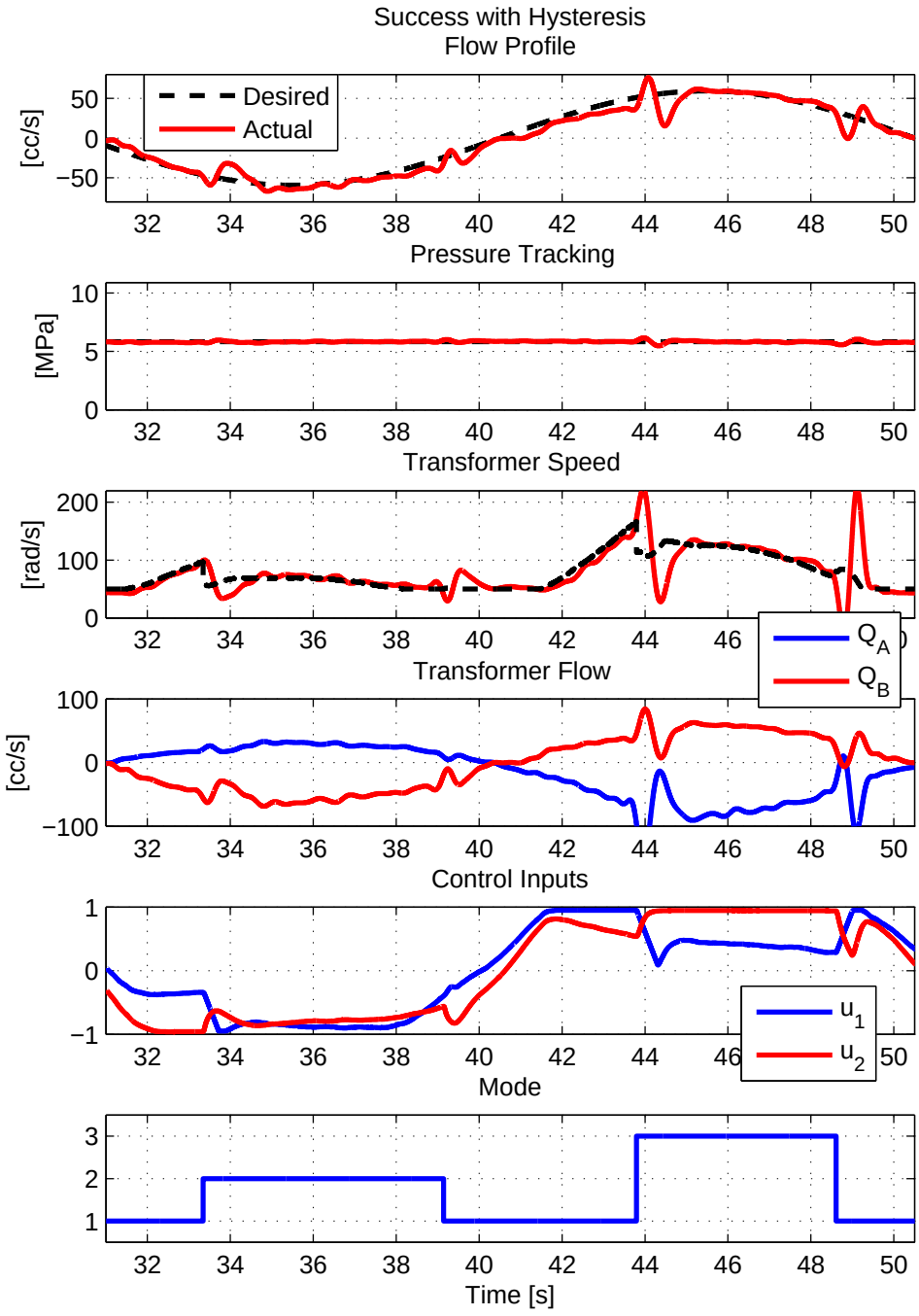

Figure 8.29: With the penalty applied in mode switching, now the experiments can run successfully without rapidly switching back and forth between modes

8.4.4 Mitigating the bump in transfer

Another consideration that should be given in implementing the mode switch is the 'bump' in the system after each configuration change. Take PM-1 and PM-3 for instance, whose torque dynamics given by Eq (2.18) and (2.21) are re-printed here for reading convenience:

$$J\dot{\omega} = \begin{cases} (P_A - P_T)\frac{D_1}{2\pi} + (P_T - P_B)\frac{D_2}{2\pi} & \text{PM-1} \\ (P_A - P_T)\frac{D_1}{2\pi} + (P_A - P_B)\frac{D_2}{2\pi} & \text{PM-3} \end{cases} \tag{8.29}$$

Focusing on the D_2 unit, it is apparent that with the pressure condition $P_A > P_T$, switching from PM-1 to PM-3 will cause a sudden increase in torque balance, causing the transformer shaft to spike up if the controller is not acting quickly. Figure. 8.30 shows a simulation result where a transformer with a known viscous friction is being asked to produce a steady flow at constant shaft speed. In an ideal case such as this scenario, the controller will detect the pressure change in transformer immediately and produce a step change in control input to keep the transformer shaft at a constant speed as desired. It can be seen in the same figure as well.

Unfortunately, such a step change in control input cannot be delivered in real life. This actuator response is modeled as a first-order low-pass filter with a form with a transfer function:

$$G_a(s) = \frac{1}{\tau s + 1} \tag{8.30}$$

where τ is the time constant for the response. Figure. 8.31 shows what will happen if this filter is applied for the control inputs produced by transformer controller. Because the displacement input fails to deliver the desired input command, transformer speed tracking is lost for a short period of time, resulting in a spike of transformer shaft speed. Since $Q_B = \frac{D_2}{2\pi}\omega u_2$, this deviation will result in spike in delivering the output flow.

In the current control algorithm, transformer controller distributes the control inputs to the two displacement commands according to the transformer mode as seen in Section 6.3.2. The command to switch the operating mode is sent to the transformer and controller at the same time. This algorithm can be tweaked such that this timing can be shifted by a small amount. Specifically, the mode switch can be delayed such that it happens slightly after the controller has been told about the mode switch. This is demonstrated by a simulation in Fig. 8.32. In this figure, vertical black dashed line corresponds to the time when transformer controller is switched to a different mode. The magenta line corresponds to the time when actual transformer mode switch occurs. In short, transformer

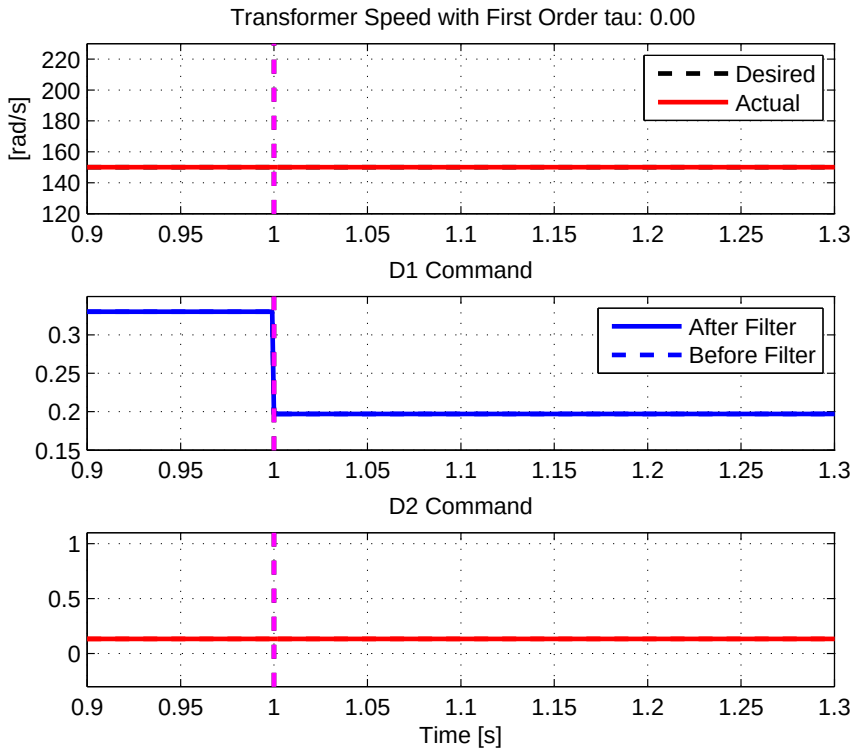

Figure 8.30: Simulated mode switch where the control inputs are provided without any delay. If the controller can instantly react to the configuration mode switch, there will not be any bump in regulating the shaft speed

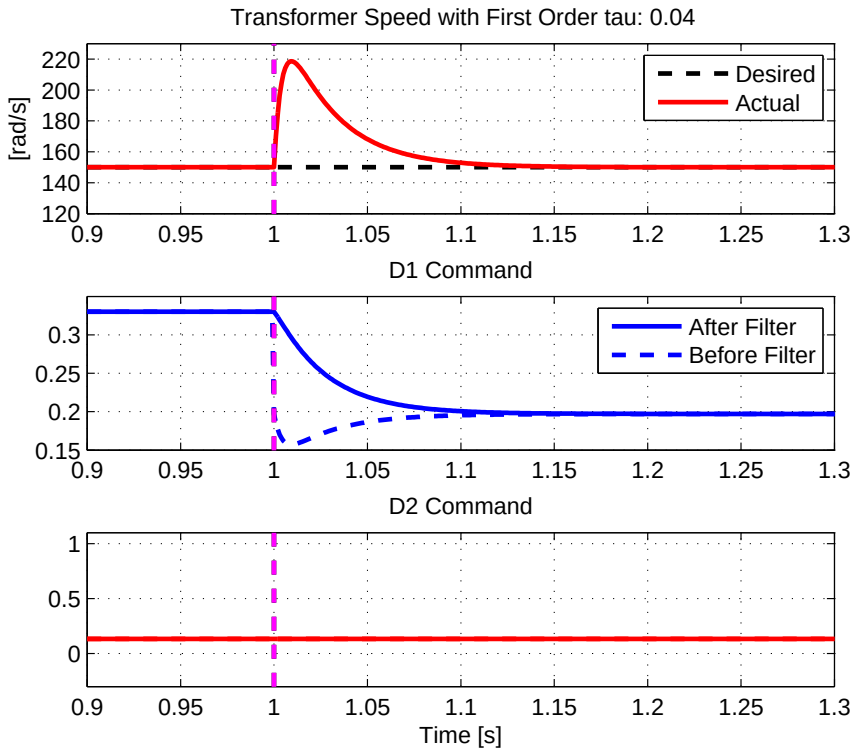

Figure 8.31: Simulated mode switch with a first order filter in control inputs, reflecting the delay in providing the desired control input in experimental system. There is a bump in regulating the shaft speed

controller acts ahead to distribute the control inputs even before the actual switching occurs. The net result of such shift is clearly visible. Whereas the peak error is 70 rad/s in Fig. 8.31, it reduces to 40 rad/s in Fig. 8.32. The RMS error in transformer speed is reduced from 16.6 rad/s to 10.8 rad/s, a 35% decrease in shaft speed error just by simply delaying the actual switch briefly.

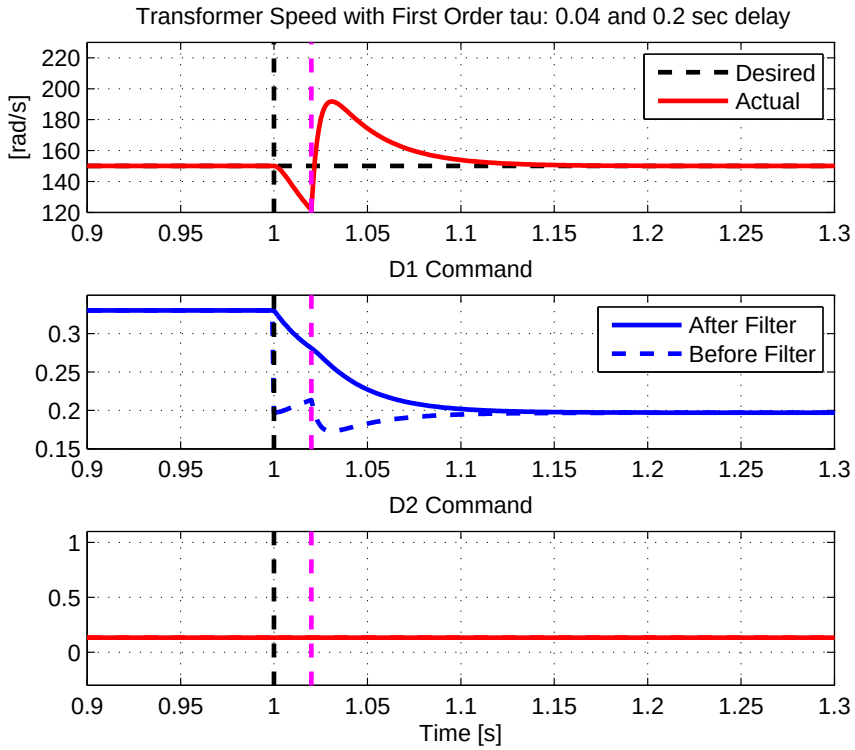

Figure 8.32: Simulated mode switch with a bump mitigation. The controller was switched at time corresponding to the black line ahead of the transformer mode switch corresponding to the magenta line

Consider Fig. 8.33 which shows the step response of the first order filter. The area A^- denotes the error in delivering desired control input after the controller switches but before the transformer switches. This area is given by:

$$\begin{aligned} A^- &= \int_0^{t_d} \Delta D(1 - e^{-\frac{1}{\tau}t})dt \\ &= \Delta D \left[(t_d - \tau) + \tau e^{-\frac{1}{\tau}t_d}\right] \end{aligned} \tag{8.31}$$

where, t_d is the time delay in actually switching the transformer operating mode, and ΔD is the magnitude of displacement change required to keep the transformer steady after

the mode switch. In a similar manner, area A^+ denotes the error after the transformer switches which is given by:

$$\begin{aligned} A^+ &= \int_{t_d}^{\infty} \Delta D e^{-\frac{1}{\tau}t} dt \\ &= \Delta D \tau e^{-\frac{1}{\tau}t_d} \end{aligned} \tag{8.32}$$

If the switching is not delayed at all such that $t_d = 0$, then the $A^- = 0$ and the error in delivering desired speed is all due to A^+. In other words, these areas are the cumulative sum of displacement error and multiplying these terms with pressure the displacement unit interact with before and after the switch P^- and P^+ translates to the torque error caused by the first order filter.

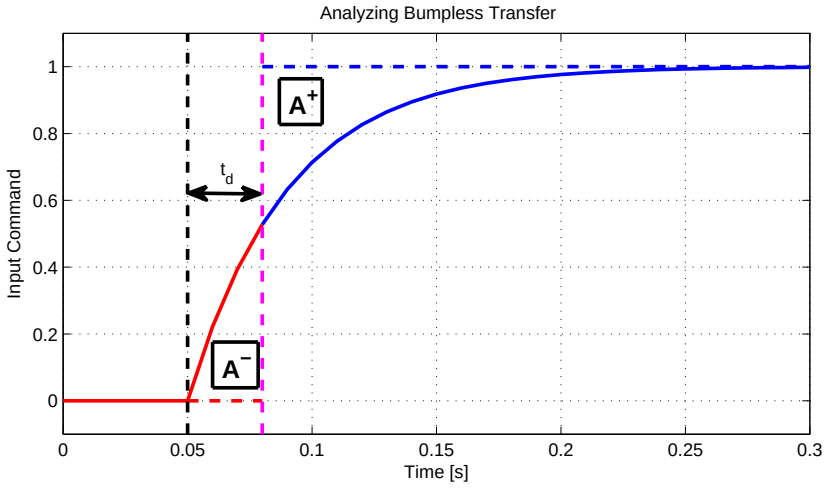

Figure 8.33: Step response of the first Order filter is utilized to find out the amount of delay in switching t_d that minimizes the effect of torque error

In order to minimize the transformer speed error, we desire to have torque error from A^- and A^+ offsetting each other such that $P^- A^- = P^+ A^+$. For a case where $P^- \neq P^+$ obtaining the closed form solution for t_d is difficult and the solution needs to be obtained numerically.

$$\begin{aligned} P^- \left[(t_d - \tau) + \tau e^{-\frac{1}{\tau}t_d} \right] &= P^+ \left[\tau e^{-\frac{1}{\tau}t_d} \right] \\ \left(\frac{P^+}{P^-} - 1 \right) \left[\tau e^{-\frac{1}{\tau}t_d} \right] &= t_d - \tau \end{aligned} \tag{8.33}$$

The numerical solution of t_d for $\tau = 0.04$ sec is shown in Fig. 8.34. In a special case $P^- = P^+$, setting $A^- = A^+$ results in

$$t_d = \tau \tag{8.34}$$

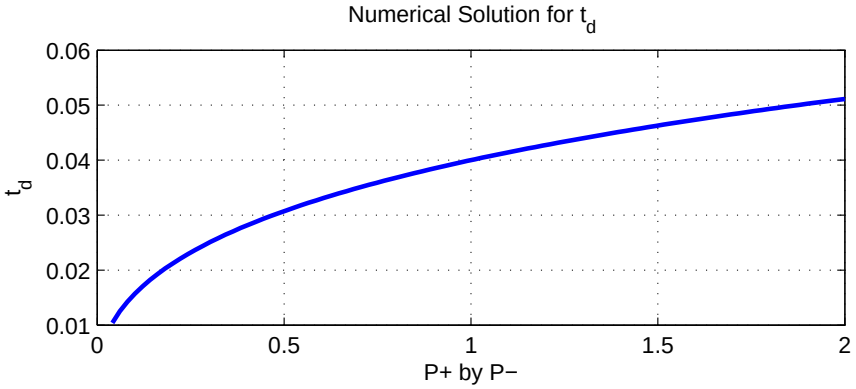

Figure 8.34: The solution for the amount of delay in switching t_d (sec) necessary to minimize the bump is plotted for ratio of P^+/P^-

Experimental Demonstration

The solenoid valves utilized for the switched mode hydraulic transformer have a response time rated at 50 ms. It means without doing anything to the controller structure, there already is a 50 ms delay between switching the controller to the actual mode switch. In the experiments described below for the 'no delay' case actually involves delaying the controller switch by 50 ms to sync the controller switch and transformer switch to happen at the same time. This needs to be considered for the implementation. The controller switch is delayed by 50 ms $-t_d$ to realize the desired t_d. The results are all shown to reflect the actual timing of the mode switch and controller switch (i.e., the mark indicating transformer mode switch does correspond to the mode switch).

Figure 8.35 shows the transformer shaft tracking as the mode switches without delay and with the delay (50 ms) for a constant desired shaft ω_d and desired flow Q_B^*. It can be seen that having a delay in mode switching reduces the RMS error in shaft speed from 26.06 rad/s to 21.63 rad/s. Figure 8.36 shows the same tracking result for a varying desired flow which results in varying ω_d. The reduction in RMS shaft speed error is more dramatic for this operating scenario, resulting in a change from 55.88 rad/s to 23.66 rad/s in RMS error in transformer shaft speed. Figure 8.37 expands onto the Fig 8.36 to show the trajectory tracking results and transformer output flow for the same set of experiments. With the mode switch delay, the transformer is able to provide a better trajectory tracking, and provide the desired flow better.

It is noteworthy, however, that the large error peaks in shaft speeds observed in Fig. 8.36 does not directly show up in trajectory tracking response. This is due to the viscous friction and fluid compressibility in the cylinder providing a compliance or damping to the motion. The difference in the efficiency observed for the time window considered is subtle. Without the delay, 54.0% efficiency is measured. With the delay, 56.6% efficiency is measured, which is only 4% increase in the efficiency.

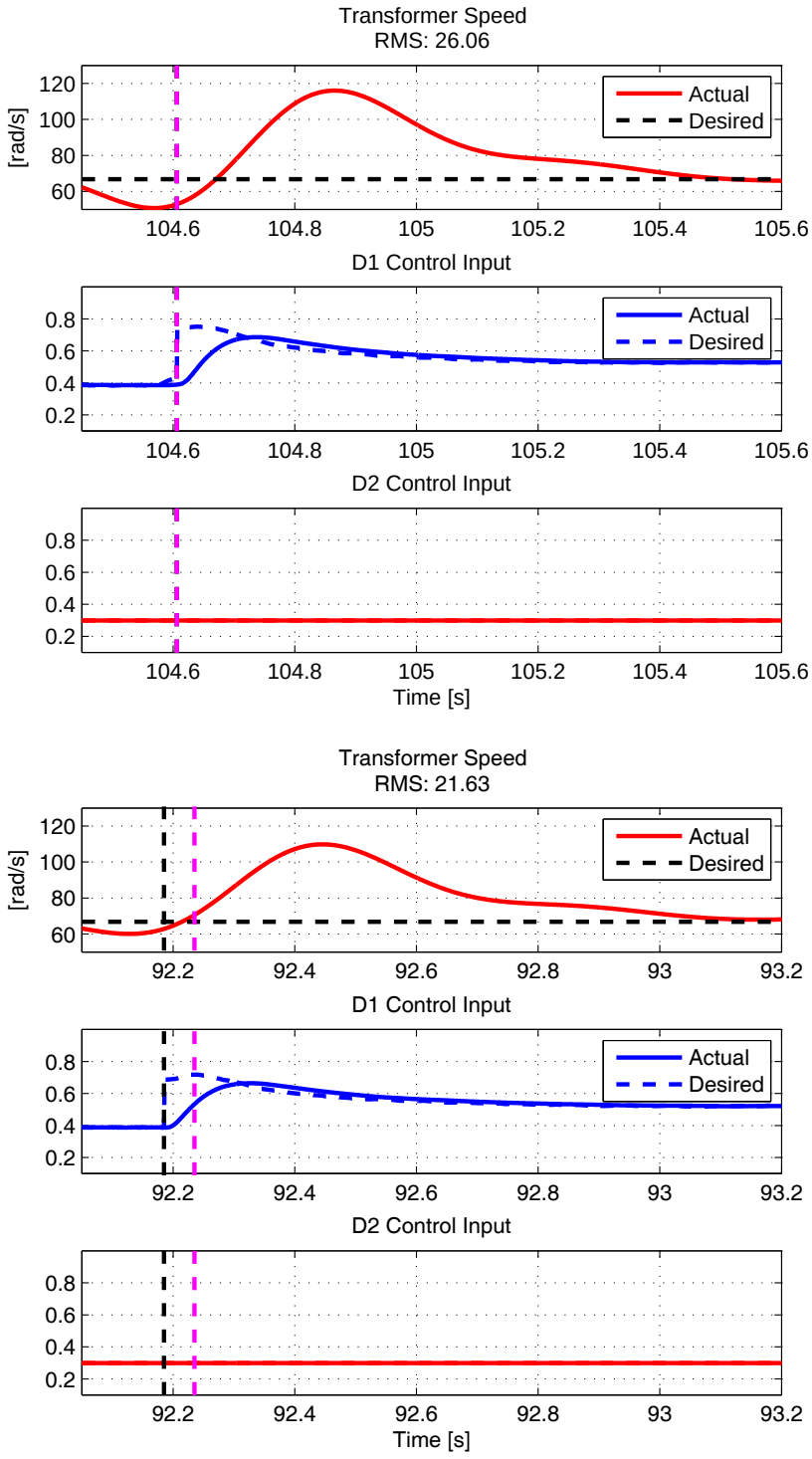

Figure 8.35: Experimental result in bumpless transfer with constant ω_d and Q_B^*. Top: No mitigation; Bottom: Controller is switched before the transformer is switched

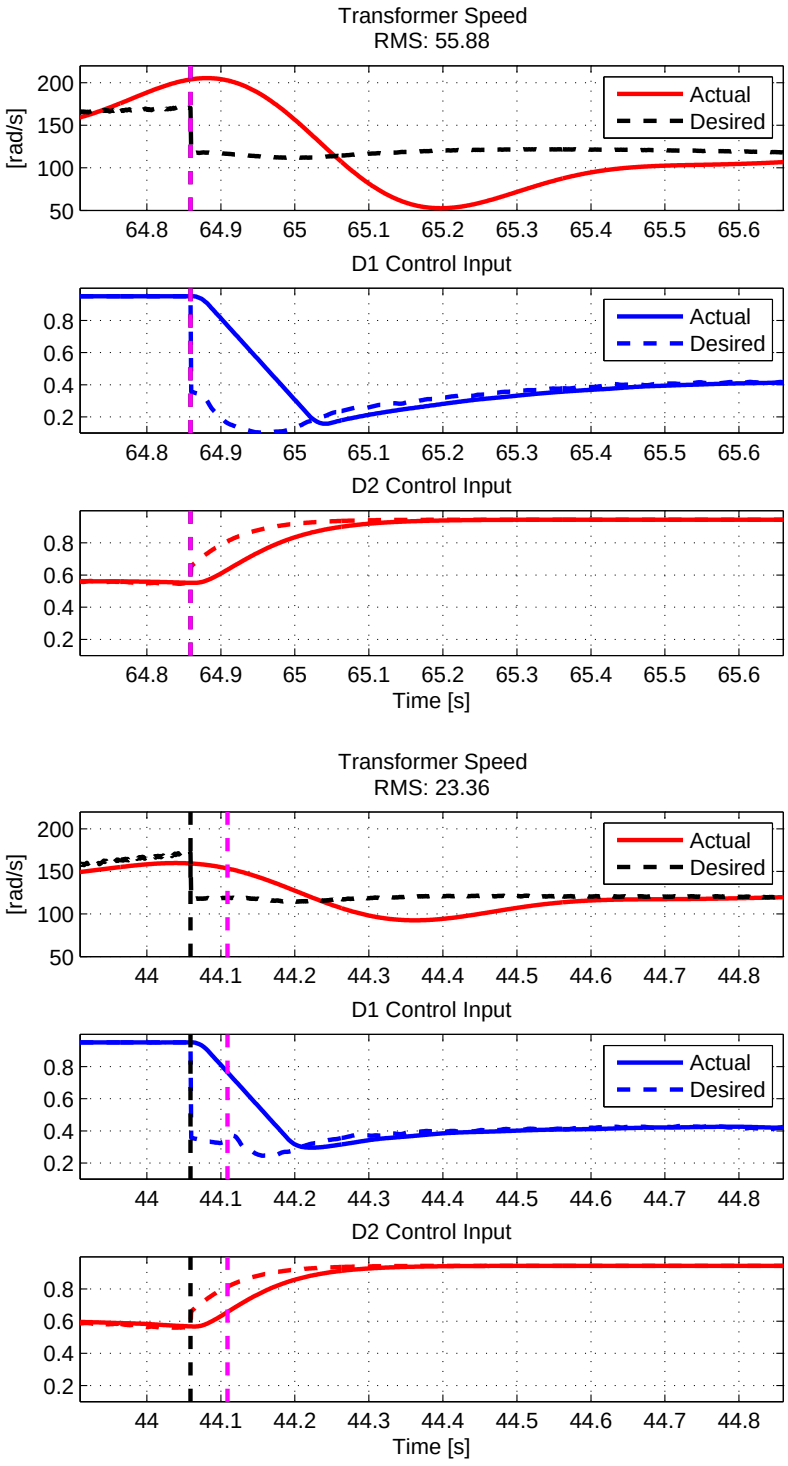

Figure 8.36: Experimental result in bumpless transfer with variable ω_d and Q_B^*. Top: No mitigation; Bottom: Controller is switched before the transformer is switched

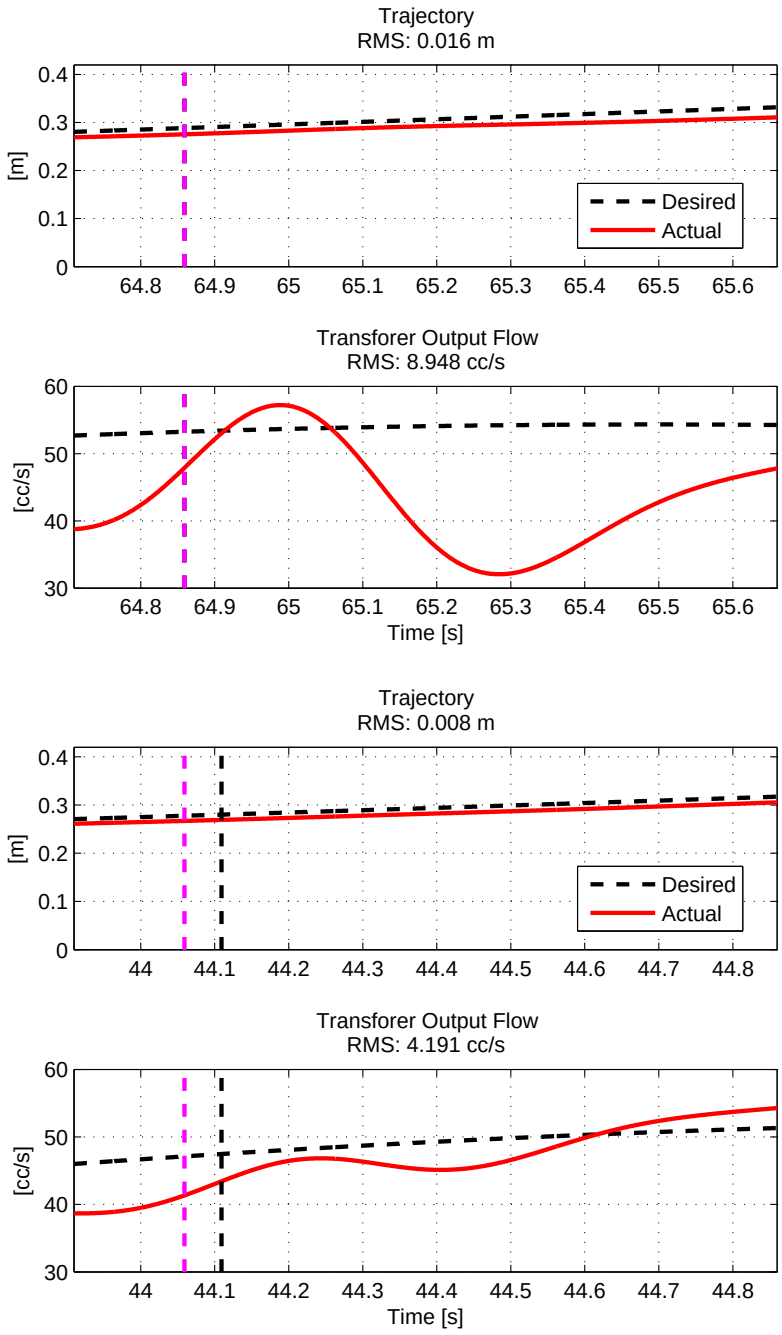

Figure 8.37: Trajectory tracking and transformer output behavior for the experiments in Fig. 8.36. Top: No mitigation; Bottom: Controller is switched before the transformer is switched. The flow error and trajectory error has reduced

8.5 Chapter Summary

This chapter discussed the challenges faced in demonstrating the efficiency of the transformer driven system. A Hardware-In-the-Loop testbed has been developed to overcome these challenges. Instead of having to acquire physical equipment corresponding to the desired pressure level, any desired pressure loading condition can be generated with HIL testbed.

The efficiency of the transformer system was defined. A supervisory controller to further improve the transformer system efficiency was developed. The first step involves regulating the transformer to operate at its optimal shaft speed for a given configuration. The next step explored an automatic selection of transformer configuration such that transformer will be switched to its most optimal configuration mode. Details to ensure the smooth operations with the mode switch were discussed. In all experiments presented, the experiments showed satisfactory match with the simulated expectations.

The next chapter will utilize findings from this chapter to demonstrate the efficiency of a transformer driven system compared with the typical system with throttling valves.

Chapter 9

Demonstration of Transformer Efficiency

This chapter presents a case study to compare the efficiency of the hydraulic transformer driven system against throttling valve driven system, which is still prevalently used in hydraulics due to their simplicity in control design, compactness, and satisfactory control performance.

Previous attempts in demonstrating the energy saving potential of the hydraulic transformers are available. In [6], fuel savings of more than 50% is reported for a wheel loader whose wheel drive and main lift cylinders are driven by floating cup IHTs in simulation. In [78], a hydraulic hybrid excavator fitted with a bent-axis IHT is expected to deliver up to 32% reduction in fuel consumption in simulation. In [36], it is shown with a simulation that up to 82.1% of the potential energy could be recovered by utilizing a PM transformer in one configuration. Pieter Gagnon, an MS graduate who worked together with me on the same project as this dissertation, presented a comparison study for a robotics duty cycle [29]. Utilizing subcomponent level mathematical modeling for PM transformer, Gagnon fitted a trajectory over the simulated efficiency map to compare the system level efficiencies between transformer driven system against a traditional throttling valve driven system. He showed more than doubling the efficiency is possible with properly sized transformer. It should be noted that all the results were performed with a simulated transformer rather than an actual prototype.

To demonstrate the potential efficiency of a transformer driven system, this dissertation differs from the mentioned previous works in following ways. Firstly, an actual prototype physical transformer is used to obtain the experimental efficiency rather than utilizing a transformer in simulation. Secondly, instead of fitting a trajectory over an efficiency

contour, the controller dynamics in meeting the trajectory and switching the configuration modes will also be incorporated in the analysis. Chapter 6 and Chapter 7 of this dissertation has already demonstrated the feasibility of using transformers to deliver satisfactory control performance. However, efficiency benefits of using transformers could not be demonstrated due to difficulties in the experimental setup as discussed in Section 8.1. Chapter 8 presented a HIL testbed to allow our transformer to be tested at any desired pressure condition, and explored algorithms that optimizes the operating shaft speed and configuration mode to maximize the efficiency benefit of utilizing transformer in a system. This chapter incorporates findings from these chapters to demonstrate the effectiveness of transformer controller and efficiency of the transformer driven system at the same time.

This chapter is organized as follows. Section 9.1 provides the description of the system to be compared, along with the definition of efficiency for the throttling system. Section 9.2 first shows the efficiency results for the three different loading cases considered separately. Another result where the different loading cases are delivered at the same time is also shown to demonstrate the full efficiency potential of utilizing hydraulic transformers in the system. Finally, Section 9.3 provides concluding remarks for this chapter.

9.1 Description of Systems to be Compared

9.1.1 Hydraulic Transformer System

A system discussed in Chapter 6 was used as a baseline for the comparison to be implemented on the Hardware-In-the-Loop testbed presented in Section 8.1. In this system, as seen in Fig. 9.1, the port 'B' of the hydraulic transformer is connected to the cap-side of the hydraulic cylinder, providing pressure P_B and flow Q_B. This transformer is a switched mode transformer as developed in Chapter 5. The supply pressure P_A to the transformer is set to be 6.9 MPa (1000 psi), and the return line pressure P_T is negligibly small. The cylinder being considered has the same dimensions as with experimental setup presented in Section 6.4, with a cap side area $A_1 = 11.87$ cm^2 and a rod side area $A_2 = 5.1$ cm^2.

Figure 9.2 shows the trapezoidal trajectory, which was generated by dissecting a sinusoidal trajectory with an amplitude of 14.7 cm and period of 0.4 rad/sec. At the peak of the sinusoidal curve, the trajectory is held up for 2 seconds before being lowered down. This is similar to the ones presented in Section 6.4.

In Fig. 9.1, a mass load attached to the cylinder is shown. Mass loads of 330kg, 660kg, and 990kg are considered for this analysis. With the supply pressure of 6.9 MPa (1000 psi), the first two cases will result in pressure conditions P_B that needs to buck the supply

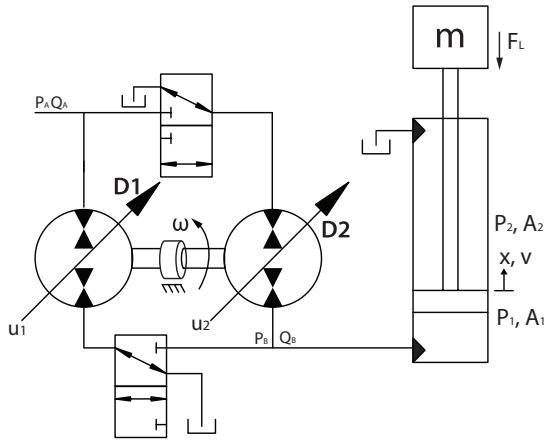

Figure 9.1: Transformer system considered for the efficiency analysis

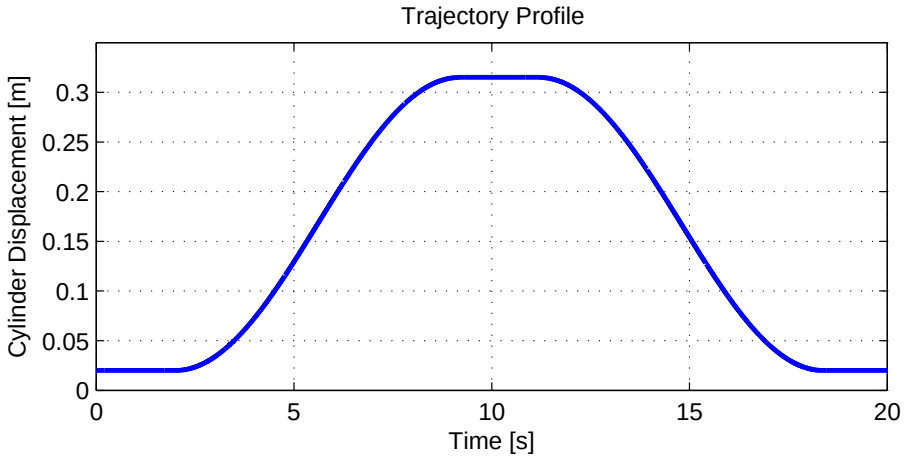

Figure 9.2: Trajectory tracking for various parameter values

pressure such that $P_B < P_A$, whereas the last one requires the supply pressure to be boosted such that $P_B > P_A$.

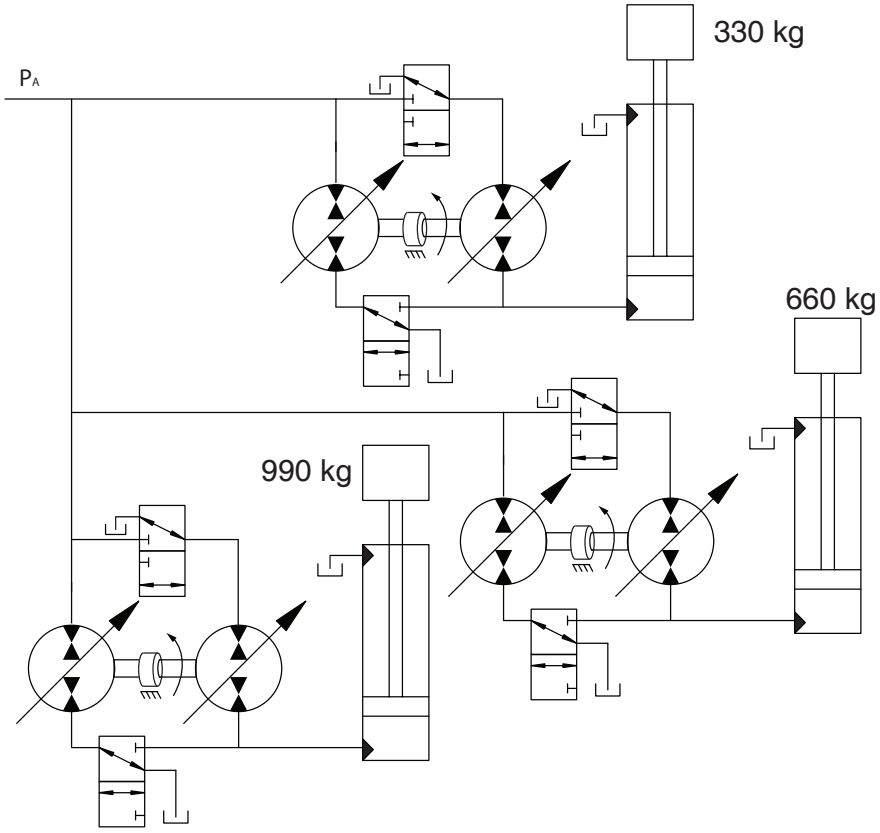

Figure 9.3: Transformer system considered for the efficiency analysis showing all 3-DoFs

Instead of considering only a single cylinder and a single transformer at a time, we analyze a scenario where multiple actuators are connected at the same time to the single supply pressure at P_A as shown in Fig. 9.3. Figures 9.4–9.6 show the tracking result for the 3 loading cases considered in this case study. Behavior of the transformer, such as the flows and control input, along with the mode selection are presented.

For a 330 kg loading case shown in Fig. 9.4, a cylinder is emulated through a Hardware-in-the-Loop system presented in Section 8.1. A trajectory controller developed in Chapter 6 was implemented, along with the supervisory controller for the shaft speed and configuration mode developed in Chapter 8.

In the meantime, 660 kg and 990 kg loading conditions shown in Figs 9.5 and 9.6 were generated from the full simulation of the transformer dynamics, backstepping controls and actuator dynamics. Simulations are used instead of experiments because the experimental setup has some difficulty executing these trajectories. When the transformer configuration

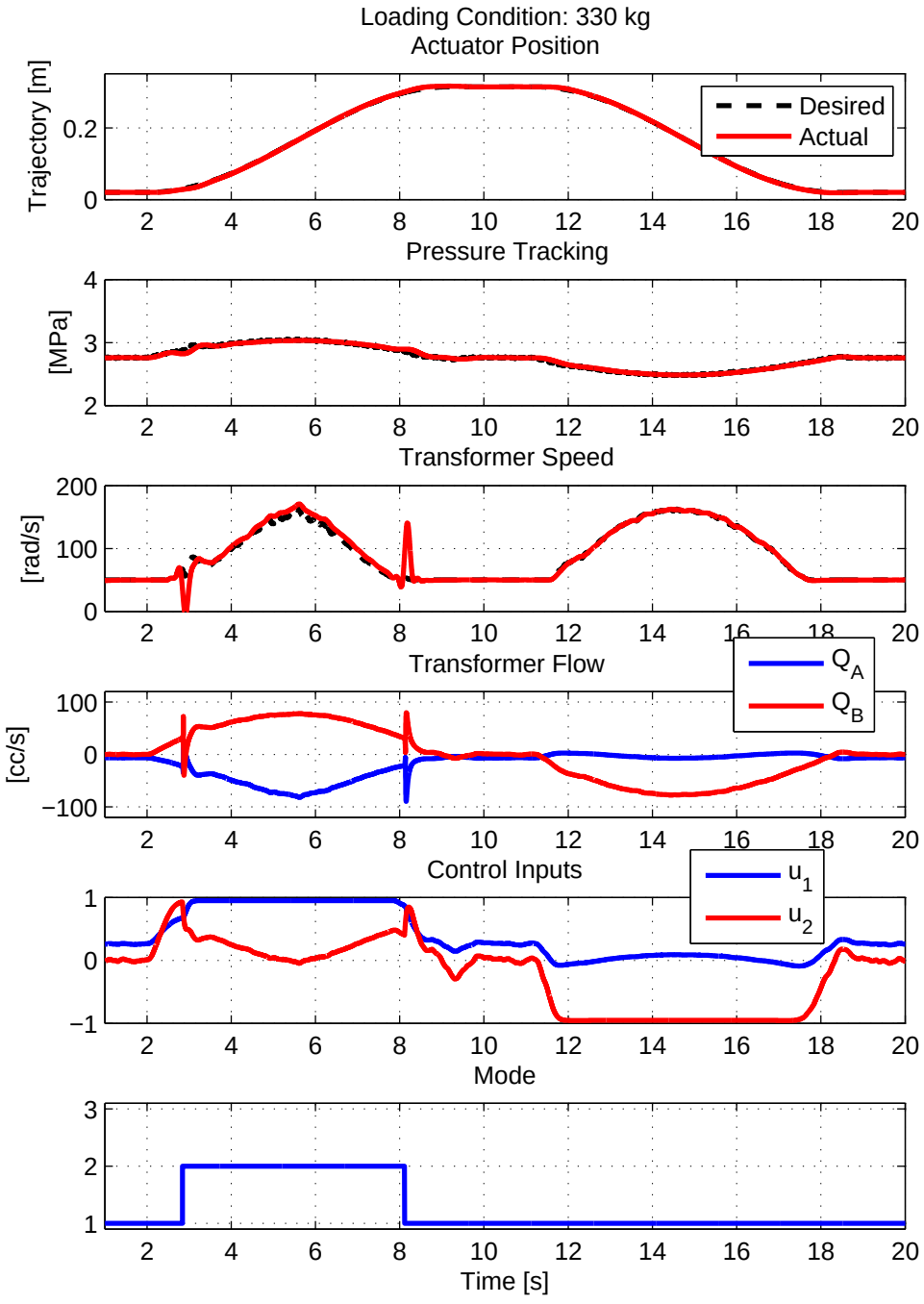

Figure 9.4: Trajectory tracking result for transformer with 330 kg load, showing pressure tracking, transformer speed, transformer port flows, control inputs and utilized mode

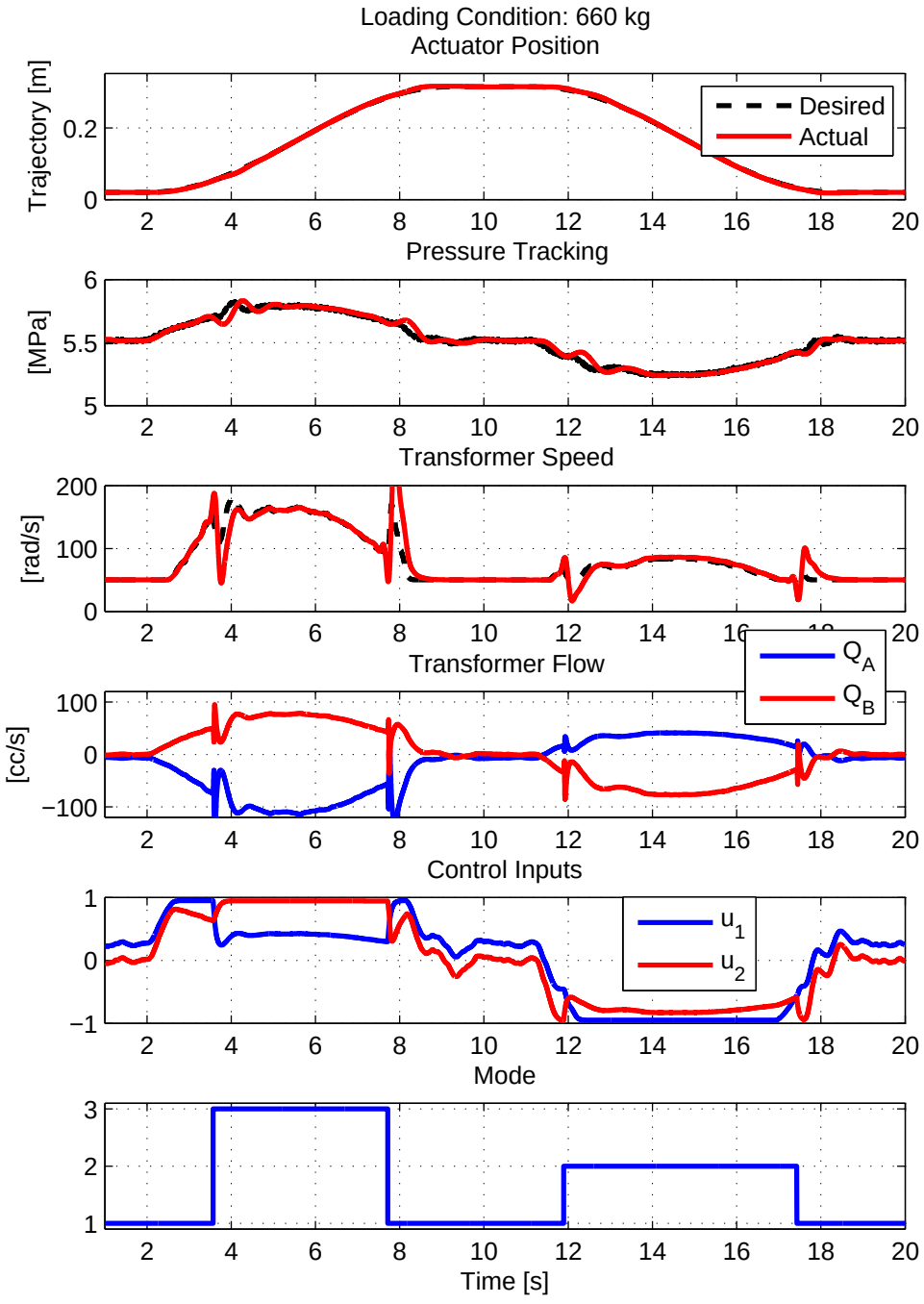

Figure 9.5: Trajectory tracking result for transformer with 660 kg load, showing pressure tracking, transformer speed, transformer port flows, control inputs and utilized mode

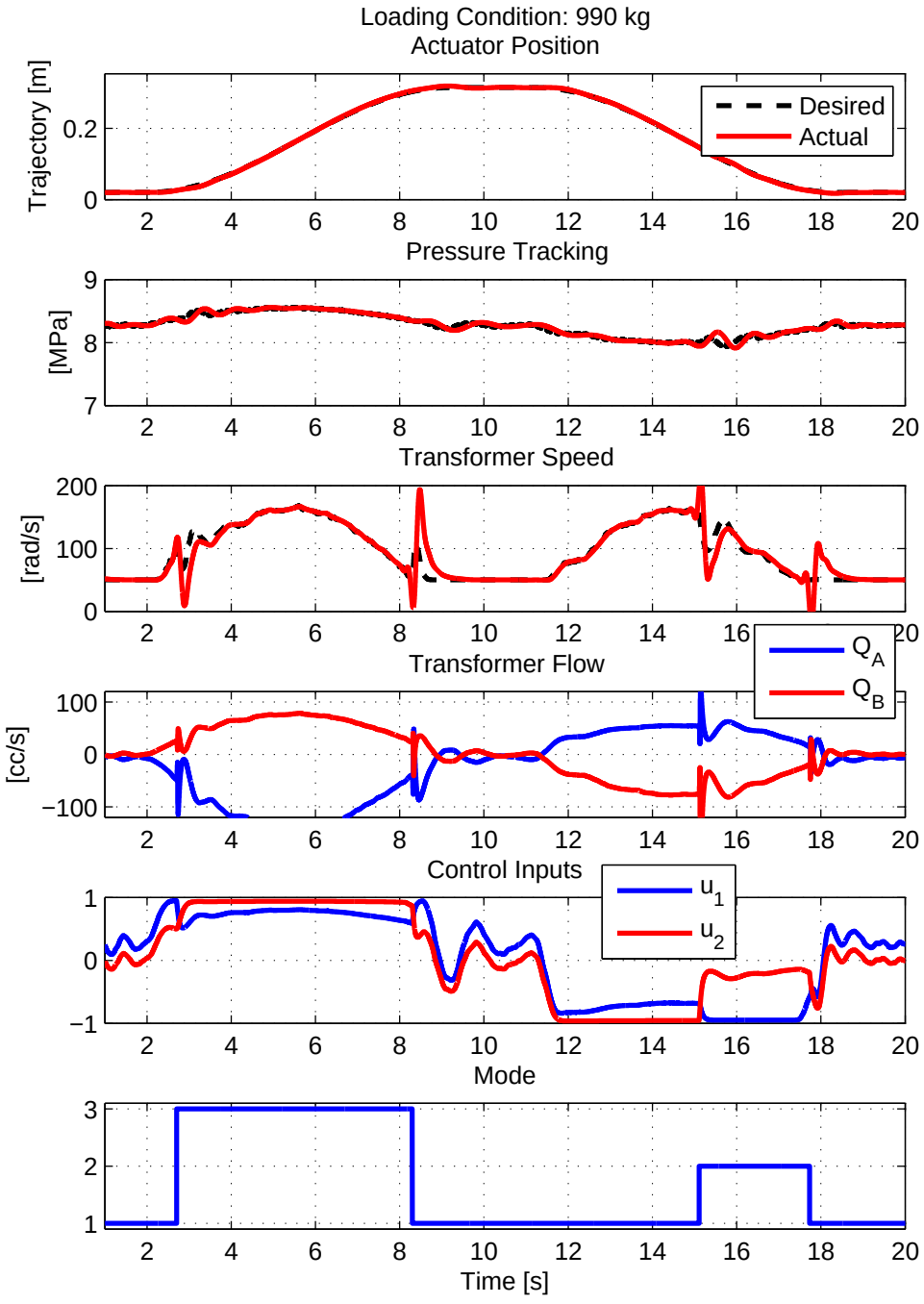

Figure 9.6: Trajectory tracking result for transformer with 990 kg load, showing pressure tracking, transformer speed, transformer port flows, control inputs and utilized mode

mode is switched from PM-3 to PM-1, the displacement ratio command has to be changed in a behavior similar to a step response curve. This is problematic especially with a motoring unit (D_1 unit) of the prototype transformer. In order to follow the command signal to increase the displacement ratio rapidly, the stepper motor has to advance rapidly to push on to the swashplate that is loaded with the cylinder barrel exposed to the port pressures. This turned out to be beyond the torque limitation and the bandwidth limitation of the stepper motor used in the swashplate actuation presented in Chapter 5.

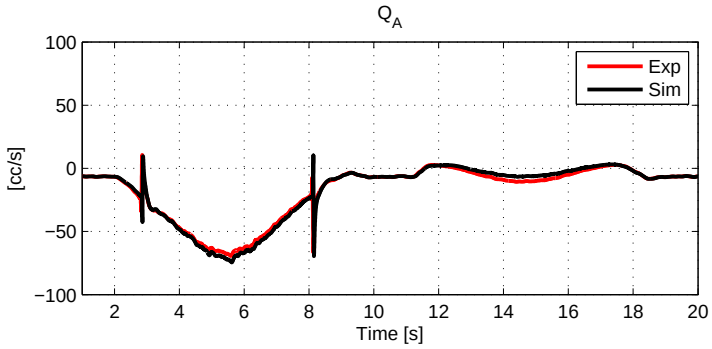

Figure 9.7: Trajectory tracking result for transformer with 330 kg load compared against the simulated condition, showing the match in Q_A

The accuracy of the simulations make it feasible to utilize the simulation results. For the experiment performed in Fig. 9.4 with the 330 kg load, a simulation was run imposing the transformer flow Q_B, shaft speed ω, and the supply pressure P_A and P_B to determine how well the model is able to predict the input power for the given output power. The simulation computes the necessary displacements and input flow Q_A. Figure 9.7 shows the flow Q_A coming from this model compared against the measured flow from an experiment. The RMS of difference between simulated flow and experimental flow is 1.92 cc/s for overall cycle. This translates to RMS of 13.3 W input power error. For overall cycle, the error in estimating the net energy consumption is 6%. The measured efficiency is 43.4% from the experiment and 41.6% from the simulation, which shows that the transformer model is able to satisfactorily anticipate the efficiency from the experiment.

The good match between simulations and experiments were shown in the previous chapters as well. In Chapter 5, Fig. 5.11 showed the model is expecting the prototype efficiency with RMS error of 4% points. In Chapter 8, experiments were performed to demonstrate the possible efficiency improvements with the supervisory control. From Table 8.3 and Table 8.4 the RMS error in expecting the cycle efficiency is 2.9% points. Thus it was determined acceptable to utilize simulation results for the 660 kg and 990 kg loading cases for the efficiency analysis presented in this chapter. The efficiency results and net

energy consumptions for the three loading cases will be presented in Section 9.2, after describing the throttling system to be compared.

9.1.2 Throttling System

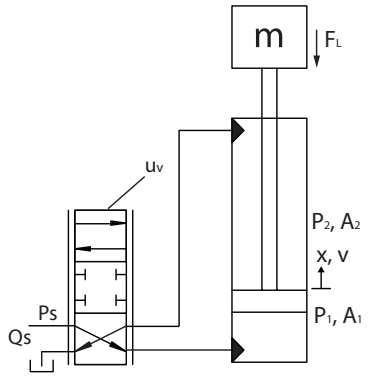

Figure 9.8: Throttling valve system considered for the efficiency analysis for a single DoF

The system in Section 9.1.1 was compared to a simulated system with throttle valves attached to the cylinder, visualized in Fig. 9.8. The same trajectory controller presented in Chapter 6 was utilized to determine the flow commands to be provided by the throttling valves. The throttling valves analyzed in this chapter are 4-way servo valves connected to a constant pressure supply P_s and the return line at pressure P_T which is negligibly small. The amount of valve opening determines flow passing through the valve to its connected port and pressure drop across it. The dynamics of the valves are not modeled in this case study, but it is assumed that valves have sufficient bandwidth to track the given trajectory as it is common to have valves with more than 200 Hz of bandwidth. The valve leakages are not considered. The only losses considered are the inevitable reduction in pressure that occurs as the fluid passes through the valve. Even with the full valve opening, there exists some pressure drop across the valve. In other words, providing P_s directly to the cylinder is impossible. To provide a demanded pressure P_d to the system, a supply pressure P_s always needs to be higher than the demanded pressure P_d (i.e. $P_s > P_d$) to compensate for the pressure drop across the throttle valve. This limitation, combined with its inability to boost the pressure is the major factors differentiating throttle valve systems from transformer systems.

In a throttling system, any motion of the actuator driven by a throttling valve is achieved by the supply flow Q_s coming from the common pressure rail held at constant pressure P_s. The fluid power supplied to the system is obtained by:

$$\mathscr{P}_{f,i} = (P_s - P_T)Q_s \tag{9.1}$$

The supply flow rate Q_s is determined by the trajectory tracking controller in Section 6.3.

$$Q_s(t) = |Q_B^d| \tag{9.2}$$

An absolute value is used because unlike in transformer system, the throttling system consumed fluid even when the load is being lowered. None of the power from the potential energy can be recovered, and the system will always consume power.

Two cases for throttling architecture will be presented as visualized in Fig. 9.9, which shows the demanded pressure P_d that corresponds to the 990 kg loading case, denoted as $P_{d,990}$. The first case assumes that the throttle system is connected to a Load Sensing (LS) pump that adjusts the supply pressure P_s level to the pressure demand P_d of the cylinder. It can be seen that P_s for this case is dynamically adjusting to the demanded pressure, leaving some margin in the pressure for the inevitable pressure drop across the throttle valve. Leaving a 20% margin, the supply pressure is set to be $P_s(t) = 1.2P_{d,990}(t)$, which has a peak pressure of 10.3 MPa ($\approx$ 1500 psi) and the lowest pressure of 9.6 MPa ($\approx$ 1390 psi). The small variation in the pressure is due to the modest trajectory being considered. A faster trajectory will result in more variation in the demanded pressure.

The second case will consider a circuit without such system installed. Without the LS, supply pressure P_s has to be set to meet the heaviest demand possible. Also leaving a 20% margin for the error, this is set to be a constant supply pressure that is $P_s = 1.2 \max(P_{d,990}) = 10.3$ MPa ($\approx$ 1500 psi).

As with the transformer cases, the 3-DoF system will be considered, each with a different mass load attached to it as shown in Fig. 9.10. With multiple actuators with different loading conditions, each DoF has a different pressure demand over a cycle. For the 660 kg and 330 kg mass loading case, the pressure demands are denoted as $P_{d,660}$ and $P_{d,330}$, respectively. Since all the loads are connected to a common supply pressure, the pressure even with the LS system, is set to match the pressure demand according to the heaviest pressure demand, $P_{d,990}$. The remaining cylinders will still have a quite large throttling loss even with the LS system. The supply pressure for the multiple actuator case is plotted in Fig. 9.11. It can be seen that P_s with the LS and without LS are the same as with just having a single load with 990 kg. A constant pressure P_A provided to the transformer is plotted to highlight the difference in supply pressure requirement. The supply pressure P_s in the throttling system is always higher than the demanded pressure

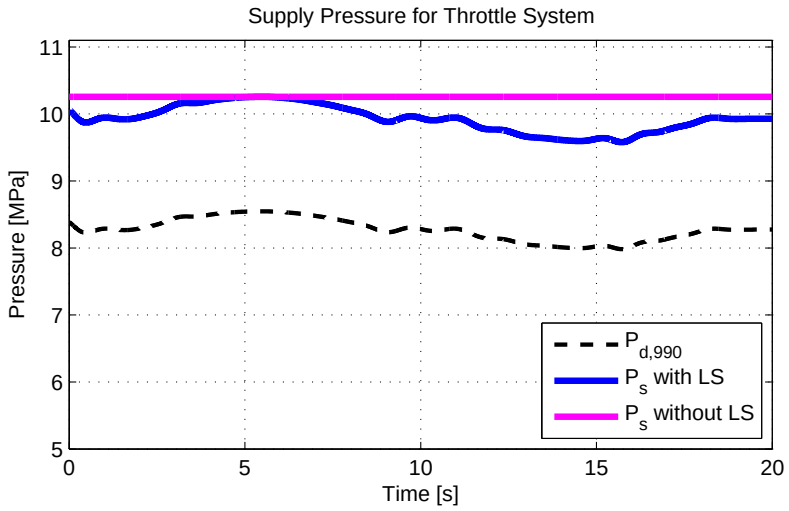

Figure 9.9: Required supply pressure for the desired pressure P_d over one cycle for a LS system and non-LS system.

P_d from all of its actuators as throttling valves can only reduce pressure whereas the transformer pressure P_A can be set to be lower than P_d of one or more of its actuators to utilize the pressure boosting ability of the hydraulic transformers.

9.1.3 Efficiency of the System

In both transformer system and throttling system, the useful mechanical energy is defined to be the integral sum of positive mechanical power output, where a positive is defined to be power flowing out of the system, and a negative represents the system absorbing power from an overrunning load. The efficiency is defined to be the ratio between this useful mechanical energy output to the net consumption of the energy as described in Eq. (8.22). For the convenience in reading these are reproduced here.

The mechanical power output associated with the actuator is:

$$\mathscr{P}_{a,o} = C_{a,o}(\mathscr{P}_a)$$

where $C_{a,o}$ is the indicator function that only takes the positive power from the cylinder

$$C_{a,o}(\mathscr{P}_a) = \begin{cases} \mathscr{P}_a & \text{if } \mathscr{P}_a > 0 \\ 0 & \text{else} \end{cases}$$

and the $\mathscr{P}_a$ is the power from the linear actuator given by its force $F_a(t)$ and velocity

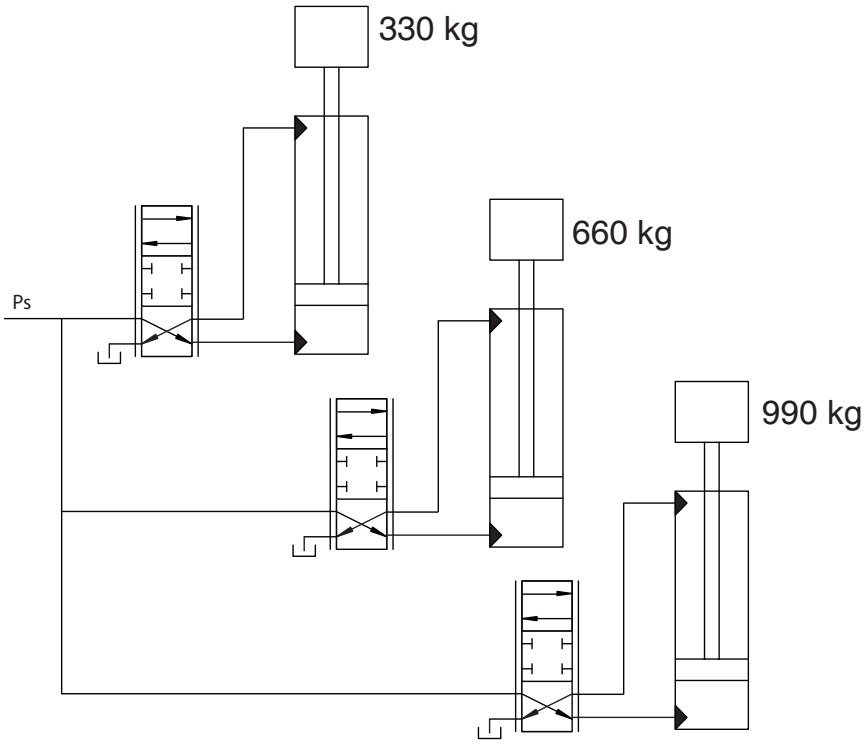

Figure 9.10: Throttling valve system considered for the efficiency analysis showing all 3-DoFs

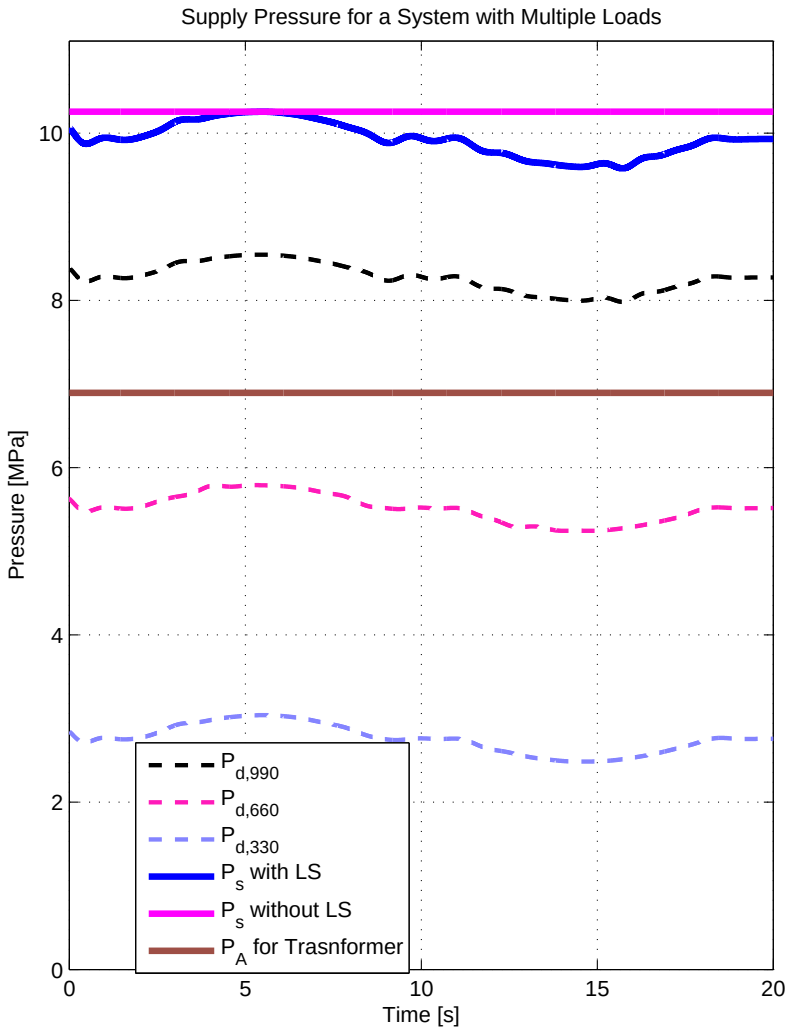

Figure 9.11: Required supply pressure for the desired pressure $P_{d,990}$, $P_{d,660}$ and $P_{d,330}$ over one cycle for a LS system. LS system can only bring down pressure to match the heaviest demand $P_{d,990}$

$v_a(t)$

$$\mathscr{P}_a = F_a(t)v_a(t)$$

Integrating the input power and output power yields the input energy to the system and the output energy from the system.

$$\begin{aligned} \mathscr{E}_i &= \int_{t_1}^{t_2} \mathscr{P}_{f,i}(t)dt \\ \mathscr{E}_o &= \int_{t_1}^{t_2} \mathscr{P}_{a,o}(t)dt \end{aligned} \tag{9.3}$$

Then, the total system efficiency η for a given trajectory can be determined as the fraction of the total output energy with respect to the total input energy:

$$\eta = \frac{\mathscr{E}_o}{\mathscr{E}_i} \tag{9.4}$$

The input power is defined in Eq. (8.17) for the transformer system and Eq. (9.1) for the throttling system.

9.2 Comparison Result

In this section, the transformer system described in Section 9.1.1 and throttling system described in Section 9.1.2 are compared in terms of the efficiency and net energy consumption. Two situations will be considered: one is where all 3 actuators simultaneously driven, and the other is where a single actuator system is considered.

9.2.1 Considering Each Actuator Simultaneously

Table 9.1 presents the cycle efficiency (Sec. 8.2.2) for the transformer system at each DoF with different loading conditions. In throttling systems, efficiency is the highest for the heaviest loading case. As shown in Fig. 9.11, the supply pressure throttling system with LS is set to meet the peak demand in pressure. Further the demanded pressure is away from the P_s, more throttling it will suffer and less efficiency is observed as a result for a lighter loading cases with lower pressure demand. The LS system shows a slight improvement over the system without LS, as the supply pressure is dynamically adjusted to reduce the throttling. However, as discussed, the pressure can only be reduced down to match the largest pressure demand, and the remaining actuators still suffer from large throttling losses even with the LS.

Table 9.1: The cycle efficiency of each actuator with a different loading condition in a 3-DoF transformer and throttling systems

Loading Condition	Transformer	Throttle with LS	Throttle without LS
330 kg	43.4%	13.6%	13.2%
660 kg	84.9%	26.1%	25.5%
990 kg	111%	38.6%	37.7%
Overall	81.2%	26.2%	25.6%

Table 9.2: Net energy consumption for each of the 3-DoFs driven by transformer or throttling systems, along with the mechanical energy output from each of the actuator.

Loading Condition	Useful Energy Output	Transformer Energy Consumption	Throttle with LS	Throttle without LS
330 kg	1039 J	2396 J	7667 J	7847 J
660 kg	2001 J	2358 J	7665 J	7849 J
990 kg	3020 J	2710 J	7821 J	8003 J
Total	6060 J	7464 J	23153 J	23700 J

Transformer system shows a significant improvement over the throttling system with LS. In a 330 kg load, 43.4% efficiency is a 220% improvement over 13.6% observed with a throttling system. For a 660 kg load, 225% improvement is observed, and for a 990 kg load, 189% improvement is observed. Considering all loading cases together, the transformer shows 210% increase in efficiency compared to the throttling system, showing 81.2% overall efficiency as opposed to 26.2% observed with the throttle system with LS, or 25.6% with the throttle system without LS.

Table 9.2, which presents the mechanical energy produced by the cylinders and the net energy consumption at each DoF for the systems being compared. The energy outputs and consumptions presented on this table were used to obtain the efficiencies presented in Table 9.1. With the trajectory presented in Fig. 9.2, the output energy scales almost directly with the attached mass. The consumed energy for the throttling valves are similar across different DoFs. Since the trajectory being delivered is the same across all actuators, the supplied flow Q_s is almost the same across all actuators, with the differences arising from the controller dynamics in providing the desired flow and pressure. As a common pressure supply at P_s is being provided, this results in the similar net energy consumptions.

For each of the actuator, transformer shows 68.75%, 69.24%, and 65.35% reduction in

the net energy consumption over the throttle valves with LS for the actuators with 330 kg, 660 kg, and 990 kg loads, respectively. Considering all actuators together, transformer shows 67.8% reduction in the net energy consumption. This is why transformer showed a significant improvement over the throttle valve system in the efficiency in Table 9.1.

In Table 9.1, a DoF with 990 kg load shows an efficiency of 111%. Efficiency over 100% is obtained because as shown in Table 9.2, the net energy consumption (2710 J) is less than the mechanical energy produced (3020 J) at this actuator. This result is possible because of the transformer's ability to recover the regenerative energy. Table 9.3 shows how much energy is recovered at the transformer at port 'B' from the overrunning loads, also with the actual energy that is recovered at port 'A' of the transformer. The ratio between these two quantities represents how much energy has been successfully recovered from the overrunning loads. Since the transformer always requires some energy to spin its shaft, a portion of the energy from the overrunning loads is consumed by the transformer. If the instantaneous power from the overrunning load is not large enough, there even will be a situation where an additional power is needed to prevent the transformer from stalling, resulting in reduction in recovered energy amount. On the other hand, with the instantaneous power large enough, the power that is still available after spinning the transformer will be recovered back to the common pressure rail, resulting in more energy regenerated.

Table 9.3: Regenerative energy consideration: an energy provided by overrunning loads is fed to the transformer, shown with the amount of energy recovered back to the common pressure rail. The ratio between the two shows how much energy has been regenerated

Loading Condition	Energy from overrunning loads	Energy recovered to CPR	Regeneration Efficiency
330 kg	927.6 J	33.8 J	3.64%
660 kg	1932 J	1322 J	68.4%
990 kg	2995 J	1942 J	64.8%

In Figs. 9.4–9.6 an overrunning case corresponds to a region where $Q_B < 0$. On the other port, $Q_A > 0$ means flow is coming out of the transformer, which in turns means the energy is being recovered back to the supply pressure line. If both $Q_B < 0$ and $Q_A < 0$, then no power is recovered from the overrunning load.

As with the positive mechanical energy from the resistive loads shown in Table 9.2, the energy from the overrunning loads scales almost directly with the attached mass. The amount energy recovered back to the common pressure rail does not have such a clear

Table 9.4: The component efficiency of the transformer and throttle system with LS for each DoF

Loading Condition	Transformer	Throttle with LS
330 kg	32.9%	13.6%
660 kg	59.7%	26.1%
990 kg	65.3%	38.6%

relationship, although in general the heavier the mass is, more energy gets recovered at the CPR. The mean pressures over one cycle of trajectory for each loading case correspond to the pressure transformation ratio from P_B to P_A at 2.5, 1.25, and 0.83, respectively for 330 kg, 660 kg, and 990 kg loads.

At such a high transformation ratio required for 330 kg, the prototype transformer shows a poor component efficiency (Defined in Section 8.2.1) and was only able to recover 3.64% of the energy from the overrunning load. The other two loading conditions results in the transformer operating much more efficiently, thus recovering more than 64% of energy from the overrunning loads. Efficient control algorithms developed in Chapter 8 ensures the maximal amount of energy is recovered when lowering the load while the minimal amount of energy is consumed when raising the load. In Figures 9.4–9.6, notice that the system undergoes a series of configuration switch as well as varying shaft speeds.

The component efficiency of the transformer and throttling valve are summarized in Table 9.4. For the throttling system, since the CPR is always providing the power into the valve, the component efficiency is the same as the cycle efficiency of the throttling system defined in Section 9.1.3. The component efficiency for hydraulic transformer was defined in Section 8.2.1. Since the transformer is able to recover energy to reduce the net consumed energy, the cycle efficiency is higher than component efficiency.

Overall, the transformer system is able to reduce the energy consumption by 67.8% to realize 210% improvement in efficiency when compared against throttling system with LS.

9.2.2 Considering Each Actuator Separately

To present a case where LS system shows its advantage, another situation is considered in this subsection where the system is assumed to be a single DoF. In other words, each of the loading cases will be run separately. In this case, the P_s for the LS system will adjust to the single actuator being considered to reduce the P_s to better match the pressure

Table 9.5: The cycle efficiency of a single DoF system driven by transformer and throttling valve for different loading conditions

Loading Condition	Transformer	Throttle with LS
330 kg	43.4%	40.6%
660 kg	84.9%	39.1%
990 kg	111%	38.6%

Table 9.6: The net energy consumption in a single DoF system driven by transformer and throttling valve for different loading conditions, along with the mechanical energy output from the actuator for each of the loading conditions

Loading Condition	Useful Energy Output	Transformer Energy Consumption	Throttle with LS
330 kg	1039 J	2396 J	2557 J
660 kg	2001 J	2358 J	5113 J
990 kg	3020 J	2710 J	7821 J

demand P_d from the actuator. This is set still set to be 20% above the $P_d(t)$ such that $P_s = 1.2P_d(t)$, as illustrated in Fig. 9.12.

Table 9.5 presents the cycle efficiency for a single DoF system with three different loading conditions. Compared to Table 9.1, the efficiency for the LS system is now higher as P_s can be reduced further when there is only one actuator to be controlled. For 330 kg load and 660 kg load, the LS system shows 207% and 53% improvement in efficiency respectively over the throttle system without the LS.

Table 9.6 shows the net energy consumption for the cases considered. Now with the P_s that better matches the P_d, LS system shows a sizable reduction over non-LS system in net energy consumption. 67% and 34.9% reduction in consumed energy is observed for 330 kg load and 660 kg load with LS system over the non-LS system.

In all cases presented, transformer still shows an advantage over the throttling system in efficiency with an exception of a 330 kg load case. It was already demonstrated in Section 9.2.1 that when different loads are considered together in a multi-DoF system, the efficiency improvement in utilizing transformers is significant.

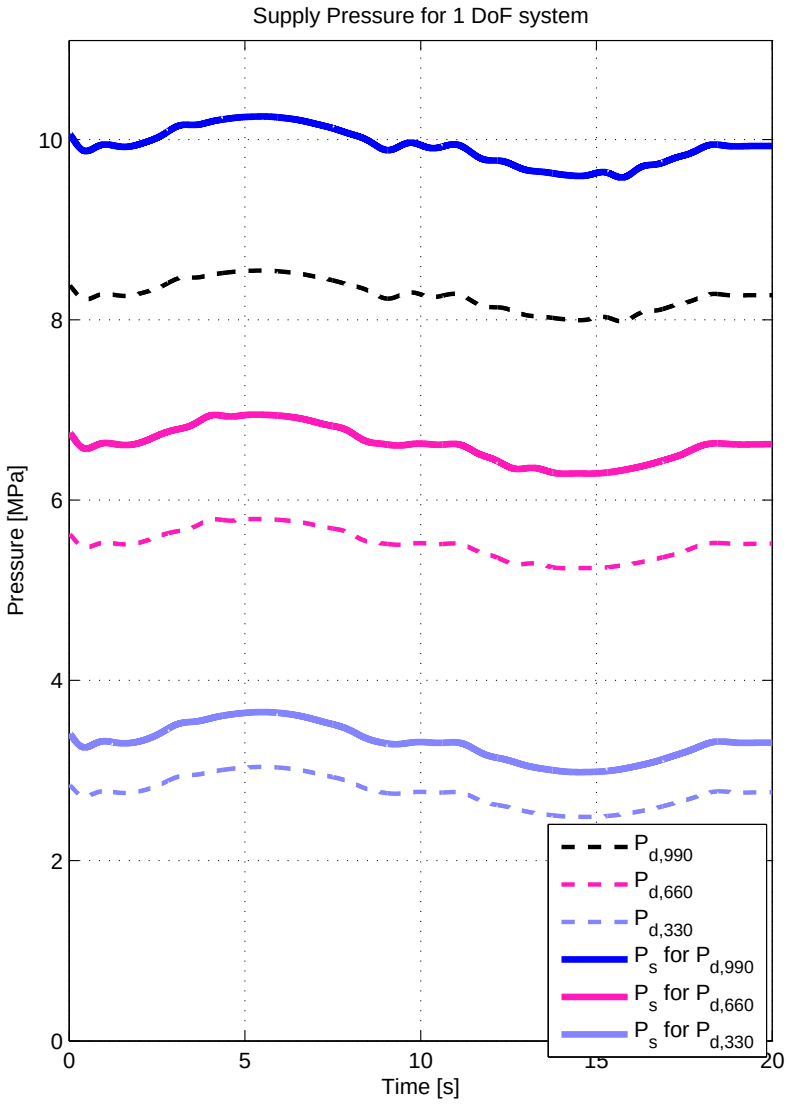

Figure 9.12: Required supply pressure for the desired pressure $P_{d,990}$, $P_{d,660}$ and $P_{d,330}$ over one cycle for a LS system, if each load is considered separately

9.3 Chapter Summary

Transformer efficiency was tested for 3 different loading cases and compared against the throttling valve system. Controllers developed in Chapters 6–8 were used to drive the cylinder in predefined trajectory. It was shown that for these conditions considered, transformer system outperformed the throttling valve system in all three loading conditions. In terms of the total combined efficiency with all three loading conditions delivered concurrently, the transformer system achieved 81.2% efficiency while throttling system only achieved 25.8%. This is more than threefold increase in efficiency. In terms of energy consumption, transformer consumes a total of 7464 J, which is 67.8% reduction from the energy consumption by a load sensing throttling valve system.

In conclusion, the hydraulic transformer system is shown to deliver the good control performance and good efficiency at the same time. High efficiency obtained is remarkable as the prototype transformer being used is relatively inefficient due to large mechanical losses. Utilizing more efficient prototype will show even higher efficiency for the transformer systems.

Chapter 10

Conclusion

10.1 Summary of Research Contents and Contributions

With its unmatched power density over other methods of power transmission, hydraulic systems will continue to have their position in high load, high force applications. However, the low efficiency stemming from the wide usage of throttling valves prevent them to be adapted in more variety of applications. The objective of this work was to design a hydraulic transformer that is compact and efficient to eliminate throttling losses, a largest contributor to the hydraulic system inefficiencies, and experimentally demonstrate its energy savings. A survey on the previous works on hydraulic transformers revealed that the research focus were mainly on the component design aspect. The energy savings of hydraulic transformers in their potential applications were demonstrated only in simulations, utilizing a possible design of transformer rather than with an actual prototype. Experimental validation of the hydraulic transformer controllers were also lacking. It still remained a question whether hydraulic transformers can deliver satisfactory control performance. This work expanded the transformer research beyond just a component design aspect to incorporate controller developments and experimental demonstrations to show that transformers can deliver accuracy and efficiency at the same time. The work in this dissertations are categorized into three aspects: understanding the hydraulic transformers; developing a controller that delivers accurate tracking performance; and developing a controller that maximizes the energy savings of utilizing hydraulic transformers.

In order to understand the hydraulic transformers, both simplified and detailed models are developed in Chapter 2. The existing literature on modeling axial piston pump and motors is adapted to present the model specific for analyzing hydraulic transformers. This allows the analysis beyond what is possible with simply scaling the manufacturer

provided data for the two most prevalent designs of hydraulic transformers. One design is a pump and motor mechanically coupled together, called PM transformer throughout this dissertation. Three different configuration methods are possible for this design. Thus all three are included in the analysis. The other design considered is called an INNAS Hydraulic Transformer (IHT), which combines the role of pump and motor into one unit by introducing a rotatable valve plate.

Using the models built, an quantitative comparison is established in Chapter 3 and Chapter 4. The comparison is made on three aspects: displacement sizing, flow ripple, and efficiency. Displacement sizing study examines the exact difference in required displacement if two transformer designs were to produce the comparable output power for all transformation ratios both in the absence of losses and with the presence of viscous friction losses. It is found that PM transformer does not necessarily have to be twice as big as IHT. In a case where the configurations could be switched, PM transformer could even be smaller than IHT. In the flow ripple study, both kinematic flow ripple (assuming an ideal, incompressible flow) and dynamic flow ripple (incorporating fluid compressibility) are considered. It is found that the very nature of rotatable valve plate in IHT causes flow ripple that is both qualitatively and quantitatively worse than flow ripple of PM transformer. Methods to improve the flow ripple for the IHT can also benefit PM transformers, which already has better flow ripple. In terms of efficiency, it is found that PM and IHT do not differ much in peak efficiency. Again, the possibility of being able to switch is suggested as a potential method to widen the region with high efficiency for the PM transformer.

The prototype hydraulic transformer is developed based on the comparison study conducted in the earlier chapter. Actuation mechanism and control approach for the swashplate actuation is presented in Chapter 5. The method to realize the configuration switch is presented, along with the testbed which allows the prototype transformer to be connected to a variety of hydraulic loads. Experimental efficiency data for the prototype is obtained and found to be matching well with the simulated efficiency data. The contributions in this area are summarized as follows:

- Detailed modeling work that combines both volumetric and mechanical loss model of an axial piston pump and motor to model both PM transformer and IHT.
- Quantitative comparison between IHT and PM Transformer, for an overall range of operating conditions rather than discrete points of operation. This identified the strengths and weaknesses of each transformer design in a fair manner.

- Demonstrated benefit of utilizing different configurations for PM transformer differing by port connections to aid with compactness and efficiency
- Developed the prototype switched mode transformer capable of realizing different configurations within the same transformer

The controllers were then developed for the prototype switched mode hydraulic transformer to demonstrate feasibility of utilizing transformers in dynamic systems to deliver accurate performances. As the first step, a trajectory tracking controller was designed in Chapter 6. A cylinder is commanded to follow a prescribed trajectory using a prototype transformer as the power source. In this controller, the flow command is designed using the natural energy storage function instead of a quadratic function in the definition of the Lyapunov function to achieve better tracking and robustness. In addition, a hydraulic transformer is controlled to provide the designed flow while also regulating its operating shaft speed. This extra degree of freedom in control was designed such that the transformer operation can be optimized to improve the efficiency. To demonstrate an application on the robotic system, a controller for a fully coupled multi-DoF hydraulic human power amplifier (HPA) was developed in Chapter 7. HPA is a tool that allows the human to operate the machine as a passive mechanical tool. A passivity-based control approach that uses natural energy storage of the hydraulic actuator is used to define the flow requirement. Additional passive dynamics that helps the user to perform specific tasks are implemented as well. The main contributions in the accurate control aspect are as follows:

- Developed a trajectory tracking controller that can be applied to all three configuration modes of the prototype hydraulic transformer. This controller was experimentally validated to demonstrate that utilizing hydraulic transformers does not require sacrifice in accurate control performance.
- Developed a controller for a fully-coupled multi-DoF human power amplifier and experimentally demonstrated even a complex control approach can be delivered by the hydraulic transformer without sacrificing the control performance over the throttling valves.

The last aspect of the research is the efficiency. Chapter 8 presented a Hardware-In-the-Loop testbed that overcomes the challenges in acquiring appropriate experimental equipment to operate a hydraulic transformer at desired pressure conditions. In addition, a supervisory control to operate a hydraulic transformer in its most optimal shaft speed and configuration mode is also developed. Special considerations necessary to allow smooth

mode switching is presented. A cost is assigned to the mode switch to prevent a rapid switching back-and-forth among the modes that is beyond the bandwidth of the hardware components. An offset in timing between the controller switch and transformer mode switch is introduced to achieve a bumpless transfer between each mode. Utilizing this supervisory controller and a trajectory tracking controller developed in Chapter 6, the efficiency of the hydraulic system driven by hydraulic transformer is compared to the system driven by throttling valves in Chapter 9. With a trajectory under different loading conditions, the transformer system showed 81.2% efficiency whereas the throttling valve system showed only 25.8% efficiency even with a load sensing system. This result is despite the relatively low unit efficiency delivered by the prototype transformer. The contributions in the efficient control aspect are summarized as:

- Developed algorithms to maximize the benefit of using a transformer. Through supervisory controls to optimize the operating shaft speed and configuration mode, the energy savings of utilizing transformer were further increased.
- Demonstrated with an actual prototype the possible energy savings possible with a transformer. More than threefold increase in efficiency is shown for the operating conditions analyzed.

This research visited various aspect in realizing hydraulic transformer systems, ranging from component analysis and design to actual prototype and control algorithm development. It has examined the existing designs of hydraulic transformer to come up with a novel idea of switching configurations modes. With the prototype switched mode transformer developed, controllers that deliver accuracy and efficiency simultaneously were developed. With more than threefold increase in efficiency demonstrated over the throttling valves, the hydraulic transformer is indeed an attractive approach to improve the efficiencies in the hydraulic systems.

10.2 Recommendations for Future Work

Despite the effort to visit as many aspects of hydraulic transformer research and explore a variety of configuration methods and control strategies, this dissertation leaves some room for further improvement. Should someone be exploring further into the hydraulic transformer research in the future, following recommendations may be helpful.

Throughout the analysis, the common pressure rail is taken to be constant for the transformer system. Load sensing system that dynamically adjusts the supply pressure

to the circuit was only considered for throttling system in comparison. There could be significant potential energy savings with load sensing common pressure rail that adjusts the common pressure rail depending on the loading conditions of the connected actuators.

The hydraulic circuit connections considered in this dissertation only considered a case where an actuator is connected to the transformer on one end and to the reservoir on the other end. This connection has its limitation that it cannot exert a force downward without utilizing a directional valve. It is possible to connect the other end to the common pressure rail. Gagnon [29] considered such connection through a series of simulations. It will be beneficial to explore the control algorithms to utilize this circuit connection method in most efficient manner.

The prototype transformer could be improved in several ways. Firstly, the current prototype suffers heavily from the low mechanical efficiency. The efficiency of the system driven by hydraulic transformer can be even higher than what was observed in Chapter 9 if a more efficient unit is to be utilized. Secondly, the unit could be designed such that swashplates are located towards the outside of the unit rather than the center of the unit. Doing so, the ports will be concentrated towards the center of the unit such that it could allow the solenoid valves necessary for the configuration mode switch to be installed within the transformer. It could considerably reduce the physical footprint of the transformer.

Most importantly, the swashplate actuation should be designed such that it utilizes more conventional hydraulic actuation rather than stepper motors. Utilizing the stepper motors for the swashplate actuation proved to be the most limiting factor in providing the bandwidth of the control. A higher bandwidth with swashplate actuation will open up a plethora of opportunities for the hydraulic transformer applications.

In terms of the project management, a team of researchers focusing on each aspect of the hydraulic transformer could be beneficial to maximize the productivity of the research. One can be working on further improving the hardware design, while the other works solely on controller algorithms. With these additional efforts and suggested improvements, a hydraulic transformer will be one step closer to become readily available in hydraulics industry.

References

[1] P. A. Achten, T. Brink, J. Potma, M. Schellekens, and G. Vael, "A four-quadrant hydraulic transformer for hybrid vehicles," in *The 11th Scandinavian International Conference on Fluid Power, Sweden*, 2009.

[2] P. A. Achten, Z. Fu, and G. Vael, "Transforming future hydraulics: a new design of a hydraulic transformer," in *The Fifth Scandinavian International Conference on Fluid Power SICFP 97*, 1997, p. 287ev.

[3] P. A. Achten and Z. Fu, "Valving land phenomena of the innas hydraulic transformer," *International journal of fluid power*, vol. 1, no. 1, pp. 1–15, 2000.

[4] P. A. Achten and B. Innas, "Changing the paradigm," in *Proc. of the 10th Scandinavian International Conference on Fluid Power (SICFP 07)*, 2007.

[5] P. A. Achten, M. Schellekens, H. Murrenhoff, and M. Deeken, "Efficiency and low speed behavior of the floating cup pump," *SAE transactions*, vol. 113, no. 2, pp. 366–376, 2004.

[6] P. A. Achten, G. Vael, and K. Heybroek, "Efficient hydraulic pumps, motors and transformers for hydraulic hybrid systems in mobile machinery," *1st International VDI Conference "Transmissions in Vehicles"*, 2011.

[7] P. A. Achten, G. Vael, J. vd Oever, and Z. Fu, "'shuttle' technology for noise reduction and efficiency improvement of hydrostatic machines," in *The Seventh Scandinavia International Conference on Fluid Power SICFP '01*, vol. **3**, May 2001, pp. 1–4.

[8] P. A. Achten, T. van den Brink, M. Schellekens, and B. Innas, "Design of a variable displacement floating cup pump," in *Proc. 9th Scandinavian Int. Conf. on Fluid Power, SICFP*, vol. 5, 2005.

[9] P. A. Achten, T. van den Brink, J. van den Oever, J. Potma, M. Schellekens, G. Vael, M. van Walwijk, and B. Innas, "Dedicated design of the hydraulic transformer," vol. 3, 2002, pp. 233–248.

[10] P. A. Achten and T. Van den Brink, "A hydraulic transformer with a swash block control around three axis of rotation," in *8th International Fluid Power Conference*, 2012, pp. 26–28.

[11] P. A. Achten, T. Van den Brink, T. Paardenkooper, T. Platzer, H. Potma, M. Schellekens, and G. Vael, "Design and testing of an axial piston pump based on the floating cup principle," in *The Eighth Scandinavian International Conference on Fluid Power SICFP '03*, May 2003, pp. 805–820.

[12] J. Bergada, S. Kumar, D. L. Davies, and J. Watton, "A complete analysis of axial piston pump leakage and output flow ripples," *Applied Mathematical Modelling*, vol. 36, no. 4, pp. 1731–1751, 2012.

[13] J. Bergada, J. Watton, and S. Kumar, "Pressure, flow, force, and torque between the barrel and port plate in an axial piston pump," *Journal of Dynamic Systems, Measurement, and Control*, vol. 130, no. 011011, 2008.

[14] E. D. Bishop, "Digital hydraulic transformer–efficiency of natural design," in *7th International Fluid Power Conference*, 2010.

[15] ——, "Digital hydraulic system," Oct. 15 2012, uS Patent App. 13/652,054.

[16] ——, "Digital hydraulic transformer-approaching theoretical perfection in hydraulic drive efficiency," in *The 11th Scandinavian International Conference on Fluid Power*, 2009, pp. 2–4.

[17] R. Bogue, "Exoskeletons and robotic prosthetics: a review of recent developments," *Industrial Robot: An International Journal*, vol. 36, no. 5, pp. 421–427, 2009.

[18] H. Cao, J. Zhu, C. Xia, H. Zhou, X. Chen, and Y. Wang, "Design and control of a hydraulic-actuated leg exoskeleton for load-carrying augmentation," in *Proceedings of 2010 International Conference on Intelligent Robotics and Application*, 2010, pp. 590–599.

[19] S. Chen, Z. Chen, B. Yao, X. Zhu, S. Zhu, Q. Wang, and Y. Song, "Adaptive robust cascade force control of 1-dof hydraulic exoskeleton for human performance augmentation," *IEEE/ASME Transactions on Mechatronics*, vol. 22, no. 2, pp. 589–600, April 2017.

[20] B.-H. Cho, H.-W. Lee, and J.-S. Oh, "Estimation technique of air content in automatic transmission fluid by measuring effective bulk modulus," *International journal of automotive technology*, vol. 3, no. 2, pp. 57–61, 2002.

[21] J. Clarke, "Hydraulic transformer using a pair of variable displacement gear pumps," Feb. 5 2001, uS Patent App. 09/776,842.

[22] E. Colgate, "Coupled stability of multiport systems - theory and experiments," *ASME Journal of Dynamic Systems, Measurements and Control*, vol. 116, no. 3, pp. 419–428, 1994.

[23] J. Dantlgraber and M. Robohm, "Hydraulic transformer with two axial piston machines with single commen swash plate," Oct. 31 2001, eP Patent 0,851,121. [Online]. Available: https://www.google.com/patents/EP0851121B1?cl=en

[24] A. M. Dollar and H. Herr, "Lower extremity exoskeletons and active orthoses: Challenges and state-of-the-art," *IEEE Transactions on Robotics*, vol. 24, no. 1, pp. 144–158, Feb 2008.

[25] Z. Du, T. Cheng, P. Y. Li, K. L. Cheong, and T. R. Chase, "Virtual vehicle control concept for hydrostatic dynamometer control," *Journal of Dynamic Systems, Measurement, and Control*, vol. 139, no. 2, p. 021009, 2017.

[26] S. Duan and T. Nielsen, "Modeling and analysis of directional control valves with tapered-angle and eccentric clearance," *2007 ASME International Mechanical Engineering Congress and Exposition*, November 2007.

[27] F. Eskilsson, "Passive control for a human power amplifier providing force amplification, guidance and obstacle avoidance," "M.S. Thesis", Department of Electrical Engineeering, Linköpings University, 2011, (Research performed as part of an international exchange at the University of Minnesota.).

[28] Y. Fang and M. Shirakashi, "Mixed lubrication characteristics between the piston and cylinder in hydraulic piston pump-motor," *Journal of tribology*, vol. 117, no. 1, pp. 80–85, 1995.

[29] P. Gagnon, "Configuration and performance of hydraulic transformer power distribution systems," "M.S. Thesis", Department of Mechanical Engineering, University of Minnesota, 2016.

[30] C. Guan, Z. Jiao, and S. He, "Theoretical study of flow ripple for an aviation axial-piston pump with damping holes in the valve plate," *Chinese Journal of Aeronautics*, 2013.

[31] T. H. Ho and K. K. Ahn, "A study on the position control of hydraulic cylinder driven by hydraulic transformer using disturbance observer," in *IEEE International Conference on Control, Automation and Systems 2008*, 2008, pp. 2634–2639.

[32] ——, "Saving energy control of cylinder drive using hydraulic transformer combined with an assisted hydraulic circuit," in *IEEE International Conference on Control, Automation and Systems 2009*, 2009, pp. 2115–2120.

[33] N. Hogan, "Controlling impedance at the man/machine interface," in *Proceedings of the IEEE International Conference on Robotics and Automation*, vol. 3. IEEE, May 1989, pp. 1626–1631.

[34] H. C. Humphreys, W. J. Book, and J. D. Huggins, "Hydraulically actuated patient transfer device with passivity based control," in *Proceedings of the ASME/BATH 2013 Symposium on Fluid Power & Motion Control, Sarasota, Florida, USA*, 2013.

[35] S. Ikeo, W. Ma, and K. Ito, "Robust Position Control of Cylinder Using Hydraulic Transformer," *6th JFPS International Symposium on Fluid Power*, vol. 36, pp. 45–50, 2005.

[36] R. Inoguchi, K. Ito, and S. Ikeo, "Pure-hydraulic hybrid cylinder drive system with hydraulic transformer," *JFPS International Journal of Fluid Power System*, vol. 5, no. 1, pp. 1–5, 2012.

[37] J. Ivantysyn and M. Ivantysynova, *Hydrostatic Pumps and Motors: Principles, Design, Performance, Modelling, Analysis, Control and Testing*, ser. Tbi edition. Tech Books International, 2003. [Online]. Available: http://books.google.com/books?id=rgfnXwAACAAJ

[38] ——, *Hydrostatic pumps and motors*, 2001.

[39] J. Jiang, C. Liu, and B. Yu, "Modeling and simulation for pressure character of the plate-inclined axial piston type hydraulic transformer," in *Information and Automation (ICIA), 2010 IEEE International Conference on*. IEEE, 2010, pp. 245–249.

[40] M. Jien, X. Bing, O. Xiaoping, and Y. Huayong, "The CFD simulation research on hydraulic transformer," *Proceedings of the 6th JFPS International*, vol. 2, p. 2, 2005.

[41] H. Kawamoto, S. Taal, H. Niniss, T. Hayashi, K. Kamibayashi, K. Eguchi, and Y. Sankai, "Voluntary motion support control of robot suit hal triggered by bioelectrical signal for hemiplegia," in *2010 Annual International Conference of the IEEE Engineering in Medicine and Biology*, Aug 2010, pp. 462–466.

[42] H. Kawamoto and Y. Sankai, "Power assist system hal-3 for gait disorder person," in *Proc. of the 2002 International Conference on Computers Helping People with Special Needs (ICCHP 2002)*, 2002, pp. 196–203.

[43] T. Kazama and A. Yamaguchi, "Application of a mixed lubrication model for hydrostatic thrust bearings of hydraulic equipment," *Journal of tribology*, vol. 115, no. 4, pp. 686–691, 1993.

[44] H. Kazerooni, A. Chu, and R. Steger, "That which does not stabilize, will only make us stronger," *International Journal of Robotics Research*, vol. 26, no. 1, pp. 75–89, 2007.

[45] O. Khatib, "Real-time obstacle avoidance for manipulators and mobile robots," *The international journal of robotics research*, vol. 5, no. 1, pp. 90–98, 1986.

[46] Y. Kita, "Rotational hydraulic transformer," Aug. 29 2000, uS Patent 6,109,884.

[47] K. Kong and M. Tomizuka, "Control of exoskeletons inspired by fictitious gain in human model," *IEEE/ASME Transactions on Mechatronics*, vol. 14, no. 6, pp. 689–698, Dec 2009.

[48] H. H. Kouns, "Hydraulic transformer," Dec. 14 1971, uS Patent 3,627,451.

[49] D. J. Lee and P. Y. Li, "Passive bilateral control and tool dynamics rendering for nonlinear mechanical teleoperators," *Robotics, IEEE Transactions on*, vol. 21, no. 5, pp. 936–951, 2005.

[50] ——, "Passive decomposition approach to formation and maneuver control of multiple rigid-bodies," *ASME Journal of Dynamic Systems, Measurement and Control*, vol. 129, pp. 662–677, September 2007.

[51] ——, "Passive decomposition of multiple mechanical systems under coordination requirements," *IEEE Transactions on Automatic Control*, vol. 58, pp. 230–235, January 2013.

[52] S. Lee, F. Eskilsson, and P. Y. Li, "Multi degree-of-freedom hydraulic human power amplifier with rendering of assistive dynamics," in *ASME 2016 Dynamic Systems and Control Conference*. American Society of Mechanical Engineers, 2016, p. V001T07A002.

[53] S. Lee and P. Y. Li, "Trajectory tracking control using a hydraulic transformer," *2014 International Symposium on Flexible Automation, Awaji Island, Japan*, 2014.

[54] ——, "Passive control of a hydraulic human power amplifier using a hydraulic transformer," in *ASME 2015 Dynamic Systems and Control Conference*. American Society of Mechanical Engineers, 2015, pp. V002T27A004–V002T27A004.

[55] ——, "Passivity based backstepping control for trajectory tracking using a hydraulic transformer," in *ASME/BATH 2015 Symposium on Fluid Power and Motion Control*. American Society of Mechanical Engineers, 2015, pp. V001T01A064–V001T01A064.

[56] P. Y. Li and M. Wang, "Natural storage function for passivity-based trajectory control of hydraulic actuators," *IEEE/ASME Transactions on Mechatronics*, vol. 19, no. 3, pp. 1057–1068, July 2014.

[57] P. Y. Li, "Design and control of a hydraulic human power amplifier," in *ASME 2004 International Mechanical Engineering Congress and Exposition*. American Society of Mechanical Engineers, 2004, pp. 385–393.

[58] ——, "A new passive controller for a hydraulic human power amplifier," in *ASME 2006 International Mechanical Engineering Congress and Exposition*. American Society of Mechanical Engineers, 2006, pp. 1375–1384.

[59] P. Y. Li and V. Durbha, "Passive control of fluid powered human power amplifiers," in *Proceedings of the 7th JFPS International Symposium on Fluid Power, Toyama, Japan*, 2008.

[60] P. Y. Li and R. Horowitz, "Passive velocity field control of mechanical manipulators," *Robotics and Automation, IEEE Transactions on*, vol. 15, no. 4, pp. 751–763, 1999.

[61] X. Li, S. Yuan, J. Hu, and J. Lv, "Mathematical model for efficiency of the hydraulic transformer," in *Power and Energy Engineering Conference, 2009. APPEEC 2009. Asia-Pacific.* IEEE, 2009, pp. 1–5.

[62] Z. Li, "Condition monitoring of axial piston pump," Ph.D. dissertation, University of Saskatchewan, 2005.

[63] L. J. Love, "Estimating the impact (energy, emissions and economics) of the U.S. fluid power industry," Oak Ridge National Laboratory (ORNL), Tech. Rep., 2012.

[64] H. Lu, "Theoretical Analysis and Experiment of Electric Control Bent Axial Piston Hydraulic Transformer," PhD Thesis, Harbin Institute of Technology, Harbin, China, 2008.

[65] G. Lv and R. Gregg, "Towards total energy shaping control of lower-limb exoskeletons," in *Proceedings of the 2017 American Control Conference*, 2017, pp. 4851–4857.

[66] ——, "Underactuated potential energy shaping with contact constraints: Application to a powered knee-ankle orthosis," *IEEE Transactions on Control Technology*, 2017.

[67] N. Manring and R. Johnson, "Modeling and designing a variable-displacement open-loop pump," *Journal of dynamic systems, measurement, and control*, vol. 118, no. 2, pp. 267–271, 1996.

[68] N. Manring, "Friction forces within the cylinder bores of swash-plate type axial-piston pumps and motors," *Journal of dynamic systems, measurement, and control*, vol. 121, no. 3, pp. 531–537, 1999.

[69] ——, "The discharge flow ripple of an axial-piston swash-plate type hydrostatic pump," *Journal of dynamic systems, measurement, and control*, vol. 122, no. 2, pp. 263–268, 2000.

[70] ——, *Fluid power pumps and motors: analysis, design and control.* McGraw Hill Professional, 2013.

[71] M. Martin and B. Taylor, "Optimised port plate timing for an axial piston pump," in *5th int fluid power symposium, Cranfield, England*, 1978, pp. 13–15.

[72] H. Merritt, *Hydraulic Control Systems.* New York, NY: John Wiley & Sons, Inc., 1966.

[73] U. Nagarajan, G. Aguirre-Ollinger, and A. Goswami, "Integral admittance shaping for exoskeleton control," in *2015 IEEE International Conference on Robotics and Automation (ICRA)*, May 2015, pp. 5641–5648.

[74] X. Ouyang, "Hydraulic Transformer Research," PhD Thesis, Zhejiang University, Hangzhou, China, 2005.

[75] X. Ouyang, H. Yang, B. Xu, and X. Xu, "Research on the hydraulic transformer with new distribution pairs," *Science in China Series E: Technological Sciences*, vol. 51, no. 4, pp. 435–442, 2008.

[76] A. Schenk, M. Zecchi, and M. Ivantysynova, "Accurate prediction of axial piston machine's performance through a thermo-elasto-hydrodynamic simulation model," in *Proceedings of the ASME/BATH 2013 Symposium on Fluid Power & Motion Control*, 2013, pp. 6–9.

[77] W. Shen, J. Jiang, X. Su, and H. R. Karimi, "Angle Displacement Robust Controller for the Port Plate of the Hydraulic Transformer," *Mathematical Problems in Engineering*, vol. 1, no. 1, pp. 1–9, 2013.

[78] ——, "Energy-saving analysis of hydraulic hybrid excavator based on common pressure rail," *The Scientific World Journal*, vol. 2013, 2013.

[79] ——, "A new type of hydraulic cylinder system controlled by the new-type hydraulic transformer," *Proceedings of the Institution of Mechanical Engineers, Part C: Journal of Mechanical Engineering Science*, vol. 228, no. 12, pp. 2233–2245, 2014.

[80] T. Ueno, K. Ito, and S. Ikeo, "A Robust Design of Velocity/Force Controller For Cylinder Using Hydraulic Transformer," *SICFP*, 2005.

[81] G. Vael and P. A. Achten, "The innas fork lift truck working under constant pressure," in *Internationales Fluidtechnisches Kolloquium*, vol. 1, 1998, pp. 301–316.

[82] G. Vael, P. A. Achten, and T. van den Brink, "Efficiency of a variable displacement open circuit floating cup pump," in *The 11th Scandinavian International Conference on Fluid Power (SICFP 07)*, 2009.

[83] G. Vael, E. Orlando, and R. Stukenbrock, "Toward maximum flexibility in working machinery, iht control in a mecalac excavator," in *Proceedings of The 4th International Fluid Power Conference Dresden, IFK 04*, 2004.

[84] G. Vael, P. A. Achten, and J. Potma, "Cylinder control with the floating cup hydraulic transformer," in *The Eighth Scandinavian International Conference on Fluid Power SICFP '03 Tampere, Finland*, May 2003, pp. 175–190.

[85] M. Vidyasagar, *Nonlinear Systems Analysis*, 2nd ed. SIAM, 2002.

[86] S. Wang, "The analysis of cavitation problems in the axial piston pump," *Journal of Fluids Engineering*, vol. 132, no. 7, p. 074502, 2010.

[87] R. Werndin and J.-O. Palmberg, "Controller design for a hydarulic transformer," in *The Fifth International Conference on Fluid Power Transmission and Control ICFP '01*, vol. 5, 2001, pp. 56–61.

[88] ——, "Hydraulic transformer in low-speed operation - a study of control strategies," in *The 5th International Symposium of Fluid Power, JFPS '02, Nara, Japan*, 2002.

[89] ——, "Hydraulic transformers - comparison of different designs," in *The Eighth Scandinavian International Conference on Fluid Power SICFP '03*, May 2003, pp. 163–174.

[90] G.-z. Yang and J.-h. Jiang, "Flow characteristics of variable hydraulic transformer," *Journal of Central South University*, vol. 22, pp. 2137–2148, 2015.

[91] L. Yi-ou, H. Yanong, Y. Jun, and L. Shen, "Simulation Study on Output Pressure Characteristics of Hydraulic Transformer Based on AMESim," *Hydromechatronics Engineering*, vol. 40, no. 19, pp. 104–108, 2012.

[92] R. Zhang, D. E. Carter, and A. G. Alleyne, "Multivariable control of an earthmoving vehicle powertrain experimentally validated in an emulated working cycle," in *ASME 2003 International Mechanical Engineering Congress and Exposition*. American Society of Mechanical Engineers, 2003, pp. 515–524.

Appendix A

Parameters for Hydraulic Transformer

Following physical parameters of this transformer were obtained from measurements of a 3.15 cc Micro Pump manufactured by Takako Industries.

Parameter or Constraint	Symbol	Value	Unit
Maximum Displacement of Rotating Group 1	$D_{1,max}$	3.15	cc
Maximum Displacement of Rotating Group 2	$D_{2,max}$	3.15	cc
Number of Pistons per Rotating Group	n	7	
Maximum swashplate angle	α_{max}	13	degrees
Maximum allowed rotation speed	ω_{max}	200	rad/sec
Maximum allowed output pressure		40	MPa
Piston diameter	d_p	9.1	mm
Piston assembly length	$L_{p,k}$	33	mm
Radial location of piston	R_p	15.3	mm
Shoe outer land radius	r_o	6.5	mm
Shoe inner land radius	r_i	3.5	mm
Piston leakage length at zero swash angle	L_0	25	mm
Piston chamber dead volume at zero swash angle	$V_{p,0}$	$3.43 \cdot 10^{-7}$	m^3
Piston bore clearance	c	8	μ m
Piston shoe average gap height	h_s	13.8	μ m
Valve plate average gap height	h_v	16.7	μ m
Valve plate parameter r1	r_1	9.8	mm
Valve plate parameter r2	r_2	12.8	mm

Valve plate parameter r3	r_3	17.3	mm
Valve plate parameter r4	r_4	22.3	mm
Barrel tip fraction		0.7	N/A
Bulk modulus of air-free oil	β	855	MPa
Discharge flow coefficient for orifice	C_d	0.5	
Fluid density	ρ	860	kg/m^3
Fluid absolute viscosity	μ	$5.855 \cdot 10^{-2}$	m^2/s
Piston eccentricity ratio	e	0.9	

Table A.1: Transformer Physical Parameters

Appendix B

List of Instrumentations

Following were used for the experimental setup

Device	Specifications	Manufacturer	Part Number
Data Acquisition Card	8 14-bit AD and DA 8 digital input and output 4 quadrature encoders, 4 counters/timers	Humusoft	MF-634
Data Acquisition Card	4 quadrature encoders	Measurement Computing	PCI-QUAD04
Flow Meter	0.063 - 126 cc/s	AW Gear Meters	JV30KG
Pressure Sensor	3000 psi	Honeywell	MLH03KPSB01A
Pressure Sensor	500 psi	Honeywell	MLH500PSB01A
Encoder	Optical, 100 count/rev	US Digital	HB6M-100-750-NE-S-H
3/2 Directional Valve	12 GPM, 50 ms response	Sun Hydraulics	DMDA-MBN
4/2 Directional Valve	12 GPM, 50 ms response	Sun Hydraulics	DMDA-MNN
Stepper Motor	320 oz-in torque	Annaheim Automation	23L306S-LW8
Motor Driver	200 to 12800 steps/rev	Annaheim Automation	MBC05641

Servo Valve	9.5 LPM	Moog	760C261A
Force Handle	15 kg capacity	Transducer Techniques	ESP-15
Force Sensor	250 lbf	Interface	SSM-AJ-250
Force Sensor	2000 lbf	Interface	SSM-AJ-2000
Cylinder	1.5 in bore 4.8 in stroke	Hydroline	HR5DC-1.5x4.8-N-0.63-1-S-H-B-1-1-J
Cylinder	25 mm bore 140 mm stroke	Parker	25BBHMI-TW14M140M1144
Operational Amplifier		Linear Technology	LT 1001
Operational Amplifier	100mA output current	Texas Instruments	LM 7171
Instrumentation Amplifier	Single gain gain set resistor	Linear Technology	LT 1920

Table B.1: Instrumentation